Convection and Magnetic Field Generation in Rotating Spherical Fluid Shells

von

Radostin D. Simitev

geboren am 29. Januar 1976
in Stara Zagora, Bulgarien

Zusammenfassung

In dieser Dissertation werden Resultate von numerischen und analytischen Untersuchungen der Konvektion und ihrer Dynamowirkung in rotierenden fluiden Kugeln und Kugelschalen dargestellt. Dieses Forschungsprogramm ist motiviert durch das geophysikalische Problem des Ursprungs des Erdmagnetfeldes und seiner Eigenschaften.

Umfangreiche numerische Simulationen wurden durchgeführt, um das Verständnis der physikalischen Komponenten und Mechanismen zu fördern, von denen angenommen wird, dass sie verantwortlich sind für die Erzeugung des geomagnetischen Feldes und seiner Variationen in der Zeit. Fragen wie die des linearen Einsetzens und der nichtlinearen Eigenschaften bei endlicher Amplitude der Konvektion, der Erzeugung und der Äquilibrierung von Magnetfeldern in elektrisch leitenden Flüssigkeiten, der nichtlinearen Rückkopplungseffekte der erzeugten Magnetfelder auf die Konvektion, der Oszillationen und kohärenten Prozesse in den turbulenten Bereichen und andere Fragen werden sowohl in Abhängigkeit von allen fundamentalen Parametern des Problems als auch für verschiedene magnetische, thermische und Geschwindigkeitsrandbedingungen und für einige sekundäre Annahmen wie die des elektrisch leitenden inneren Kerns und für verschiedene Temperaturprofile des Grundzustands untersucht. Wegen der fehlenden Kenntnis der Eigenschaften des Erdkerns und der unsicheren Details der Prozesse, die sich dort abspielen, ist diese Art der Forschung notwendig, damit Hilfsmittel für die Extrapolation zu realistischen Modellen des Geodynamos zur Verfügung gestellt werden können. Von besonderem Interesse sind die verschiedenen Arten der Oszillationen des Dipolfeldes. Im Gegensatz zu quadrupolaren und hemisphärischen Dynamos wurden dipolare Dynamos ursprünglich als nicht-oszillatorisch angesehen. Aber die sechs verschiedenen Arten von dipolaren Oszillationen, darunter die "unsichtbare", die in dieser Dissertation vorgestellt werden, haben diese Ansicht geändert. Die Erzeugung von Magnetfeldern durch Konvektion zeigt eine starke Abhängigkeit von der Prandtlzahl des Fluids. Diese Tatsache hat jedoch in der Vergangenheit wenig Aufmerksamkeit gefunden. Konvektionsgetriebene Dynamos für Prandtlzahlen größer als eins werden untersucht mit dem Ziel, die Gültigkeit der magnetostrophischen Approximation zu testen. Letztere stellt sich als nur schlecht gültig heraus für $P < 300$. Dynamos in diesem Bereich erfordern magnetische Prandtlzahlen Pm, die mit P anwachsen. Der gleiche Trend setzt sich für Werte von P unterhalb von eins fort. Für $Pm = P = 0.1$ wird ein hemisphärischer Dynamo gefunden im Fall des Rotationsparameters $\tau = 10^5$. Eine weitere Verringerung von Pm führt zum Abfall des Magnetfeldes unabhängig von der benutzten Rayleighzahl.

Zusätzlich zu den numerischen Simulationen und Parameterstudien beinhaltet die Dissertation auch eine analytische Studie der inertiellen Konvektion in rotierenden Kugeln im Limes kleiner Prandtlzahlen und hoher Rotationsraten. Explizite Ausdrücke für die Abhängigkeit der Rayleighzahl von der azimuthalen Wellenzahl und von dem Produkt τP sind abgeleitet worden und neue Resultate für den Fall des nahezu thermisch isolierenden Randes werden angegeben. Beschränkte Vergleiche mit den beobachteten Eigenschaften des geomagnetischen Feldes werden ebenfalls präsentiert. Ein Beispiel sind die torsionalen Alfvénwellen, die in den numerischen Simulationen dieser Dissertation gefunden wurden und die geophysikalisch relevant sind als möglicher Ursprung der beobachteten Impulse der Säkularvariation des Erdmagnetfeldes. Das Umklappen der Magnetfeldpolarität wurde ebenfalls in unseren Simulationen beobachtet. Die Intermittenz des Dynamos und die Wechselwirkung zwischen dipolaren und quadrupolaren Komponenten sind Voraussetzungen für ein aperiodisches Umklappen des Dipols in ähnlicher Weise wie im Fall des Erdmagnetfeldes. Die Gelegenheiten für quantitative Vergleiche mit geophysikalischen Beobachtungen sind jedoch ziemlich beschränkt wegen der Komplexität des selbst-konsistenten Dynamoproblems und wegen der beschränkten Computerkapazität für die numerischen Simulationen.

Abstract

The dissertation reports results from numerical and analytical studies of convection and dynamo action in rotating fluid spheres and spherical shells. This research is motivated by the geophysical problem of the origin and properties of the Earth's magnetism.

Extensive numerical simulations are performed in order to advance the understanding of the basic physical components and mechanisms believed to be responsible for the generation and the variations in time of the main geomagnetic field. Questions such as linear onset and nonlinear finite-amplitude properties of rotating convection, generation and equilibration of magnetic fields in electrically conducting fluids, nonlinear feedback effects of the generated magnetic fields on convection, spatio-temporal structures of magnetic and velocity fields, oscillations and coherent processes in turbulent regimes and other questions are studied in dependence on all basic parameters of the problem, as well as for various choices of the magnetic, thermal and velocity boundary conditions and for some secondary assumptions such as a finitely-conducting inner core and various basic temperature profiles. Because of the lack of knowledge of the properties of the Earth's core and the uncertain details of the processes that take place there, this research is necessary in order to provide the tools for extrapolation to realistic models of the geodynamo. Of particular interest are various types of oscillations of dipolar fields. In contrast to quadrupolar and hemispherical dynamos dipolar dynamos have been originally considered to be non-oscillatory. But the six different types of dipolar oscillations, among which is the "invisible" one, reported in this dissertation alter this view. Generation of magnetic fields by convection shows a strong dependence on the Prandtl number P of the fluid. But this fact has received little attention in the past. Convection-driven dynamo action at Prandtl numbers larger than unity is studied with the goal to test the validity of the magnetostrophic approximation. The latter is found to be poorly satisfied for $P < 300$. Dynamos in this regime require magnetic Prandtl numbers Pm which increase with P. The same trend continues to hold for values of P less then unity and this regime thus seems to be best suited to reach the goal of minimal values of Pm. For $Pm = P = 0.1$ a hemispherical dynamo is obtained in the case of a rotation parameter $\tau = 10^5$. A further reduction of Pm leads to a decay of magnetic field irrespective of the Rayleigh numbers used.

Apart from numerical simulations and parameter studies of basic physical mechanisms, the dissertation includes an analytical study of inertial convection in rotating spheres in the limit of small Prandtl numbers and large rotation rates. Explicit expressions for the dependence of the Rayleigh number on the azimuthal wavenumber and on the product of $P\tau$ are derived and new results for the case of a nearly thermally insulating boundary are obtained. Limited comparisons with actually observed features of the geomagnetic field are also presented. An example are the torsional Alfvén waves found in the numerical simulations of this dissertation. They are geophysically relevant as a possible cause for the observed secular variation impulses of the Earth's magnetic field. Reversals of the magnetic field polarity have also been observed in our simulations. Dynamo intermittency and interaction between dipolar and quadrupolar components are preconditions for aperiodic dipolar reversals similar to those of the Earth's main field. However, the opportunities for quantitative comparisons with geophysical observations are rather limited by the complexity of the self-consistent dynamo problem and by the computational restrictions of our numerical simulations.

Contents

1. Introduction

1.1 Topic of dissertation

That the Earth is magnetic has been known for thousands of years [96], but the reasons for this and for the many puzzling features of the Earth's magnetic field have been explained on sound physical grounds only during the last century. It is now widely accepted that the main magnetic field of the Earth, as well as those of a great variety of cosmical objects, are generated by dynamo processes [102]. According to dynamo theory, motions of a conducting fluid may amplify an initial magnetic field from arbitrary small amplitudes and sustain it at finite intensity against ohmic dissipation [89]. Seismological and other geophysical studies, indeed, find that the outer core which is a significant part of the Earth's deep interior is fluid and mainly composed of electrically conducting molten iron [85]. Further estimations of the material properties of the Earth indicate that the fluid outer core must be in a vigorously convecting turbulent motion [115]. Thus, it is ideally suited to host a dynamo process which could generate the main geomagnetic field. In mathematical terms dynamo theory seeks solutions of a combination of the governing equations of fluid mechanics and electrodynamics [104] and in the case of the Earth also of those of thermodynamics and physical chemistry [9]. Because of the nonlinear nature of these equations which have no known analytical solutions in their geophysically relevant form, the geodynamo problem is a challenging one which has been in the focus of intensive research for more than half a century but is still far from being fully understood [18]. Nonlinear numerical simulations represent a promising path of research since they provide the only method to obtain self-consistent three-dimensional solutions and model the geodynamo process from first principles without drastic over-simplifications [79]. The past decade has, indeed, seen significant advances in computational simulations of convection and magnetic field generation in the Earth's core with many workgroups taking part in the effort [56, 76, 80, 30, 94, 105, 59, 71] and others. Although dynamically self-consistent models of the geodynamo have simulated magnetic fields that appear in some ways quite similar to the geomagnetic field, none are able to run in an Earth-like parameter regime because of the considerable spatio-temporal resolution that is required [103].

The dissertation reports results from numerical and analytical studies of convection and dynamo action in rotating fluid spheres and spherical shells. The research is motivated by one of the fundamental problems of Geophysics – the problem of the origin and properties of the Earth's magnetic field. In order to overcome the deficiencies of computational methods and technology and the uncertainties connected with the roughly estimated material properties of the Earth's deep interior, two strategies of numerical simulations have been pursued. On the one hand detailed models that attempt to include as many secondary effects and to come as close to geophysically realistic parameter values as possible have been attempted [56, 80]. However, this choice requires introduction of artificial assumptions such as hyperdiffusivities, spurious symmetries etc., which might modify the very dynamics of the dynamo process and lead to non-realistic effects [128, 61]. Those models still remain remote in their parameter values from geophysical realism. This dissertation follows a second approach to the topic advocated by [30, 59]. The basic equations are solved numerically without introduction of

additional assumptions. The parameter range is more limited but the spatio-temporal properties of the convection and dynamo process, the mechanisms of magnetic field generation, the nonlinear saturation of magnetic fields and their influence on convection may be studied in detail. It is believed that the same basic processes operate not only at the parameter values within reach but at those of the Earth as well. Thus, it is both of geophysical as well and of more general dynamical interest to explore the parameter dependences of those phenomena [23] in order to provide tools for extrapolation to realistic geodynamo models. Apart from clarification and parameter studies of basic physical mechanisms, the dissertation includes an analytical study of rotating convection in the limit of small Prandtl numbers and large rotation rates as well as attempts some comparisons with actually observed geomagnetic features. However, the opportunities for analytic studies and direct geophysical implications are rather limited by the complexity of the self-consistent dynamo problem and by the computational restrictions on the numerical simulations.

1.2 Structure of dissertation

The general structure of the dissertation is best reflected by its Table of Contents, while the most important results and an outlook to future research objectives are presented in the concluding chapter 9. Therefore, here we restrict to several notes. To compensate this short introduction, the dissertation starts with the introductory chapter 2. It's purpose is not to provide a comprehensive description of dynamo theory but rather to outline the place of the research topics reported in the dissertation among the other branches of the field, to provide physical motivation, to list some open questions driving the research, and to justify the choices made. Chapters 3 and 4 provide a rigorous mathematical formulation of the problems considered in the thesis and a description of the numerical methods used for their solution. Two major subtopics of research are pursued in the dissertation – non-magnetic rotating spherical convection and convection-driven dynamos. The non-magnetic convection problem is essential for understanding the properties of the Earth's magnetic field. Convection is responsible for the majority of features of dynamo solutions. In fact, self-sustained magnetic fields may be considered as a bifurcation from a non-magnetic convective state [23]. For this reason a large part of the thesis is devoted to studies of convection in rotating fluid spheres and spherical shells. The results of these studies are presented in chapters 5 and 6 which discuss linear and finite-amplitude properties of convection, respectively. Except near onset of convection, the generated magnetic fields exhibit chaotic spatio-temporal behavior which has no simple description. Extensive numerical simulations of convection-driven spherical dynamos are performed, spanning the computationally accessible parameter space and employing several possibilities for the magnetic and mechanical boundary conditions in order to study this behavior. Thus, chapter 7 is necessary to provide a first account and typical examples of the most characteristic features of the dynamo solutions reported in the dissertation and to outline those regions in the parameter space where our main computational efforts have been concentrated. The spatio-temporal chaos of the magnetic solutions is then most conveniently described in two parts. The time- and space-averaged properties of magnetic fields, and its effects on convection as functions of the parameters of the problem are presented in chapter 8. The spatio-temporal structures of dynamo solutions, such as coherent structures, oscillations, intermittency, reversals etc., are discussed in chapter 9. Reversals and torsional oscillations are of special interest since they may be related to actual geomagnetic observations. The last sections of chapter 9 are devoted to a discussion of those topics.

1.3 List of relevant publications

The thesis is directly connected to the following publications in which results of this doctoral work have been or will be published:

- Journals

(1) **Simitev, R.**, Busse, F.H., *Patterns of convection in rotating spherical shells*, New J. Phys., **5**, pp. 97.1–97.20, 2003.

(2) Busse, F.H., **Simitev, R.**, *Inertial convection in rotating fluid spheres*, J. Fluid Mech., **498**, pp. 23–30, DOI: 10.1017/S0022112006947, 2004.

(3) **Simitev, R.**, Busse, F.H., *Prandtl number dependence of convection driven dynamos in rotating spherical fluid shells*, (submitted to JFM).

- Reviewed Collections

(4) Grote, E., Busse, F.H., **Simitev, R.**, *Buoyancy driven convection in rotating spherical shells and its dynamo action*, in "High Performance Computing in Science and Engineering '01", E. Krause, W. Jäger, (eds.), Springer, pp. 12–34. 2001.

(5) **Simitev, R.**, Busse, F.H., *Parameter dependences of convection driven spherical dynamos*, in "High Performance Computing in Science and Engineering '02", E. Krause, W. Jäger, (eds.), Springer, pp. 15–35, 2002.

(6) Busse, F.H., Grote, E., **Simitev, R.**, *Convection in rotating spherical shells and its dynamo action*, in "Earth's Core and Lower Mantle", C.A. Jones, A.M. Soward and K. Zhang, (eds.), Taylor & Francis, pp. 130–152, 2003.

(7) Busse, F.H., **Simitev, R.**, *Convection in rotating spherical fluid shells and its dynamo states*, in "Fluid Dynamics and Dynamos in Astrophysics and Geophysics" A.M. Soward, C.A. Jones, D.W. Hughes, N.O. Weiss (eds.), Taylor & Francis, *(to be published, 2004)*.

(8) **Simitev, R.**, Busse, F.H., *Spatio-temporal structures of convection and convection-driven dynamos in rotating spherical fluid shells*, in "High Performance Computing in Science and Engineering '04", E. Krause, W. Jäger, (eds.), Springer, 2005, *(submitted)*.

- Proceedings, Technical Reports

(9) Busse, F.H., **Simitev, R.**, *Current state and future challenges of the dynamo theory of planetary magnetism*, in Proc. 5th International PAMIR Conference "Fundamental and Applied MHD", Ramatuelle, A. Alemany (ed.), LEGI Grenoble, pp. L1–L13, 2002.

(10) **Simitev, R.**, *Inertial wave convection in rotating spherical fluid shells*, in "2002 GFD Program on Bounds of Turbulent Transport", J. Whitehead (ed.), Woods Hole Oceanographic Institution Technical Report, WHOI-02-16, Woods Hole, MA, pp. 148-175, 2002.

(11) Busse, F.H., **Simitev, R.**, *Convection in rotating spherical fluid shells*, in "Mathematical Aspects of Natural Dynamos", E. Dormy (ed.), Caramulo, *(to be published, 2004)*.

2. Dynamo Theory of Geomagnetism

A fundamental goal of geophysics is to explain the origin and properties of the main magnetic field of the Earth. The topic has long been a source of fascination for natural philosophers[1], but only in the last half a century with the emergence of **dynamo theory** a sound physical theory of geomagnetism has been developed. Although a purely classical theory, geodynamo theory is in the forefront of modern geophysical and applied mathematical research because of the thrilling challenges if faces:

Lack of observational data. Measurements of the geomagnetic field are provided by a dense network of magnetic observatories, by airborne and satellite surveys and by paleomagnetic records extending to about 200 Ma ago [96]. Nevertheless, the collected data appears to be incomplete because no direct observations of the conducting fluid outer core of the Earth are possible. The nearly three thousand kilometer thick mantle renders inaccessible for measurement the entire toroidal part of the field which probably accounts for about half of the intensity in the Earth's core as well as the small scale features of the poloidal part which decay faster with distance than the large scale ones. The material properties, the composition elements, the precise structure and dynamics of the core and lower mantle are poorly known for the same reason [85]. Furthermore, even the detailed recent observations cover at best a few centuries which is a minute period in comparison with the geological time scale and the time scales of the variations of the main geomagnetic field.

General difficulty of relevant experiments. Self-excited magnetic fields have been generated by dynamo action under laboratory conditions only very recently [91], [52]. The technical challenges of attaining high magnetic Reynolds numbers make these experiments so difficult that in the near future they are likely to provide only a confirmation of theoretical ideas rather than an useful guidance and insight. The laboratory investigation of thermal convection which is believed to be the main type of motion within the Earth's core is more feasible [27, 66]. Experimental studies of the material properties of the core and lower mantle are difficult because of the extremely high pressures of about $130 - 330$ GPa which would be necessary to reproduce the real conditions in the deep interior of the planet.

Nonlinear nature of the governing partial differential equations. The geodynamo is governed by the coupled equations of fluid mechanics, electrodynamics, thermodynamics and physical chemistry [9]. They form a highly nonlinear and non-local system of partial differential equations which are in general intractable in analytical form and even their partial mathematical analysis is largely nontrivial. For instance, the Navier–Stokes equations [53] which describe fluid motions of gases and liquids in both laminar and turbulent flows on scales ranging from below a millimeter to astronomical lengths have been known and studied already for about two hundred years. Nevertheless, they continue to pose formidable mathematical challenges such as resolving the mathematical questions of existence, uniqueness,

---

[1] For instance, W Gilbert, author of *"De Magnete"*, London, (1600). This text is regarded as one of the first scientific texts written after the decline of the ancient Greeks and Romans. It is based on experimental observations and predates Galileo's *"Dialogues"*, (1624) and Newton's *"Principia"*, (1687).
C.F. Gauss provided the first mathematically consistent description of the geomagnetic field as a decomposition in spherical harmonics presented in his *"Allgemeine Theorie des Erdmagnetismus"*, Leipzig, (1839).

and regularity of solutions, and the more physical questions of giving an effective mathematical description of turbulence, boundary-layer behavior and many others. The fact that the geodynamo problem involves two further partial differential equations with a complicated nonlinear feedback between magnetic and velocity fields certainly makes neither the problem easier nor the dynamics simpler. In view of the principle inaccessibility of "explicit" analytical solutions, one has to resort to numerical and topological analysis of the problem.

In summary, huge but incomplete data, impossibility of conducting crucial experiments, imprecise knowledge of key material values and lack of understanding of important physical ingredients coupled with severe difficulties of treating nonlinear models make the description of the geomagnetic field a highly nontrivial problem. These formidable challenges turn geodynamo theory into a key to the successful clarification of a number of other problems:

Planetary and cosmical magnetic fields. Intrinsic magnetic fields are an important property of virtually all types of celestial objects – meteorites, planets, stars, galaxies, clusters of galaxies and extracluster formations [45], and it is widely believed that many of them could be explained by some type of dynamo theory. Geodynamo theory is particularly relevant as an explanation of the magnetic fields of the other planets in the Solar system.
Earth's interior structure and dynamics. Geomagnetism is an integral part of geophysics. The terrestrial field is used as a diagnostic tool for probing the depth of the Earth and study properties of the upper mantle and the crust such as conductivity, to look for petroleum and mineral deposits, etc. But a well-developed dynamo theory could have a much deeper contribution to Earth sciences. Because the main field is generated by motions within the planet, forward and inverse modeling of the geomagnetic field based on a physical theory would necessarily reveal most of the basic facts about the composition, structure and dynamics of the Earth's deep interior.
Novel physical, mathematical and computational methods. The severe challenges due to the nonlinear nature of its governing equations place dynamo theory in the center of exciting theoretical research. The dynamo problem is related to a number of topics in magnetohydrodynamics (MHD), geophysical fluid dynamics, turbulence, stability theory and numerical methods. The research on the dynamics of rotating fluids and convection is of interest to meteorology and oceanography. Since dynamo theory is essentially a study of nonlinear partial differential equations, progress on this particular topic may have deep implications on the studies of other processes described in similar mathematical terms. MHD itself could be considered one notable example since the very idea of merging fluid dynamics and electrodynamics was born in the attempt to explain the Solar magnetic field. At present MHD is a well-developed field with many applications in astrophysics, plasma physics, metallurgy and a wealth of mathematical and computational techniques. Overviews of the methods used in geodynamo theory are given in [38, 103, 18, 52].

The purpose of this chapter is threefold. First, in order to provide a physical motivation for the study of the dynamo problem the large scale natural magnetic fields in the Universe and on the Earth will be described in section 2.1. Second, dynamo theory will be briefly outlined in section 2.2 in order to put the results presented in the dissertation in a wider context. Third, the choice of research questions addressed in this report will be justified by presenting some open questions of the theory in section 2.3.

2.1 Phenomenology and physical motivation

The electroweak interaction is one of the fundamental interactions in Nature along with the gravitational and the strong ones. The fact that it acts at all distances ranging from 10^{-13}

m to 10^7 m determines its central role in a major part of physics. A manifestation of the electromagnetic interaction is, for example, provided by the existence of large scale natural magnetic fields in the Universe. Apart from being a thrilling subject of mathematical study, these fields are thought to play a profound role in the cosmical evolution. The electric and magnetic fields are, of course, manifestations of a more fundamental object – the electromagnetic field since at a deeper level Maxwell's equations can be deduced from Coulomb's law plus Lorentz transformation of special relativity. Nevertheless, from a classical viewpoint and in many practical situations the electric and magnetic phenomena can be considered separately. Such is the case in MHD where the electric fields play only a secondary role as shown in section 3.2.5.

2.1.1 Cosmical magnetic fields

Cosmical objects of virtually all types and scales – from the tiniest meteorites through planets and stars to galaxies and clusters of galaxies possess magnetic fields [45]. These magnetic fields exhibit a variety of spatial structures, time variations, intensity and origin and play a major role in many astrophysical processes. Although they rarely contain more than a tiny fraction of the total energy of the corresponding astronomical object they may have a significant impact on the transport processes occurring in the interior and the surroundings of the cosmical object. Magnetic fields are found to significantly influence convection, diffusion, angular momentum distribution, accretion, cosmic ray distribution and other phenomena. Thus they can modify, if not completely control, the evolution of cosmical objects and the mutual interactions between them.

Solar and stellar magnetic fields. The most intense magnetic fields ever observed belong to the stars. Because of the great astronomical distances, the finest details of the structure, variation, and strength of the stellar magnetic fields can be resolved sufficiently well only in the case of the **solar magnetic field**. The solar convection zone, photosphere and corona are largely influenced, even dominated, by the solar magnetic field which consists of a global field with an intensity of about 10^{-4} T and very intense local fields associated with a variety of small structures visible on the solar surface. At high latitudes the global field has a dipolar structure while at lower latitudes it consists of four sectors of alternating polarity twisted in spiral-like fashion away from the Sun due to its rotation. The most characteristic examples of local magnetic fields are those associated with *sunspots*. The sunspots are darker regions on the solar surface with typical diameters of about 10^3 to 10^4 km. They are highly magnetic with intensities of about 0.1 T and appear dark because magnetic fields of such a strength suppress convection and reduce heat transport. The solar field has a 22-year period in which the number and polarity of sunspots show a cycle and the global dipole reverses. A variety of other local magnetic structures such as *coronal streamers, prominences, loops, solar flares, plages* etc. are also observed. The temperatures in the photosphere and the corona are sufficient to supply kinetic energy to charged particles to escape the Sun's gravitational attraction and form a conducting *solar wind*. The influence of the solar magnetic field and the solar wind are detected far beyond Saturn and probably Pluto. For instance, this **interplanetary magnetic field** has an intensity of about 5 nT in the neighborhood of the Earth and is responsible for the short term variations of the geomagnetic field.

Other **main sequence stars** also possess magnetic fields which are believed to share many common features with the solar field. Starspots and magnetic field reversals are observed although their detailed structure is difficult to resolve. Other types of stars are even more magnetic. The *Ap* or *peculiar stars* have fields of the order of 1 T but a strange feature is that they do not have convection zones where these fields might be generated. The *neutron stars*,

the *white dwarfs* and the *X-ray stars* have magnetic fields of about 10^4 to 10^7 T. Most of these objects are in the final stage of their evolution and represent extremely compact bodies with immense mass. Their fields are believed to be so intense because of the compression of the magnetic field of the progenitor stars to volumes as small as the volume of a neutron star (≈ 10 km^3). Recently, *magnetars* which are believed to be the most magnetic objects in Nature have been discovered. They represent a peculiar source of γ- and X-rays with an intensity of the magnetic field of about 10^{14} T. They glow quietly in the X-ray region for several years then suddenly become vigorously active for a period of a few weeks to months and emit bursts of γ-rays with luminosities billions of times higher than that of the Sun. The explanation is that as magnetar's colossal magnetic field drifts through the solid crust of the star it might crack it and produce a starquake. Since the magnetar is very conductive, the starquake will generate Alfvén waves which in turn accelerate clouds of particles with immense energy into the interstellar space. At this field strength the magnetic confinement is so strong that the space available to an electron becomes comparable to the smallest region within which it can be localized quantum-mechanically.

Galactic and extragalactic fields. Magnetic fields of significant strength are detected on yet larger scales. Most **spiral galaxies** have fields with intensity of about 10^{-9} T. The energy density of the magnetic fields is comparable with the energy densities of the other components of the interstellar medium – the *cosmic rays* and the *interstellar gas*, an observation known as *equipartition of energies*. Usually a pronounced *regular* and a *fluctuating* component of the field may be distinguished. The regular component have length scales comparable with the visible disk of spiral galaxies and consists of *magnetic spiral arms* analogous to the material spiral arms but sometimes situated between them. The regular field strength increases towards the center of galaxies. The intensity of the total magnetic field of our Galaxy, **the Milky way**, is $6\pm2\times10^{-10}$ T locally and that of its local regular field is only $4\pm1\times10^{-10}$ T. The Galactic field is particular in that it features reversals which have been rarely detected for external galaxies. **Elliptical, barred and irregular galaxies** are also known to be magnetic but the available data is less detailed. In contrast to spirals their fields appear to be more random and with lengths much smaller than the galactic scale.

Observations on even larger scale show the existence of magnetic fields in **clusters of galaxies** and even **extracluster formations**. Estimates of the intensity of their regular components range from 2×10^{-11} to 3×10^{-10} T. There are no detections of a purely **cosmological magnetic field**, i.e. a field which is not associated with any gravitationally bound or collapsing structure or which has a length scale greater than the scale of the largest known structures in the Universe (50 Mpc).

2.1.2 The geomagnetic field

The geomagnetic field has been among the very first subjects to provoke scientific interest. It is central to the present report and we briefly touch on its phenomenology.

The Earth's interior. The nature of the Earth's deep interior is deduced from seismological, geomagnetic and other geophysical observations (paths of earthquake waves traveling through the Earth, experiments on surface minerals and rocks at high pressure and temperature, motions of the Earth in the Solar System, its gravity and magnetic fields, heat flow from inside the Earth etc.). Our planet consists concentrically of a solid inner core, a fluid outer core, a solid rocky mantle and a thin crust on the very surface of the Earth. The fluid in the **outer core** is believed to be well-mixed and therefore homogeneous and in an adiabatic thermal state. However, there might be layers especially at the top which are stably stratified. The seismic observations indicate that the **inner core** has a finite rigidity but perhaps is not

Table 2.1. *Main constituent fields and their properties.*

Constituent field	Location source	Intensity (max.)	Morphology	Time variation
1) Main field	outer core	50000 nT (70000 nT)	mainly dipole	secular variation $\sim 10^3$ yrs; reversals $\sim 10^6$ yrs
2) Local field	crust above Curie point	mean 100 nT (as high as 10^5 nT)	very irregular wave lengths as short as 1 m	none
3) Regular storm field	magnetosphere	150 nT (500 nT)	approx. uniform external field	4 to 10 h; recovery – 2 to 3 days
4) Irregular storm field	ionosphere, magnetosphere	100 nT (200 nT in Aurora)	global but more intense near Aurora	5 to 100 min
5) Diurnal variation	ionosphere	50 nT (200 nT)	global; mainly P_2^1, P_3^2 harmonics	periodic 24, 12, 8 h
6) Pulsations	magnetosphere	few nT	quasi-global	quasi-periodic 1 sec to 30 min
7) Induced fields	crust, upper mantle, oceans	about $\frac{1}{2}$ of above four fields	global but irregular in places	same as above four fields

completely solid. Rather it might be a mushy semi-frozen mixture of solid and liquid phases at a temperature close to the solidification temperature. The composition of the core is not precisely known but cosmochemistry and high pressure studies show that it is composed primarily of some iron-rich alloy with an admixture of less dense nonmetals. The most likely other metal in the core is Ni, while Si, S, O and H have been proposed as possible nonmetallic constituents. An important question is whether a sufficient amount of radioactive elements are present in the core to produce significant heating which can serve as an energy source driving the liquid core motions. Most likely candidates are ^{40}K, ^{232}Th, ^{235}U, and ^{238}U.

The **mantle** itself consists of several layers with significant differences in structure, composition, and dynamics. Its properties especially in the lower part are not precisely known. For our purposes the mantle can be considered a solid insulator which due to its thickness contributes more to the obstruction of the magnetic field than to its generation. However, above the core-mantle boundary an anomalous layer called D''-layer has been identified. It is approximately 150 – 200 km thick and might play an important role in the geodynamic and geothermal behavior. The D''-layer is the most probable source of mantle plumes of hot material that emerge from the Earth's deep interior and give rise to hot spots important in plate tectonics. The thermal, electric, and topological properties of D'' determine the degree of thermal and dynamic coupling between the core and the mantle through a possible influence on the outward transport of heat from the Earth's core or introduction of electromagnetic or viscous forces that could affect the process of field generation. The **crust** is the main source of the anomalous or crustal magnetic field but has no role in the generation of the main field.

Further details of properties of the Earth's interior and estimates for the values of its material parameters are provided in references [85, 103].

Constituent fields. The field measured at the surface of the Earth is a vector sum of a number of constituent fields. They originate in different locations and have very different spatio-temporal scales and dynamical behavior. Their superposition results in a complex

field the variations of which range over many orders of magnitude: the time variations extend from well over 10^3 Hz where they merge into the radioelectric noise spectrum to probably more than 100 million years while the spatial variations range from meters to thousand of kilometers. The various constituent fields may be classified by a number of criteria but probably the most illuminating one is the classification based on their physical origin. Four major parts may be identified: **(1)** the external field, **(2)** the induced field, **(3)** the local (crustal) field and **(4)** the main field. A more precise account of the major constituent fields, their place of origin, morphology, intensity and time variation is given in table 2.1. Since a theory of the main field is the subject of the dissertation, we proceed to describe some of its properties and abandon the other constituents which represent large subjects of their own.

The main field. The main field shows both temporal and spatial variations with typical scales ranging from 0.1 yr to possibly more than 100 million yrs and from roughly about 3000 km to tens of thousands of kilometers, respectively. The shortest time variation with a period of the order of 1 yr or less is the so called *geomagnetic jerk* and the shortest length scale of a main field feature which can be measured at the surface of the Earth is about 3000 km. Observational methods for measuring the present day field as well as for extracting information about it from archaeological or geological sources have been developed. Although these methods have their difficulties and yield large error bars a number of large datasets of reliable measurements of the elements describing the geomagnetic field are presently available. The observations can be conveniently assigned to one of the three time records: recent (10 - 100 yrs), archaeomagnetic ($10^2 – 10^4$ yrs) and paleomagnetic record ($> 10^4$ yrs ago).

The morphology of the main field is well known only for the recent field. Figure 2.1 represents its total intensity at epoch 2000. Worthy of note is the maximum values of about 65000 nT in the north in Canada and Russia and in the south in Antarctica. The lowest value of about 20000 nT occurs in South America and it is the reason why charged particles from the ionosphere and magnetosphere penetrate down to very low altitudes in this region. Besides the chart of the total intensity the magnetic field is traditionally represented by a number of charts of other *field elements* such as the *horizontal intensity* H, the *vertical component* Z of the magnetic field vector, the angles of *declination* D from the geographic North and *inclination* I from the horizontal direction. Apart from the graphical representations the field can be expressed in a convenient mathematical form by the geomagnetic potential,
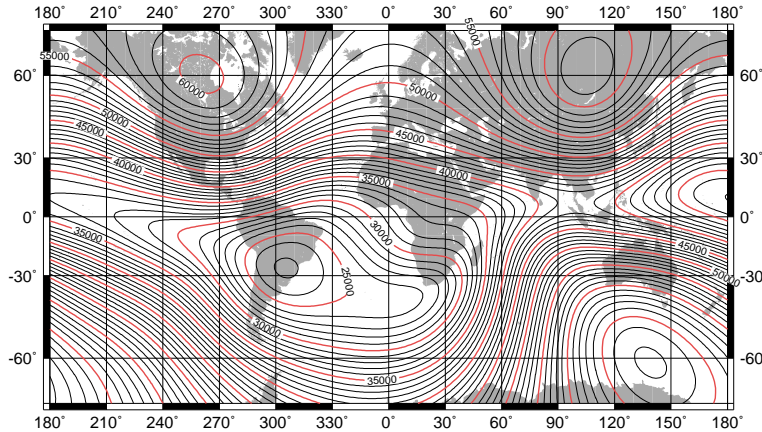
$$\Psi = R \sum_{l,m} \left(\frac{R}{r} \right)^{l+1} P_l^m(\cos\theta)(g_l^m \cos m\varphi + h_l^m \sin m\varphi), \qquad (2.1)$$

where g_l^m, h_l^m are called *Gauss coefficients*, R is the radius of the Earth and P_l^m are the Legendre functions. If it is assumed that the mantle is an insulator this expression gives the field everywhere outside the core as

$$\boldsymbol{B} = -\nabla\Psi. \qquad (2.2)$$

Since detailed description of the phenomenology of the main field is outside the scope of the thesis, we only enumerate some of its most interesting features and refer the reader to [42].

- The main magnetic field existed over at least 70% of the geological time.
- **Dominance of the axial dipole.** About 90% of the magnetic field energy at the surface of the Earth is due to a dipole moment which is described by the g_1^m and h_1^m coefficients in (2.1). Its axis is called the *geomagnetic axis* and is inclined at about 11° to the Earth's rotation axis. The points where the geomagnetic axis intersects the surface are the *geomagnetic poles*. They differ from the *magnetic poles* defined as the locations where the

Fig. 2.1. *World Magnetic Chart of total intensity (in nT) of the main geomagnetic field at Earth's surface based on IGRF (International Geomagnetic Reference Field) at epoch 2000.*

magnetic field vector $\boldsymbol{B}$ is perpendicular to the surface. Paleomagnetic studies show that the axial dipole has dominated throughout geological past. This is the most characteristic feature of the main geomagnetic field.

- **Westward drift.** The main magnetic field changes in time. This variation is called the *secular variation.* One of the best known features of the secular variation is the westward drift of some features of the main field at about $0.2°$ per year. Examples of such features are the point of zero declination, the region of maximum declination, the nondipole field etc. Features that do not exhibit a westward drift also exist.

- **Other main characteristics of the recent secular variation.** Apart from the westward drift, other noticeable time variations are **(1)** decrease in the dipole moment, $\partial_t g_1$, $\partial_t g_1^1$, $\partial_t h_1^1$, and **(2)** northward shift of the axial dipole, $\partial_t g_2$.

- **Magnetic field polarity reversals.** One of the most spectacular phenomena in geophysics are the magnetic field polarity reversals [88] during which the north magnetic pole is replaced by the south magnetic pole and vice versa. Although the details of the reversal process are incompletely understood, the occurrence of reversals is well-documented in volcanic rocks, sediments and oceanic magnetic anomalies. The main field has no preference for one polarity over the other. The reversal frequency has not been constant through geological time. In the last 20 Myrs it is about 5 per Myr but steadily decreases as we go back in time. Between 85 and 125 Myrs ago there was a long interval without any reversal known as the Cretaceous Long Normal (CLN) Interval (Superchron). The change in polarity is estimated to take 2000 to 5000 years. The change in polarity is accompanied by a preceding decrease in intensity of about 20% of its pre-reversal value and subsequent increase after the change has been completed.

- **Other time and space variations.** Further observations some of which controversial are: **(1)** geomagnetic impulses (jerks); **(2)** patches of intense magnetic field at high latitudes at both hemispheres; **(3)** excursions during which the magnetic poles wander far away from the geographic poles the field does not reverse its polarity; **(4)** reversals dominated by nondipole components; **(5)** oscillations of the dipole moment and others.

2.2 Overview of dynamo theory

The marvels of the large scale natural magnetic fields and in particular the terrestrial magnetic field can hardly be described on few pages. But the most intriguing part of their study still lies ahead – a theory that could explain the observed phenomena from first principles has to be developed. In this section we will provide a brief overview of dynamo theory – the modern theory aspiring to explain the magnetism of cosmical objects.

2.2.1 The dynamo problem

It has been known for centuries that the Earth is magnetic but the reason for this and for the many puzzling features of the Earth's magnetic field have been convincingly explained only during the last century. A key discovery was made by Oldham in 1906 that the Earth possesses a fluid core. Further seismological and density considerations pointed out that the liquid in the Earth's deep interior is most probably molten iron with significant electrical conductivity. In view of these facts the original idea proposed by Larmor [83] in 1919 that a possible dynamo mechanism could explain the properties of the magnetic fields in sunspots became very appropriate in terrestrial context and was later adopted by Elsasser [48] in 1946 and Bullard [10] in 1949 to solve the problem of geomagnetism. At present this idea is generally accepted, widely studied and has a number of observational and mathematical confirmations. However, many important questions still remain open such as those concerning the energy source driving the fluid motions and the precise physical state of the Earth's interior.

According to the *dynamo hypothesis*, motions within the outer conducting liquid core can amplify a magnetic field from arbitrary small amplitudes and sustain it at the observed finite strength against ohmic dissipation. The mathematical formulation of this idea and the notation are presented in detail in Chapter 3 of the dissertation. The evolution of the magnetic field is governed by the *induction equation* (3.28). The fluid velocity appearing in it is not an arbitrary field but must be subject to the constraints imposed by the general equations of fluid dynamics, i.e. the *conservation laws of mass* (3.3), *momentum* (3.12) and *energy* (3.19). Equations describing less important physical effects such as compositional convection, conductivity of the inner core etc. may also be included. The general dynamo problem requires solution of those basic equations under the relevant boundary conditions and in the appropriate parameter regime. Even in simple approximations, this is clearly a formidable task which is far from being achieved. Fortunately, progress can be made as the problem is attacked at various levels of complication and below the traditional division of the theory into *Kinematic Theory* and *Fully Self-Consistent Theory* will be briefly outlined.

2.2.2 Kinematic theory

The kinematic problem. A substantial simplification of the general dynamo problem can be achieved if the fluid dynamical equations (3.3) and (3.12) are discarded and instead an arbitrary velocity field $\boldsymbol{u}$ is prescribed. Then only the magnetic induction equation (3.28) need to be considered. Such a reduction of the problem is called the *kinematic dynamo problem* [104, 18, 19, 20]. Mathematically, it is a linear homogeneous problem for the magnetic field $\boldsymbol{B}$. Written in a non-dimensional form,

$$\frac{\partial}{\partial t}\boldsymbol{B} = Rm\nabla \times (\boldsymbol{u} \times \boldsymbol{B}) + \nabla^2\boldsymbol{B}, \tag{2.3}$$

it depends on a single parameter called the *magnetic Reynolds number* $Rm = Ud/\lambda$ which gives the ratio between the magnitude of the advective and diffusive terms where U and d are typical velocity and length scales and d^2/λ is a time scale.

Excluding irrelevant choices for the prescribed velocity $\boldsymbol{u}$ and situations such as fields growing to infinity or magnetic solutions due to sources of the field (chemical EMF, permanent magnetism, etc.) the main problem of the kinematic theory is to answer the questions: *Can a prescribed velocity field $\boldsymbol{u}$ of bounded kinetic energy in a fluid of finite conductivity sustain a magnetic field $\boldsymbol{B}$ of non-vanishing energy as time increases to infinity? What should the structure of the flow $\boldsymbol{u}$ be? What will the structure of the solution $\boldsymbol{B}$ be? Can a physical mechanism be identified?*

Antidynamo theorems. The first of these questions may sound rather surprising in view of the well-known "bicycle" disk dynamo which can certainly sustain magnetic field if kept at motion. The analogy is justified but misleading since the disk dynamo is multiply-connected and highly asymmetric device with a very complex conductivity distribution which allows generation of magnetic field by simple rotational motion. Just the opposite extreme is represented by the homogeneous fluid dynamo which is simply-connected with uniform conductivity distribution and thus requires very complex three-dimensional motions in order to support self-excitation of magnetic fields. Indeed, early in the history of dynamo theory Cowling [43] suggested his famous theorem stating that an axisymmetric (or two-dimensional) magnetic field cannot be maintained by dynamo action. Since the observed terrestrial field is in first approximation exactly of this kind the result cast severe doubts in the validity of the dynamo hypotheses. But because no other reasonable hypotheses seemed to exist, it became imperative to either establish the existence of homogeneous dynamos or to rule them out by a general anti-dynamo theorem. Fortunately Nature favors the first possibility. The existence of magnetic fields sustained by dynamo process in a singly connected volume of a homogeneous fluid was rigorously proved by Backus [4] and Herzenberg [67] in 1958. After these decisive results the ongoing quest for *anti-dynamo theorems* did not stop but changed its main objective from ruling out the general possibility of dynamo action to ruling out particular classes of magnetic and velocity fields. The main negative results may be summarized as follows. Magnetic fields cannot be maintained by purely toroidal motions $\boldsymbol{u} = \nabla \times w \boldsymbol{r}$ if the diffusivity λ is a function of $|\boldsymbol{r}|$ only [11], nor by purely radial motions [92], nor can plane two-dimensional motions sustain a dynamo [89], nor can even time-dependent and compressible flows of arbitrary λ sustain axisymmetric poloidal fields [86], etc.

Necessary conditions for dynamo action. Even if a velocity field is not banned by any anti-dynamo theorem, it may still not be able to give rise to a magnetic field. As already mentioned, for a velocity of given structure and magnitude the solutions of (2.3) depend on the non-dimensional parameter Rm and the generation of $\boldsymbol{B}$ may be regarded as a bifurcation phenomenon. For $Rm = 0$ the induction equation reduces to a vector diffusion equation the solutions of which decay in time. As Rm is increased from zero, the advection becomes capable of counteracting diffusion and above some critical value of $Rm > Rm_c$ solutions of (2.3) which are non-decaying and are of bounded magnetic energy emerge. Using the methods of stability theory a variety of *necessary conditions* for dynamo action, i.e. lower bounds for Rm at which bifurcation of a solution with non-decaying magnetic field occurs have been derived. Comparing energy integrals, Backus [4] derived $Rm' \geq \pi^2$. A general relationship of particular utility to the Earth's core is given by Busse [16]. It has to be emphasized that these lower bounds represent only necessary but not sufficient conditions for dynamo action. With a look towards the full self-consistent problem it would be particularly desirable to obtain necessary conditions in terms of forces acting on the fluid or velocities prescribed at the boundaries but this still poses a challenging mathematical problem.

Mechanisms of magnetic field generation. Having established the existence of singly-connected homogeneous dynamos and restricted the class of eligible velocities, kinematic theory turns to identifying possible mechanisms of magnetic field generation. Following [104] we separate $\boldsymbol{B}$ and $\boldsymbol{u}$ into axisymmetric (denoted by $\bar{\cdot}$) and asymmetric parts (denoted by $'$) and further divide the axisymmetric part into zonal and meridional parts:

$$\boldsymbol{B} = \overline{\boldsymbol{B}} + \boldsymbol{B}' = B(s,z)\hat{\boldsymbol{e}}_\varphi + \boldsymbol{B}_M + \boldsymbol{B}', \text{ where } \boldsymbol{B}_M = \nabla \times A(s,z)\hat{\boldsymbol{e}}_\varphi, \tag{2.4a}$$

$$\boldsymbol{u} = \overline{\boldsymbol{u}} + \boldsymbol{u}' = u(s,z)\hat{\boldsymbol{e}}_\varphi + \boldsymbol{u}_M + \boldsymbol{u}', \text{ where } \boldsymbol{u}_M = \nabla \times \xi(s,z)\hat{\boldsymbol{e}}_\varphi. \tag{2.4b}$$

Equation (2.3) can be similarly separated into axisymmetric and asymmetric parts and evolution equations for A and B can be obtained from the axisymmetric one:

$$\partial_t A + s^{-1} \boldsymbol{u}_M \cdot \nabla(sA) = \lambda(\nabla^2 - s^{-2})A + \overline{(\boldsymbol{u}' \times \boldsymbol{B}')}_\varphi, \tag{2.5a}$$

$$\partial_t B + s\boldsymbol{u}_M \cdot \nabla(s^{-1}B) = \lambda(\nabla^2 - s^{-2})B + s\boldsymbol{B}_M \cdot \nabla u + (\nabla \times \overline{(\boldsymbol{u}' \times \boldsymbol{B}')})_\varphi. \tag{2.5b}$$

If the axisymmetric part of the EMF $\overline{\boldsymbol{u}' \times \boldsymbol{B}'} = 0$ then the last terms in (2.5a) and (2.5b) vanish. The equation (2.5a) contains no source term and so the vector potential A of the axisymmetric meridional field is subject only to a form of diffusion and decays to zero as time increases. Then the second term on the right-hand side of (2.5b) which is the only source term in the absence of the last term vanishes too and so does the axisymmetric zonal field. Apart from being the idea behind the proof of Cowling's theorem such considerations provide insight into the mechanisms of field generation. We notice that in the absence of $\overline{\boldsymbol{u}' \times \boldsymbol{B}'}$ the zonal field may be generated by sweeping of the field lines of $\boldsymbol{B}_M$ by $\boldsymbol{u}_M$ known as ω-*effect*. Thus $\boldsymbol{B}_M$ can maintain $B\hat{\boldsymbol{e}}_\varphi$ but $B\hat{\boldsymbol{e}}_\varphi$ cannot support $\boldsymbol{B}_M$. A source of $\overline{\boldsymbol{u}' \times \boldsymbol{B}'}$ must be found to maintain $\boldsymbol{B}_M$. Such a source always exists if $\overline{\boldsymbol{B}} \neq 0$ in the presence of asymmetric flow, $\boldsymbol{u}' \neq 0$, as can be seen by the asymmetric part of the induction equation (2.3)

$$\partial_t \boldsymbol{B}' - \nabla \times (\overline{\boldsymbol{u}} \times \boldsymbol{B}' + (\boldsymbol{u}' \times \boldsymbol{B}')') - \lambda\nabla^2\boldsymbol{B}' = \nabla \times (\boldsymbol{u}' \times \overline{\boldsymbol{B}}), \tag{2.6}$$

which right-hand side represents a source term. Because of (2.6), $\boldsymbol{B}'$ and $\overline{\boldsymbol{u}' \times \boldsymbol{B}'}$ are linear functionals of $\overline{\boldsymbol{B}}$ and therefore if the flow is isotropic but not mirror symmetric

$$\overline{\boldsymbol{u}' \times \boldsymbol{B}'} = \alpha\overline{\boldsymbol{B}}. \tag{2.7}$$

Equation (2.7) provides a non-zero EMF which generates both meridional and zonal components of the axisymmetric magnetic field through the last terms in equations (2.5). The effect is called α-*effect* after the symbol denoting the pseudo-tensor α in (2.7). In addition to the insight of how magnetic field is generated, the α pseudo-tensor can be postulated on the basis of additional considerations which makes possible to obtain simple solutions of the kinematic problem. The α-*effect* was originally introduced [111] as an effect due to small-scale isotropic turbulence and gave rise to the so called *mean field electrodynamics*.
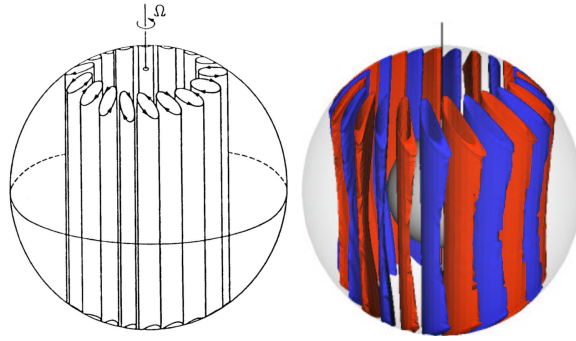
In addition to its mathematical beauty, kinematic theory is useful since it provides rigorous proofs of the existence of homogeneous dynamos, necessary conditions for dynamo action, insight into the magnetic field generation mechanisms, guidance and validity checks for numerical models and experiments.

2.2.3 Dynamically self-consistent theory

The next level of complication of dynamo theory is the consideration of the complete self-consistent set of equations (3.3), (3.12) and (3.28). Akin to other problems of such overwhelming complexity it has been separated to simpler subproblems which provide key insights to its overall solution. One possible subdivision consists of the questions:

- Determine a non-magnetic flow realized in a rotating fluid shell under the action of Coriolis and viscous forces, gravity and buoyancy, i.e. solve only the fluid-dynamical part of the problem (3.12) and (3.19). The solution turns out to be convective flow.
- Study the influence of an imposed magnetic field on the preferred non-magnetic solution. This is usually referred to as magnetoconvection.
- Attempt solution of the full self-consistent dynamo problem under various simplifying assumptions or numerically.

To facilitate the discussion of those topics, we note that the governing equations may be nondimensionalized. One possible way is presented in section 3.3.3 where the material properties of the system are combined in several nondimensional parameters, the most important

Fig. 2.2. *On the left: Qualitative sketch of the preferred structure of convection near onset at values of the Prandtl number close to unity and high rotation rates (from [13]). On the right: Isosurfaces of z-component of vorticity of a convection solution at $R = 3.8 \times 10^5$, $P = 10$ and $\tau = 10^4$.*

of which are the Rayleigh number R, the Coriolis number τ, the Prandtl number P, and the magnetic Prandtl number Pm. A large part of the dissertation is devoted to studying the effects of their variation.

Convection in rotating spherical shells. It is widely believed that the fluid motions in the core are driven by buoyancy of thermal or chemical origin and thus represent convective flows. Besides application in geomagnetism, convection is a key problem in hydrodynamic stability theory, bifurcation theory, transitions to turbulence, pattern formation etc. , and is relevant to many other geophysical and astrophysical systems. The geometrical configuration appropriate for modeling the convection in the Earth's core is that of a rotating self-gravitating sphere or shell. Apart from nonlinear effects preventing analytical treatment of convection at finite amplitudes, the rigorous analysis of the linear onset is hindered by the non-constant angle between Coriolis and gravity forces throughout the volume of the shell. The polar regions resemble a plane layer rotating about a vertical axis while the equatorial region is similar to a rotating cylindrical annulus. These two geometries allow reduction to two dimensions and are somewhat easier to address analytically but the results are not fully applicable to spherical geometry. A sound basis for the study of the problem, though restricted to linear analysis in terms of axisymmetric solutions was laid by Chandrasekhar [36]. Fundamental advances were made by Roberts [100] and Busse [13] who recognized that the important modes in the rapidly rotating system with Prandtl number of order unity are non-axisymmetric and found that the convection is characterized by a "cartridge belt" pattern as illustrated in figure 2.2. Later works [110, 74] have provided additional rigor and details to this basic picture. Experimental studies [27] have confirmed the qualitative features predicted by the theories for the range of Prandtl numbers of the working fluids used. A fundamentally different equatorially-attached convection regime has been found at sufficiently low values of the Prandtl number [124] and interpreted as modified inertial oscillations [121]. Linear numerical studies [124, 3] have found that the form of convection pattern is strongly dependent on almost all parameters which enter the formulation of the problem and identified various regimes of convection. Due to recent advances in numerical models the properties of finite amplitude convection have been studied up to hundred times the critical Rayleigh number [114, 59]. It is surprising that the remnants of the columnar structure discovered in the linear studies persist well into the chaotic regime of convection. A particularly relevant recent review of the topic is [24] and chapters 5 and 6 are also entirely devoted to studies of convection in rotating spherical systems.

Magnetoconvection. The subproblem closest to the full MHD dynamo problem is that of magnetoconvection in which the effects of imposed magnetic fields on convection are studied. The basic phenomena can be easily understood if the Lorentz force is represented as

$$(\nabla \times \boldsymbol{B}) \times \boldsymbol{B} = (\boldsymbol{B} \cdot \nabla)\boldsymbol{B} - \nabla(\frac{1}{2}|B|^2). \tag{2.8}$$

The second term on the right hand side can be absorbed into the modified pressure gradient of (3.12) and therefore is of little importance while the first one is interpreted as magnetic tension along the field lines. This tension has components parallel and perpendicular to the field lines and the perpendicular component is of particular importance because it opposes any distortion of the field lines making them behave like elastic strings. Since according to the Alfvén theorem the field lines are "frozen" in a conducting fluid such a distortion may be due to a flow perpendicular to the field lines. As a result in a perfectly conducting fluid oscillations known as Alfvén waves occur alternatively if the fluid has a finite conductivity the fluid motion is damped by imposed magnetic fields and convection is inhibited. It is also of interest to consider the combined effect of rapid rotation and imposed magnetic fields on convective flows. Since the viscous and inertial forces are negligible in the Earth's core ($\tau \approx 10^{15}$ and the ratio of inertial to Coriolis forces $\approx 10^{-6}$), the leading order steady balance in (3.12) is the *magnetostrophic balance*
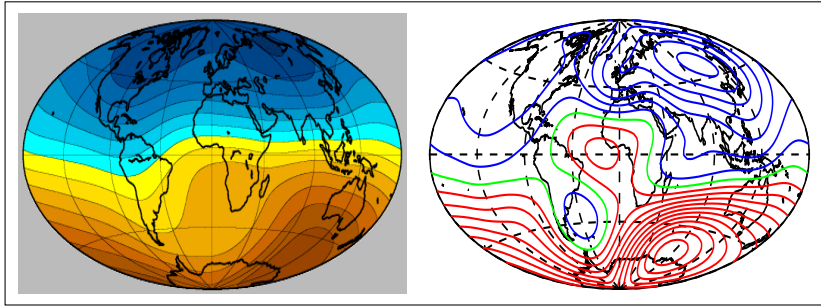
$$0 = -\nabla \pi + 2\boldsymbol{u} \times \boldsymbol{\Omega} + \delta\rho(\Theta, \Gamma)\boldsymbol{g} + \frac{1}{\mu\rho}(\nabla \times \boldsymbol{B}) \times \boldsymbol{B}. \qquad (2.9)$$

A small $\boldsymbol{B}$ acts to relax the constraint of the rotation given by the *geostrophic balance* of the first two terms in (2.9) rather than to inhibit convection and thus facilitates the flow. But for a large $\boldsymbol{B}$ the inhibiting effect of the magnetic field is much stronger than its relaxing effect. Thus at a particular value of the imposed magnetic field a minimum critical Rayleigh number exists. It has been found that this minimum is reached at a value of the Elsasser number $\Lambda \approx 1$ where $\Lambda = 2B^2 Pm/\tau$ and consequently suggested that planetary dynamos may operate near this value. However, this picture is true only for steady fields and some studies suggest [127] that there is no optimal state of magnetoconvection. For a comprehensive review refer to [129].

Solutions of the full nonlinear governing equations. Despite enormous difficulties a large amount of literature is devoted to investigation of the full coupled set of MHD equations (3.3), (3.12), (3.19) and (3.28), as discussed in the reviews [23, 103, 79]. Two approaches to the problem can be identified: predominantly analytical and predominantly numerical.

Analytical solutions. The analytical approach can be further subdivided into weak and strong field models. The first working MHD dynamos were produced by Busse in 1973 [14] and Childress and Soward in 1972 [37] in rapidly rotating plane layers. A second model by Busse [15] far more appropriate for the Earth considers a rotating annulus with inclined top and bottom boundaries resembling a spherical shell. The analysis consists of four steps: **(1)** Neglecting the Lorentz force and solving (3.12) and (3.19) to obtain the flow which close to onset is similar to the one shown in figure 2.2; **(2)** Solving the kinematic problem (3.28) for this flow; **(3)** Modification of step 1 to take into account the Lorentz force; **(4)** Recalculation of $\boldsymbol{B}$ using the modified flow. Such models are "weak field" because $\boldsymbol{B}$ must be small in order to be neglected in the first step and to allow expansion in powers of its small amplitude. Moreover, according to Lenz' rule $\boldsymbol{B}$ modifies $\boldsymbol{u}$ so as to remain small. The weak field models are useful because they regard the dynamo problem as a stability problem and allow a rigorous investigation of the first several bifurcations after onset of dynamo action which is nearly impossible by other means.

Though they are beautiful examples of applied mathematics, the weak field dynamos are irrelevant as an explanation of the geomagnetism and thus models producing strong magnetic fields come into consideration. The main idea is due to Taylor [112] who suggested that in view of the conditions in the Earth's core the inertial and viscous forces should be negligible and the magnetostrophic balance (2.9) must hold. Using such a force balance and the boundary condition $\boldsymbol{u}_r = 0$, he derived the so called *Taylor's constraint*

Fig. 2.3. *On the left: Radial magnetic field at Earth's surface calculated using data from the CHAMP and Ørsted magnetic field satellites (from [70]). Values range between* -0.1 *mT and* 0.1 *mT. On the right: Radial magnetic field at* $r = r_o + 1.6$ *of a dynamo solution with* $R = 10^6$, $P = 5$, $\tau = 5 \times 10^3$, $Pm = 10$. *Values range between* -0.0816 *mT and* 0.0512 *mT.*

$$\int_{C(s)} [(\nabla \times \boldsymbol{B}) \times \boldsymbol{B}]_\varphi \, \mathrm{d}S = 0, \tag{2.10}$$

where $C(s)$ is an an arbitrary coaxial cylinder intersecting the contained fluid. Then the reverse considerations imply that if (2.10) is satisfied the magnetostrophic balance (2.9) with the boundary condition $\boldsymbol{u}_r = 0$ has solutions. Since this balance is much simpler than the original Navier-Stokes equation a procedure to find the solutions may be developed as described in [101]. The integrations of the magnetostrophic balance following these ideas have so far not provided a satisfactory converged solutions.

Numerical solutions. Though possibly less appealing than neat analytical results, numerical solutions are often more revealing and in cases as difficult as the MHD dynamo problem probably the only possible solutions suffering no over-simplifications. Numerical modeling is not new and has assisted dynamo theory in any stage. It can be traced back to 1954 when Bullard and Gellman [11] made a first attempt to solve the kinematic problem. Later examples including linear and nonlinear studies of convection in various geometries, integrations of strong field models, magnetoconvection, not fully three dimensional or time dependent models etc., are much too numerous to be cited here. The computational approach applied to the fully self-consistent problem has brought almost revolutionary advances during the last decade. For the first time in the long history of geomagnetism the terrestrial magnetic field is being modeled from first principles without any drastic *ad hoc* assumptions.

The most popular technique for solving the dynamo equations numerically is the pseudo-spectral method recently described by Tilgner [113] and first applied to the geodynamo by Glatzmaier and Roberts [56]. The vector fields $\boldsymbol{u}$ and $\boldsymbol{B}$ are expanded into toroidal and poloidal parts and these scalar fields together with the Θ (and Γ) field are expanded in spherical harmonics. In the radial direction either a finite difference scheme or expansion in Chebishev polynomials is used. These expansions are inserted into the governing equations (3.3), (3.12), (3.19) and (3.28) and time dependent equations for the coefficients are obtained. The linear diffusion operators are handled by an implicit scheme such as the Crank-Nicholson method while the nonlinear terms are handled explicitly by converting from spectral to physical space so that the required operations can be treated easily.However, it requires large computing resources since in addition to the need of computing three-dimensional fields in a large domain further problems such as the lack of an efficient fast Legendre transform and the need of small time steps at high τ make the execution times very long.

Following a similar procedure a number of geodynamo models [56, 76, 80, 30, 94, 59], among others have been reported in the literature. They employ various nondimensionali-

sations, boundary conditions, parameter regimes, energy sources and distributions, density approximations and many of them include some less important physical ingredients such as conducting inner core, inhomogeneous heat flux, various models of the core-mantle coupling and topology etc. Despite long computation times these simulations are not restricted to single runs and rather extensive parameter and model studies have already been conducted [68, 76, 117, 40, 62, 82] Most models routinely simulate several magnetic diffusion times and produce self-excited magnetic fields which at the surface of the Earth have an intensity, an axial dipole dominated structure and a westward drift of the nondipole features that are all qualitatively similar to those of the geomagnetic field. As an illustration of the quality and detail of the fully self-consistent simulations, figure 2.3 represents a snapshot of the radial magnetic field of one of our recent runs compared to the observed radial geomagnetic field. The apparent similarity of the features indicates that such models capture the essential physics but one should not be tempted to believe that the problem of geomagnetism has been solved and such comparisons must always be supplemented with an outline of the deficiencies of the numerical models.

The primary dynamics of the core is controlled by **(1)** rapid rotation, **(2)** small viscosity, **(3)** buoyancy **(4)** self-generated magnetic fields and the difficulties are rooted in this particular combination of main effects. To see this we need to estimate the values of the Coriolis parameter τ and a further nondimensional number – the Reynolds number $Re = Ud/\nu$. Using the value 3×10^{-4} m/s for U obtained from the observed westward drift of nondipole features of the main field and the often-quoted value 10^{-6} m^2/s for the molecular viscosity ν, we find that $Re \sim 10^9$ and $\tau \sim 10^{15}$. These extremely large values are due to the small viscosity and the high rotation rate characteristic for the Earth. The Reynolds number gives the ratio between the inertial and viscous forces and its large value means that the Earth's core is in a highly turbulent state where a large number of scales are present. The viscous forces are negligible everywhere except in the boundary layers and in the smallest eddies at the end of the turbulent energy cascade where they become capable of dissipating the energy transfered from the large scale fluid motions. The *Kolmogorov microscales*, i.e. the time and length scales of the smallest dynamically significant flow structures which appear in such a turbulent regime can be estimated in terms of the Reynolds number and the large-scale parameters U and d of the flow. Using the formulas:

$$d' = dRe^{-3/4}, \qquad t' = \frac{d}{U}Re^{-1/2}. \tag{2.11}$$

we obtain 2.3×10^5 s and 0.4 m for the time and length scales of the smallest turbulent eddies. It is beyond hope to resolve such tiny scales with the aid of the present of near-future computing resources in which a high numerical resolution case normally deals with length scales larger than 10^4 m. Because of the impossibility to resolve small turbulent scales any numerical model represents a large eddy simulation where the viscous forces are much stronger than in the fluid core of the Earth and have a significant dynamical effect. Thus numerical dynamo models simply operate in the wrong dynamical regime which might well have qualitative differences compared to the real state of the Earth where the main balance must be between the Lorentz and Coriolis forces and the viscous force must be negligible.

2.3 Open problems

Many open questions remain in almost any branch of dynamo theory. Below we restrict the attention to those of numerical nature most relevant to the thesis. As noted, the current numerical simulations of the geodynamo can be regarded as modeling from first principles,

i.e. without employing any drastic *ad hoc* assumptions. However, simulations face a number of paramount difficulties. First, the values of many of the material properties of the core and lower mantle are unknown. Additional uncertainties concerning the structure of the deep Earth's interior and the phenomena taking place there also exist. These facts restrict the accuracy to which the exact Earth-like parameter values are known to very rough estimates. Second, these roughly estimated values correspond to an extremely turbulent state with huge range of significant time and length scales which are impossible to resolve with the present day computing power. Two main methods have been used to approach an Earth-like parameter regime within the current computational constraints: the concept of hyperdiffusion [56, 80, 105] and the so called "$2\frac{1}{2}$-dimensional dynamos", [73]. However it has been found that both methods introduce unphysical effects [128], [61]. On the other hand simulations of dynamos without the use of hyperdiffusivities are restricted to relatively low Rayleigh and Coriolis numbers but at least no artificial effects are introduced. Since it is of a more general physical interest to study the parameter dependence of rotating spherical dynamos, several groups have performed simulations on this basis ([68, 76, 117, 40, 62] and others).

This current state of matters suggests the directions of future research in the field. The numerical geodynamo modeling should solve simultaneously the forward and the inverse problem with two main goals. On the one hand it should help to study the convection and magnetic field generation and enhance the understanding of their mechanisms. On the other hand it should provide comparisons with the observations of the actual geomagnetic records and test various hypotheses suggested about the dynamical regime and structure in the Earth's core. In particular several main tasks may be identified as described below.

Systematic investigation of parameter dependences. The influence of the control parameters should be explored systematically wherever possible instead of relying on a single computation. Indeed cases with two attractors have been found (see Chapter 9) suggesting that results should be checked for stability and robustness. Furthermore, any particular set of parameters even the hypothetic Earth-like values is too specific and might fail to provide insight to important physical processes. And still, there will certainly be phenomena which appear at other parameter values but not at the particular set under investigation. A further important reason to study the influence of parameters is that it provides the possibility to extrapolate results towards realistic dynamo regimes which is impossible by other means.

Although a considerable region of the parameter space has been explored further efforts are needed in order to address more geophysically interesting cases. It has not been possible, for instance, to reach magnetic Prandtl numbers Pm considerably lower than 0.1 and to simulate dynamos for which viscous dissipation is small compared to Ohmic dissipation as is typical for the Earth's core. The range of accessible Rayleigh numbers R appears to be sufficient since at the order of 20 times its critical value R_c strong magnetic flux expulsion and dominance of convection in the polar regions are found which are not typical for the geodynamo. But it is desirable to increase the Coriolis parameter τ which is dimensionless measure of the rotation rate Ω. The currently accessible value of $\tau \approx 10^5$ is many orders of magnitude lower than the estimated value of 10^{15} for the Earth. While there is little doubt that values of Pm as low as possible should be reached, there is more uncertainty about the most appropriate value of the Prandtl number P. The traditionally used value $P = 1$ ([40, 62, 80, 82, 59]) may not be appropriate for the Earth's core. From experimental measurements [2] as well as from theoretical considerations [49] it is evident that even in highly turbulent systems diffusivity ratios such as the Prandtl number are not necessarily equal to unity. The value $P = 0.05$ based on molecular diffusivities is preferred by Braginsky and Roberts [9]. But values much higher than unity cannot be dismissed in view of the fact that concentration gradients are probably a very significant source of buoyancy.

Introduction of second order physical effects. Another important direction of research where much remains to be done is the introduction of second order physical effects in dynamo simulations. The main purposes of such complication is to develop more realistic numerical models as well as to test whether the additional effects in question do actually exist or are hypothetical and clarify their role and importance.

In many previous studies the **inner core** has been assumed electrically insulating which has been justified with the facts that it has a relatively small volume and does not participate in the generation of the magnetic field because of its rigidity. However it certainly has a conductivity similar to that of the outer fluid core and can have significant effects [69] on the time evolution of the convection flow and the magnetic field. Two possible influences of a conducting inner core may be expected: **(1)** a dynamic effect of changing the fluid flow through the viscous coupling with the outer core and thus the dynamo process and **(2)** a magnetic effect due to a slower time scale of the magnetic field variations in the inner core.

In the basic models the mantle has also been assumed to be electrically insulating impenetrable region with no influence on the generation of the magnetic field or convection flow other than through the boundary conditions. However, this is much too simplistic. The **lowermost layers of the mantle** probably have some finite conductivity and are not completely spherical and rigid [51, 8]. Such layers could form when the heat flow through the core-mantle boundary were subadiabatic which is a distinct possibility [84]. The layer could also consist of accumulated light material set free as the inner core grows. In a stable layer the fluid flow would be almost entirely toroidal [115] and large differences in the detailed field structure at the CMB are therefore expected between cases where up/downwellings reach the boundary and cases where they are blocked by a stable layer.

Another physical effect due to the mantle is the **inhomogeneous heat transport** through the core-mantle boundary. Among the features of the geomagnetic field that most clearly demonstrate the influence of lateral inhomogeneities are the persistent regions of high magnetic flux under Siberia and Arctic Canada [63]. There is general agreement that lateral inhomogeneities in the lowermost mantle are responsible for the property of apparent locking between the dynamo process in the core and the mantle. Since there is evidence that some cold slabs penetrate all the way from the upper mantle to the core-mantle boundary, inhomogeneities in the heat transport could lead to a locking between convection flows in the core and mantle. Another cause for such a locking could be topographic features of the core mantle boundaries. Bumps of the order of a few km have been proposed by [90] on the basis of seismic evidence.

The well established seismic anisotropy of the inner core suggests that the conditions at the **inner core-outer core boundary** are also not homogeneous. It has been proposed [78] that a slow flow of material driven by Lorentz forces occurs throughout the inner core from the poles to the equator such that solidification occurs only near the poles while melting takes place near the equator.

A further effect is the **gravitational coupling** between the mantle and the core proposed by Jault and LeMouël [72]. Mantle heterogeneity causes a perturbation of the gravity potential that departs from azimuthal symmetry. A fixed inner core would deform viscously until its surface coincides with an equipotential surface. If the inner core is rotated out of phase relative to the gravity perturbation by Lorentz or viscous torques, a counteracting gravitational torque develops that may be as large as $10^{21}\,\mathrm{N\,m}$. Simultaneously the viscous inner core deforms to readjust to the equipotential surface thus reducing the gravitational torque. Such a strong torque can effectively lock inner core and mantle and therefore inhibit any relative rotation. Incorporating the exchange of angular momentum between inner core, outer core, and mantle into a numerical dynamo model allows to compute inner core and

mantle rotation rates. These results can be compared with seismic estimates of inner core rotation and changes in length of day.

Most geophysicists agree that **two sources of buoyancy**, one due to the gradient of the concentration of light elements and a second one due to a superadiabatic gradient of the temperature play a role in the dynamics of the Earth's outer core [9]. Lister and Buffett [84] have estimated that compositional convection provides 80% and thermal convection 20% of the power for the geodynamo. For convection driven solely by a concentration gradient the effective Prandtl number would be large compared to unity while the opposite relationship is obtained in the case when the thermal diffusivity is most relevant; thus it seems appropriate to include both as competing buoyancy sources. The problem of the onset of convection in a rotating layer with two sources of buoyancy associated with different diffusivities has been analyzed by Pearlstein [97]. The most dramatic effect is the fingering instability that occurs in the case of stabilizing thermal stratification which may exist in the outer part of the fluid core [115]. The possibility of other new dynamical phenomena associated with double buoyancy has also been pointed out by Busse [25].

Another second order effect which should receive more attention in numerical simulations is the modeling of the **density variations** in the core. Most models have so far adopted the convenient but not quite appropriate Boussinesq approximation. The anelastic approximation [58] has also been used in simulations [57] but has not been found to yield any drastic differences. Chapter 3 reports an simplified **pseudo-anelastic** approximation in order to account for the density variations in the Earth's core.

Comparisons between numerical simulations and geomagnetic observations. Dynamo modeling is approaching a state where it becomes possible to compare results from the numerical simulations with geomagnetic observations [46]. Some of the features of the main field were already discussed in subsection 2.1.2 and here we comment on those which could provide validity tests for the numerical models.

The most important dynamical feature of the geodynamo are its **reversals and excursions**. Robust characteristics of reversals are described in references [46] and [88]. Several reversing dynamo models ([55, 54, 106, 75, 82, 69, 116]) have been compared with some aspects of the reversal process but the results are inconclusive and often contradictory. No generally accepted simple explanation of the reversal mechanism is available to date and more efforts are needed to understand this basic geomagnetic phenomenon. For this reason section 9.4 of the dissertation is devoted to a numerical study of geomagnetic polarity transitions and provides further details and original results on the topic.

Another convenient opportunity to test numerical results against observations is provided by **secular variation impulses** or **jerks**. These are rather abrupt changes in the time derivatives of the spherical harmonic coefficients of the geomagnetic field which is observed on a global scale [41]. Because of their global nature jerks are most likely to be caused by a coherent phenomenon in the core and torsional oscillations seem to provide a reasonable explanation as proposed by Braginsky [7]. Section 9.5 of the dissertation reports a first observation of torsional oscillations in three dimensional numerical simulations.

3. Mathematical Modeling of the Self-Consistent Dynamo Problem in Rotating Spherical Fluid Shells

The great diversity of processes which contribute to the formation of the geomagnetic field, leaves no hope of constructing a single model encompassing the whole of geomagnetism. Fortunately, the first order physical effects responsible for the generation of the main field may be considered on the basis of the general laws of conservation of mass, momentum and energy plus a reduced set of Maxwell's equations, which are applied to a conducting fluid in a bounded domain. The chapter introduces the assumptions and equations on which the research presented in the thesis is based. Additional notes on technical details and notation are given in appendix A.

3.1 Setting of the problem
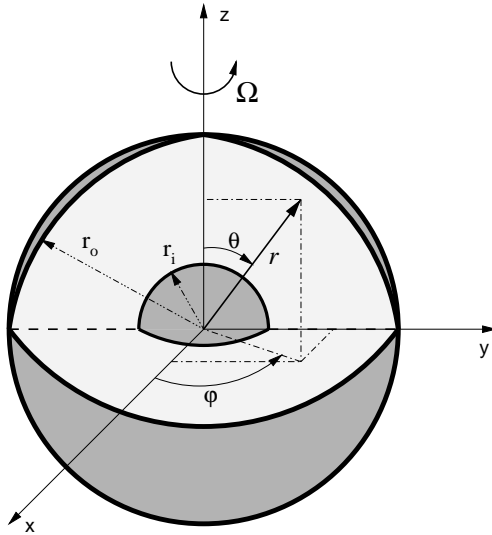
Geometrical configuration. In order to approximate the structure of the Earth's core we set a spherical polar coordinate system (r, θ, φ) and consider an idealized geometrical configuration as shown in figure 3.1. It consists of two concentric spherical surfaces the centers of which coincide with the origin of the coordinate system and with radii r_i and r_o, respectively. The surfaces form a spherical shell which may be alternatively defined by the thickness of the shell d and the ratio between its inner and outer radii, η. The following transformations between these pairs of parameters hold:

$$
\left|
\begin{aligned}
& d = r_o - r_i \\
& \eta = \frac{r_i}{r_o}
\end{aligned}
\right.
\qquad \Longleftrightarrow \qquad
\left|
\begin{aligned}
& r_i = \frac{\eta d}{1 - \eta} \\
& r_o = \frac{d}{1 - \eta}
\end{aligned}
\right. .
\tag{3.1}
$$

The inner and the outer spherical surfaces mimic the inner–outer core and the core-mantle boundaries, respectively. However, any deviations of the inner or outer core from the spherical shape, i.e. their ellipticities due to rotation, the anisotropic growth of the inner core, surface bumps, as well as other effects such as the existence of mushy or transient layers etc., are neglected but may be subsequently included by additional considerations. The spherical shell rotates with a constant angular velocity $\boldsymbol{\Omega}$ about the z-axis.

Physical ingredients. The region inside the shell, $r_i < r < r_o$, is entirely filled with fluid. It represents the liquid outer core of the Earth and is assumed to be a binary mixture of a principal heavy and a secondary light element. The fluid satisfies the continuum hypothesis, i.e. it is assumed that all macroscopic length and time scales of interest are considerably larger than the largest molecular length and time scales. Furthermore, the fluid moves at non-relativistic velocities and has a finite electrical conductivity. Under such assumptions the laws of Fluid Dynamics and Magnetohydrodynamics (MHD) apply and a solution supporting a self-sustained magnetic field is a distinct possibility.

The regions $r < r_i$ and $r > r_o$, external to the spherical shell are assumed to be impervious to the fluid. They can be either both electrically insulating or the inner one can be conducting

Fig. 3.1. *Geometrical configuration of the problem. The two spherical surfaces with radii r_i and r_o are dark-shaded. A part of the outer surface is removed to expose the interior of the shell (light-shaded), where the fluid is confined.*

while the outer one is always insulating. In either case they are penetrated by magnetic field lines but play only a passive role in magnetic field generation.

In view of the inaccuracies of our knowledge of the Earth's deep interior, no further specifications of material properties or structural details are necessary at this stage. This simplified setting is believed to encompass the most relevant features of the structure and composition of the core and lower mantle. Moreover, it is general enough to serve, with minor modifications, for modeling of other planetary cores.

3.2 Primitive governing equations

A thorough account of Fluid Dynamics is provided in [5] and in the first chapter of [36]. The basics of MHD and dynamo theory are presented in [44, 89] and [102] and of convection in [22]. A particularly relevant discussion of these topics may be found in [64].

3.2.1 Reynolds' transport theorem and its applications

Reynolds' transport theorem. A basic kinematic relation in Fluid Mechanics, leading to a general formulation of conservation laws, is the Reynolds' transport theorem for a fluid moving with velocity $\boldsymbol{u}$,

$$\frac{\mathrm{d}}{\mathrm{d}t} \int_{\zeta(t)} Z \, \mathrm{d}\zeta = \int_{\zeta(t)} (\mathrm{D}_t Z + Z \nabla \cdot \boldsymbol{u}) \, \mathrm{d}\zeta. \tag{3.2}$$

The theorem governs the rate of change of the integral of any material property $Z(\boldsymbol{r}, t)$ of the fluid (scalar, vector, etc.) over a material volume $\zeta(t)$. A *material volume* is one that consists of the same fluid particles as they evolve in time, i.e. it is locked into the fluid. A derivation of the theorem is given in appendix A.2.

Equation of continuity. An immediate consequence of the Reynolds' transport theorem is the equation of **mass conservation**. Substituting Z in (3.2) by the density $\rho(\boldsymbol{r}, t)$ of the fluid, taking into account that the mass of a material volume $\int_\zeta \rho \, \mathrm{d}\zeta$ cannot change since such a volume consists always of the same particles, and dropping the integral signs, we obtain

$$\partial_t \rho + \nabla \cdot (\rho \boldsymbol{u}) = 0. \tag{3.3}$$

This is the *equation of continuity* and the first of our governing equations.

Conservation laws. Upon replacement of Z by ρZ and simplification of the right-hand side of (3.2) with the help of the equation of continuity (3.3), we obtain the identity

$$\frac{\mathrm{d}}{\mathrm{d}t} \int_\zeta \rho Z \, \mathrm{d}\zeta = \int_\zeta \rho \mathrm{D}_t Z \, \mathrm{d}\zeta. \tag{3.4}$$

The left-hand side of (3.4) represents the rate of change of any extensive property of the fluid (kinetic energy, momentum, entropy etc.). Since the total amount of such quantities change due to sources or external influences (e.g. forces, fluxes, etc.) with effective strength Q at a rate given by $\int Q \, \mathrm{d}\zeta$, a general **conservation law** for Z takes the form

$$\rho \mathrm{D}_t Z = Q. \tag{3.5}$$

The momentum, energy and concentration equations considered in the following sections provide examples of (3.5).

3.2.2 Equation of motion

The momentum $\int \rho \boldsymbol{u} \, \mathrm{d}\zeta$ of a material volume changes due to the forces acting on the fluid particles. Two types of forces may be distinguished – *long range* and *short range* forces. The long range forces with density $\boldsymbol{F}$ (e.g. gravity) penetrate the volume of the fluid and act on all fluid particles, thus their alternative name - *volume forces*. The short range forces are usually of molecular origin and act only between neighboring fluid particles. They can be described by a *stress tensor* $\hat{\boldsymbol{S}}$ and modeled as *surface forces*, $\int \hat{\boldsymbol{S}} \cdot \boldsymbol{n} \, \mathrm{d}A$, acting on the surface element $\boldsymbol{n} \, \mathrm{d}A$. Then the **momentum conservation** may be written in the form of (3.5)

$$\rho \mathrm{D}_t \boldsymbol{u} = \rho \boldsymbol{F} + \nabla \cdot \hat{\boldsymbol{S}}. \tag{3.6}$$

Rotating reference frame. Since the setting of the problem involves rotation with constant angular velocity $\boldsymbol{\Omega}$, it is convenient to transform (3.6) into a reference frame rotating with this angular velocity. Applying the rotation operator $\hat{\Re} \mathrm{D}_t \boldsymbol{p} = (\mathrm{D}_{t'} + \boldsymbol{\Omega} \times) \boldsymbol{p}'$, derived in appendix A.3, to the velocity $\mathrm{D}_t \boldsymbol{r}$ and dropping primes we obtain in the rotating reference frame

$$\rho \mathrm{D}_t \boldsymbol{u} = 2\rho \boldsymbol{u} \times \boldsymbol{\Omega} - \rho \boldsymbol{\Omega} \times (\boldsymbol{\Omega} \times \boldsymbol{r}) + \rho \boldsymbol{F} + \nabla \cdot \hat{\boldsymbol{S}}, \tag{3.7}$$

where the *Coriolis* term $2\rho \boldsymbol{\Omega} \times \boldsymbol{u}$ and the *centrifugal* term $\rho \boldsymbol{\Omega} \times (\boldsymbol{\Omega} \times \boldsymbol{r})$ may be regarded as additional volume forces emerging in the non-inertial reference frame. The *Poincaré force*, $\rho(\partial_t \boldsymbol{\Omega}) \times \boldsymbol{r}$ vanishes since we consider a constant angular velocity $\boldsymbol{\Omega}$.

Forces. We proceed to specify the surface and volume forces. The stress tensor describing the surface forces depends in general on the properties of the fluid. We consider simple isotropic Newtonian fluids with kinematic viscosity ν for which the stress tensor has the form [5]:

$$S_{ij} = -p\delta_{ij} + S'_{ij}, \quad S'_{ij} = 2\rho\nu(e_{ij} - \frac{1}{3}\delta_{ij}e_{kk}), \quad e_{ij} = \frac{1}{2}(\partial_i u_j + \partial_j u_i), \tag{3.8}$$

where p is the thermodynamic pressure and S'_{ij} is the part of the stress tensor which accounts for viscous friction and further dissipative effects, e_{ij} is the *rate-of-strain tensor*, δ_{ij} is the Kronecker symbol and u_i is the i-th component of the velocity. A constant dynamic viscosity $\rho\nu$ and a vanishing bulk viscosity is assumed in (3.8).

Besides the fictitious Coriolis and centrifugal forces, two other volume forces appear, namely the *Lorenz force* and the *gravitational force*. The Lorentz force $\boldsymbol{F}_L$, is due to the

conductivity of the moving fluid and the presence of magnetic fields and will be considered in section 3.2.5.

The gravitational force is conservative and may be written as the gradient of a potential, which satisfies the Poisson's equation

$$\nabla^2\Psi = -4\pi G\rho \approx -4\pi G\tilde{\rho}_0(r), \tag{3.9}$$

where $G = 6.673 \,\mathrm{m}^3/(\mathrm{kg.s}^2)$ is the gravitational constant, and it is assumed that the density does not vary much from a basic static radial profile $\tilde{\rho}_0(r)$. Hence

$$\boldsymbol{F}_g(r) = \nabla\Psi = -\left[4\pi G\frac{1}{r^2}\int_0^r \tilde{\rho}_0(r')r'^2\,\mathrm{d}r'\right]\frac{\boldsymbol{r}}{r} \equiv -\tilde{\gamma}(r)\boldsymbol{r}. \tag{3.10}$$

The centrifugal force may also be written as the gradient of a scalar potential with the help of the vector identity

$$\boldsymbol{\Omega}\times(\boldsymbol{\Omega}\times\boldsymbol{r}) = -\nabla\left[\frac{1}{2}(\boldsymbol{\Omega}\times\boldsymbol{r})^2\right]. \tag{3.11}$$

In this form it may always be combined with the gravitational potential, i.e. $\Psi' = \Psi - (\boldsymbol{\Omega}\times\boldsymbol{r})^2/2$. However, at constant density it is even more convenient to add this term to the pressure gradient, i.e. $\pi = p - \rho_0(\boldsymbol{\Omega}\times\boldsymbol{r})^2/2$. In both cases the centrifugal term does not play an important dynamical role other than modifying the equipotential surfaces in the core.

Equation of motion. Plugging the force terms into (3.7), the equation of motion becomes

$$\rho(\partial_t + \boldsymbol{u}\cdot\nabla)\boldsymbol{u} = \tag{3.12}$$
$$-\nabla p + 2\rho\boldsymbol{u}\times\boldsymbol{\Omega} + \frac{\rho}{2}\nabla(\boldsymbol{\Omega}\times\boldsymbol{r})^2 - \rho\tilde{\gamma}\boldsymbol{r} + \rho\nu\nabla^2\boldsymbol{u} + \frac{1}{3}\rho\nu\nabla(\nabla\cdot\boldsymbol{u}) + \boldsymbol{F}_L.$$

This equation is also known as the *Navier-Stokes equation*. It governs the dynamics of the fluid flow in the rotating spherical shell.

3.2.3 Energy conservation equation

The third fundamental conservation law, which any fluid system has to obey, is the law of **energy conservation**. The total energy of a material volume of fluid, ϵ, is the sum of its kinetic energy and internal energy, e. It changes due to the work done and the heat delivered to the fluid in this volume. Therefore equation (3.5) acquires the form

$$\rho\mathrm{D}_t\epsilon = \rho\mathrm{D}_t(e + \frac{\boldsymbol{u}^2}{2}) = \rho\boldsymbol{u}\cdot\boldsymbol{F} + \nabla\cdot(\boldsymbol{u}\cdot\hat{\boldsymbol{S}}) + \nabla\cdot(\kappa_T'\nabla T) + \rho q. \tag{3.13}$$

The first and second term on the right-hand side represent the rate at which work is done by the volume and surface forces, respectively. The third term gives the rate at which heat is transfered to the material volume from the outside, where Fourier's law of heat conduction is used. Gauss' theorem has been applied to the second and third terms in order to transform them into volume integrals. ρq represents the heat source density. Equation (3.13) reduces to a balance of the internal energy if we take the divergence of the second term, use (3.6) and cancel the terms corresponding to the kinetic energy,

$$\rho\mathrm{D}_t e = S_{ij}\partial_j u_i + \partial_i(\kappa_T'\partial_i T) + \rho q. \tag{3.14}$$

The term $S_{ij}\partial_j u_i$ may be separated into reversible and dissipative parts using (3.8)

$$S_{ij}\partial_j u_i = S_{ij}e_{ji} = -pe_{jj} + 2\rho\nu(e_{ij})^2 - \frac{2}{3}\rho\nu(e_{jj})^2 = -\rho p \mathrm{D}_t\frac{1}{\rho} + \rho\Phi. \qquad (3.15)$$

The terms quadratic in the rate-of-strain tensor correspond to irreversible viscous dissipation and have been denoted by $\rho\Phi$ while pe_{jj} has been transformed with the help of the continuity equation (3.3). Hence equation (3.14) becomes

$$\mathrm{D}_t e + p\mathrm{D}_t\frac{1}{\rho} = T\mathrm{D}_t s = \frac{1}{\rho}\nabla\cdot(\kappa'_T\nabla T) + q + \Phi, \qquad (3.16)$$

where it has been further expressed as an entropy balance, since $\mathrm{d}e = T\,\mathrm{d}s - p\,\mathrm{d}\zeta$.

It is useful to to express (3.16) in terms of temperature and pressure since in applications these are the most readily known thermodynamic variables. Using the definitions of the heat capacity c_p and of the expansion coefficient α_T and a Maxwell relation

$$c_p = T\left[\frac{\partial s}{\partial T}\right]_p, \quad \alpha_T = -\frac{1}{\rho}\left[\frac{\partial\rho}{\partial T}\right]_p, \quad \left[\frac{\partial s}{\partial p}\right]_T = -\left[\frac{\partial\zeta}{\partial T}\right]_p = -\frac{\alpha_T}{\rho} \qquad (3.17)$$

we write the total differential of the entropy s in T and p,

$$\mathrm{d}s = \left[\frac{\partial s}{\partial T}\right]_p \mathrm{d}T + \left[\frac{\partial s}{\partial p}\right]_T \mathrm{d}p, \qquad (3.18)$$

and upon substituting it in equation (3.16) we obtain

$$c_p\mathrm{D}_t T - \frac{\alpha_T T}{\rho}\mathrm{D}_t p = \frac{1}{\rho}\nabla\cdot(\kappa'_T\nabla T) + q + \Phi. \qquad (3.19)$$

Equations (3.16) and (3.19) provide convenient formulations of the law of conservation of energy in a moving fluid.

3.2.4 Equation of concentration of light component

In order to model *compositional convection*, we assume that the fluid in the shell is a mixture of a heavy and a light component. The inner core is a result of solidification of the fluid core. The light alloying element is released as the heavy element freezes onto the inner-outer core boundary and then rise buoyantly stirring the entire fluid core. In general, the presence of two constituents with different chemical potentials contributes to the internal energy balance considered in the preceding section. However, one may argue that this effect is not of first order importance and focus only on the buoyancy force due to the release of the light component. Then the concentration C of light element may be regarded as an extensive quantity satisfying a conservation law of the type (3.5)

$$\mathrm{D}_t C = \frac{1}{\rho}\nabla\cdot(\kappa_C\nabla C). \qquad (3.20)$$

Here the flux of light component is proportional to the gradient ∇C, as given by Fick's law, and κ_C is the diffusion coefficient of the light component.

3.2.5 Magnetic induction equation

Next, we focus on the electromagnetic part of the dynamo problem. We consider a moving electrically conducting fluid, the velocity of which is small compared to the velocity of light c, i.e. $|\boldsymbol{u}| \ll c$ and $d/\underline{t} \ll c$, where d and $\underline{t}$ are a length and a time scale, respectively. The objectives of this section are to demonstrate the secondary importance of the electric field and to derive a governing equation for the magnetic fields.

MHD approximation. The Maxwell's equations for continuous media state

$$\nabla \cdot \boldsymbol{E} = \frac{\rho_e}{\varepsilon_0}, \quad \nabla \times \boldsymbol{E} = -\partial_t \boldsymbol{B}, \quad \nabla \cdot \boldsymbol{B} = 0, \quad \nabla \times \boldsymbol{B} = \mu_0 \boldsymbol{J} + \mu_0 \varepsilon_0 \partial_t \boldsymbol{E}, \qquad (3.21a,b,c,d)$$

where the inductions $\boldsymbol{D}$ and $\boldsymbol{B}$ and the intensities $\boldsymbol{E}$ and $\boldsymbol{H}$ of the electric and magnetic field are assumed related by the simple constitutive relations $\boldsymbol{H} = \boldsymbol{B}/\mu_0$ and $\boldsymbol{D} = \varepsilon_0 \boldsymbol{E}$. This is a reasonable assumption, since melted iron under high pressure and temperature cannot be permanently magnetized or polarized. The set of equations is closed by Ohm's law

$$\boldsymbol{J} = \sigma \boldsymbol{E}' + \rho_e \boldsymbol{u}, \tag{3.22}$$

where σ is the electrical conductivity. $\boldsymbol{E}'$ is the electric field measured in a reference frame moving with the fluid and it is given by the Lorentz transformation

$$\boldsymbol{E}' = (1 - \gamma_1)\frac{(\boldsymbol{u} \cdot \boldsymbol{E})\boldsymbol{u}}{u^2} + \gamma_1(\boldsymbol{E} + \boldsymbol{u} \times \boldsymbol{B}), \tag{3.23a}$$

$$\boldsymbol{B}' = (1 - \gamma_1)\frac{(\boldsymbol{u} \cdot \boldsymbol{B})\boldsymbol{u}}{u^2} + \gamma_1(\boldsymbol{B} - \mu_0\varepsilon_0\boldsymbol{u} \times \boldsymbol{E}), \tag{3.23b}$$

where $\gamma_1 = \sqrt{1 - u^2/c^2}$. Estimating the relative magnitude of terms in (3.21) and (3.23b)

$$\frac{|\boldsymbol{E}|}{|\boldsymbol{B}|} \approx \frac{d}{\underline{t}} \approx u, \quad \frac{|\mu_0\varepsilon_0\partial_t\boldsymbol{E}|}{|\nabla \times \boldsymbol{B}|} \approx \frac{u^2}{c^2} \ll 1, \quad \frac{|\mu_0\varepsilon_0\boldsymbol{u} \times \boldsymbol{E}|}{|\boldsymbol{B}|} \approx \frac{u^2}{c^2} \ll 1, \tag{3.24}$$

we may obtain the *pre-Maxwell equations*,

$$\nabla \cdot \boldsymbol{E} = \frac{\rho_e}{\varepsilon_0}, \quad \nabla \times \boldsymbol{E} = -\partial_t \boldsymbol{B}, \quad \nabla \cdot \boldsymbol{B} = 0, \quad \nabla \times \boldsymbol{B} = \mu_0 \boldsymbol{J}, \qquad (3.25a,b,c,d)$$

which are Galilei invariant, i.e. $\boldsymbol{E}' = \boldsymbol{E} + \boldsymbol{u} \times \boldsymbol{B}$, $\boldsymbol{B}' = \boldsymbol{B}$, and thus Ohm's law becomes

$$\boldsymbol{J} = \sigma(\boldsymbol{E} + \boldsymbol{u} \times \boldsymbol{B}). \tag{3.26}$$

The *Lorentz force* acting on the conductor due to electromagnetic fields may also be approximated

$$\boldsymbol{F}_L = \rho_e \boldsymbol{E} + \boldsymbol{J} \times \boldsymbol{B} \approx \boldsymbol{J} \times \boldsymbol{B} = \mu_0^{-1}(\nabla \times \boldsymbol{B}) \times \boldsymbol{B}, \tag{3.27}$$

since $|\rho_e\boldsymbol{E}|/|\boldsymbol{J} \times \boldsymbol{B}| \approx u^2/c^2 \ll 1$ and the force due to the electric field acting on the charge distribution can be neglected. The last relation follows from equation (3.25d).

The MHD equations (3.25) represent a self consistent approximation to the order $(u/c)^2$ of the full Maxwell's equations, where the displacement current $\mu_0\varepsilon_0\partial_t\boldsymbol{E}$ is neglected. To the same order the electric force $\rho_e\boldsymbol{E}$ in (3.27) due to charge distribution is negligible and the Lorentz transformations reduce to the Galilei transformations, which result in (3.26) for the current density. The pre-Maxwell equations (3.25) do not describe the phenomenon of electromagnetic radiation which, however, plays no role in geomagnetism.

Induction equation. A major consequence of the MHD approximation is that the electric and magnetic fields are not equally important in (3.25). Indeed an evolution equation involving $\boldsymbol{B}$ alone may be readily obtained. To eliminate $\boldsymbol{E}$, we take the curl of Ohm's law (3.26) and substitute (3.25b) and (3.25d) in the resulting expression. Using (3.25c) we arrive at the *induction equation*

$$\partial_t \boldsymbol{B} = \nabla \times (\boldsymbol{u} \times \boldsymbol{B}) + \lambda \nabla^2 \boldsymbol{B}, \qquad \lambda = (\mu_0\sigma)^{-1}. \tag{3.28}$$

Thus, $\boldsymbol{B}$ is of central importance in MHD, since once it is obtained from (3.28) for a given $\boldsymbol{u}$, the electric field can be extracted from the Ohm's law

$$\boldsymbol{E} = (\lambda\nabla - \boldsymbol{u}) \times \boldsymbol{B}. \tag{3.29}$$

Then, $\boldsymbol{E}$ serves only to determine the charge density ρ_e from the Gauss' law (3.25a), which in turn plays a negligible role in view of the approximation (3.27) to the Lorentz force.

The induction equation (3.28), with the first term on the right-hand side rewritten as

$$(\partial_t + \boldsymbol{u}\cdot\nabla)\boldsymbol{B} = \boldsymbol{B}\cdot\nabla\boldsymbol{u} - \boldsymbol{B}\nabla\cdot\boldsymbol{u} + \lambda\nabla^2\boldsymbol{B}, \qquad \lambda = (\mu_0\sigma)^{-1}, \tag{3.30}$$

has a simple physical interpretation. Its left-hand side is the material derivative which gives the rate of change of the field moving with the fluid velocity. The first term on the right-hand side represents stretching of the field lines by $\boldsymbol{u}$, the second one accounts for the change due to compression of the fluid, while the last one is the change due to electric diffusion.

Finally we note that $\boldsymbol{B}$ and $\boldsymbol{J}$ are invariant under rotation and therefore the induction equation (3.28) is valid in the rotating reference frame discussed in section 3.2.2.

3.2.6 Boundary conditions

Velocity boundary conditions. The fluid is confined to the spherical shell, $r_i \leq r \leq r_o$, the boundaries of which are impenetrable and solid. It is natural to choose the *no-slip* boundary conditions which require that all components of the velocity vanish on the boundaries

$$\boldsymbol{u} = 0 \qquad \text{at} \quad r = r_i, r_o. \tag{3.31}$$

In the presence of rotation these boundary conditions lead to the development of so-called *Ekman layers*. A significant feature of the Ekman layer is the effect of suction of fluid from below or pumping it downwards, depending on whether the radial component of the vorticity of the flow beneath the layer is positive or negative. Thus the Ekman layer can play an important dynamical role because it is capable of controlling the flow far from the boundaries through the effects of suction or pumping.

On the other hand the Ekman layer has a thickness of about $\sqrt{\nu/\Omega} \approx d/\sqrt{\tau}$, where ν is the kinematic viscosity and τ is the Coriolis parameter defined by (3.3.3). But the value of τ, discussed in section 2.2.3, is as large as 10^{15}, which leads to a layer thickness of the order of centimeters. It is hard to believe that a layer with negligible thickness can influence the dynamo process significantly. The numerical difficulties of resolving such a thin layer are also significant. These arguments lead to the consideration of the *stress-free* velocity boundary conditions. Since the boundaries are impenetrable to the fluid the normal component of the velocity still vanishes

$$u_r = 0 \qquad \text{at} \quad r = r_i, r_o \tag{3.32}$$

just as in the case of no-slip boundaries, but in contrast to the latter the stress-free conditions require vanishing of the tangential components of the stress tensor on the boundaries

$$S_{r\theta} = S_{r\varphi} = 0 \qquad \text{at} \quad r = r_i, r_o. \tag{3.33}$$

Using the explicit expressions for the components of the stress tensor in spherical polars [5] and (3.32) this reduces to

$$\partial_r \frac{u_\theta}{r} = \partial_r \frac{u_\varphi}{r} = 0 \qquad \text{at} \quad r = r_i, r_o. \tag{3.34}$$

The majority of results reported in the thesis make use of the stress-free boundary conditions. Nevertheless many cases were computed under the assumption of no-slip boundaries, notably those including a conducting inner core. If the opposite has not been specified explicitly we assume the use of stress-free boundary conditions for the velocity field.

Thermal boundary conditions. Since the total volume of the shell is fixed, no work can be done on the fluid. The only way in which the total energy of the fluid may vary is by exchange of heat with its environment. The change of heat at fixed volume is proportional to the change of the temperature in the volume, which in turn is determined by specification either of the heat flux through the boundary, the temperature on the boundary or a linear combination of them. Neither of these choices is well-established because of lack of precise knowledge of the thermal properties of the mantle and the inner core.

In the vast majority of the cases reported in the thesis fixed temperature on the boundaries have been assumed

$$\Theta = T - T_s = 0 \qquad \text{at} \quad r = r_i, r_o, \tag{3.35}$$

where T_s is a basic static temperature state. However, fixed-flux boundary conditions have also been used to study non-magnetic convection as reported in chapter 5.

Concentration boundary conditions. The flux of light material in equation (3.12) plays a role analogous to the flux of heat. Moreover, we assume that the light component is released only during the solidification process taking place at the inner-outer core boundary and is accumulated on the core-mantle boundary. Thus it is convenient to require fixed values of the concentration on the boundaries of the shell

$$\Gamma = C - C_s = 0 \qquad \text{at} \quad r = r_i, r_o, \tag{3.36}$$

where Γ is the deviation from a basic static state of concentration distribution C_s.

Magnetic field boundary conditions. In contrast to the velocity the magnetic field is not confined to the spherical shell but extends into the inner and outer regions. The field in the external regions needs to be determined and matched to the field in the shell. Two possibilities for the electrical conductivities of the external regions are employed in the thesis, namely when both regions are insulating, and when the outer region is insulating but the inner one has a finite conductivity equal to that of the fluid.

Matching conditions. We first consider the matching conditions at the boundary between insulating and conducting media. We select a cylindrical volume intersecting the boundary so that its axis is normal to the bounding surface. Integrating the solenoidal condition $(3.25c)$ over this volume, transforming to a surface integral with the help of Gauss' theorem and taking the cylindrical surface to be so small that the integrals over the side walls are negligible, we find the marching condition for the normal components of the fields in the two regions

$$\lim_{\substack{r \to r_b \\ r < r_b}} (\boldsymbol{B}_i \cdot \hat{\boldsymbol{e}}_r) - \lim_{\substack{r \to r_b \\ r > r_b}} (\boldsymbol{B}_e \cdot \hat{\boldsymbol{e}}_r) = 0, \tag{3.37}$$

where the normal to the surface coincides with the unit vector $\hat{\boldsymbol{e}}_r$, r_b is the radius of the spherical boundary and $\boldsymbol{B}_i$ and $\boldsymbol{B}_e$ are the fields in the conducting and the external insulating regions, respectively. Similarly, using $(3.25d)$ and taking into account that the current density $\boldsymbol{J}$ on an insulating boundary must vanish, the condition for the tangential components is

$$\lim_{\substack{r \to r_b \\ r < r_b}} \boldsymbol{B}_i \times \hat{\boldsymbol{e}}_r - \lim_{\substack{r \to r_b \\ r > r_b}} \boldsymbol{B}_e \times \hat{\boldsymbol{e}}_r = \boldsymbol{0}. \tag{3.38}$$

Therefore in the case when both external regions are insulating the magnetic field $\boldsymbol{B}$ must remain continuous through the boundaries.

In the case of a finitely conducting inner core no real jump in the electromagnetic properties of the medium actually occurs. Therefore $\boldsymbol{B}$ must once again remain continuous on

the boundary with the conducting inner core. The significant difference to the case of the insulating inner core consists of the nature of the field in these regions in the two cases, which we discuss below.

The field in the external regions. Since there is no electric current, $\boldsymbol{J} = \boldsymbol{0}$, in an insulator, one can use (3.25c) and (3.25d) to find that the field in the case of insulating external regions is derivable from a scalar potential U which satisfies the Laplace equation,

$$\boldsymbol{B}_e = -\nabla U, \qquad \nabla^2 U = 0. \tag{3.39}$$

The general solution of equation (3.39) in terms of spherical harmonics is given by

$$U = \sum_{l=0}^{\infty} \sum_{m=-l}^{l} (a_l^m r^l + b_l^m r^{-(l+1)}) Y_l^m(\theta, \varphi) = \begin{cases} \sum_{l,m} a_l^m r^l Y_l^m(\theta, \varphi) & \text{at } r < r_i, \\ \sum_{l,m} b_l^m r^{-(l+1)} Y_l^m(\theta, \varphi) & \text{at } r > r_o. \end{cases} \tag{3.40}$$

Taking in consideration that $\boldsymbol{B}_e$ must vanish when $r \to \infty$, while the U must have no singularity when $r \to 0$ we obtain that $\boldsymbol{B}_e$ is described only by the terms proportional to r^l in the region $r < r_i$, and only by the terms proportional to $r^{-(l+1)}$ in $r > r_o$.

The field in an inner core of finite conductivity is governed by the induction equation (3.28) in which the velocity is assumed to be one of a rigid body rotating about the z-axis, i.e. $u_\varphi = \Omega_{ic} r_i \sin(\theta)$, where Ω_{ic} is determined by the balance of the viscous and magnetic torques on the inner core

$$C \frac{\partial \Omega_{ic}}{\partial t} = \rho \nu \oint_{ICB} r \frac{\partial}{\partial r} \left(\frac{\partial}{\partial r} \right)_{r_i} u_\varphi r_i \sin\theta |\, \mathrm{d}S| + \frac{1}{\mu_0} \oint_{ICB} B_\varphi B_r r_i \sin\theta |\, \mathrm{d}S| \tag{3.41}$$

Here C is the moment of inertia of the inner core and ICB denotes the surface of the inner-outer core boundary. In order for the viscous torque to exist no-slip boundary conditions for the velocity field must be assumed on the ICB.

3.3 Pseudo-anelastic approximation

The equations derived in the preceding section apply to almost any fluid-dynamical system. In this form, however, they are too general to be useful in modeling the dynamics of the core. Further simplifications are required, which will both reduce the primitive equations to a more easily tractable form and will exclude physical effects of no interest with respect to the geodynamo problem.

Most models of the geodynamo have so far adopted the *Boussinesq approximation* of the governing equations, [36, 22]. Its main assumption is that the density of the fluid in the shell is uniform and constant except in the gravity term of the momentum equation, where it depends weakly on temperature thus accounting for the buoyancy effect. This approximation is mathematically convenient and, due to its simplicity, well-suited for theoretical and numerical analysis. Moreover, it gives reasonably accurate description of the main processes within the core without obscuring the picture by effects of secondary importance. The Boussinesq approximation is extensively employed in the present report as well. However, it neglects the effects of compressibility and density stratification which may have a significant role in the core dynamics. The situation may be rectified by employing the more general *anelastic approximation*, originally introduced in meteorological studies [58] and discussed in the geodynamo context in [9] and [64]. The anelastic equations are rather complicated but when solved numerically [57] no drastic differences to the Boussinesq equations are encountered.

In this section we shall formulate a generalization of the Boussinesq approximation, which however, is still short of the full anelastic approximation. We assume that the fluid is compressible but only in the basic reference state of the core and introduce static density variation in radial direction. Thus, we retain the relative simplicity of the Boussinesq equations.

3.3.1 Assumptions

To justify the assumptions on which our pseudo-anelastic approximation rests, we illustrate how the density profile in the core is usually estimated. If a uniform composition of the core is assumed, so that the density ρ is a function of only two state variables, say pressure and entropy, the density gradient is given by

$$\frac{\mathrm{d}}{\mathrm{d}r}\rho(r) = \left[\frac{\partial\rho}{\partial p}\right]_s \frac{\mathrm{d}p}{\mathrm{d}r} + \left[\frac{\partial\rho}{\partial s}\right]_p \frac{\mathrm{d}s}{\mathrm{d}r}. \tag{3.42}$$

Since the entropy in the Earth's core is well mixed by convection, the second term is zero. Defining the compressibility at constant entropy as $\chi_s = \rho(\partial p/\partial\rho)_s$ and using the equation of hydrostatic equilibrium in the basic state, $\nabla p = \rho\boldsymbol{g}$, one arrives at

$$\frac{\mathrm{d}}{\mathrm{d}r}\rho(r) = -\frac{\rho^2\boldsymbol{g}}{\chi_s}. \tag{3.43}$$

The compressibility χ_s may be estimated from measurements of velocities of seismic waves, and once a reliable value is available the *Adams-Williamson equation* (3.43) may be solved to obtain the radial density profile $\rho(r)$. However, the assumptions of a homogeneous and uniform composition are not well satisfied especially near the core boundaries and χ_s is not well known and as a result various density profiles may be suggested. Motivated by these arguments we modify the Boussinesq approximation to include a density stratified basic state.

The primitive equations (3.3), (3.12), (3.19), (3.20), (3.25c) and (3.28) governing the dynamics in the rotating spherical shell are simplified subject to the following assumptions:

(1) The density ρ is assumed equal to an empirical basic static profile, $\tilde{\rho}_0(r)$, depending on the distance from the center. ρ is replaced by $\tilde{\rho}_0(r)$ in all terms of the primitive equations except in the gravity term, which accounts for the buoyancy effect.

(2) In the gravity term the dependence of the density variations on pressure is neglected in comparison with the dependence on temperature and concentration. Furthermore, these dependences are assumed to be weak.

(3) All material properties of the fluid, e.g. the coefficient of thermal expansion α_T and α_C, the heat capacity c_V, the viscosity ν etc. are assumed to be constant. The heat produced by viscous and ohmic dissipation Φ is considered negligible.

Mathematically assumptions **(1)** and **(2)** can be written as

$$\rho(\boldsymbol{r},t) = \tilde{\rho}_0(r)[1 - \alpha_T(T - T_s) - \alpha_C(C - C_s)], \tag{3.44}$$
$$\text{where} \quad \alpha_T, \alpha_C \to 0, \quad g \to \infty, \quad \text{but} \quad \alpha_T g, \alpha_C g \quad \text{are \textbf{finite}.}$$

The conditions for validity of our assumptions are similar to those of the Boussinesq approximation. i.e.

$$\alpha_T\Theta \ll 1, \qquad \alpha_C\Gamma \ll 1, \qquad \frac{\rho g d}{\chi T} \ll 1. \tag{3.45}$$

The first two inequalities express the weak dependence of the density on temperature Θ and concentration variations Γ from a reference value, while the last one is the condition of negligible dependence on pressure.

However, the assumption of a basic density profile, $\tilde{\rho}_0(r)$, relaxes an important constraint on the Boussinesq approximation, namely the typical length of the convective region, d, need not be much smaller than the density scale height, i.e. the distance over which an isentropic density distribution varies by a factor e. The introduction of a basic density profile in the model accounts for compressibility at least in the basic reference state.

3.3.2 Basic reference state

The governing equations are most conveniently treated in terms of deviations from a basic static equilibrium state. Technically one may view the equations describing the reference state and the deviations from it as the zeroth and the first order equations in a perturbation scheme about equilibrium.

We choose the reference state to be one of no motion $\boldsymbol{u} = \boldsymbol{0}$, no magnetic field $\boldsymbol{B} = \boldsymbol{0}$, and with static temperature $T_s(r)$, concentration $C_s(r)$, and pressure $p_s(r)$ distributions. The primitive equations (3.3), (3.12), (3.19), (3.20), (3.25c) and (3.28) reduce to

$$0 = \nabla p_s + \frac{\tilde{\rho}_0}{2}\nabla(\boldsymbol{\Omega}\times\boldsymbol{r})^2 + \tilde{\rho}_0\tilde{\gamma}\boldsymbol{r}, \tag{3.46a}$$

$$0 = \kappa_T\nabla^2 T_s + \frac{q}{c_p} \tag{3.46b}$$

$$0 = \kappa_C\nabla^2 C_s, \tag{3.46c}$$

where $\kappa_T = \kappa'_T/(\tilde{\rho}_0 c_p)$ is the coefficient of thermal diffusivity.

The equation (3.46a) does not actually need to be solved, since under our assumptions the pressure loses its thermodynamical significance in the sense that it does not determine the temperature or density variations. Therefore we need merely to subtract (3.46a) from the primitive momentum equation (3.12) in order to obtain the equations for the deviations from equilibrium.

The general solution of the heat equation (3.46b) for the static temperature is given by

$$T_s(r) = \beta_0 - \frac{\beta}{2}r^2 + \beta_1\frac{1}{r}, \tag{3.47}$$

where $\beta = q/(3\kappa_T c_p)$=const. The other two constants of integration are determined from the conditions of fixed temperatures on the boundaries

$$\left|\begin{array}{l} T_s(r_i) = T_1 \\ T_s(r_o) = T_2 \\ \Delta T = T_2 - T_1 \end{array}\right. \qquad \Longleftrightarrow \qquad \left|\begin{array}{l} \beta_0 = T_1 - \dfrac{\Delta T}{1-\eta} \\ \beta_1 = \dfrac{\eta d}{(1-\eta)^2}\Delta T \end{array}\right. . \tag{3.48}$$

The solution of (3.46c) is obtained in a similar fashion,

$$C_s(r) = \left[C_1 - \frac{\Delta C}{1-\eta}\right] + \frac{\eta d}{(1-\eta)^2}\Delta C\frac{1}{r}. \tag{3.49}$$

3.3.3 Equations for the deviations from equilibrium

Once the equilibrium basic state is defined we proceed to obtain equations for the deviations of the dependent variables from it. We use the assumption of constant material parameters and the equation of state (3.44) to simplify the primitive equations (3.3), (3.12), (3.19), (3.20), (3.25c) and (3.28). Taking the limits α_T, $\alpha_C \to 0$ is effectively equal to substituting ρ by $\tilde{\rho}_0$

in all terms except in the gravity term, where the products $g\alpha_T$ and $g\alpha_C$ remain finite. In addition this procedure eliminates the $\alpha_T T \mathrm{D}_t p$ term in the left-hand side of the energy conservation equation (3.19) which reduces to a heat diffusion equation. Further simplifications are obtained by subtracting the basic equilibrium balances (3.46) and plugging in the explicit basic state solutions for the temperature (3.47) and the concentration (3.49).

The perturbation equations obtained in this fashion may be further simplified by scaling and introduction of nondimensional parameters. The scaling reduces the number of parameters in the model and facilitates comparisons with experimental observations and estimation of the relative magnitudes of the various terms. Any choice of scaling is arbitrary and is chosen to suit the problem in question. Here the thickness of the shell d is used as a length scale, d^2/ν as a time scale, $\nu^2/(\bar\gamma\alpha_T d^4)$ as a temperature scale, $\nu^2/(\bar\gamma\alpha_C d^4)$ as a concentration scale, $\bar\rho$ as a density scale and $\nu\sqrt{\mu_0\bar\rho}/d$ as a magnetic induction scale, i.e.

$$x = dx', \ \ t = \frac{d^2}{\nu}t', \ \ \tilde\rho_0 = \bar\rho\tilde\rho_0', \ \ T = \frac{\nu^2}{\bar\gamma\alpha_T d^4}T', \ \ C = \frac{\nu^2}{\bar\gamma\alpha_C d^4}C', \ \ \boldsymbol{B} = \frac{\nu\sqrt{\mu_0\bar\rho}}{d}\boldsymbol{B}', \tag{3.50}$$

where $\bar\rho$ and $\bar\gamma$ are the mean values of the density and gravity acceleration in the shell and the primes denote nondimensional variables. Substituting (3.50) in the primitive equations simplified by the outlined procedure and dropping the primes we obtain the nondimensional equations for the deviations from the basic state in the pseudo-anelastic approximation,

$$\nabla \cdot \boldsymbol{m} = 0, \tag{3.51a}$$

$$\partial_t\boldsymbol{m} + \boldsymbol{m}\cdot\nabla\frac{\boldsymbol{m}}{\tilde\rho_0} = -\frac{d^2}{\bar\rho_0\nu^2}\nabla p_1 + \tau\boldsymbol{m}\times\hat{\boldsymbol{e}}_{\boldsymbol{z}} + \tilde\rho_0\tilde\gamma(\Theta + \Gamma)\boldsymbol{r} \tag{3.51b}$$

$$+ \tilde\rho_0\nabla^2\frac{\boldsymbol{m}}{\tilde\rho_0} + \frac{1}{3}\tilde\rho_0\nabla(\nabla\cdot\frac{\boldsymbol{m}}{\tilde\rho_0}) + (\nabla\times\boldsymbol{B})\times\boldsymbol{B}, \tag{3.51c}$$

$$P\left(\partial_t + \frac{\boldsymbol{m}}{\tilde\rho_0}\cdot\nabla\right)\Theta = \frac{1}{\tilde\rho_0}\nabla^2\Theta + \frac{1}{\tilde\rho_0}\left(R_i + R_e\frac{\eta}{(1-\eta)^2}\frac{1}{r^3}\right)\boldsymbol{r}\cdot\boldsymbol{m}, \tag{3.51d}$$

$$L\left(\partial_t + \frac{\boldsymbol{m}}{\tilde\rho_0}\cdot\nabla\right)\Gamma = \frac{1}{\tilde\rho_0}\nabla^2\Gamma + \frac{1}{\tilde\rho_0}R_\Gamma\frac{\eta}{(1-\eta)^2}\frac{1}{r^3}\boldsymbol{r}\cdot\boldsymbol{m}, \tag{3.51e}$$

$$\nabla \cdot \boldsymbol{B} = 0, \tag{3.51f}$$

$$\partial_t\boldsymbol{B} = \nabla\times\left(\frac{\boldsymbol{m}}{\tilde\rho_0}\times\boldsymbol{B}\right) + Pm^{-1}\nabla^2\boldsymbol{B}, \tag{3.51g}$$

where the momentum vector $\boldsymbol{m} \equiv \tilde\rho_0(r)\boldsymbol{u}$ has been used.

The seven nondimensional parameters, which appear in equations (3.51), are the internal and external thermal Rayleigh numbers R_i and R_e, the compositional Rayleigh number R_Γ, the Coriolis number τ, the Prandtl number P, the Lewis number L, and the magnetic Prandtl number Pm, which are defined as follows:

$$R_i = \frac{\alpha_T\bar\gamma\beta d^6}{\nu\kappa}, \quad R_e = \frac{\alpha_T\bar\gamma\Delta T d^4}{\nu\kappa}, \quad R_\Gamma = \frac{\alpha_C\bar\gamma\Delta C d^4}{\nu\kappa},$$

$$\tau = \frac{2\Omega d^2}{\nu}, \quad P = \frac{\nu}{\kappa_T}, \quad L = \frac{\nu}{\kappa_C}, \quad Pm = \frac{\nu}{\lambda}. \tag{3.52}$$

The various Rayleigh numbers measure the energy input into the system, i.e. R_e is proportional to the heat exchange due to the fixed temperatures of the boundaries, R_i accounts for the heat generated by internally distributed heat sources and R_Γ is the compositional analogue of R_e. The Prandtl number P, the Lewis number L, and the magnetic Prandtl number Pm describe the relative importance of the diffusive processes involved and the Coriolis number τ is the ratio of the Coriolis to the viscous force.

3.3.4 Scalar equations

Equations (3.51) are written in terms of the momentum vector $\boldsymbol{m} \equiv \tilde{\rho}_0(r)\boldsymbol{u}$ instead the velocity vector $\boldsymbol{u}$. The reason for this choice is that the momentum vector is divergence-free and thus allows a decomposition in toroidal and poloidal components. This property is of great utility because it allows to substitute the four vector equations of (3.51) (i.e. total of twelve scalar equations) by four scalar ones.

Poloidal-toroidal decomposition. Any solenoidal vector may be represented as a sum of poloidal and toroidal components [4]. Since both the momentum, $\boldsymbol{m}$, and the magnetic field vector, $\boldsymbol{B}$, are solenoidal by equations (3.51a) and (3.51f) they may be represented as

$$\boldsymbol{m} = \nabla \times \boldsymbol{r}w + \nabla \times (\nabla \times \boldsymbol{r}v), \tag{3.53a}$$

$$\boldsymbol{B} = \nabla \times \boldsymbol{r}g + \nabla \times (\nabla \times \boldsymbol{r}h). \tag{3.53b}$$

The poloidal and toroidal scalar functions v and w (h and g) are uniquely determined when the condition holds that the averages of v and w (h and g) over surfaces of $r = $ const. vanish. Additional details on the poloidal-toroidal representation are given in appendix A.4.

Scalar equations. Operating with $\boldsymbol{r}\cdot\nabla\times$ and $\boldsymbol{r}\cdot\nabla\times\nabla\times$ on the momentum equation (3.51b) results in two scalar equations. A second pair of scalar equations is obtained by operating with $\boldsymbol{r}\cdot$ and $\boldsymbol{r}\cdot\nabla\times$ on the induction equation (3.51g). The heat (3.51d) and the concentration equations (3.51e) are already scalar. Hence equations (3.51) acquire the form

$$\left[(\nabla^2 - \partial_t)\mathcal{L}_2 + \tau\partial_\varphi \right] w - \tau\mathcal{Q}v =$$
$$\boldsymbol{r} \cdot \nabla \times \left[\boldsymbol{m} \cdot \nabla(\tilde{\rho}_0^{-1}\boldsymbol{m}) - (\nabla \times \boldsymbol{B}) \times \boldsymbol{B} - \boldsymbol{F}_v^{RHS} \right], \tag{3.54a}$$

$$\left[(\nabla^2 - \partial_t)\mathcal{L}_2 + \tau\partial_\varphi \right] \nabla^2 v + \tau\mathcal{Q}w - \tilde{\rho}_0\tilde{\gamma}\mathcal{L}_2(\Theta + \Gamma) =$$
$$- \boldsymbol{r} \cdot \nabla \times \nabla \times \left[\boldsymbol{m} \cdot \nabla(\tilde{\rho}_0^{-1}\boldsymbol{m}) - (\nabla \times \boldsymbol{B}) \times \boldsymbol{B} - \boldsymbol{F}_v^{RHS} \right], \tag{3.54b}$$

$$\nabla^2\Theta + [R_i + R_e\eta(1 - \eta)^{-2}r^{-3}]\mathcal{L}_2 v = P\tilde{\rho}_0[\partial_t + \tilde{\rho}_0^{-1}\boldsymbol{m} \cdot \nabla]\Theta, \tag{3.54c}$$

$$\nabla^2\Gamma + R_\Gamma\eta(1 - \eta)^{-2}r^{-3}\mathcal{L}_2 v = L\tilde{\rho}_0[\partial_t + \tilde{\rho}_0^{-1}\boldsymbol{m} \cdot \nabla]\Gamma, \tag{3.54d}$$

$$\nabla^2\mathcal{L}_2 h = Pm[\partial_t\mathcal{L}_2 h - \boldsymbol{r} \cdot \nabla \times ((\tilde{\rho}_0^{-1}\boldsymbol{m}) \times \boldsymbol{B})], \tag{3.54e}$$

$$\nabla^2\mathcal{L}_2 g = Pm[\partial_t\mathcal{L}_2 g - \boldsymbol{r} \cdot \nabla \times \nabla \times ((\tilde{\rho}_0^{-1}\boldsymbol{m}) \times \boldsymbol{B})]. \tag{3.54f}$$

Here the negative Laplacian $\mathcal{L}_2$, the $\mathcal{Q}$ operator, and the $\boldsymbol{F}_v^{RHS}$ part of the viscous force are defined by

$$\mathcal{L}_2 \equiv (\boldsymbol{r} \times \nabla)^2 = \partial_r r^2 \partial_r - r^2\nabla^2 = -(\sin\theta)^{-1}\partial_\theta \sin\theta\partial_\theta - (\sin\theta)^{-2}\partial_\varphi^2, \tag{3.55a}$$

$$\mathcal{Q} \equiv r\cos\theta\nabla^2 - (\mathcal{L}_2 + r\partial_r)(\cos\theta\partial_r - r^{-1}\sin\theta\partial_\theta), \tag{3.55b}$$

$$\boldsymbol{F}_v^{RHS} \equiv \tilde{\rho}_0 \left[2(\partial_r\tilde{\rho}_0^{-1})(\partial_r\boldsymbol{m}) + (r^{-2}\partial_r r^2\partial_r\tilde{\rho}_0^{-1})\boldsymbol{m} + 1/3\nabla(\nabla \cdot \tilde{\rho}_0^{-1}\boldsymbol{m}) \right]. \tag{3.55c}$$

One may note that equations (3.51a) and (3.51f) are automatically satisfied when the poloidal-toroidal representation (3.53) is used. The pressure gradient also vanishes when we take the curl of the momentum equation. The nonlinear terms on the right-hand side of the scalar equations (3.54) are not explicitly evaluated in terms of poloidal and toroidal scalars. Although possible in general such explicit evaluation will result in lengthy expressions. However, the explicit form of these terms is of no significant importance. Indeed in a numerical integration of (3.54) it is much more convenient and computationally efficient to implement the terms in their compact vector form. On the other hand an analytical analysis is usually possible in linear or weakly nonlinear cases only, where these nonlinear terms will normally be neglected. One exception is the diffusion part of the viscous force which is a linear term and has already been separated from $\boldsymbol{F}_v^{RHS}$.

3.3.5 Boundary conditions

It is convenient to use the representation (3.53) and formulate the boundary conditions in terms of the poloidal and toroidal scalars of the velocity and magnetic fields.

Velocity field. To obtain the velocity boundary conditions in scalar form we substitute $\boldsymbol{u} = \tilde{\rho}_0(r)^{-1}\boldsymbol{m}$ in (3.31), (3.32) and (3.34) and use the fact that the momentum vector $\boldsymbol{m}$ is solenoidal.

　　No-slip boundary conditions. According to condition (3.31),

$$\boldsymbol{u}|_{r_i,r_o} = \frac{1}{\tilde{\rho}_0}\begin{bmatrix} m_r \\ m_\theta \\ m_\varphi \end{bmatrix}_{r_i,r_o} = \frac{1}{\tilde{\rho}_0}\begin{bmatrix} \frac{1}{r}\mathcal{L}_2 v \\ \partial_\theta \frac{1}{r}\partial_r rv + \frac{1}{r\sin\theta}\partial_\varphi w \\ \frac{1}{\sin\theta}\partial_\varphi \frac{1}{r}\partial_r rv - \partial_\theta w \end{bmatrix}_{r_i,r_o} = \boldsymbol{0} \tag{3.56}$$

must be satisfied for all values of θ and φ. The vanishing of the r-component of $\boldsymbol{m}$ requires that $v = 0$ at the boundaries. Using the requirements $\partial_\theta \sin\theta(m_\theta) + \partial_\varphi(m_\varphi) = 0$ and $\partial_\varphi(m_\theta) - \partial_\theta \sin\theta(m_\varphi) = 0$ we obtain the full set of no-slip boundary conditions:

$$v = \partial_r v = w = 0 \qquad \text{at} \qquad r = r_i, r_o. \tag{3.57}$$

　　Stress-free boundary conditions. With the help of an analogous procedure we transform the stress-free boundary conditions (3.32) and (3.34) into

$$\begin{vmatrix} \tilde{\rho}_0^{-1} m_r = 0 \\ \partial_r \tilde{\rho}_0^{-1} m_\theta = 0 \\ \partial_r \tilde{\rho}_0^{-1} m_\varphi = 0 \end{vmatrix} \quad \Longleftrightarrow \quad \begin{vmatrix} \tilde{\rho}_0^{-1} m_r = 0 \\ \partial_\theta \sin\theta(\partial_r \tilde{\rho}_0^{-1} m_\theta) + \partial_\varphi(\partial_r \tilde{\rho}_0^{-1} m_\varphi) = 0 \\ \partial_\varphi(\partial_r \tilde{\rho}_0^{-1} m_\varphi) - \partial_\theta \sin\theta(\partial_r \tilde{\rho}_0^{-1} m_\theta) = 0 \end{vmatrix} \tag{3.58}$$

which results in:

$$v = \partial_r \frac{1}{\tilde{\rho}_0}\partial_r v = \partial_r \frac{w}{\tilde{\rho}_0 r} = 0 \qquad \text{at} \qquad r = r_i, r_o. \tag{3.59}$$

Temperature and concentration fields. The temperature and the concentration boundary conditions (3.35) and (3.36) do not need to be changed in order to be valid with the scalar system of equations (3.54).

Magnetic fields. The matching conditions (3.37) and (3.38) require that both the poloidal and toroidal scalars of the magnetic field are continuous through the boundaries. The poloidal and toroidal scalars h_e and g_e of the external fields may be obtained using the formulas

$$h_e = (\mathcal{L}_2)^{-1}\boldsymbol{r} \cdot \boldsymbol{B}_e, \qquad g_e = (\mathcal{L}_2)^{-1}\boldsymbol{r} \cdot (\nabla \times \boldsymbol{B}_e) = 0, \tag{3.60}$$

where the external field is given by (3.40) in the case when the inner core region is assumed insulating. Since the external field is curl-free because it is potential, its toroidal component will vanish on the boundaries. Thus in the case of an insulating inner core region the magnetic field matching conditions may be summarized as:

$$g = h - h_e = \partial_r(h - h_e) = 0 \qquad \text{at} \qquad r = r_i, r_o. \tag{3.61}$$

In the case of a finitely conducting inner core, the induction equation must be simultaneously solved in the inner core in order to obtain the magnetic field in this region. However the toroidal scalar in the inner core will not vanish in general, hence:

$$g - g_e = \partial_r(g - g_e) = h - h_e = \partial_r(h - h_e) = 0 \qquad \text{at} \qquad r = r_i, \tag{3.62a}$$

$$g = h - h_e = \partial_r(h - h_e) = 0 \qquad \text{at} \qquad r = r_o. \tag{3.62b}$$

3.4 Boussinesq approximation

A considerable part of the results presented in the dissertation is based on the more widely-used Boussinesq approximation. In this approximation the assumption of a basic static density profile which varies with the distance from the center of the shell is replaced by the assumption of a uniform and constant density in the basic static state, i.e.

$$\tilde{\rho}_0(r) \longrightarrow \rho_0 = \text{const.} \tag{3.63}$$

Assumptions (**2**) and (**3**) of section 3.3.1 still hold. The governing equations may be simplified by either using derivations similar to those utilized in the case of the pseudo-anelastic approximation or simply taking the limit (3.63). Here we only summarize the main results.

Boussinesq equations. In the case of constant static density ρ_0 in the reference state the nondimensional governing equations (3.51) reduce to

$$\nabla \cdot \boldsymbol{u} = 0, \tag{3.64a}$$

$$(\partial_t + \boldsymbol{u} \cdot \nabla)\boldsymbol{u} = -\frac{d^2}{\bar{\rho}_0 \nu^2} \nabla \frac{p_1}{\rho_0} + \tau \boldsymbol{u} \times \hat{\boldsymbol{e}_z} + (\Theta + \Gamma)\boldsymbol{r} \tag{3.64b}$$

$$+ \nabla^2 \boldsymbol{u} + (\nabla \times \boldsymbol{B}) \times \boldsymbol{B}, \tag{3.64c}$$

$$P\left(\partial_t + \boldsymbol{u} \cdot \nabla\right)\Theta = \nabla^2 \Theta + \left(R_i + R_e \frac{\eta}{(1-\eta)^2}\frac{1}{r^3}\right)\boldsymbol{r} \cdot \boldsymbol{u}, \tag{3.64d}$$

$$L\left(\partial_t + \boldsymbol{u} \cdot \nabla\right)\Gamma = \nabla^2 \Gamma + R_\Gamma \frac{\eta}{(1-\eta)^2}\frac{1}{r^3}\boldsymbol{r} \cdot \boldsymbol{u}, \tag{3.64e}$$

$$\nabla \cdot \boldsymbol{B} = 0, \tag{3.64f}$$

$$\partial_t \boldsymbol{B} = \nabla \times (\boldsymbol{u} \times \boldsymbol{B}) + Pm^{-1}\nabla^2 \boldsymbol{B}. \tag{3.64g}$$

Several important simplifications may already be noticed. The equations become truly incompressible even in the basic reference state. The velocity vector in addition to than the momentum vector is solenoidal. Upon division of both sides of the momentum equation by ρ_0 the density is eliminated from the equation. It still appears in the pressure gradient term which vanishes when the curl of the equation is taken. In the case of constant density the gravity becomes proportional to the distance from the center by virtue of equation (3.10). Similar simplification occurs in the viscous force the second term, $\frac{1}{3}\mu\nabla(\nabla \cdot \boldsymbol{u})$, of which vanishes since $\boldsymbol{u}$ is divergence-free.

Scalar equations. The scalar equations resulting from (3.64) (or equivalently from rewriting (3.54)) are significantly simpler as well. Notably $\boldsymbol{r} \cdot \nabla \times \nabla \times$ of the viscous force, which was left in implicit form in equation (3.54b) may now be easily evaluated, since it consists of only one term where no additional derivatives due to the radial dependence of ρ_0 appear. The scalar equations are:

$$\left[(\nabla^2 - \partial_t)\mathcal{L}_2 + \tau\partial_\varphi\right]w - \tau\mathcal{Q}v = \boldsymbol{r} \cdot \nabla \times \left[\boldsymbol{u} \cdot \nabla\boldsymbol{u} - (\nabla \times \boldsymbol{B}) \times \boldsymbol{B}\right], \tag{3.65a}$$

$$\left[(\nabla^2 - \partial_t)\mathcal{L}_2 + \tau\partial_\varphi\right]\nabla^2 v + \tau\mathcal{Q}w - \mathcal{L}_2(\Theta + \Gamma) =$$
$$-\boldsymbol{r} \cdot \nabla \times \nabla \times \left[\boldsymbol{u} \cdot \nabla\boldsymbol{u} - (\nabla \times \boldsymbol{B}) \times \boldsymbol{B}\right], \tag{3.65b}$$

$$\nabla^2\Theta + [R_i + R_e\eta(1-\eta)^{-2}r^{-3}]\mathcal{L}_2 v = P[\partial_t + \boldsymbol{u} \cdot \nabla]\Theta, \tag{3.65c}$$

$$\nabla^2\Gamma + R_\Gamma\eta(1-\eta)^{-2}r^{-3}\mathcal{L}_2 v = L[\partial_t + \boldsymbol{u} \cdot \nabla]\Gamma, \tag{3.65d}$$

$$\nabla^2\mathcal{L}_2 h = Pm[\partial_t\mathcal{L}_2 h - \boldsymbol{r} \cdot \nabla \times (\boldsymbol{u} \times \boldsymbol{B})], \tag{3.65e}$$

$$\nabla^2\mathcal{L}_2 g = Pm[\partial_t\mathcal{L}_2 g - \boldsymbol{r} \cdot \nabla \times \nabla \times (\boldsymbol{u} \times \boldsymbol{B})]. \tag{3.65f}$$

However, one should keep in mind that the these equations are formulated in terms of the poloidal and toroidal scalars of the velocity field rather than the momentum vector as was the case with equations (3.54).

Boundary conditions. Only the boundary conditions for the velocity field differ from the conditions required by the pseudo-anelastic . The full set of boundary conditions is:

no-slip boundary conditions:
$$v = \partial_r v = w = 0, \tag{3.66a}$$
stress-free boundary conditions:
$$v = \partial_r^2 v = \partial_r \frac{w}{r} = 0, \tag{3.66b}$$
$$\Theta = 0 \tag{3.66c}$$
$$\Gamma = 0 \tag{3.66d}$$
in the case of an insulating inner core:
$$g = h - h_e = \partial_r(h - h_e) = 0 \qquad \text{at} \qquad r = r_i, r_o \tag{3.66e}$$
in the case of a finitely conducting inner core:
$$g - g_e = \partial_r(g - g_e) = h - h_e = \partial_r(h - h_e) = 0 \qquad \text{at} \qquad r = r_i,$$
$$g = h - h_e = \partial_r(h - h_e) = 0 \qquad \text{at} \qquad r = r_o, \tag{3.66f}$$
in the case of a perfectly conducting inner core:
$$\partial_r g = h = 0 \qquad \text{at} \qquad r = r_i,$$
$$g = h - h_e = \partial_r(h - h_e) = 0 \qquad \text{at} \qquad r = r_o. \tag{3.66g}$$

And the rain descended, and the floods came, and the wind blew and beat upon that house; and it fell not: for it was founded on rock.

Matthew, vii:24-25

4. Methods of Numerical Analysis

Various approaches to the self-consistent dynamo problem have been discussed in section 2.2.3 of chapter 2. The analytical methods described there rely, however, either on drastic oversimplifications of the problem or on assumptions which cannot be easily justified. The solutions obtained by such methods are usually irrelevant for comparisons with the real geomagnetic field. The same assertions hold for the problem of finite amplitude convection. An important simplification in this case is that the essential nonlinearity due to the magnetic field no longer appears, and the governing equations may be linearized to study the onset of convection. But then difficulties due to the geometry of the spherical shell restrict analytical linear results to particular regions in the parameter space or asymptotic regimes. Even less may be achieved analytically in studies of nonlinear convection.

Probably the only satisfactory approach to the dynamo problem involves numerical simulations based on some reasonable approximation of the first principles similar to those formulated in chapter 3. A great part of the research presented in this thesis also relies heavily on computational methods. This chapter describes the numerical scheme used to simulate the equations of the pseudo-anelastic (3.54) and of the Boussinesq approximation (3.65), as well as some auxiliary numerical techniques.

4.1 Method of solution

The factors, determining the choice of a particular numerical method are its accuracy, stability, memory requirements and efficiency. The estimation of the last two criteria follows in a straightforward manner from the definition of the method and the nature of the equations to be solved. Methods for numerical accuracy and stability analysis exist [47] and in general these quantities depend on the truncation errors and on the structure of the equations solved. However, estimation of these criteria are not easy or even possible except for simple model equations and experiments with various numerical methods are often necessary.

There are several numerical approaches to the spatial discretization of the dynamo problem in spherical geometry. The most obvious is a straightforward finite-difference method which, however, is never used in practice. The main problem with finite-differencing is the uneven distribution of grid points which accumulate near the poles on a spherical surface. It seems more intuitive to use an evenly distributed grid on the sphere and to discretize the equations with a finite-element or finite-volume method. Spectral methods, however, turn out to be most suitable for a number of reasons. In the first place, they provide a very high accuracy, since the error of a spectral method is $O(N^{-N})$ and decreases with increasing resolution, N, faster than any polynomial. This is due to the fact that an expansion in orthogonal functions provide information everywhere instead of only at the grid points. In addition, all spatial derivatives can be computed exactly in spectral space. For this reason, the spectral methods require only about half the resolution of finite difference or finite element methods in each spatial direction to achieve the same accuracy. This, in turn, results in a considerable reduction of memory and computational time, especially for a three-dimensional problem

such as the present one. Secondly, one of the major advantages of the finite-element methods, namely their easy applicability to complex geometries is of no big use here, because the spherical geometry is already pretty simple. Even, on the contrary, natural expansion functions exist for a spherical shell problem, namely the spherical harmonics. Among their many nice properties when used as basis functions they eliminate the "pole problem". A drawback of of the spectral methods, concerning the dynamo problem, is the lack of an efficient fast Legendre transform to be used in the frequent transformations between spectral and physical space. This fact poses some difficulties, especially for the effective use of massively parallel architectures.

In contrast to the discretization in space, spectral decomposition in time is not possible and more conventional finite-difference methods have to be employed. The reason is that while the functions which need to be discretized are well-known in the entire spatial domain at some moment t^k, their values at future moments t^{k+1} are not available. A large number of consistent temporal finite-difference schemes may be constructed and one is faced with the task to select a suitable scheme. For the dynamo problem, or indeed for the Navier-Stokes, or an advection-diffusion equation, a very popular scheme uses a combination of Adams-Bashforth explicit and Crank-Nicolson implicit method [35]. The implicit part is especially well-suited to terms of diffusion type and for which its unconditional stability may be shown and large time step may be used while still following the physical solution. In addition it provides numerical accuracy but requires the solution of a set of matrix equations at each time step. However, when one treats the Coriolis, the advection and the other nonlinear terms explicitly the remaining linear terms including the diffusion term decouple in spherical harmonic degree and order and the implicit operations are relatively easy to perform. A readable introduction to the variety of finite-differencing time schemes and analysis of their accuracy and stability, is given in [47], while a detailed experimental comparison of the performance of various methods for computing the convection part of the dynamo problem is the paper of Tilgner [113].

Based on these arguments we choose to simulate the scalar equations (3.54) of the pseudo-anelastic or (3.65) of the Boussinesq approximation using a pseudo-spectral method [113]. Such a method was first applied to the geodynamo problem by Glatzmaier and Roberts [56].

The chapter discusses the numerics of the more general pseudo-anelastic equations (3.54). The the Boussinesq case (3.65) is analogous and may be obtained by reduction.

4.1.1 Spatial discretization of the scalar equations

Spectral decomposition of the unknown functions. Basic to the method is the decomposition of the unknown functions in spherical harmonics in the angular directions and in Chebyshev polynomials in the radial direction.

Angular decomposition. The spherical harmonics expansions of the poloidal and toroidal scalars (3.53) of the momentum vector $\boldsymbol{m}$ and the magnetic field $\boldsymbol{B}$ as well as of the temperature and concentration deviations are

$$v = \sum_{l=0}^{\infty} \sum_{m=-l}^{l} V_l^m(r,t) P_l^m(\cos\vartheta) e^{im\varphi}, \quad w = r \sum_{l=0}^{\infty} \sum_{m=-l}^{l} W_l^m(r,t) P_l^m(\cos\vartheta) e^{im\varphi}, \qquad (4.1a)$$

$$g = \frac{1}{r} \sum_{l=0}^{\infty} \sum_{m=-l}^{l} G_l^m(r,t) P_l^m(\cos\vartheta) e^{im\varphi}, \quad h = \frac{1}{r} \sum_{l=0}^{\infty} \sum_{m=-l}^{l} H_l^m(r,t) P_l^m(\cos\vartheta) e^{im\varphi}, \qquad (4.1b)$$

$$\Theta = \sum_{l=0}^{\infty} \sum_{m=-l}^{l} \Theta_l^m(r,t) P_l^m(\cos\vartheta) e^{im\varphi}, \quad \Gamma = \sum_{l=0}^{\infty} \sum_{m=-l}^{l} \Gamma_l^m(r,t) P_l^m(\cos\vartheta) e^{im\varphi}, \qquad (4.1c)$$

where P_l^m denotes the associated Legendre functions some details about which may be found in section 4.1.3. The factors r and r^{-1} in (4.1a) and (4.1b) are not essential but contribute to the numerical stability of the method. A convenient simplification is that $F_l^{-m} = (-1)^m (F_l^m)^*$, where F_l^m is the coefficient in any of the expansions (4.1). The symmetry holds because all fields must be real, for example $v = v^*$, etc. Thus only the coefficients with $m \geq 0$ need to be stored, which reduces the memory requirements of the method.

Radial decomposition. Chebychev polynomials $T_n(r)$, defined on the interval $[0,1]$, are used for the discretization in the radial direction. The expansions are identical for all coefficients F_l^m in (4.1) and are given by

$$F_l^m(r,t) = \sum_{n=0}^{N-1} f_{l,n}^m(t) T_n(r). \tag{4.2}$$

Definition of the Chebyshev polynomials $T_n(r)$ is provided in appendix A.5.

Spatial derivatives and operators. Apart from the time derivative relevant in in temporal discretization, the Laplacian ∇^2, its angular part L_2, the radial derivative ∂_r, and the longitudinal derivative ∂_φ appear in the left-hand sides of (3.54).

A major advantage of the Chebyshev expansion is that it provides a very convenient method of computing the radial derivatives ∂_r of a function in spectral space. Consider the expansions of a function $f(x) = \sum_{n=0}^N a_n T_n(x)$ and of its derivative

$$\frac{\mathrm{d}}{\mathrm{d}x} f(x) = \sum_{n=1}^N a_n \frac{\mathrm{d}}{\mathrm{d}x} T_n(x) = \sum_{n=0}^{N-1} b_n T_n(x). \tag{4.3}$$

To relate the coefficients b_n of the derivative to the coefficients a_n of the function we substitute the recurrence relation

$$T_n = \frac{1}{2(n+1)} \frac{\mathrm{d}}{\mathrm{d}x} T_{n+1} - \frac{1}{2(n-1)} \frac{\mathrm{d}}{\mathrm{d}x} T_{n-1}. \tag{4.4}$$

into (4.3) and equate the coefficients in front of the corresponding Chebyshev functions. This results in a set of equations involving b_n and a_n, which when solved yields the recurrence relation

$$
\begin{aligned}
b_{N-1} &= 2N\, a_N \\
b_{N-2} &= 2(N-1)\, a_{N-1} \\
b_n &= 2(n+1)\, a_{n+1} + b_{n+2}, \qquad 1 \leq n \leq N-3 \\
b_0 &= a_1 + \tfrac{1}{2} d_2.
\end{aligned}
\tag{4.5}
$$

In a similar fashion the expansion in spherical harmonics facilitates the computation of the angular derivatives. In spectral space the angular momentum operator L_2, and the longitudinal derivative ∂_φ are simply replaced by their eigenvalues, i.e.

$$L_2 \left[P_l^m(\cos\theta)\, e^{im\varphi} \right] = l(l+1) \left[P_l^m(\cos\theta)\, e^{im\varphi} \right] \tag{4.6a}$$

$$\partial_\varphi e^{im\varphi} = im\, e^{im\varphi} \tag{4.6b}$$

With the help of the relation, $\nabla^2 = r^{-2}\partial_r r^2 \partial_r - r^{-2} L_2$, the Laplacian is then computed by taking radial derivatives ∂_r and operating with L_2.

Evaluation of the nonlinear terms. Because of their complexity, the nonlinear terms, the Coriolis force and parts of the viscous force are evaluated in physical space. Furthermore, this allows for efficient application of the implicit Crank-Nicolson method to the diffusive part of the equations (3.54). The following types of expressions need to be calculated.

Vectors, curls and cross products in spherical polars. The momentum $\boldsymbol{m}$ and the magnetic field $\boldsymbol{B}$ as well as their cross products and curls appear in the right-hand side of (3.54). To compute these expressions we make use of formula (A.13) for the components of poloidal and toroidal vectors and the expansions (4.1) and (4.2). As an example, the components of the momentum vector are

$$
\begin{bmatrix} m_r \\ m_\theta \\ [2ex]m_\varphi \end{bmatrix} = \sum_{l=0}^{\infty} \sum_{m=-l}^{l} \begin{bmatrix} \frac{l(l+1)}{r} V_l^m(r) P_l^m(\cos\theta) e^{im\varphi} \\ [2ex]\frac{1}{r}\partial_r r V_l^m(r)\partial_\theta P_l^m(\cos\theta) e^{im\varphi} + \frac{im}{\sin\theta} W_l^m(r) P_l^m(\cos\theta) e^{im\varphi} \\ \frac{im}{r\sin\theta}\partial_r r V_l^m(r) P_l^m(\cos\theta) e^{im\varphi} - W_l^m(r)\partial_\theta P_l^m(\cos\theta) e^{im\varphi} \end{bmatrix}.
$$
(4.7)

The cross product of two vectors and the curl of a vector may be obtained in a similar way using the familiar rules in spherical polars. The results will not be listed here.

The terms $\boldsymbol{m} \cdot \nabla \Theta$ and $\boldsymbol{m} \cdot \nabla \Gamma$. Taking advantage of the fact that $\boldsymbol{m}$ is solenoidal, these terms are equivalent to $\nabla \cdot (\Theta \boldsymbol{m})$ and $\nabla \cdot (\Gamma \boldsymbol{m})$, respectively, and are computed by the method outlined above.

The advection term $\boldsymbol{F}_a$. This term is most convenient to use when written as

$$
\boldsymbol{F}_a = \boldsymbol{m} \cdot \nabla \frac{1}{\tilde{\rho}_0} \boldsymbol{m} = \tilde{\rho}_0 \left[\frac{\boldsymbol{m}}{\tilde{\rho}_0} \cdot \nabla \frac{\boldsymbol{m}}{\tilde{\rho}_0} \right] = \tilde{\rho}_0 \left[\left(\nabla \times \frac{\boldsymbol{m}}{\tilde{\rho}_0} \right) \times \frac{\boldsymbol{m}}{\tilde{\rho}_0} + \frac{1}{2} \nabla \left(\frac{\boldsymbol{m}}{\tilde{\rho}_0} \right)^2 \right].
$$
(4.8)

Both terms in the square brackets can now be evaluated as described above. An additional simplification is that the gradient term vanishes when $r \cdot \nabla \times$ of (4.8) is taken. However, $r \cdot \nabla \times \nabla \times$ of the gradient term is nonzero and must be computed.

Viscous force. The viscous force in equations (3.54a) and (3.54b) has been already separated in two parts,

$$
\tilde{\rho}_0 \nabla^2 (\tilde{\rho}_0^{-1} \boldsymbol{m}) + 1/3 \tilde{\rho}_0 \nabla (\nabla \cdot \tilde{\rho}_0^{-1} \boldsymbol{m}) = \nabla^2 \boldsymbol{m} + \boldsymbol{F}_v^{RHS} = \tag{4.9}
$$
$$
\nabla^2 \boldsymbol{m} + \tilde{\rho}_0 \left[2(\partial_r \tilde{\rho}_0^{-1})(\partial_r \boldsymbol{m}) + (r^{-2}\partial_r r^2 \partial_r \tilde{\rho}_0^{-1}) \boldsymbol{m} + 1/3 \nabla (\nabla \cdot \tilde{\rho}_0^{-1} \boldsymbol{m}) \right].
$$

The first term may be efficiently treated with the Crank-Nicolson method while the second one is more easily computed in physical space at the right-hand side of the equations. The gradient term in (4.9) vanishes in the toroidal equation (3.54a).

Applying $\boldsymbol{r} \cdot \nabla \times$ and $\boldsymbol{r} \cdot \nabla \times \nabla \times$ on the nonlinear terms. After the terms at the right-hand side of (3.54) are completely evaluated we are left with vectors in physical space on which the operators $\boldsymbol{r} \cdot \nabla \times$ and $\boldsymbol{r} \cdot \nabla \times \nabla \times$ must be applied. In order to avoid an additional transformation between physical and spectral spaces the auxiliary quantities $P_r = S_r$, $P_\theta = S_\theta (r\sin\theta)^{-1}$ and $P_\varphi = S_\varphi (r\sin\theta)^{-1}$ are defined. Expressions for the desired derivatives may then be written directly in spectral space:

$$
[\hat{\boldsymbol{r}} \cdot \nabla \times \boldsymbol{S}]_l^m = (l+1)\frac{l-m}{2l-1}[P_\varphi]_{l-1}^m - l\frac{l+m+1}{2l+3}[P_\varphi]_{l+1}^m - im[P_\theta]_l^m \tag{4.10a}
$$

$$
[\hat{\boldsymbol{r}} \cdot \nabla \times \nabla \times \boldsymbol{S}]_l^m = l(l+1)[P_r]_l^m + \tag{4.10b}
$$
$$
\frac{1}{r^2}\frac{\mathrm{d}}{\mathrm{d}r}\left(r^2 \{(l+1)\frac{l-m}{2l-1}[P_\theta]_{l-1}^m - l\frac{l+m+1}{2l+3}[P_\theta]_{l+1}^m + im[P_\varphi]_l^m \} \right).
$$

Special care must be given to the points with l equal to the truncation parameter L.

Transformations between spectral and physical space. Of a paramount importance to the computational scheme are the methods of transformation between (r, θ, φ)- and (n, l, m)-spaces. Conversions need to be performed in order to treat efficiently the nonlinear terms as well as to compute derivatives which is most conveniently done in spectral space.

Radial transformation. The Chebyshev polynomials are defined as

$$T_n(x') = \cos\left(n \arccos(x')\right), \qquad x' \in [-1, 1], \tag{4.11}$$

(see also appendix A.5). However, the grid points r_j need to be situated in the volume of the spherical shell, i.e. between $r_i = 0$ and $r_o = 1$, which may be achieved by the change of variable $x' = 2(r - r_i) - 1$. The transformation between direct and Chebyshev space is facilitated by the special choice of the collocation points[1]

$$r_j = r_i + \frac{1}{2}(1 + \cos\pi\frac{j-1}{N-1}), \qquad j = 1 .. N, \tag{4.12}$$

In this case (4.11) gives $T_n(r_j) = \cos(n\pi\frac{j-1}{N-1})$ and the sum (4.2) becomes

$$F_l^m(r_j, t) = \sum_{n=0}^{N-1} f_{l,n}^m(t) \cos(n\,\pi\,\frac{j-1}{N-1}). \tag{4.13}$$

This, however, is precisely a cosine transform and we may greatly benefit from the existence of very efficient FFT (Fast-Fourier Transform) algorithms in order to perform the conversion between radial and Chebyshev spaces.

Angular transformations. In general, a function $f(r, \theta, \varphi)$ is transformed into its coefficients $F_l^m(r)$ and back with the transformations:

$$f(r, \theta, \varphi) = \sum_{m=-l}^{l} e^{im\varphi} \sum_{l=0}^{\infty} P_l^m(\cos\theta)F_l^m(r) \tag{4.14a}$$

$$F_l^m(r) = (-1)^m\frac{2l+1}{4\pi}\int_{-1}^{1} dx\, P_l^{-m}(x) \int_{0}^{2\pi} d\varphi\, e^{-im\varphi}f(r, \arccos x, \varphi), \quad x = \cos\theta \tag{4.14b}$$

The transformation (4.14a) $(l, m) \to (\theta, \varphi)$ requires a weighted sum of associated Legendre functions (a matrix-vector multiplication) followed by an FFT over the index m. The inverse transformation (4.14b) starts with the FFT and then needs to compute the projection integral. This is done with a Gauss quadrature which approximates the integral over x by the sum:

$$\int_{-1}^{1} g(x)\, dx = \sum_{i=0}^{L} w_i g(x_i) \tag{4.15}$$

The Gauss-Legendre weights w_i and the abscissas x_i are computed with the procedures of ref. [99]. The latitudinal transformation $l \leftrightarrow \theta$ represents the narrowest bottleneck of the numerical scheme, since no fast Legendre transform is presently known. It is however possible to optimize the matrix-vector multiplication used to compute (4.14a) by taking into account the symmetry properties of the Legendre functions.

---

[1] When the induction equation is solved for a conducting inner core grid points need to be placed in the inner core as well. The relevant change of variable is $x' = 1/d_1[2(r - r_s) - d_1]$, and the location of grid points is $r_j = r_s + d_1/2[1 + \cos\pi\frac{j-1}{N-1}]$. Here r_s is the radius of a negligibly small insulating sphere placed at the origin in order to prevent singularities and d_1 is the thickness of the inner core.

Spatially discretized equations. As a summary of the methods of spatial discretization we present the complete system of scalar equations in spectral space,

$$\partial_t W_l^m - \left(\mathcal{A}_l + \frac{2}{r^2}\right) W_l^m = \frac{4}{r}\partial_r W_l^m - \tag{4.16a}$$
$$- (l(l+1))^{-1} \left[\boldsymbol{r} \cdot \nabla \times \left(\boldsymbol{F}_a - (\nabla \times \boldsymbol{B}) \times \boldsymbol{B} - \boldsymbol{F}_v^{RHS} - \tau \boldsymbol{m} \times \hat{\boldsymbol{e}}_{\boldsymbol{z}}\right)\right]_l^m r^{-1},$$

$$\mathcal{D}_l(\partial_t - \mathcal{D}_l)V_l^m = -\tilde{\rho}_0\tilde{\gamma}[\Theta + \Gamma]_l^m + \tag{4.16b}$$
$$+ \frac{1}{l(l+1)} \left[\boldsymbol{r} \cdot \nabla \times \nabla \times \left(\boldsymbol{F}_a - (\nabla \times \boldsymbol{B}) \times \boldsymbol{B} - \boldsymbol{F}_v^{RHS} - \tau \boldsymbol{m} \times \hat{\boldsymbol{e}}_{\boldsymbol{z}}\right)\right]_l^m,$$

$$\partial_t\Theta_l^m - \frac{1}{P\tilde{\rho}_0}\mathcal{A}_l\Theta_l^m = \frac{1}{P\tilde{\rho}_0}\frac{2}{r}\partial_r\Theta_l^m - \tag{4.16c}$$
$$- \tilde{\rho}_0^{-1}\left[\nabla \cdot (\Theta\boldsymbol{m})\right]_l^m + (P\tilde{\rho}_0)^{-1}[R_i + R_e\eta(1-\eta)^{-2}r^{-3}]L_2 V_l^m,$$

$$\partial_t\Gamma_l^m - \frac{1}{L\tilde{\rho}_0}\mathcal{A}_l\Gamma_l^m = \frac{1}{L\tilde{\rho}_0}\frac{2}{r}\partial_r\Gamma_l^m - \tag{4.16d}$$
$$- \tilde{\rho}_0^{-1}\left[\nabla \cdot (\Gamma\boldsymbol{m})\right]_l^m + (L\tilde{\rho}_0)^{-1}R_\Gamma\eta(1-\eta)^{-2}r^{-3}L_2 V_l^m,$$

$$\partial_t H_l^m - \frac{1}{Pm}\mathcal{A}_l H_l^m = r(l(l+1))^{-1}\left[\boldsymbol{r} \cdot \nabla \times \left(\tilde{\rho}_0^{-1}\boldsymbol{m} \times \boldsymbol{B}\right)\right]_l^m, \tag{4.16e}$$

$$\partial_t G_l^m - \frac{1}{Pm}\mathcal{A}_l G_l^m = r(l(l+1))^{-1}\left[\boldsymbol{r} \cdot \nabla \times \nabla \times \left(\tilde{\rho}_0^{-1}\boldsymbol{m} \times \boldsymbol{B}\right)\right]_l^m. \tag{4.16f}$$

The advection term, $\boldsymbol{F}_a$, and the F_v^{RHS} part of the viscous force evaluated in direct space are inserted in the form of expressions (4.8) and (4.9), respectively. The spectral Laplacian $\mathcal{D}_l$ and the operator $\mathcal{A}_l$ are defined as

$$\mathcal{D}_l = \partial_r^2 + 2r^{-1}\partial_r - l(l+1)/r^2, \qquad \mathcal{A}_l = \partial_r^2 - l(l+1)/r^2. \tag{4.17}$$

The boundary conditions described in section 3.3.5 need to be transformed into spectral space as well. The detail worth mentioning here is how an explicit boundary condition involving only the poloidal scalar of the internal magnetic field is obtained. One expands the r-, θ-, and φ-components of the external potential field given by formulas (3.39) and (3.40) in spherical harmonics, and the internal field by an expansion analogous to (4.7). Taking into account that the toroidal field vanishes on the boundaries, one matches the expansions of the radial components as well as the expansions of any one of the angular components of the external and internal fields. These two equations allow to eliminate all unknowns related to the external field and provide the boundary condition for the poloidal magnetic scalar in spectral form,

$$\left[\left(\partial_r - \frac{l+1}{r}\right) H_l^m(r)\right]_{r=r_i} = 0, \qquad \left[\left(\partial_r + \frac{l}{r}\right) H_l^m(r)\right]_{r=r_o} = 0. \tag{4.18}$$

The rest of the boundary conditions are easily transformed into spectral space

$$0 = G_l^m = \Theta_l^m = \Gamma_l^m = \begin{cases} V_l^m = \partial_r V_l^m = W_l^m & \text{no-slip,} \\ V_l^m = \partial_r \tilde{\rho}_0^{-1}\partial_r V_l^m = \partial_r \tilde{\rho}_0^{-1}W_l^m & \text{stress-free} \end{cases} \bigg|_{r=r_i,r_o}. \tag{4.19}$$

4.1.2 Integration in time

Combination of Crank-Nicolson and Adams-Bashforth schemes. To introduce the temporal discretization schemes in use we consider the model equation,

$$\partial_t y(t) = f(y, t), \tag{4.20}$$

which needs to be integrated in time for the unknown function $y(t)$. Here the right-hand side $f(y, t)$ represents any functional relationship involving the unknown function and the independent variable t, which is discretized with a step of Δt. A large variety of finite difference formulas approximating the real solution may be constructed. We introduce the two of them which have been shown to be best suited to simulate equations (4.16) on the basis of their accuracy, stability, efficiency and storage requirements [113, 35].

Crank-Nicolson method. This is an implicit method, i.e. it approximates the time derivative ∂_t with the help of the values of the unknown function at a time when this value is still not known. In order for this to be done a system of algebraic equations must be solved at each time step. In spite of that it may be demonstrated that the method is very efficient when terms of diffusion type are treated. Furthermore, it is unconditionally stable for such terms, which allows for larger time steps. The Crank-Nicolson formula of second order is

$$y^{k+1} - y^k = \Delta t/2 \left[f^{k+1} + f^k \right]. \tag{4.21}$$

Here the value of a function at the k-th time step is denoted by a superscript k.

Adams-Bashforth method. This is an explicit method, i.e. it approximates the time derivative ∂_t with the help of the values of the unknown function which are already available from the previous time steps. Therefore it is conceptually simpler especially for right-hand side functions $f(y, t)$ which are complicated to evaluate (e.g. nonlinear terms) and for advective terms. The Adams-Bashforth formula second order is

$$y^{k+1} - y^k = \Delta t/2 \left[3f^k - f^{k-1} \right]. \tag{4.22}$$

Combined scheme. Very often the structure of the terms in the equation to be solved is such that different schemes are appropriate for the different terms. Let us consider a right-hand side of (4.19) with the structure $f(y, t) = f_{CN}(y, t) + f_{AB}(y, t)$, where f_{CN} is well suited to the Crank-Nicolson scheme, while f_{AB} to the Adams-Bashforth scheme. To take advantage of both we construct the combined formula

$$y^{k+1} - y^k = \Delta t/2 \left[f_{CN}^{k+1} + f_{CN}^k \right] + \Delta t/2 \left[3f_{AB}^k - f_{AB}^{k-1} \right]. \tag{4.23}$$

For the first time step the Adams-Bashforth scheme must be replaced by the Euler first order scheme, since no previous values are available at this point

$$y^1 - y^0 = \Delta t/2 \left[f_{CN}^1 + f_{CN}^0 \right] + \Delta t \ f_{AB}^0. \tag{4.24}$$

Application to equations (4.16)**.** The structure of equations (4.16) may be schematically represented by an equation of the type

$$\partial_t F_l^m(r, t) - \hat{\mathcal{L}} F_l^m(r, t) = N_l^m(F, r, t). \tag{4.25}$$

Here the operator $\hat{\mathcal{L}}$ represents the linear terms of diffusion type treated with the help of the Crank-Nicolson method, while N_l^m stands for the nonlinear, Coriolis and the part of the viscous term which are better suited to the Adams-Bashforth scheme and $F_l^m(r, t)$ are the coefficients in the angular expansion of any of the unknown scalar quantities (4.1). Making use of the combined formula (4.23) we obtain

$$\left(1 - \frac{\Delta t}{2} \hat{\mathcal{L}} \right) [F_l^m]^{k+1} = \left\{ \left(1 + \frac{\Delta t}{2} \hat{\mathcal{L}} \right) [F_l^m]^k + \frac{\Delta t}{2} \left(3[N_l^m]^k - [N_l^m]^{k-1} \right) \right\}, \tag{4.26}$$

for the unknowns $F_l^m(r,t)$ at the $k+1$-th time step. Because of the implicit Crank-Nicolson scheme equation (4.26) is in fact a matrix equation representing a system of N linear equations for every pair l, m i.e. $M_l^m f_l^m = b_l^m$, after $F_l^m(r,t)$ and the right-hand side b_l^m have been expanded by (4.2). The first and the last rows of the matrices M_l^m correspond to the dynamic equations at the inner and outermost collocation points and are replaced by the boundary conditions. The matrices M_l^m are LU decomposed, inverted and stored during initialization. The inverted matrices multiply the right-hand side $b_{l,n}^m$ of (4.26) at each time step in order to obtain $[f_{l,n}^m]^{k+1}$. The procedure may be illustrated by the schematic equation

$$
\begin{bmatrix}
\left[f_{l,0}^m\right]^{k+1} \\
\left[f_{l,1}^m\right]^{k+1} \\
\vdots \\
\left[f_{l,N-2}^m\right]^{k+1} \\
\left[f_{l,N-1}^m\right]^{k+1}
\end{bmatrix}
=
\begin{bmatrix}
\underline{\hspace{2cm} b.c._1 \hspace{2cm}} \\
\vdots \\
(1 - \frac{\Delta t}{2}\hat{\mathcal{L}})T_n(r)\big|_{r=r_j} \\
\vdots \\
\overline{\hspace{2cm} b.c._2 \hspace{2cm}}
\end{bmatrix}^{-1}
\begin{bmatrix}
b.c._1 \\
\vdots \\
\left[b_{l,n}^m\right]^k \\
\vdots \\
b.c._2
\end{bmatrix}
, \tag{4.27}
$$

where $b.c.$ denotes the corresponding boundary conditions.

The poloidal velocity equation. The equation (4.16b) is more complicated in that it is forth order and involves two boundary conditions. The above method may, nevertheless, be applied but this would waist total of four collocation points near the boundaries. The so-called influence matrix method is used instead. It replaces the inhomogeneous poloidal velocity problem by two problems and splits the pair of boundary conditions between them so no extra collocation points are waisted. The first problem is inhomogeneous and is given by the system

$$
\mathcal{D}_l \tilde{u}_l^m = -\tilde{\rho}_0 \tilde{\gamma} [\Theta + \Gamma]_l^m +
$$
$$
+ \frac{1}{l(l+1)} \left[\boldsymbol{r} \cdot \nabla \times \nabla \times \left(\boldsymbol{F}_a - \tilde{\rho}_0^{-1}(\nabla \times \boldsymbol{B}) \times \boldsymbol{B} - \boldsymbol{F}_v^{RHS} - \tau \boldsymbol{m} \times \hat{\boldsymbol{e}}_{\boldsymbol{z}} \right) \right]_l^m ,
$$
$$
\tilde{u}_l^m(r_i) = \tilde{u}_l^m(r_o) = 0, \tag{4.28a}
$$
$$
(\partial_t - \mathcal{D}_l)u_l^m = \tilde{u}_l^m, \qquad u_l^m(r_i,t) = u_l^m(r_a,t) = 0. \tag{4.28b}
$$

The second equation (4.28b) is introduced merely to reduce the order of the original equation. The second problem is

$$
\mathcal{D}_l \, \tilde{u}_{1,l} = 0, \qquad\qquad \tilde{u}_{1,l}(r_i) = 1, \; \tilde{u}_{1,l}(r_a) = 0, \tag{4.29a}
$$
$$
\mathcal{D}_l \, \tilde{u}_{2,l} = 0, \qquad\qquad \tilde{u}_{2,l}(r_i) = 0, \; \tilde{u}_{2,l}(r_a) = 1, \tag{4.29b}
$$
$$
(\partial_t - \mathcal{D}_l) \, u_{j,l} = \tilde{u}_{j,l}, \qquad u_{j,l}(r_i,t) = u_{j,l}(r_a,t) = u_{j,l}(r,t=0) = 0, \quad j = 1,2. \tag{4.29c}
$$

The equations (4.29a) and (4.29b) are precomputed during initialization since they are time independent. The equations (4.28) and (4.29c) are already in a form which may be stepped with the method used for the rest of the spectral equations. The actual poloidal field is finally obtained as a sum of the solutions of the two subproblems

$$
[V_l^m]^{k+1} = [u_l^m]^{k+1} + a_{1,l}^m [u_{1,l}]^k + a_{2,l}^m [u_{2,l}]^k. \tag{4.30}
$$

The coefficients $a_{1,l}^m$ and $a_{2,l}^m$ are uniquely determined by the second boundary condition for the poloidal field (4.19).

4.1.3 Algorithm of implementation

In order to put together the details of the numerical methods we describe the general scheme of the code used to simulate the geodynamo problem. The sequence of operations executed by the program is as follows:

(1) Read the parameters of the run (resolution N, L, M, dimensionless parameters etc.). Allocate the necessary memory space. With all auxiliary variables, the total storage requirement adds up to about $20 \times N \times L \times 2M$ real numbers, depending on details of the implementation. Complex numbers occur at intermediate stages of the algorithm. These are stored in real arrays with real and imaginary parts alternating between adjacent entries of the arrays.

(2) Compute and invert all the matrices required in the implicit time step, equations (4.26), (4.28) and (4.29). Fill tables of values of associated Legendre functions, their derivative, and functions with negative index m. These numbers will be needed when computing $\boldsymbol{m}$ and $\nabla \times \boldsymbol{m}$ and during the transformations from (l, m) to (θ, φ) space and back. The P_l^m are computed with a recursion over l

$$(l - m)P_l^m(x) = x(2l - 1)P_{l-1}^m(x) - (l + m - 1)P_{l-2}^m(x), \tag{4.31a}$$

$$P_m^m(x) = (-1)^m \cdot 1 \cdot 3 \cdot 5 \cdot \ldots (2m - 1)(1 - x^2)^{m/2}, \tag{4.31b}$$

$$P_{m+1}^m(x) = x(2m + 1)P_m^m(x). \tag{4.31c}$$

The derivative is obtained from
$$(1 - x^2)\frac{\mathrm{d}}{\mathrm{d}x}P_l^m(x) = -l\,x\,P_l^m(x) + (l + m)P_{l-1}^m(x). \tag{4.32}$$

The functions with negative m are calculated as

$$P_l^{-m}(x) = (-1)^m \frac{(l - m)!}{(l + m)!} P_l^m(x), \tag{4.33}$$

and occur in the orthogonality relation

$$\int_{-1}^{1} P_{l'}^{-m}(x)P_l^m(x)\ \mathrm{d}x = (-1)^m \frac{2}{2l + 1}\delta_{ll'}. \tag{4.34}$$

(3) Load the initial $f_{l,n}^m$-fields in spectral space and compute their first and second derivatives, equations (4.6a).

(4) Evaluate the explicit terms in the right-hand sides of equations (4.16), using formulas (4.7) to (4.15). This step may be performed in parallel over the radial index on a multiprocessor platform.

(5) Start the main time stepping loop in which the implicit Crank-Nicolson method is coupled to an explicit Adams-Bashforth step for the non-linear terms as given by (4.26). For the very first time step replace the Adams-Bashforth which needs to know the results from the previous time step by the Euler formula as in (4.24). Matrix-vector multiplications need to be performed which may run in parallel over the azimuthal index m. Load balancing is a problem here, because there is a different number of matrix-vector multiplications to be computed for each m. At the end of the time step, compute the radial derivatives of $f_{l,n}^m$ and save the right hand sides of (4.16).

(6) Same as **(4)**.

(7) At regular intervals, call a routine which saves various quantities of interest, such as the instantaneous kinetic and magnetic energy of the flow. The reconstruction of the various observables from the solution of equations (4.16) will be addressed in the next section.

(8) End of time stepping loop. Save the final state. End of program.

The CPU intensive procedures are those involving matrix multiplications, i.e. the implicit time step and the $l - \theta$ transformations.

4.2 Observables and visualization

The three-dimensional numerical simulations of the geodynamo easily produce massive giga-byte sets of data. Scientific visualization, which transforms this raw numbers into vivid 2D or 3D images, is an essential if not the major way to understand the large-scale datasets.

4.2.1 Velocity and magnetic field visualization

Being four-dimensional vector fields (three spatial coordinates and time), the $\boldsymbol{u}$– and $\boldsymbol{B}$–fields pose a major challenge to represent. Expressions (4.7) for the components of $\boldsymbol{u}$ and $\boldsymbol{B}$ have already been given. Although very often 3D images of a scalar quantity (see figures 2.2, 5.1, 6.20, 7.7) or of field lines, as well as animations in time have been created, by far the most efficient spatial visualization of $\boldsymbol{u}$ and $\boldsymbol{B}$ is the method of stream functions. It can be shown that these vector fields can be represented as a superposition of three stream functions, the contour lines of which are streamlines on the meridional planes, the cones of constant latitude and the spherical surface of constant radius,

$$\boldsymbol{u} \equiv \begin{bmatrix} u_r \\ u_\theta \\ u_\varphi \end{bmatrix} = \begin{bmatrix} 0 \\ \sin\theta^{-1}\partial_\varphi F_r \\ -\partial_\theta F_r \end{bmatrix} + \begin{bmatrix} -(r^2\sin^2\theta)^{-1}\partial_\varphi F_\theta \\ 0 \\ (r\sin\theta)^{-1}\partial_r F_\theta \end{bmatrix} + \begin{bmatrix} -(r^2\sin\theta)^{-1}\partial_\theta F_\varphi \\ (r\sin\theta)^{-1}\partial_r F_\varphi \\ 0 \end{bmatrix}, \quad (4.35a)$$

where the stream functions are given by

$$F_r = w, \quad F_\theta = r\frac{\partial}{\partial\varphi}v \quad \text{and} \quad F_\varphi = r\sin\theta\frac{\partial}{\partial\theta}v. \quad (4.35b)$$

There is no convenient and short method for representing the solution fields in time on paper and one simply resorts to plotting selected sequences of the data as is often done in this report.

4.2.2 Some global quantities

Averages. Various averages $\langle f(x)\rangle \equiv X^{-1}\int_0^X \mathrm{d}x f(x)$ are used in the dissertation, for which we adopt the notation: • $\overline{X}$ – azimuthal average, • $\langle X\rangle_{\theta,\varphi}$ – average over a spherical surface with radius r, • $\langle X\rangle$ – volume average • $\langle X\rangle_t$ – time average.
Energy densities. To assess conveniently the role of various flow and magnetic field components, the total kinetic and magnetic energy densities,

$$E \equiv \Big\langle \frac{1}{2}\boldsymbol{u}^2 \Big\rangle = \overline{E}_p + \overline{E}_t + \check{E}_p + \check{E}_t, \qquad M \equiv \Big\langle \frac{1}{2}\boldsymbol{B}^2 \Big\rangle = \overline{M}_p + \overline{M}_t + \check{M}_p + \check{M}_t, \quad (4.36)$$

are separated in parts, where ‾ indicates an axisymmetric component, ˇ indicates a non-axisymmetric (fluctuating) component and the indexes p and t – poloidal and toroidal parts. The definitions of these densities are given by

$$\overline{E}_p = \frac{1}{2}\langle |\ \nabla\times(\nabla\overline{v}\times\boldsymbol{r})\ |^2\rangle, \qquad \overline{E}_t = \frac{1}{2}\langle |\ \nabla\overline{w}\times\boldsymbol{r}\ |^2\rangle,$$

$$\check{E}_p = \frac{1}{2}\langle |\ \nabla\times(\nabla\check{v}\times\boldsymbol{r})\ |^2\rangle, \qquad \check{E}_t = \frac{1}{2}\langle |\ \nabla\check{w}\times\boldsymbol{r}\ |^2\rangle, \quad (4.37)$$

and analogously for M. For numerical purposes we list the equivalent spectral expressions

$$\overline{E}_p = \frac{3(1-\eta)^3}{2(1-\eta^3)} \int \mathrm{d}r \sum_l \frac{l(l+1)}{2l+1}[l(l+1)|V_l^0|^2 + |r\frac{\mathrm{d}}{\mathrm{d}r}V_l^0 + V_l^0|^2], \tag{4.38a}$$

$$\overline{E}_t = \frac{3(1-\eta)^3}{2(1-\eta^3)} \int \mathrm{d}r \sum_l \frac{l(l+1)}{2l+1}r^4|W_l^0|^2, \tag{4.38b}$$

$$\check{E}_p = \frac{3(1-\eta)^3}{1-\eta^3} \int \mathrm{d}r \sum_l \sum_{m=1}^l \frac{l(l+1)}{2l+1}\frac{(l+m)!}{(l-m)!}[l(l+1)|V_l^m|^2 + |r\frac{\mathrm{d}}{\mathrm{d}r}V_l^m + V_l^m|^2], \tag{4.38c}$$

$$\check{E}_t = \frac{3(1-\eta)^3}{1-\eta^3} \int \mathrm{d}r \sum_l \sum_{m=1}^l \frac{l(l+1)}{2l+1}\frac{(l+m)!}{(l-m)!}r^4|W_l^m|^2. \tag{4.38d}$$

Ohmic and viscous dissipations, $O \equiv \langle|\boldsymbol{J}|^2\rangle$ and $V \equiv \langle 2(e_i j^2 - 1/3 e_j j^2)\rangle$, are decomposed in a similar way, and for example

$$\bar{V}_p = \langle|\nabla^2\nabla \times \boldsymbol{r}\,\bar{v})|^2\rangle, \qquad \bar{V}_t = \langle|\nabla \times (\nabla \times \boldsymbol{r}\,\bar{w})|^2\rangle,$$
$$\check{V}_p = \langle|\nabla^2\nabla \times \boldsymbol{r}\,\check{v})|^2\rangle, \qquad \check{V}_t = \langle|\nabla \times (\nabla \times \boldsymbol{r}\,\check{w})|^2\rangle. \tag{4.39}$$

Nusselt number is the ratio of the convective heat transport to the conductive heat transport in the basic state through a spherical surface with radius r, and thus it is defined as

$$Nu = \frac{\langle -P^{-1}\nabla T + \boldsymbol{u}\,T\rangle_{\theta,\varphi}}{\langle -P^{-1}\nabla T_s\rangle_{\theta,\varphi}} = 1 + \frac{\langle -P^{-1}\nabla\Theta + \boldsymbol{u}\,T\rangle_{\theta,\varphi}}{\langle -P^{-1}\nabla T_s\rangle_{\theta,\varphi}}. \tag{4.40}$$

Helicity, which plays an important role in some mean-field dynamo models, is given by

$$H = \int_{hemisphere} (\nabla \times \boldsymbol{u}) \cdot \boldsymbol{u}\,\mathrm{d}V. \tag{4.41}$$

5. Linear Onset of Convection in Rotating Fluid Spheres and Shells
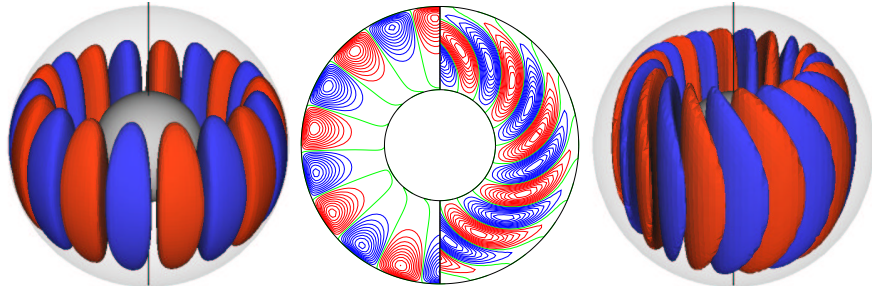
5.1 Introduction

Topic and motivation. The present chapter focuses the attention on the properties of the linear onset of convection in rotating fluid spheres and shells. The topic may seem not too relevant in view of the fact that linear convection has not yet been observed to generate magnetic fields. However, the properties of convection at onset provide much insight to finite-amplitude convection. Indeed, it is remarkable how many of the features and mechanisms of convection at onset can still be recognized even in a highly turbulent state. The linear solutions of the governing equations thus provide a firm foundation on which the nonlinear results reported in the dissertation may be understood. The present chapter is essentially a revised and extended version of references [107, 109, 34, 32].

The introductory discussion 2.2.3 has already outlined the role of convection in modern theory of geomagnetism and its relations to other branches. However, the importance of convection is not restricted to geomagnetism. Convection provides a relatively simple dynamical system where transition to turbulence and other aspects of the Navier-Stokes equations may be studied analytically, numerically and experimentally under controlled conditions. Rotating convection represents one of the fundamental systems on which a considerable part of the understanding of many observed geophysical, planetary and astrophysical phenomena is based. Examples include mantle and solar convection, ocean circulation, cloud patterns, differential rotation on the surface of the major planets and others [26].

Basic results. Difficulties. Rotating thermal convection has attracted much attention in the last half a century following the famous monograph of Chandrasekhar [36] who presented a rigorous formulation, a summary and an extension of the early results on both non-rotating and rotating plane layer and spherical systems. Innumerable research papers, a large number of review articles as well as several monographs have been published since. A brief summary of the principal results and further references have already been provided in section 2.2.3.

Although a large number of properties of rotating thermal convection have been investigated [24, 125], many difficulties and open questions still remain. The nonlinear governing equations do not possess general analytical solutions at finite amplitudes. The rigorous analysis of the linear onset is also difficult because of the varying angle between the Coriolis and gravity forces throughout the volume of the spherical shell which renders the problem truly three-dimensional. The preferred mode of convection is usually non-axisymmetric and strongly time dependent even at onset. On the numerical side the investigation of the problem is hindered by the large number of parameters including the Rayleigh and Prandtl numbers, the Coriolis parameter τ as well as the radius ratio of the spherical shell η. In addition, various choices of the boundary conditions, heating model and variation of gravity, concentration of light elements, density distribution etc. must also be addressed. Because a radially directed buoyancy force cannot be easily realized in an Earth-bound laboratory, one has to resort to the use of centrifugal acceleration [27] or even spacecrafts [66] for an experimental study. Thus, it is not surprising that place for new developments in the field of rotating thermal convection in spherical geometries still exists.

Fig. 5.1. *The major types of convection near onset: inertial convection at $P = 0.025$, $\tau = 10^5$ and $R = 3.1 \times 10^5$ (left part) and columnar convection at $P = 1$, $\tau = 10^4$ and $R = 2.8 \times 10^5$ (right part). Blue and red surfaces in the left and right plots correspond to negative and positive values of u_r. The middle plot shows equatorial streamlines $r \, \partial_\varphi v = const$.*

Types of convective flows. The behavior of convection in a rapidly rotating system differs fundamentally from that in a non-rotating one. The Coriolis force exerts a dominant control on the dynamics of the flow and provides a constraint that must be broken before convection can occur. Once convection sets in, this constraint must be surmounted for an efficient heat transfer to exist. In the case when a magnetic field is not present, it is the Prandtl number P that mainly controls how the rotation constraint is broken and opposed. The various convection modes may conveniently be classified according to the magnitude of P. Two fundamentally different forms of convection may be distinguished (see figure 5.1):

- **columnar convection** [13] has rolls aligning with the axis of rotation and intercepting the outer spherical surface at mid-latitudes; the azimuthal length scale of the roll is much shorter than the radial scale; it is observed at moderate and large values of P,
- **inertial convection** [124] exhibits rolls trapped near the outer spherical surface in the equatorial region and large azimuthal length scale compatible to the radial scale; it is realized at small values of P.

Contents. A large range of values of P extending from 10^{-7} to 10^2 will be considered and new results on columnar, inertial and intermediate types of convection will be reported.

In section 5.2 we outline the reduction of the basic equations (3.64) and (3.65) to the linear case of non-magnetic convection. In section 5.3 we briefly describe a Galerkin method used to perform the numerical studies reported in the chapter.

In section 5.4 the linear onset of columnar convection is investigated. We extend the studies reported in references [124] and [3] to the case of fixed-flux thermal boundary conditions. We return to the case of fixed-temperature conditions and construct a surface representing the critical Rayleigh number R_c in P–τ space. The numerical values are compared with the asymptotic expressions derived by Busse [13] on the basis of the annulus model. These results have proved to be very valuable in our simulations of nonlinear convection and dynamo action since they facilitate the correct estimation of the values of R necessary to generate magnetic field or to enter a particular finite-amplitude convection regime thus reducing the number of trial computational runs and providing insight into the dynamics of the flow.

In section 5.5 the onset of inertial convection as well as the patterns intermediate to the non-rotating regime and to asymptotically high rotation rates τ at very small values of P are investigated numerically. Results with both fixed-temperature and fixed-flux thermal boundary conditions are reported. Convection at small values of P seems to support magnetic field generation even at very low values of the magnetic Prandtl number Pm. Reaching values of Pm as small as possible is an important goal of geodynamo simulations since the actual

value of this parameter in the case of the Earth is estimated to be as low as 10^{-6} [23]. Following this path values as small as $Pm = 0.1$ has been reached in our simulations as will be reported in chapter 7. Additional motivation for the study of inertial convection is that previous works reach neither very low values of P nor very high values of τ. For example, both papers of Zhang & Busse [124] and Ardes *et al.* [3] which are the closest in scope to the present analysis discuss only cases in the ranges $0.1 \leq P \leq 10^2$ and $10 \leq \tau \leq 10^6$ while it is found that many interesting features occur outside this domain as shall be reported in section 5.5. Some particular goals are to outline the border between regions of retrograde and prograde drifting modes in P–τ–η space to verify the prediction that in the regime of inertial convection the ratio between the frequency ω and the rotation rate must remain constant for a broad range of rotation rates and has little radial dependence. A study of the dependences of R_c and ω on the radius ratio has also not yet been investigated in previous studies.

Motivated by the numerical results, we report an analytical theory for the onset of inertial convection in section 5.6. Inertial convection is a form of fluid motion which is a combination of inertial oscillations and thermal convection. Inertial oscillations represent the simplest time-dependent motion in a rotating fluid system. Just like the Taylor-Proudman theorem they describe the motion of a uniform inviscid rotating fluid in the absence of magnetic forces but in contrast the time-dependence of the flow is retained, i.e. all terms except $\partial_t \boldsymbol{u}$, the pressure and the Coriolis term in the primitive Navier-Stokes equations (3.3) and (3.12) are neglected. The reduced equations are then equivalent to the *Poincaré equation*

$$\partial_t^2 \nabla^2 \pi + 4\Omega\, \partial_z^2 \pi = 0, \tag{5.1}$$

where π is the pressure and Ω is the angular velocity. General solutions of (5.1) for a sphere are given in [126]. The connection between inertial waves and thermal convection at vanishing P in a rapidly rotating fluid layer was first noticed by Chandrasekhar [36]. At sufficiently small values of P inertial oscillations are weakly influenced by convection. Following this idea more systematic studies for various convection systems were undertaken by Zhang [120, 121, 122]. The buoyancy term and viscous dissipation are introduced in the equation of motion as perturbations of inviscid inertial waves and the balance of the two terms is used to determine the critical value of the Rayleigh number. In section 5.6 we extend this approach to the case of a spherical boundary of low thermal conductivity on the one hand and to an alternative method of analysis on the other hand which allows us to obtain explicit expressions for the dependence of the Rayleigh number and frequency on the azimuthal wave number and the product τP. The analytical results are compared with direct numerical solutions.

5.2 Reduction of the governing equations to the linear case

The scope of the present chapter does not require the use of the full set of primitive governing nonlinear equations (3.3), (3.12), (3.19), (3.20), (3.25c) and (3.28) derived in chapter 3. Here we present a reduced set of equations forming the mathematical basis for the linear analysis, reported in this chapter.

We restrict the attention to non-magnetic convection driven only by thermal buoyancy. The appropriate starting point are the Boussinesq equations (3.64) of chapter 3. We drop entirely the equations for the magnetic field (3.64f) and (3.64g) and for the concentration of light material (3.64e) and therefore also the Lorentz force $(\nabla \times \boldsymbol{B}) \times \boldsymbol{B}$ and the compositional buoyancy force $\Gamma \boldsymbol{r}$ from the momentum equation (3.64b). Furthermore, we assume a simple gravity field and basic temperature distribution

$$\boldsymbol{g} = -\gamma \boldsymbol{r}, \qquad T_s = \beta_0 - \beta r^2/2. \tag{5.2}$$

Such temperature distribution is due to a homogeneous distribution of internal heat sources. Thus, we drop the term $R_e\eta(1-\eta)^{-2}r^{-3}\boldsymbol{r}\cdot\boldsymbol{u}$ from the temperature equation (3.64d). Since only the Rayleigh number due to heat sources R_i is left in the problem we shall omit the subscript "i" and denote it simply by R. We neglect the nonlinear terms $\boldsymbol{u}\cdot\nabla\boldsymbol{u}$ and $\boldsymbol{u}\cdot\nabla\Theta$ in the remaining equations since we consider the problem of the onset of convection in the form of small disturbances. Using the scalings and the definitions of the nondimensional parameters introduced in sections 3.3.3 and 3.4, we arrive at the reduced set of linear equations,

$$\nabla\cdot\boldsymbol{u} = 0, \tag{5.3a}$$

$$\partial_t\boldsymbol{u} + \tau\boldsymbol{e}_z\times\boldsymbol{u} - \nabla\pi = \Theta\boldsymbol{r} + \nabla^2\boldsymbol{u}, \tag{5.3b}$$

$$R_c\boldsymbol{r}\cdot\boldsymbol{u} + \nabla^2\Theta - P\partial_t\Theta = 0, \tag{5.3c}$$

where π denotes a modified pressure.

Using a poloidal-toroidal representation of the solenoidal velocity field of the type (A.11) and applying the operators $\boldsymbol{r}\cdot\nabla\times$ and $\boldsymbol{r}\cdot\nabla\times\nabla\times$ on the momentum equation (5.3b), it is written in terms of scalar fields

$$[(\partial_t - \nabla^2)\mathcal{L}_2 - \tau\partial_\varphi]\nabla^2 v - \tau\mathcal{Q}w = 0, \tag{5.4a}$$

$$[(\partial_t - \nabla^2)\mathcal{L}_2 - \tau\partial_\varphi]w + \tau\mathcal{Q}v = 0, \tag{5.4b}$$

where the operators $\mathcal{L}_2$ and $\mathcal{Q}$ are defined by (3.55a) and (3.55b).

To complete the mathematical formulation we need to specify appropriate boundary conditions. We shall assume stress-free conditions for the velocity field with either a fixed temperature (case A) or a fixed flux on the boundaries (case B),

$$0 = v = \partial_r^2 v = \partial_r\frac{w}{r} = \begin{cases} \Theta, & \text{case A} \\ \partial_r\Theta, & \text{case B} \end{cases} \quad \text{at } r_i \text{ and } r_o. \tag{5.5}$$

Further more specific details on the mathematical formulation will be given in section 5.6 where we will report analytical results on inertial convection in a rotating fluid sphere.

5.3 Numerical method of linear analysis

The onset of convection is, of course, only a part of the general self-consistent dynamo process driven by thermal and compositional convection. Therefore, it may be investigated with the help of the general numerical methods described in chapter 4. However, these methods are not well-suited for treating the linear problem. In particular, no assumptions for the form of the time dependence of solutions can be made since in the general nonlinear case such dependence is not known and it is the aim of the numerical integration to find it. In contrast, the form of the time dependence of the solution is well-known in the linear case – because the equations are autonomous, an exponential ansatz for the time dependence can be used. Equations (5.4) and (5.3c) then form a linear eigenvalue problem for the critical Rayleigh number R_c and frequency ω. The linear problem of the onset of convection thus becomes considerably less demanding in terms of computational resources and time.

Galerkin spectral methods. In order to realize this idea we use a Galerkin spectral method. In general, the method reduces a partial differential equation $\mathcal{M}\,y = 0$ for the unknown $y(x,t)$ to a set of N ordinary differential equations in time by posing a truncated expansion for $y(x,t)$ in terms of some basis functions f_n,

N	$P = 10^{-4}$, $\tau = 10^6$, $\eta = 0.1$, $m = 4$		$P = 0.1$, $\tau = 10^3$, $\eta = 0.1$, $m = 4$		$P = 0.1$, $\tau = 10^5$, $\eta = 0.4$, $m = 8$	
	R_c	ω	R_c	ω	R_c	ω
3	18016.3	127520.6	18016.3	108.2	134883.58	865.17
10	18851.7	130446.6	18851.7	106.1	910277.11	1767.1
20	18853.3	130588.1	18853.3	106.0	1297336.2	1813.5
26	18857.6	130601.1	18857.6	104.9	1266116.9	1831.8

Table 5.1. *Dependence of the critical Rayleigh number R_c and frequency ω on the truncation parameter N in the case A of fixed-temperature boundary conditions.*

$$\hat{y}(x,t) = \sum_{n=1}^{N} a_n(t) f_n(x) \tag{5.6}$$

and by requiring that the residual $\mathcal{M}\hat{y}$ is orthogonal to this set of basis functions,

$$\int \mathrm{d}x \ g_n(x) \ \mathcal{M}\hat{y} = 0, \qquad n = 1..N \tag{5.7}$$

where g_n satisfies $\int \mathrm{d}x \ g_n(x) f_{n'}(x) = \delta_{n,n'}$. The Galerkin projection, as the integral in (5.7) is called, yields N equations for the N unknown expansion coefficients a_n.

Particular realization. In the particular case the dependent variables of equations (5.4) and (5.3c) are expanded in a basis of functions satisfying the boundary conditions (5.5),

$$v = \sum_{l,n} a_{nl} \exp\{i(m\varphi + \omega\tau t)\} P_l^m(\cos\theta) \sin n\pi(r - r_i) \tag{5.8a}$$

$$w = \sum_{\hat{l},n} c_{n\hat{l}} \exp\{i(m\varphi + \omega\tau t)\} P_{\hat{l}}^m(\cos\theta) \cos(n-1)\pi(r - r_i) \tag{5.8b}$$

$$\Theta = \begin{cases} \sum_{l,n} b_{nl} \exp\{i(m\varphi + \omega\tau t)\} P_l^m(\cos\theta) \sin n\pi(r - r_i), & \text{case A} \\ \sum_{\hat{l},n} b_{n\hat{l}} \exp\{i(m\varphi - \omega\tau t)\} P_{\hat{l}}^m(\cos\theta) \cos(n-1)\pi(r - r_i), & \text{case B} \end{cases} \tag{5.8c}$$
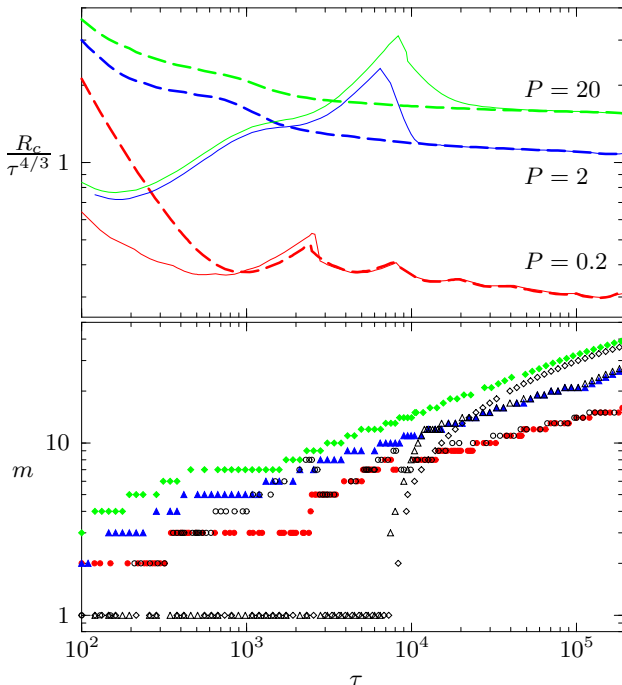
This representation has been chosen in such a way that solutions in the form of drifting waves which are m-periodic in the azimuthal direction are described by constant coefficients a_{ln}, etc. The method is not restricted to linear problems and more complex nonlinear solutions can be described by time-dependent coefficients $a_{ln}(t)$, etc. In both cases the conditions

$$a_{ln} = a_{-ln}^+ \ , \ b_{ln} = b_{-ln}^+ \ , \ c_{\hat{l}n} = c_{-\hat{l}n}^+, \tag{5.9}$$

must be satisfied for the expressions (5.8) to be real, where the superscript "+" indicates the complex conjugate. Of particular interest are solutions that are symmetric with respect to the equatorial plane in which case the subscript l runs through $m + 2j$ for $j = 0, 1, 2 \dots$ while the subscript $\hat{l}$ runs through $m + 2j + 1$ for the same j. The associated Legendre polynomials will be assumed in such a form that the average of $[P_l^m]^2$ over the unit sphere is unity, i.e.

$$P_l^m(x) = \left[\frac{(l-m)!(2l+1)}{(l+m)!} \right] 2^{-l}(l!)^{-1}(-1)^m(1-x^2)^{m/2} \frac{\mathrm{d}^{l+m}}{\mathrm{d}x^{l+m}}(x^2-1)^l. \tag{5.10}$$

In the case of the linear problem the projection (5.7) of the basic equations (5.4) and (5.3c) onto the space of the expansion functions used in (5.8) gives rise to a linear system of algebraic equations for the coefficients a_{ln} etc. This system contains the frequency ω as an eigenvalue. For given values of m, τ and P the Rayleigh number R is increased until the lowest imaginary part of the eigenvalue ω becomes negative indicating the onset of convection. The corresponding R_c, ω, and set of coefficients a_{ln}, b_{ln}, c_{ln} constitute the linear solution sought.

Fig. 5.2. *The critical Rayleigh number R_c (upper plot) and wavenumber m (lower plot) as functions of τ in the case $\eta = 0.4$ for values of the Prandtl number $P = 0.2$ (red, circles), $P = 2$ (blue, triangles), $P = 20$ (green, diamonds) and thermal boundary conditions of case A (thick broken lines, filled symbols) and case B (thin lines, empty black symbols).*

Truncation scheme and accuracy of results. The numerical accuracy and convergence of the solution depends mainly on the truncation parameter N to which the series (5.8) must be truncated in a numerical implementation. We assume a triangular truncation condition that all coefficients and corresponding equations are neglected whose subscripts satisfy

$$2n + l - \mid \nu \mid m + 2 \mid \nu \mid > 3 + 2N. \tag{5.11}$$
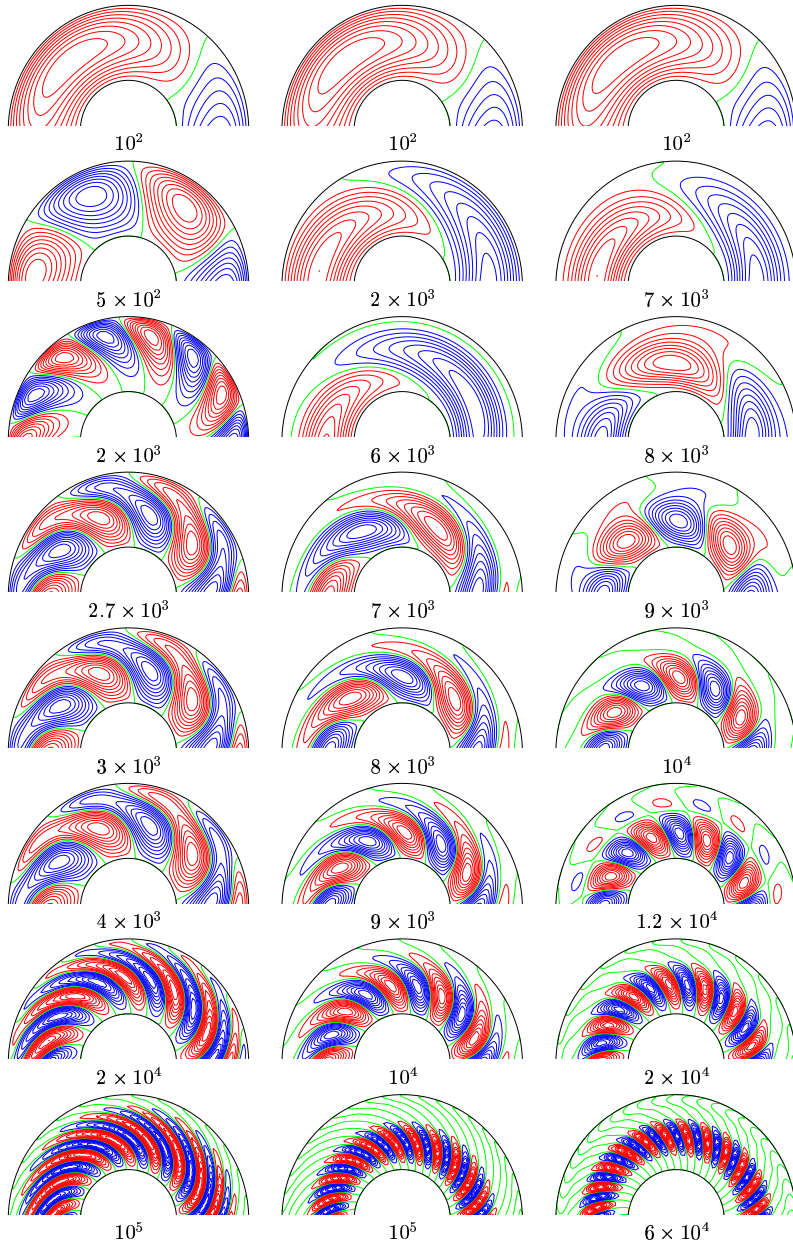
The same condition applies for $\hat{l}$. In order to obtain an idea about the rate of convergence and the reliability of the results we present table 5.1 which shows values of R_c and ω as functions of N for several sets of typical parameter values. The value of $N = 16$ with a total of 816 coefficients has most often been used in the computations since it provides a reasonable compromise between accuracy and computational time.

The numerical methods of linear analysis have been adopted from [3] with modifications concerning the introduction of the fixed-flux thermal boundary conditions of Case B.

5.4 Onset of convection at moderate and high values of the Prandtl number

In this section we focus the attention on the onset of convection in rotating spherical fluid shells at moderate ($0.1 \leq P \leq 1$) and high values ($P \geq 1$) of the Prandtl number P. The regions of "moderate" and "high" values of P are, of course, only roughly determined according to the criterion that predominantly columnar convection should be observed there. The values of the Coriolis number τ are restricted only by computational constraints.

Basic physical mechanisms. Before discussion of numerical results, it is useful to recall qualitatively the basic physical mechanisms which drive convective motions at those values of the parameters. Because analytical solutions of the governing equations (5.3) do not exist in spherical geometry an useful approach has been to investigate simpler systems approximating various aspects of convection in rotating spherical fluid shells. For example, the polar regions
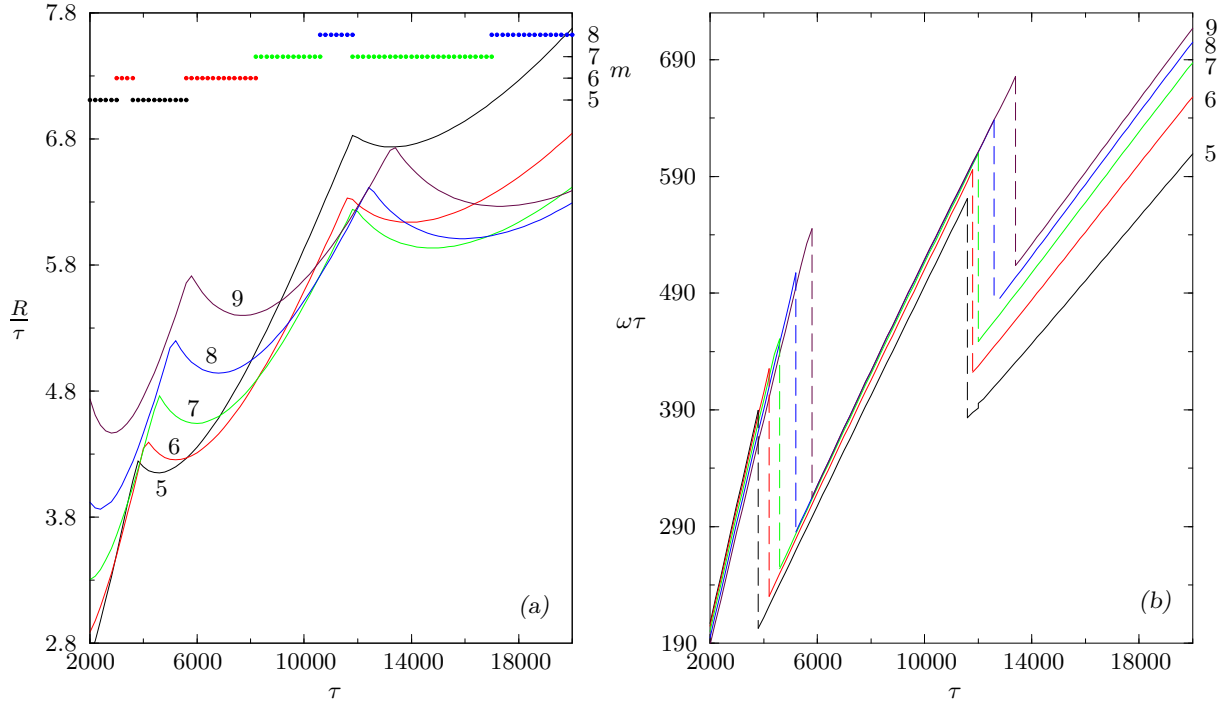
Fig. 5.3. *Sequence of plots of the equatorial streamlines $r\partial_\varphi v = $ const. for increasing values of τ as indicated in the figure and for values of $P = 0.2$ (left column), $P = 2$ (middle column), $P = 20$ (right column), $\eta = 0.4$ and thermal boundary conditions of type B.*

may be considered as plane layers rotating about vertical axes while the equatorial region may be approximated by a rotating cylindrical annulus.

The most essential effect due to rotation with angular velocity $\boldsymbol{\Omega}$ of a fluid system is the preference for two-dimensional motions, resulting from the Taylor-Proudman theorem

$$\boldsymbol{\Omega} \cdot \nabla \boldsymbol{u} = 0. \tag{5.12}$$
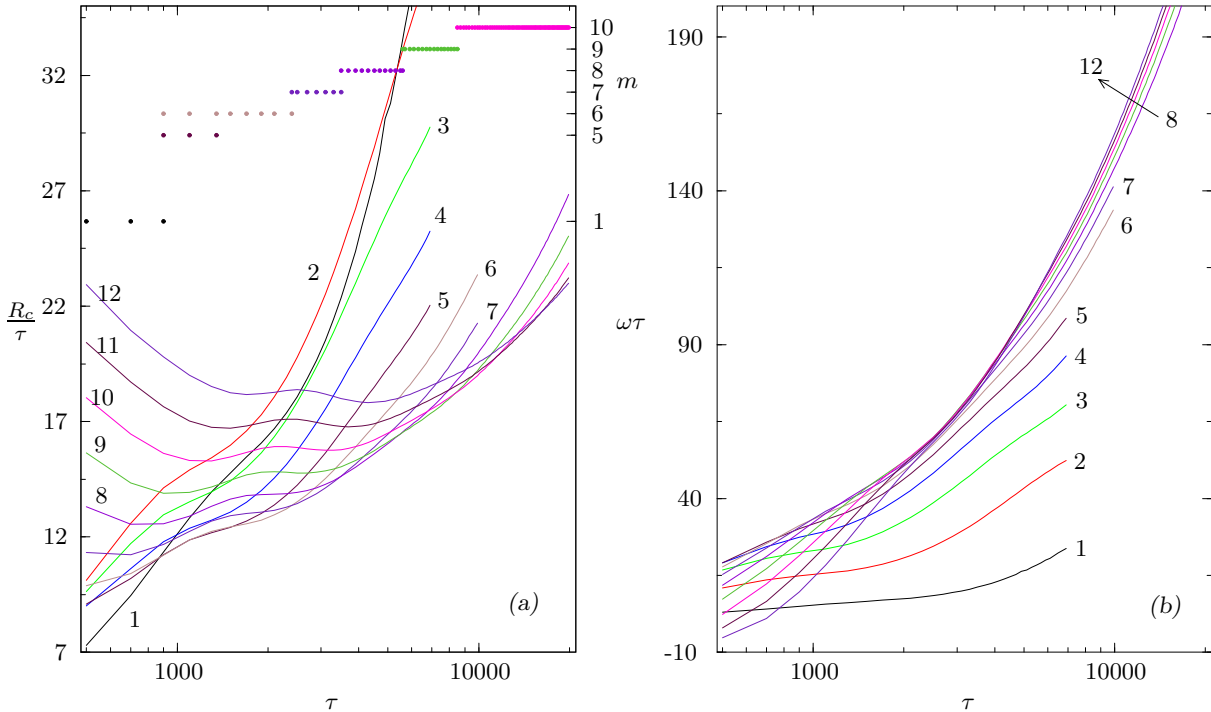
This result is obtained when all terms in the momentum equation except the Coriolis force and the pressure gradient are neglected in order to isolate the effect of rotation in its simplest form. Because of the constraint (5.12), the velocity of rotating fluids is preferably oriented in a direction perpendicular to the axis of rotation. Therefore, convective motions in a plane layer rotating about a vertical axis are suppressed because the fluid needs to carry heat vertically against the constraint (5.12). For this reason, convection in a rotating layer occurs at higher values of R_c than in a non-rotating one. Similar arguments hold for the polar region of the

Fig. 5.4. *The critical Rayleigh numbers R_c (in (a)) and frequencies ω (in (b)) corresponding to various values of the wavenumber m (indicated in the plots) as well as the preferred value of m (circles, plot (a), right ordinate) as functions of τ. The Prandtl number is $P = 0.1$, the radius ratio is $\eta = 0.4$ and fixed-flux thermal boundary conditions of case B are used.*

rotating spherical shell where convection sets in long after the other parts of the shell have started to convect. Another simpler model which has been very successful in describing the properties of convection in the equatorial region is the rotating cylindrical annulus shown in figure 1 of reference [24]. An important ingredient of this geometrical configuration are the conical boundaries at top and bottom which cause a variation in height with distance from the axis of rotation. Without this variation in height, steady two-dimensional convection rolls aligned with the axis of rotation will be realized since they obey the Proudman-Taylor condition. The Coriolis force is entirely balanced by the pressure gradient in this case and the value of R_c in the small gap limit is given by the Rayleigh-Bénard value for a non-rotating layer. As soon as the height changes in the radial direction any flow involving a radial velocity component can no longer satisfy the geostrophic balance (5.12). Instead, a weak time dependence is required and the flow assumes the character of Rossby waves. The dynamics of Rossby waves can be visualized if the action of the vorticity acquired by the fluid columns displaced radially from the middle of the gap is considered. As indicated in figure 2 of [24] columns shifted inward acquire cyclonic vorticity because they are stretched owing to the increasing height. The opposite sign of vorticity is exhibited by columns moving outward. Since their moments of inertia are increased they must rotate anti-cyclonically relative to the rotating system in order to conserve angular momentum. The action of the acquired motion of sinusoidally displaced columns on their neighbors results in the propagation of a wave as shown in figure 2 of [24]. The phase velocity is in the prograde (retrograde) direction when the height decreases (increases) with distance from the axis.

The annulus model provides insight to another important aspect of rotating convection, namely the generation of differential rotation in which the outer fluid rotates faster/slower than the inner one. When curved cones instead of straight cones are used as upper and lower
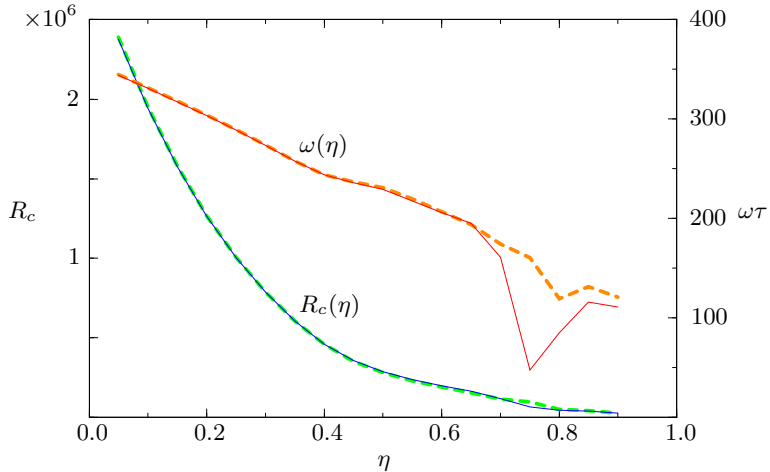
Fig. 5.5. *The critical Rayleigh numbers R_c (in (a)) and frequencies ω (in (b)) corresponding to various values of the wavenumber m (indicated in the plots) as well as the preferred value of m (circles, plot (a), right ordinate) as functions of τ. The Prandtl number is $P = 1$, the radius ratio is $\eta = 0.4$ and fixed-flux thermal boundary conditions of case B are used.*

boundaries the slope near the outer cylinder is larger/smaller than the slope near the inner cylinder (*convex/concave case*). In the convex case, for instance, as a result of the variable slope the thermal Rossby wave will propagate faster on the outside than on the inside. This leads to a tilt in the convection columns. When the columns are tilted in the prograde sense towards the outside, prograde momentum is carried outwards and retrograde momentum is transported inwards leading to differential rotation. The differential rotation could not be a very strong effect if a feedback process did not come in as well. Indeed, the steady differential rotation created by the balance of Reynolds and viscous stresses tends to increase the tilt of the convection cells and thus enhances its own source.

The analytical theory of the cylindrical annulus is favored by the fact that the problem may be reduced from three to two spatial dimensions [13, 21]. Further features and references for convection in the cylindrical case are given in [24] and [32].

Onset of convection in the case of fixed-flux thermal boundary conditions and comparison with the case of fixed-temperature boundary conditions. Detailed computations addressing the onset of convection with fixed-temperature boundary conditions at moderate and high Prandtl numbers have been performed in the past by Zhang & Busse [124] and Ardes *et al.* [3]. Their studies provide a comprehensive picture of the flow regimes and the various types of mode competition. Here we extend their analysis to higher values of the Coriolis parameter τ and to the case of fixed-flux thermal boundary conditions.
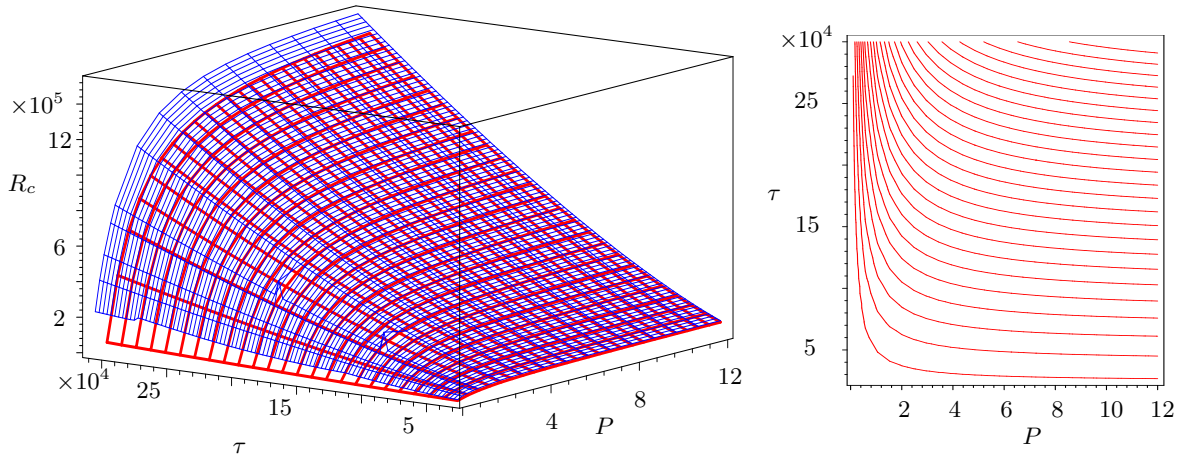
In figure 5.2 an overview of the numerical results is given for $\eta = 0.4$. The critical R_c and m are plotted for three different values of P as functions of τ. The case with the lowest value of the Prandtl number $P = 0.2$ is, in fact, a marginal one since inertial convection is already observed for the smaller values of τ as will be discussed in connection with figure 5.3. The

Fig. 5.6. *The critical Rayleigh number R_c (blue & green, left ordinate) and frequency ω (orange & red, right ordinate) as functions of the radius ratio of the shell η for cases A (thick broken lines) and B (thin solid lines) for $P = 1$, $\tau = 2 \times 10^4$ and $m = 12$.*

cases $P = 2$ and $P = 20$ are not very different, suggesting that those values of P are sufficient for observing the typical phenomena of columnar convection. Asymptotic scaling is used to plot R_c in figure 5.2 in order to test the validity of the asymptotic relations (5.13). Indeed, for high values of τ the scaled Rayleigh number $R_c \tau^{-4/3}$ tends to approach a constant value in the average. As discovered in the work of Ardes *et al.* [3], the preferred wavenumber m does not always increase monotonically. Non-monotonic behavior of m is observed in the case $P = 0.2$ and is more pronounced in the case of fixed-flux conditions. As can be seen in figure 5.3 this is due to a change in the style of convection. The most significant difference between the cases of fixed-flux and fixed-temperature thermal boundary conditions appears in the value of the preferred wavenumber and is especially strong for $P = 2$ and $P = 20$. For these values of P, $m = 1$ is the preferred wavenumber of convection with fixed-flux conditions as τ is increased from values of the order unity up to 8×10^3 while $m = 1$ is never exhibited except for very low values of τ and η in the fixed-temperature case. The transition of m from unity to higher values in case B may be observed in the lower panel of figure 5.2. It occurs abruptly and is followed by a fast monotonic increase of m. This transition results in a well-defined sharp peak in the critical Rayleigh number as seen in the upper panel of figure 5.2 near $\tau = 7 \times 10^3$ as well as in significantly lower values of R_c in the case of fixed-flux conditions compared to the case of fixed-temperature ones at lower values of τ. This result is important because those are exactly the values of P and τ genuinely accessible for nonlinear finite-amplitude convection and dynamo simulations. It indicates that a simple variation in the thermal boundary conditions may result in a totally different scale of convection and magnetic fields of drastically different dynamical behavior. Similar effect has been suggested in [25] due to a second source of buoyancy with sufficiently different diffusivity. For values of τ larger than 2×10^4 the two cases show little difference.
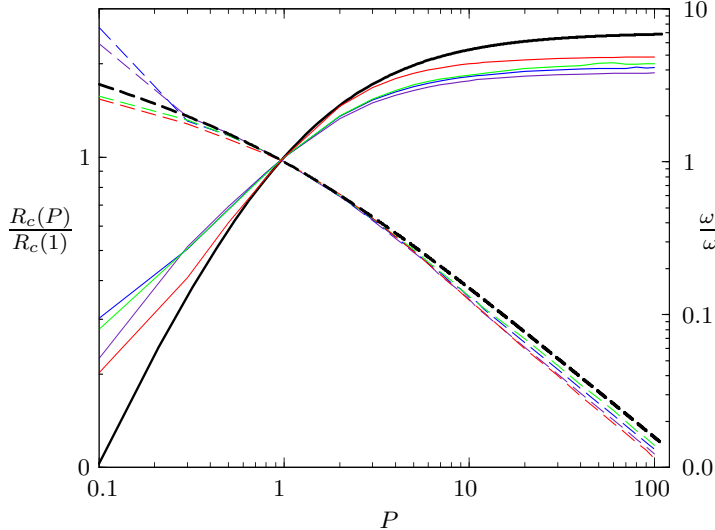
Additional insight into those features may be gained from figures 5.3, 5.4 and 5.5. Figure 5.3 exhibits a collection of flow patterns of convection with fixed-flux thermal boundary conditions. The three columns in the figure correspond to the three values of the Prandtl number used in figure 5.2. Two main tendencies may be observed, namely that the number of convection columns increases with increasing τ while their spiralling decreases with increasing P so that the columns are much more radially oriented at $P = 20$ than at $P = 0.2$. The flow patterns, however, exhibit a number of finer details. The $P = 0.2$ case is the richest in structure. In particular the transition from equatorially-attached inertial convection to columnar convection may be observed here. At sufficiently low values of τ a large-scale $m = 1$ pattern is preferred. As τ is increased above few hundreds, higher wavenumbers enter and the flow assumes the form of cells attached to the outer surface of the shell near its

Fig. 5.7. *The critical Rayleigh number R_c as a function of the Prandtl number P and the Coriolis number τ in the case of fixed-temperature boundary conditions (case A) and $\eta = 0.4$. The upper surface shown with a thin blue wireframe is a result of numerical solution of equations (5.4) and (5.3c), while the lower surface shown with thick red wireframe corresponds to expression (5.13). Also shown are isolines $R_c = const.$ in the $P - \tau$ – plane (right plot).*

equator as is typical for inertial convection. Examples of this type of flow are provided by the second ($\tau = 5 \times 10^2$) and third ($\tau = 2 \times 10^3$) plots of the first column in figure 5.3. Beyond these values of τ the transition to columnar convection occurs in a manner very similar to the one reported by Ardes *et al.* [3] in the case of fixed-temperature boundary conditions. The equatorially attached cells are replaced by double-humped cells the centers of which gradually displace from the outer towards the inner spherical surface. Simultaneously the cells extend in vertical direction. The forth ($\tau = 2.7 \times 10^3$), fifth ($\tau = 3 \times 10^3$) and sixth ($\tau = 4 \times 10^3$) plots corresponding to $P = 0.2$, provide examples of double-humped rolls. The humped pattern gradually transforms to typical columnar rolls as τ is increased further.

It is of particular interest to investigate the mode competition mechanism behind the transition from inertial to columnar convection. In figure 5.4 the neighborhood of the region of non-monotonic dependence of m where this transition occurs is shown in detail. Fixed-flux conditions and a slightly lower value of $P = 0.1$ than those of the previous figures are used. The figure may be readily compared with the similar figure 4 of Ardes *et al.* [3] for case A thermal boundary conditions. The most notable features of the plot are the many kinks in the R_c–curves for the various wavenumbers m. Those kinks represent transitions between different eigenvectors of the solution for a fixed value of m. In other words, for a fixed number of rolls at given set of parameter values, P, τ, η, etc. the governing equations (5.3) allow various types of convection modes, e.g. inertial, columnar, etc. Of all these eigenvectors, one has the lowest value of R_c and is the actually realized solution. However, with changes in the values of the parameters a different mode for the same number of rolls may have a lower R_c and at the point in the parameter space where this happens a kink in the critical Rayleigh number curve for the given m is observed. The transition between competing mode is especially evident in the discontinuity of the corresponding frequencies as shown in figure 5.4*b*. Examples of the flow patterns corresponding to such a transition appear as already discussed in the first column of figure 5.3 for $\tau = 2 \times 10^3$ and $\tau = 2.7 \times 10^3$. These two plots exhibit the same number of rolls $m = 7$ but the first of them shows equatorially attached convection while the second one shows a double-humped mode which occurs after a kink in R_c. In the process of mode competition R_c exhibits a complicated dependence on τ. As a consequence not only the various modes belonging to some fixed m compete but the various wavenumbers m also

PSfrag replacements
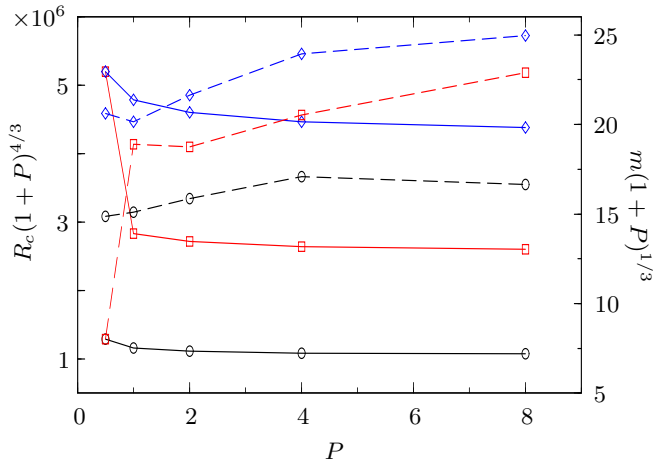
Fig. 5.8. *The critical Rayleigh number R_c and frequency ω (broken lines, right ordinate) as functions of P in the case $\eta = 0.4$ for $\tau = 5 \cdot 10^3$ (violet), 10^4 (blue), $1.5 \cdot 10^4$ (green) and 10^5 (red). The thick black lines correspond to expressions* (5.13a) *and* (5.13c). *The reference value $R_c(1)$ equals 80296, 190140, 318395, 3665919 for $\tau = 5 \cdot 10^3, 10^4, 1.5 \cdot 10^4, 10^5$, respectively. For expression* (5.13a) *$R_c(1)$ is given by $0.67543 \cdot \tau^{4/3}$.*

compete with each other as is evident from the numerous intersections of the R_c-curves in figure 5.4a. This leads to a change in the preferred wavenumber and eventually to recurrence of the same or even lower values of m and thus to its non-monotonic behavior.

A different scenario of mode competition occurs at higher values of P and is illustrated in figure 5.5 for fixed-flux thermal boundary conditions. The figure also helps to clarify the preference for the $m = 1$ mode of convection at low values of τ for this type of boundary conditions. In contrast to convection at lower values of P no kinks in the R_c-curves and no discontinuities in the corresponding frequencies ω are observed. The R_c depends smoothly on τ. This is an indication that modes competing with the critical one always have higher values of R_c. Thus the τ-dependence of R_c is determined only by the competition of various wavenumbers. For a large range of values of τ between 10 and 900 for the set of parameter values used in figure 5.5, $m = 1$ remains the preferred wavenumber. At $\tau = 900$ a jump to $m = 5$ occurs which results in a sharp peak in the critical Rayleigh number. For a short range of values of τ, immediately following the jump a coexistence of $m = 5$ and $m = 6$ patterns is possible after which m rapidly assumes increasing values. The R_c- and ω-curves corresponding to the various values of $m > 5$ are rather similar and their envelopes determine the actual critical Rayleigh number and frequency. Examples of flow patterns corresponding to this situation are shown in the second and third columns of figure 5.3. The large $m = 1$ patterns are abruptly replaced by patterns having higher wavenumbers. However, the rolls remain always attached to the inner spherical boundary of the shell as is typical for columnar convection. The columns become less spiralling and more radially oriented as P is increased.

Dependence on the radius ratio η of the spherical shell. The parameter dependence of the onset of convection becomes more complex as spherical shells of finite radius ratio η are considered. Fortunately, the influence of η is relatively weak if the Coriolis parameter is sufficiently high and η does not approach unity too closely. Moreover, the definition of R is based on the gap width d of the shell rather than the radius ratio η. A radius ratio $\eta = 0.4$ has been traditionally used in linear studies [124, 3] as well as in finite amplitude convection and dynamo simulations [114, 30, 62]. A ratio $\eta = 0.4$ will also be preferred in the major part of this report. However, dependence of the linear as well as the finite-amplitude properties of convection on η certainly exists. For example, a very thin spherical shell may be approximated by locally by plane layers rotating about inclined axes while $\eta = 0$ corresponds to a full sphere. This two cases are fundamentally different and exhibit fundamentally different types of flow. Since the complete investigation of the η-dependence constitutes an enormous task,

Fig. 5.9. *The critical Rayleigh number R_c multiplied by $(1+P)^{4/3}$ (left ordinate, solid lines) and the wavenumber (right ordinate, broken lines) multiplied by $(1+P)^{1/3}$ as functions of P in the case of fixed-temperature boundary conditions (Case A). For the points connected by black, red and blue lines, $\tau P = 20000$, $\tau P = 40000$ and $\tau P = 60000$, respectively.*

here we only present figure 5.6. It shows decrease in the values of R_c and ω as the spherical shell becomes thinner. The two different types of thermal boundary conditions (A and B) do no cause much difference. The values of all other parameters have been kept fixed to typical values in order to diminish the amount of computation. Additional results on the dependence of the onset of convection on the radius ratio appear in section 5.5.

R_c-surface in $P - \tau$ space in the case of fixed-temperature boundary conditions and comparison with analytical expressions. Finally, we present some results which may serve as a summary of the properties of the onset of convection at moderate and high Prandtl numbers reported above. Extensive numerical computations have been performed in order to obtain the critical Rayleigh number R_c and frequency ω for the onset of convection as functions of the Prandtl and Coriolis numbers and an entire surface in $P - \tau$ space have been constructed. A strong motivation is the need of a reference point for finite-amplitude convection and dynamo simulations. Having reliable values of the R_c helps to prevent computer runs which could have decaying solutions because of insufficient energy input and facilitates the comparisons between various runs. Fixed-temperature boundary conditions have been assumed and the radius ratio of the shell has been set to $\eta = 0.4$ since these assumptions have most often been employed in our finite-amplitude convection and dynamo calculations.
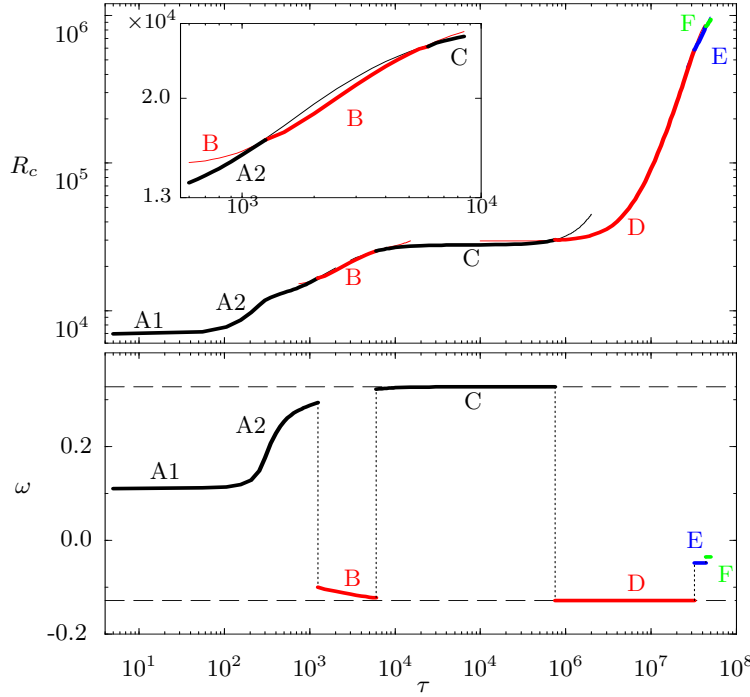
A further motivation has been to test the approximate analytical expressions

$$R_c = 3 \left(\frac{P\tau}{1+P} \right)^{\frac{4}{3}} (\tan \theta_m)^{\frac{8}{3}} r_m^{-\frac{1}{3}} 2^{-\frac{2}{3}}, \tag{5.13a}$$

$$m = \left(\frac{P\tau}{1+P} \right)^{\frac{1}{3}} (r_m \tan \theta_m)^{\frac{2}{3}} 2^{-\frac{1}{6}}, \tag{5.13b}$$

$$\omega = \left(\frac{1}{(1+P)^2 \tau P} \right)^{\frac{1}{3}} 2^{-\frac{5}{6}} (\tan^2 \theta_m / r_m)^{\frac{2}{3}}, \tag{5.13c}$$

derived on the basis the annulus model by Busse [13, 21]. Here r_m refers to the mean radius of the fluid shell $r_m = (r_i + r_o)/2$, and θ_m to the corresponding colatitude $\theta_m = \arcsin(r_m(1-\eta))$. Those expressions do not take into account the radial dependence of the convection columns at onset. In fact, it is the property that the onset of convection in the rotating cylindrical annulus becomes independent of the gap width in the asymptotic limit of high τ which make relationships of this kind applicable to spherical shells and other axisymmetric containers. For a rigorous asymptotic analysis including the radial dependence we refer to [74]. In figure 5.7 the expression (5.13a) is compared with accurate numerical values of R_c in the P-τ-plane which indicates that the general trend is well represented by the analytical expressions. The
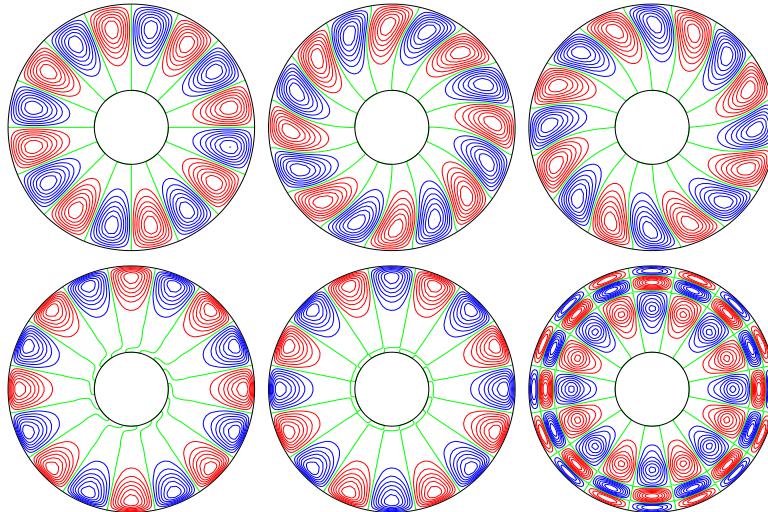
Fig. 5.10. *The critical Rayleigh number R_c (upper plot) and frequency ω (lower plot) as functions of τ for $P = 10^{-4}$, $m = 8$, $\eta = 0.3$ and fixed-temperature (Case A) thermal boundary conditions. The analytical expressions (5.14) for ω are shown with dashed lines.*

analytical expressions give values of R_c and ω lower than the numerical. Although the three-dimensional plot demonstrates well the global form of the dependence of R_c on P and τ, it is not well-suited for a precise comparison with expressions (5.13). Thus, we present figure 5.8 which provides a closer look to several cuts through the surface. Both the critical Rayleigh number R_c– and frequency ω-curves in figure 5.8 change their slope and noticeably start to deviate rather rapidly from the analytical expressions below Prandtl numbers of about 0.2. This is not surprising since in this region convection changes its type from columnar to inertial type and the analytical expressions are no longer valid. We address this question and develop an analytical theory of the low Prandtl number convection in section 5.6

A rule of thumb stating that when the Prandtl number P is increased, one should decrease the Coriolis number τ by some amount in order to observe similar effects is often used in simulations of finite-amplitude convection and dynamo action. In fact it may be rigorously shown that only the single parameter τP is significant in inertial convection (see section 5.6). Similar facts are suggested by expressions (5.13) where, for instance, R_c does not change when $P = 0.5$ instead of $P = 1$ is used while τ is increased by 50%. More generally (5.13a) and (5.13b) state that $R_c(1 + P)^{4/3}$ and $m(1 + P)^{1/3}$, respectively should depend only on τP. Figure 5.9 tests the numerical results against this prediction and shows that they deviate especially for small values of P. This is not very surprising since at small P the inertial effects become increasingly important. A more precise guideline of how P and τ should be varied in order to keep the Rayleigh number fixed may, of course, be obtained by the plot of the isolines of R_c in the $P - \tau$ plane shown in the right part of figure 5.7.

5.5 Onset of convection at low values of the Prandtl number

Results of the numerical investigation of the onset of convection at low values of the Prandtl number P are reported in this section. A slightly different approach than the one used in the preceding section is adopted here. Instead of determining the preferred wavenumber m as a part of the solution, its value is prescribed. The reason is that the competition of various wavenumbers is expected to be very similar to the one already reported for high
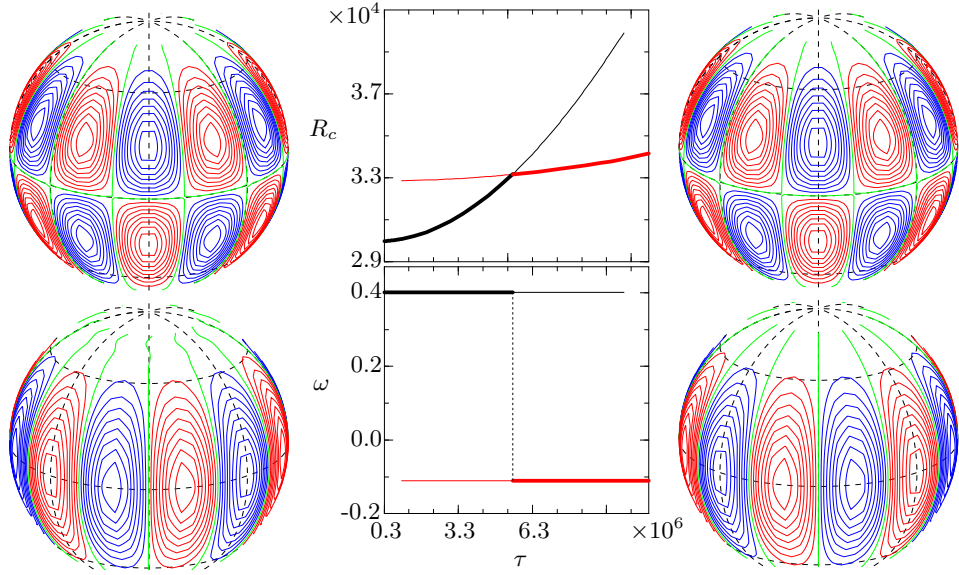
Fig. 5.11. *Isolines of the streamfunction* $r\partial_\varphi v$=const. *in the equatorial plane illustrating the sequence of transitions for the same parameters as in figure* 5.10 *and values of* $\tau = 5$, 950, 1500, 6×10^5, 8×10^5, 3.5×10^7.

and moderate Prandtl numbers in the previous section. Thus the attention is focused on the mechanisms of mode competition for a single fixed wavenumber. The parameter exploration includes a large number of points in the ranges of $10^{-7} \leq P \leq 1$, $0 < \tau$ and $0.1 \leq \eta \leq 0.8$. This region is roughly determined by the expectation that inertial convection should be predominant here. Of course, the scenario of the evolution of the onset of convection with increasing rotation parameter τ as will be described below is valid for a smaller region of approximately $10^{-7} \leq P \leq 10^{-2}$. Fixed-temperature (Case A) thermal boundary conditions are used throughout this section, except in figure 5.17 where comparison with the fixed-flux (Case B) conditions is presented.

Modes of inertial convection with increasing rotation rate. Ideally, the way to investigate a given parameter region is to keep the values of all parameters of the problem fixed and vary in a continuous way only one of them. When the dependence on this parameter is well understood the process is repeated for all remaining parameters. Practically, this is rarely possible. In an experimental situation, for example, the variation of the Prandtl number is limited to the set of available working fluids. In a numerical study one has much weaker restrictions and we have found the rotation rate to be relatively easy to vary in a wide range. Furthermore, any non-monotonic behavior is an indication of a well-defined transition between different states.

Following this approach, numerous cases in the low Prandtl number region have been investigated. Figures 5.10 and 5.11 represent typical examples of the results obtained in this region and provide an overview of most of the various regimes of convection which occur here. Figure 5.10 shows the Rayleigh number R_c and the corresponding frequency ω as functions of τ. The $\omega-$ curve is particularly instructive and several different states of the preferred mode can be immediately identified from its discontinuities. Figure 5.11 provides view of the flow patterns corresponding to these different states. The values of the parameters $P = 10^{-4}$, $m = 8$, $\eta = 0.3$ are kept fixed. However, their variation within the region of interest leads only to qualitative changes in the figures but preserves their general features.

Submode A1. At very low rotation rates τ of order unity the convection cells form near the outer surface in the equatorial region of the spherical shell as can be seen in the first plot of figure 5.11. At this values of the rotation parameter τ the values of the Rayleigh number are still rather small. The preferred mode indicated by A1 in figure 5.10 has a positive frequency which indicates a retrograde drift with time. The solution has a relatively small toroidal component which vanishes in the limit $\tau \longrightarrow 0$, indicating that this state is marginal to the states of non-rotating convection.
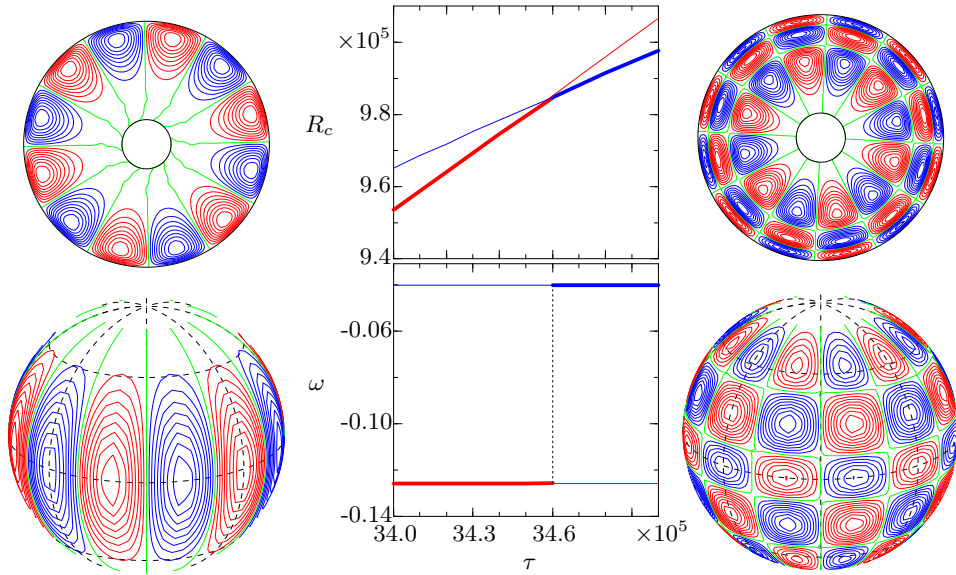
Fig. 5.12. *Graphs in the center show the critical Rayleigh numbers R_c of the competing prograde (red line) and retrograde (black line) modes as well as the actual critical value (thick lines) and the corresponding frequencies ω as functions of τ for $P = 0.00001$, $m = 6$, $\eta = 0.2$. Contours of $u_r = $ const. (lower plots) and $w = $ const. (upper plots) on the spherical surface $r = r_i + 0.9$ for $\tau = 10^6$ and 10^7 are shown on the left- and right-hand sides, respectively.*

Submode A2. A new mode which does not exist at $\tau = 0$ enters and a switch-over phenomenon similar to the one first described by Zhang & Busse [124] and illustrated in figure 6 of their paper is observed. The two competing modes approach each other but do not cross. As a result the R_c- and $\omega-$curves of the two modes exhibit smooth bends but for some time the initial mode is still preferred. The modified initial mode is denoted by A2 in figure 5.10 in order to be distinguished from the same state A1 when it is in its pure form. During the gradual transition the pattern of convection also changes gradually. The rolls are no longer straight and strictly radially oriented as they are near $\tau = 0$ but change their shape and become inclined as illustrated in the second plot of figure 5.11. The frequency still keeps its positive sign and the pattern exhibits a retrograde drift.

Mode B. Past a particular value of the Coriolis number τ the value of the critical Rayleigh number R_c of the competing mode becomes lower than that of the initially preferred mode A such that an abrupt jump occurs. This is especially obvious from the discontinuity of the $\omega-$curve in figure 5.10. During this transition the frequency changes sign. The change of sign indicates a change in the direction of the drift of the pattern which now drifts in the prograde direction. Because the new state denoted by B in figure 5.10 is still affected by the switch-over competition the corresponding R_c- and $\omega-$curves continue to bend and the flow pattern exhibits spiraling rolls as can be noticed in the third plot of figure 5.11.

Modes C and D. In a completely analogous way a second transition occurs and the preferred mode changes back to a retrograde drift. This next transition occurs at about $\tau = 8000$ for the values of the parameters used in figure 5.10 and takes the flow in the region where inertial (equatorially-attached) convection in its pure form is observed. The equatorially attached mode was first found by Zhang & Busse [124] and is quite distinct from the columnar modes discussed in the preceding section 5.4. A detailed numerical study together with some analytical approximations can be found in the paper of Ardes *et al.* [3]. The results of their efforts have turned out to be rather complex since the preferred inertial modes travel in the
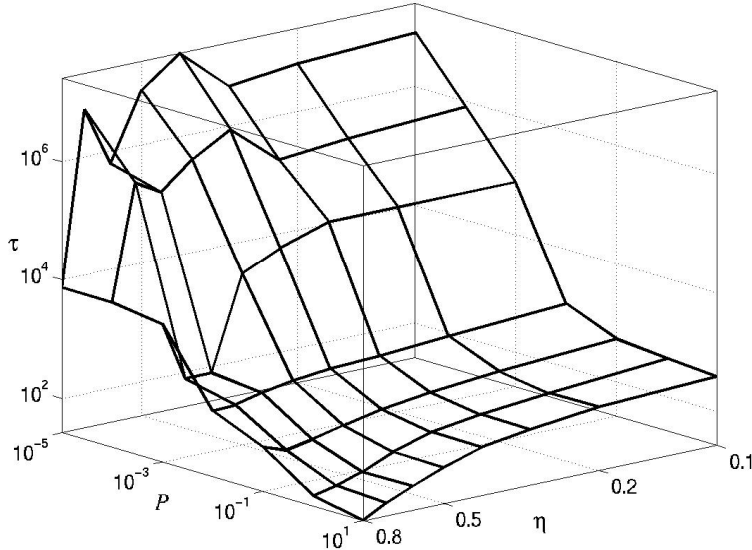
Fig. 5.13. *Graphs in the center show the critical Rayleigh numbers R_c of the competing prograde single-cellular (red lines) and multi-cellular (blue lines) drifting modes as well as the actual critical value (thick lines) and the corresponding frequencies ω as functions of τ for $P = 0.001$, $m = 6$, $\eta = 0.2$. Isolines of the equatorial streamfunction $r\partial_\varphi v = const.$ (upper plots) as well as contours of $u_r = const.$ (lower plots) on the spherical surface $r = r_i + 0.9$ for $\tau = 3.4 \times 10^6$ and $\tau = 3.5 \times 10^6$ are shown on the left- and right-hand sides, respectively.*

prograde as well in the retrograde directions depending on the parameters of the problem. Moreover, the azimuthal wavenumber m of convection does not increase monotonically with the Coriolis parameter τ as is usually found for the columnar mode at higher values of P. Whenever τ is sufficiently large the frequency ω is closely approximated by the frequency of the corresponding inertial modes which is given by the analytical expression [121, 3],

$$\omega = \frac{1}{m + 2}(1 \pm [(1 + m(m + 2)(2m + 3)^{-1}]^{\frac{1}{2}}). \tag{5.14}$$
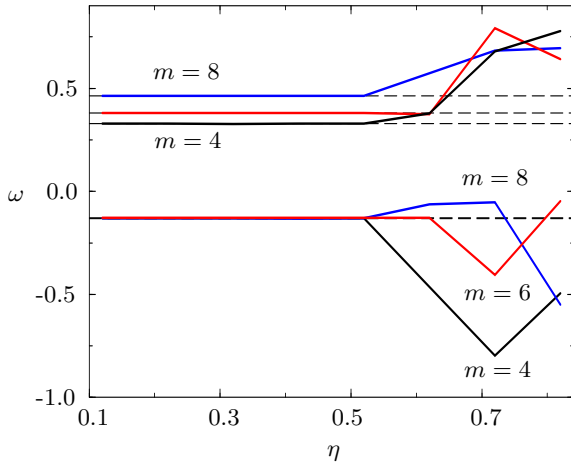
The positive (negative) sign applies for modes drifting in the retrograde (prograde) direction. Explicit values of expression (5.14) are given in figure 5.10 for comparisons with the numerically determined values. The close agreement between them exhibited for the modes denoted by C and D is a strong indication that these are indeed examples of the retrograde and the prograde drifting modes of inertial convection. The two modes differ little in their form. The most characteristic difference is the opposite phase between the toroidal and poloidal components of motion as indicated in figure 5.12. This figure also provides a closer look to the process of transition from the retrograde to the prograde drifting mode. At lower values of the rotation parameter τ the retrograde mode has a lower value of the critical Rayleigh number and therefore is preferred to the prograde mode. As τ is increased the critical Rayleigh number R_c of the retrograde mode grows faster than that of the competing prograde mode and at some critical value of τ eventually becomes larger. At this point the transition from retrograde to prograde mode occurs. The frequency exhibits a discontinuity, changes sign and the whole pattern starts drifting in the opposite direction. The corresponding flow patterns in the equatorial plane are, in fact, identical except for their drift velocity and direction and are given in the fifth and sixth plot of figure 5.11. The analytical theory developed in section 5.6 applies to these two modes C and D and is capable of predicting all of the properties of the two inertial modes as reported here.
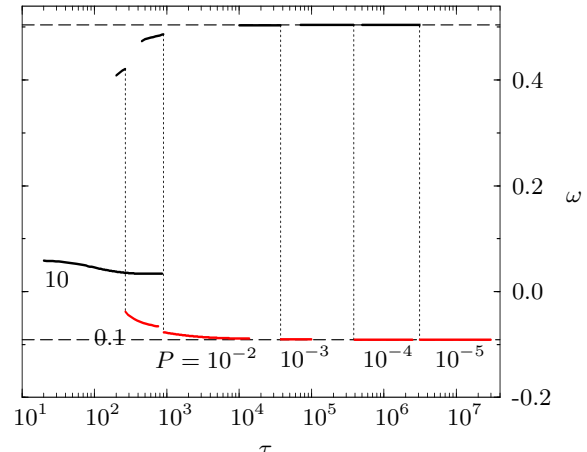
Fig. 5.14. *The boundary separating the retrograde (below the surface) and prograde drifting modes (above the surface) for a fixed value of the wavenumber $m = 6$.*

Modes E and F. In addition to the simple single-cellular inertial modes, multi-cellular modes have been found in the rotating annulus problem both analytically [118] and numerically [98]. Such multi-cellular solutions in the case of a spherical shell are observed here for the first time and are indicated by E and F in figure 5.10. Examining the plots of the Rayleigh numbers R_c and frequencies ω of the competing modes in figure 5.13, the same mechanism of transition as the one just described in connection with the retrograde - prograde transition is identified. But in all other aspects this mode is rather different from the previous ones. Although the frequency again exhibits a finite discontinuity, it does not change sign and the pattern continues to drift in the prograde direction. A major change in the structure of the convection solution can be observed. The wall-attached cells are replaced by several concentric layers of convection cells. The whole pattern resembles a chess play-board in the sense that the streamlines of any given cell are directed in the opposite direction with respect to the streamlines of all neighboring cells. This multi-cellular solution seems to emerge as a result of the extremely high values of the rotation parameter. As might be seen from the plots of ω in figures 5.13 and 5.10, this transition does not occur in a gradual manner but rather sharply at a well-determined value of τ. The multi-cellular modes are found to replace the single-cellular inertial modes at sufficiently high values of τ and low values of P. Although the precise border between the two regimes is not investigated in the present report, the transition to multi-cellular convection has been found in all examined cases regardless of the radius ratio η and for all Prandtl numbers $P \leq 10^{-2}$. In contrast to the multi-hump and spiraling columnar solutions described in the preceding section 5.4 the multi-cellular solution is oriented strictly in the radial direction. The sharp border between the single-cellular and the multi-cellular modes as well as the radial orientation of the multi-cellular structures suggest that this mode is not connected with the transition to columnar convection. It is, in fact, believed that this is a pure inertial mode, corresponding to a different class of solutions of the Poincaré equation (5.1) with a more complicated structure as reported in [126]. This suggestion might be tested by using an approach analogous to the one developed in section 5.6 for the single-cellular solutions. However, this has yet to be done.

Some properties of the inertial modes of convection. Figure 5.14 represents an attempt of an approximate determination of the border between the retrograde and the prograde drifting modes of inertial convection in $P - \tau - \eta$ space. The surface is smoother towards lower values of the radius ratio $\eta \leq 0.5$. This is not surprising since at higher values of η

Fig. 5.15. *The frequency ω of the retrograde ($\omega > 0$) and the prograde ($\omega < 0$) drifting modes as a function of η for $P = 10^{-5}$ and wavenumbers as indicated in the plot.*
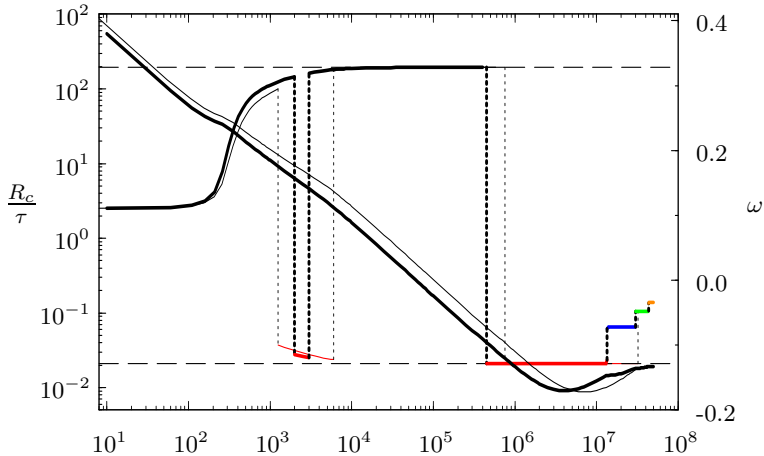
Fig. 5.16. *The frequency ω as a function of τ for $m = 4$, $\eta = 0.2$ and different values of P as indicated in the plot. Values corresponding to expression 5.14 are plotted with dashed lines.*

the inner spherical boundary of the shell has a significant effect on the structures of the flow which start to show similarities to the case of plane layer convection and are much better described by the small-gap limit approximation. The availability of the border between the two modes opens a new possibility for tests of various analytical theories which aspire to predict the preferred mode of inertial convection.

The expression (5.14) for the frequency ω is independent of the radius. It is of interest to test whether this requirement is fulfilled by the numerical results. For this reason in figure 5.15 the numerically determined values of ω are plotted as functions of the radius ratio η and compared with those obtained from expression (5.14). For values of the radius ratio $\eta \leq 0.5$ a perfect agreement can be observed. For values higher than that neither a good agreement nor a well-established dependency on the radius ratio η is obvious. The discrepancy is due to the significant change of the geometry of the system which leads to significant changes in the type of convective flow.

The question of the transition between columnar and inertial convection is of particular interest. Some details of the dependence of this transition on the Coriolis parameter τ have been already discussed in the preceding section 5.4 where the transition from inertial to double-humped and finally to columnar convection was highlighted. Figure 5.16 demonstrates that this transition is gradual rather than abrupt not only for the variation of τ but for the variation of the Prandtl number P as well. The figure shows the ω-curve plotted against τ for fixed values of the wavenumber $m = 4$ and the radius ratio $\eta = 0.2$ and for several different values of the Prandtl number P. The theoretical prediction (5.14) for ω is also plotted with dashed lines. At $10^{-5} \leq P \leq 10^{-2}$ the theoretical and the numerical values almost coincide which indicates that these points are well in the regime of inertial convection. At higher values of $P \geq 10^{-1}$ they are in the marginal region of the regime and the analytical prediction is only approached. The gradual transition between the two modes is due to the fact that the two types of convection result from different dynamical balances rather than from a direct mode competition mechanism. However, if the wavenumber m is allowed to vary sudden jumps between competing wavenumbers might occur. A detailed plot of the region where inertial convection is expected to occur is presented in figure 5 of the work of Ardes *et al.* [3].

The effect of fixed-flux thermal boundary conditions on the onset of convection at low values of P. The results reported so far in the present section are obtained for

Fig. 5.17. *The critical Rayleigh number R_c (left ordinate) and frequency ω (right ordinate) as functions of τ for $P = 10^{-4}$, $m = 8$, $\eta = 0.3$ and fixed-flux (thick solid lines) and fixed-temperature (thin-solid lines) thermal boundary conditions. The dashed lines correspond to expression (5.14) for ω.*

fixed-temperature (Case A) thermal boundary conditions. Only minor quantitative changes are observed when fixed-flux (Case B) boundary conditions are used. To illustrate this we present figure 5.17 where the results for the two types of boundary conditions are directly compared for a set of fixed parameters. The figure is analogous to figure 5.10 and the same number and type of modes and transitions may be observed.The main differences between the two types of boundary conditions are that the fixed-flux case has a lower value of the Rayleigh number R_c for the mode drifting in the retrograde direction while a higher value of R_c is obtained for the mode drifting in the prograde direction. Furthermore, the transition between these two states occurs at lower values of τ in the fixed-flux case. The frequencies of the two modes are nearly identical. A transitions to multi-cellular modes is also found for high values of τ in the case of fixed-flux thermal boundary conditions. For a more detail explanation of these differences we refer once again to the following section 5.6.

5.6 Analytical theory of inertial convection in rotating fluid spheres

This section reports an analytical theory of inertial convection in rotating fluid spheres and more precisely of the modes denoted by C and D in figure 5.10 of the preceding section. It provides explicit expressions for the Rayleigh number R_c as a function of the wavenumber, the Prandtl and the Coriolis numbers. Both fixed-temperature and fixed-flux thermal boundary conditions are considered. Using the explicit expressions for R_c we are able to determine precisely the border between the retrograde and the prograde drifting modes and the value of the preferred wavenumber at fixed values of the other parameters. The theory is tested against direct numerical results and excellent agreement is found. The numerically observed phenomena reported in the preceding section 5.5 can now be understood much better.

Below we attach our[1] article [34] in which the analytical theory was recently published[2]. The article is short, contains all relevant analytical results and is self-contained which makes its inclusion in the section appropriate. There is only a minor overlap with section 5.2. A small number of additional details which have been too lengthy or descriptive to be included in the published version can be provided at several points. They appear in the form of notes at the end of the present section.

---

[1] Prof. Dr. F.H. Busse is the doctoral adviser of the second author.
[2] In the article R_c is denoted simply by R.

Inertial convection in rotating fluid spheres

By F. H. BUSSE AND R. SIMITEV

Institute of Physics, University of Bayreuth, D-95440 Bayreuth, Germany
Busse@uni-bayreuth.de

The onset of convection in the form of inertial waves in a rotating fluid sphere is studied through a perturbation analysis in an extension of earlier work by Zhang (1994). Explicit expressions for the dependence of the Rayleigh number on the azimuthal wavenumber are derived and new results for the case of a nearly thermally insulating boundary are obtained.

1. Introduction

Convection in the form of slightly modified inertial waves is a well-known phenomenon in geophysical fluid dynamics. The analysis of the onset of convection in a horizontal fluid layer heated from below and rotating about a vertical axis was first done by Chandrasekhar more than 50 years ago. For an account of this early work we refer to his famous monograph (Chandrasekhar 1961). He found that convection sets in at high rotation rates in the form of modified inertial waves when the Prandtl number is less than about 0.6 depending on the boundary conditions. Another important case in which convection in the form of modified inertial waves occurs is the rotating fluid sphere heated from within and subject to a spherically symmetric gravity field. The transition from convection in the form of columns aligned with the axis of rotation to inertial convection in the form of equatorially attached modes has been demonstrated by Zhang & Busse (1987). In a later series of papers Zhang (1993, 1994, 1995) developed an analytical theory for the critical parameter values for the onset of convection based on a perturbation approach. The buoyancy term and viscous dissipation are introduced in the equation of motion as small perturbations of inviscid inertial waves and the balance of the two terms is then used for the determination of the critical value of the Rayleigh number. In this paper we extend this approach to case of a spherical boundary of low thermal conductivity on the one hand and to an alternative method of analysis on the other hand which will allow us to obtain explicit expressions for the dependence of the Rayleigh number on the azimuthal wavenumber.

2. Mathematical formulation of the problem

We consider a homogeneously heated, self-gravitating fluid sphere rotating with the constant angular velocity Ω about an axis fixed in space. A static state thus exists with the temperature distribution $T_S = T_0 - \beta r_0^2 r^2 / 2$ and the gravity field given by $\boldsymbol{g} = -\gamma r_0 \boldsymbol{r}$ where $\boldsymbol{r}$ is the position vector with respect to the centre of the sphere and r is its length measured in fractions of the radius r_0 of the sphere. In addition to the length r_0, the time r_0^2/ν and the temperature $\nu^2/\gamma \alpha r_0^4$ are used as scales for the dimensionless description of the problem where ν denotes the kinematic viscosity of

the fluid and κ is its thermal diffusivity. The density is assumed to be constant except in the gravity term where its temperature dependence given by $\alpha \equiv (\mathrm{d}\varrho/\mathrm{d}T)/\varrho =$ const. is taken into account. The basic equations of motion and the heat equation for the deviation Θ from the static temperature distribution are thus given by

$$\partial_t \boldsymbol{u} + \tau \boldsymbol{k} \times \boldsymbol{u} + \nabla \pi = \Theta \boldsymbol{r} + \nabla^2 \boldsymbol{u}, \tag{2.1a}$$

$$\nabla \cdot \boldsymbol{u} = 0, \tag{2.1b}$$

$$R\boldsymbol{r} \cdot \boldsymbol{u} + \nabla^2 \Theta - P\partial_t \Theta = 0, \tag{2.1c}$$

where the Rayleigh number R, the Coriolis parameter τ and the Prandtl number P are defined by

$$R = \frac{\alpha \gamma \beta r_0^6}{\nu \kappa}, \quad \tau = \frac{2\Omega r_0^2}{\nu}, \quad P = \frac{\nu}{\kappa}. \tag{2.2}$$

We have neglected the nonlinear terms $\boldsymbol{u} \cdot \nabla \boldsymbol{u}$ and $\boldsymbol{u} \cdot \nabla \Theta$ in equations (2.1) since we restrict the attention to the problem of the onset of convection in the form of small disturbances. In the limit of high τ the right-hand side of equation (2.1a) can be neglected and the equation for inertial waves is obtained. For the description of inertial wave solutions $\boldsymbol{u}_0$ we use the general representation in terms of poloidal and toroidal components for the solenoidal field $\boldsymbol{u}_0$,

$$\boldsymbol{u}_0 = \nabla \times (\nabla v \times \boldsymbol{r}) + \nabla w \times \boldsymbol{r}. \tag{2.3}$$

By multiplying the $(\text{curl})^2$ and the curl of the inertial wave equation by $\boldsymbol{r}$ we obtain two equations for v and w,

$$[\partial_t \mathscr{L}_2 - \tau \partial_\varphi] \nabla^2 v - \tau \mathscr{Q} w = 0, \tag{2.4a}$$

$$[\partial_t \mathscr{L}_2 - \tau \partial_\varphi] w + \tau \mathscr{Q} v = 0, \tag{2.4b}$$

where ∂_t and ∂_φ denote the partial derivatives with respect to time t and with respect to the angle φ of a spherical system of coordinates r, θ, φ and where the operators $\mathscr{L}_2$ and $\mathscr{Q}$ are defined by

$$\mathscr{L}_2 \equiv -r^2 \nabla^2 + \partial_r (r^2 \partial_r), \tag{2.5a}$$

$$\mathscr{Q} \equiv r \cos\theta \nabla^2 - (\mathscr{L}_2 + r\partial_r)(\cos\theta \partial_r - r^{-1}\sin\theta \partial_\theta). \tag{2.5b}$$

General solutions in explicit form for inertial waves in rotating spheres have recently been obtained by Zhang *et al.* (2001). Here only solutions of equations (2.4) for which v is symmetric with respect to the equatorial plane and does not possess a zero in its θ-dependence are of interest since only those are connected with the preferred modes for the onset of convection (Zhang 1994). These modes are given by

$$v_0 = P_m^m(\cos\theta)\exp\{im\varphi + i\omega\tau t\}f(r), \quad w_0 = P_{m+1}^m(\cos\theta)\exp\{im\varphi + i\omega\tau t\}g(r), \tag{2.6}$$

with

$$f(r) = r^m - r^{m+2}, \quad g(r) = r^{m+1}\frac{2im(m+2)}{(2m+1)(\omega_0(m^2 + 3m + 2) - m)}, \tag{2.7a}$$

$$\omega_0 = \frac{1}{m+2}(1 \pm (1 + m(m+2)(2m+3)^{-1})^{1/2}). \tag{2.7b}$$

Before considering the full problem (2.1) we have to specify the boundary conditions. We shall assume a stress-free boundary with either a fixed temperature (case A) or a

thermally insulating boundary (case B),

$$\mathbf{r} \cdot \mathbf{u} = \mathbf{r} \cdot \nabla(\mathbf{r} \times \mathbf{u})/r^2 = 0 \quad \text{and} \quad \left. \begin{array}{ll} \Theta = 0 & \text{(case A)} \\ \partial_r \Theta = 0 & \text{(case B)} \end{array} \right\} \quad \text{at} \quad r = 1. \tag{2.8}$$

Following Zhang (1994) we use a perturbation approach for solving equations (2.1),

$$\mathbf{u} = \mathbf{u}_0 + \mathbf{u}_1 + \ldots, \quad \omega = \omega_0 + \omega_1 + \ldots. \tag{2.9}$$

The perturbation $\mathbf{u}_1$ consists of two parts, $\mathbf{u}_1 = \mathbf{u}_i + \mathbf{u}_b$, where $\mathbf{u}_i$ denotes the perturbation of the interior flow, while $\mathbf{u}_b$ is the Ekman boundary flow which is required since $\mathbf{u}_0$ satisfies the first of conditions (2.8), but not the second.

After the ansatz (2.9) has been inserted into equations (2.1a) and (2.1b) we obtain the solvability condition for equation (2.1a) for $\mathbf{u}_1$ by multiplying it with $\mathbf{u}_0^*$ and averaging it over the fluid sphere,

$$i\omega_1 \langle |\mathbf{u}_0|^2 \rangle = \langle \Theta \mathbf{r} \cdot \mathbf{u}_0^* \rangle + \langle \mathbf{u}_0^* \cdot \nabla^2(\mathbf{u}_0 + \mathbf{u}_b) \rangle, \tag{2.10}$$

where the brackets $\langle \ldots \rangle$ indicate the average over the fluid sphere and $*$ indicates the complex conjugate. The evaluation of the second term on the right-hand side of (2.10) yields

$$\langle \mathbf{u}_0^* \cdot \nabla^2(\mathbf{u}_0 + \mathbf{u}_b) \rangle = \langle (\nabla \times \mathbf{u}_0^*) \cdot (\nabla \times \mathbf{u}_b)) \rangle + \frac{3}{4\pi} \oint [\mathbf{u}_0^* \cdot \nabla \mathbf{u}_b - \mathbf{u}_0^* \cdot (\mathbf{r} \cdot \nabla)\mathbf{u}_b] \, d^2 S, \tag{2.11}$$

since $\nabla^2 \mathbf{u}_0$ vanishes (Zhang 1994). Since $\mathbf{u}_b$ is of the order $\tau^{-1/2}$ and vanishes outside a boundary layer of thickness $\tau^{-1/2}$, only the term involving a radial derivative of $\mathbf{u}_b$ makes a contribution of order one on the right-hand side of equation (2.11). This term can easily be evaluated because of the condition $\mathbf{r} \cdot \nabla \mathbf{r} \times (\mathbf{u}_0 + \mathbf{u}_b)/r^2 = 0$ at the surface of the sphere. Using expressions (2.6) and (2.7a) we thus obtain

$$\langle \mathbf{u}_0^* \cdot \nabla^2 \mathbf{u}_b \rangle = \frac{3}{2} \int_{-1}^{1} \left| P_m^m \right|^2 d(\cos\theta) \, m(m+1)(2m+1) \left[4 + (m+2)\frac{(2m+1)}{2m+3} \right]$$

$$\times \left| \frac{2(m+1)^2 - 2}{(2m+1)(\omega_0(m+1)(m+2) - m)} \right|^2, \tag{2.12}$$

where the relationship

$$\int_{-1}^{1} \left| P_m^{m+1} \right|^2 d\cos\theta = \frac{(2m+1)^2}{2m+3} \int_{-1}^{1} \left| P_m^m \right|^2 d\cos\theta \tag{2.13}$$

has been used.

3. Explicit expressions in the limit $P\tau \ll 1$

The equation (2.1c) for Θ can most easily be solved in the limit of vanishing $\tau P\omega_0$. In this limit we obtain for Θ,

$$\Theta = P_m^m(\cos\theta)\exp\{im\varphi + i\omega\tau t\}h(r), \tag{3.1}$$

with

$$h(r) = m(m+1)R\left(\frac{r^{m+4}}{(m+5)(m+4) - (m+1)m} - \frac{r^{m+2}}{(m+3)(m+2) - (m+1)m} - cr^m\right), \tag{3.2}$$

26   *F. H. Busse and R. Simitev*

where the coefficient c is given by

$$c = \begin{cases} \dfrac{1}{(m+5)(m+4)-(m+1)m} - \dfrac{1}{(m+3)(m+2)-(m+1)m} & \text{(case A)}, \\[2ex] \dfrac{(m+4)/m}{(m+5)(m+4)-(m+1)m} - \dfrac{(m+2)/m}{(m+3)(m+2)-(m+1)m} & \text{(case B)}. \end{cases} \tag{3.3}$$

Since Θ is real ω_1 must vanish according to the solvability condition (2.10) and we obtain for R the final result

$$R_{\pm} = \left(\frac{m^2(m+2)^3}{(2m+3)[(m+1)(1 \pm \sqrt{(m^2+4m+3)/(2m+3)}) - m]^2} + 2m + 1 \right)$$
$$\times (2m+9)(2m+7)(2m+5)^2(2m+3)^2/b, \tag{3.4}$$

where the two possibilities for the sign originate from the two possibilities for the sign in the expression (2.7b) for ω_0. The coefficient b takes the values

$$b = \begin{cases} (m+1)m(10m+27) & \text{(case A)}, \\ (m+1)(14m^2+59m+63) & \text{(case B)}. \end{cases} \tag{3.5}$$

Obviously, the lowest value of R is reached for $m=1$ and the value R_+ for convection waves travelling in the retrograde direction is always lower than the value R_- for the prograde waves. Expression (3.4) is also of interest, however, in the case of spherical fluid shells when the ($m=1$)-mode is affected most strongly by the presence of the inner boundary. Convection modes corresponding to higher values of m may then become preferred at onset since their r-dependence decays more rapidly with distance from the outer boundary according to relationships (2.7).

4. Solution of the heat equation in the general case

For the solution of equation (2.1c) in the general case it is convenient to use the Green's function method. The Green's function $G(r,a)$ is obtained as solution of the equation

$$[\partial_r r^2 \partial_r + (-\mathrm{i}\omega_0 \tau P\, r^2 - m(m+1))]G(r,a) = \delta(r-a), \tag{4.1}$$

which can be solved in terms of the spherical Bessel functions $j_m(\mu r)$ and $y_m(\mu r)$,

$$G(r,a) = \begin{cases} G_1(r,a) = A_1 j_m(\mu r) & \text{for } 0 \leqslant r < a, \\ G_2(r,a) = A j_m(\mu r) + B y_m(\mu r) & \text{for } a < r \leqslant 1, \end{cases} \tag{4.2}$$

where

$$\mu \equiv \sqrt{-\mathrm{i}\omega_0 \tau P}, \quad A_1 = \mu \left(y_m(\mu a) - j_m(\mu a)\frac{j_m(\mu)}{y_m(\mu)} \right), \tag{4.3a,b}$$

$$A = -\mu j_m(\mu a)\frac{y_m(\mu)}{j_m(\mu)}, \quad B = \mu j_m(\mu a). \tag{4.3c,d}$$

A solution of equation (2.1c) can be obtained in the form

$$h(r) = -\int_0^1 G(r,a)m(m+1)(a^m - a^{m+2})a^2\,\mathrm{d}a$$
$$= -\int_0^r G_2(r,a)m(m+1)(a^m - a^{m+2})a^2\,\mathrm{d}a - \int_r^1 G_1(r,a)m(m+1)(a^m - a^{m+2})a^2\,\mathrm{d}a.$$
$$\tag{4.4}$$

Evaluation of these integrals for $m = 1$ yields the expressions

$$
h(r) = \begin{cases}
\dfrac{2R}{(\omega_0 \tau P)^2}\left(r(\mu^2 + 10) - \mu^2 r^3 - \dfrac{10(\mu r \cos(\mu r) - \sin(\mu r))}{r^2(\mu \cos\mu - \sin\mu)} \right) & \text{(case A)}, \\[3ex]
\dfrac{2R}{(\omega_0 \tau P)^2}\left(r(\mu^2 + 10) - \mu^2 r^3 - \dfrac{(\mu^2 - 10)(\mu r \cos(\mu r) - \sin(\mu r))}{r^2(2\mu \cos\mu - (2 - \mu^2)\sin\mu)} \right) & \text{(case B)}.
\end{cases}
$$

$$(4.5)$$

Slightly more complex expressions are obtained for $m > 1$. Expressions (4.5) can now be used to calculate R and ω_1 on the basis of equation (2.1). In the case $m = 1$ we obtain

$$
R = 21(\omega_0 \tau P)^2 \left(1 + \frac{9}{5(6\omega_0 - 1)^2} \right)
$$

$$
\times \begin{cases}
\left[2 - 1050\mu^{-4} - \operatorname{Re}\left\{ \dfrac{350\mu^{-2}\sin\mu}{\mu\cos\mu - \sin\mu} \right\} \right]^{-1} & \text{(case A)}, \\[3ex]
\left[9 + 525\mu^{-4} - \operatorname{Re}\left\{ \dfrac{(7\mu^2 - 70 + 175\mu^{-2})\sin\mu}{2\mu\cos\mu + (\mu^2 - 2)\sin\mu} \right\} \right]^{-1} & \text{(case B)},
\end{cases}
$$

$$(4.6)$$

where $\operatorname{Re}\{\}$ indicates the real part of the term enclosed by $\{\}$. Expressions (4.6) have been plotted together with the expressions obtained for higher values of m in figures 1(a) and 1(b) for the cases A and B, respectively. We also show by broken lines numerical values which have been obtained through the use of a modified version of the Galerkin method of Ardes, Busse & Wicht (1997). Because the numerical computations have been done for the finite value 10^5 of τ the results differ slightly from those of the analytical theory. Since there are two values of ω_0 for each m, two functions $R(\tau P)$ have been plotted for each m. For values τP of order unity or lower, expressions (3.4) are approached well and the retrograde mode corresponding to the positive sign in (2.7b) yields always the lower value of R. But the prograde mode corresponding to the negative sign in (2.7b) becomes the preferred mode as τP becomes of order 10 or larger depending on the particular value of m. This transition can be understood on the basis of the increasing difference in phase between Θ and u_r with increasing τP. While the mode with the largest absolute value of ω_0 is preferred as long as Θ and u_r are in phase, the mode with the minimum absolute value of ω becomes preferred as the phase difference increases since the latter is detrimental to the work done by the buoyancy force. The frequency perturbation ω_1 usually makes only a small contribution to ω, which tends to decrease the absolute value of ω.

For very large values of τP the Rayleigh number R increases in proportion to $(\tau P)^2$ for fixed m. In spite of this strong increase Θ remains of order τP on the right-hand side of equation (2.1a). The perturbation approach thus continues to be valid for $\tau \longrightarrow \infty$ as long as $P \ll 1$ can be assumed. For any fixed low Prandtl number, however, with increasing τ the onset of convection in the form of prograde inertial modes will be replaced at some point by onset in the form of columnar convection because the latter obeys an approximate asymptotic relationship for R of the form $(\tau P)^{4/3}$ (see, for example, Busse 1970). This second transition depends on the value of P and will occur at higher values of τ and R for lower values of P. There is little chance that inertial convection occurs in the Earth's core, for instance, since P is of the order 0.03 while the usual estimate for τ is 10^{15}.

28   *F. H. Busse and R. Simitev*
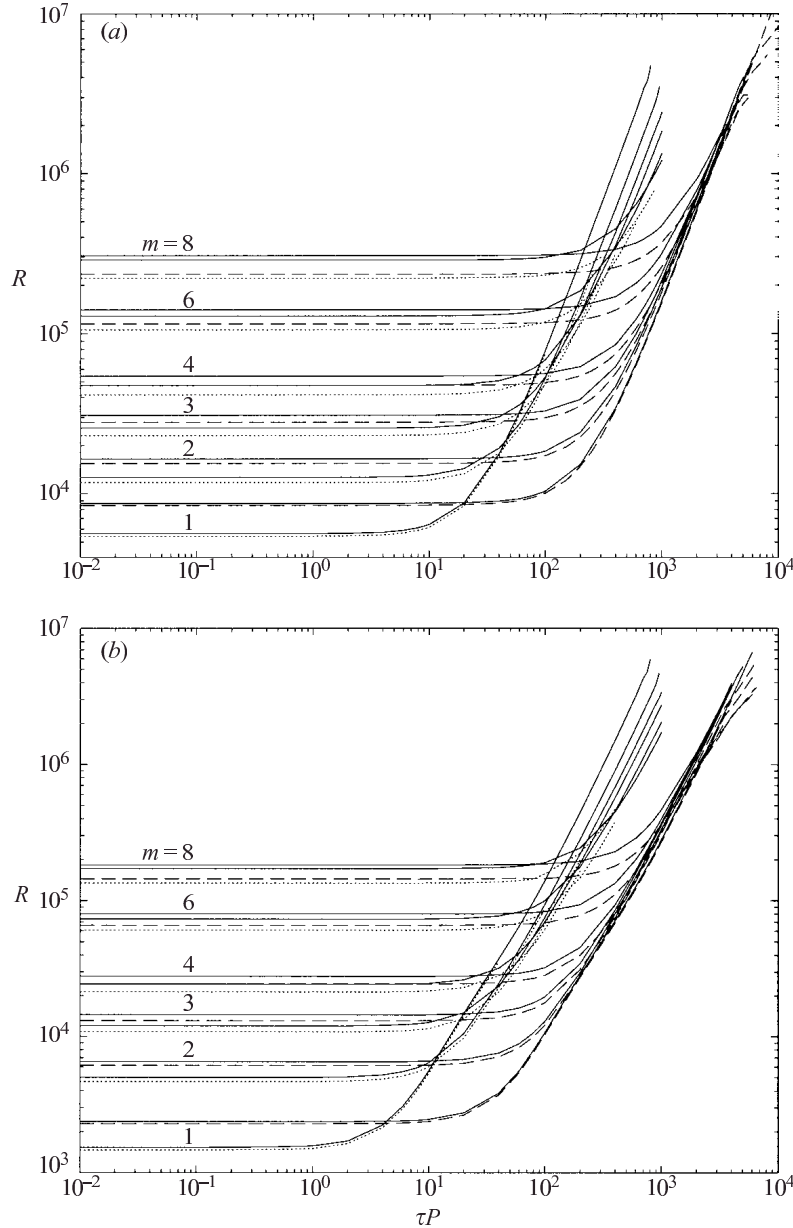
FIGURE 1. The Rayleigh number R as a function of τP for $m = 1, 2, 3, 4, 6$ and 8. Results based on explicit expressions such as (4.6) in the case of $m = 1$ (solid lines) are shown in comparison with the results obtained with a Galerkin numerical scheme (dotted lines for retrograde mode, dashed lines for prograde mode). (a) Case A, fixed temperature boundary conditions. (b) Case B, insulating thermal boundary conditions.

5. Discussion

Since the curves $R(\tau P, m)$ intersect at values of τP of order 10^3 in figures 1(a) and 1(b), a different way of plotting the results has been adopted in figure 2. Here the preferred value of m has been indicated by a filled circle in the case of the prograde inertial mode. The results of figure 2(a) agree well with those of figure 4 of Zhang (1994) even though only an approximate method had been used for the
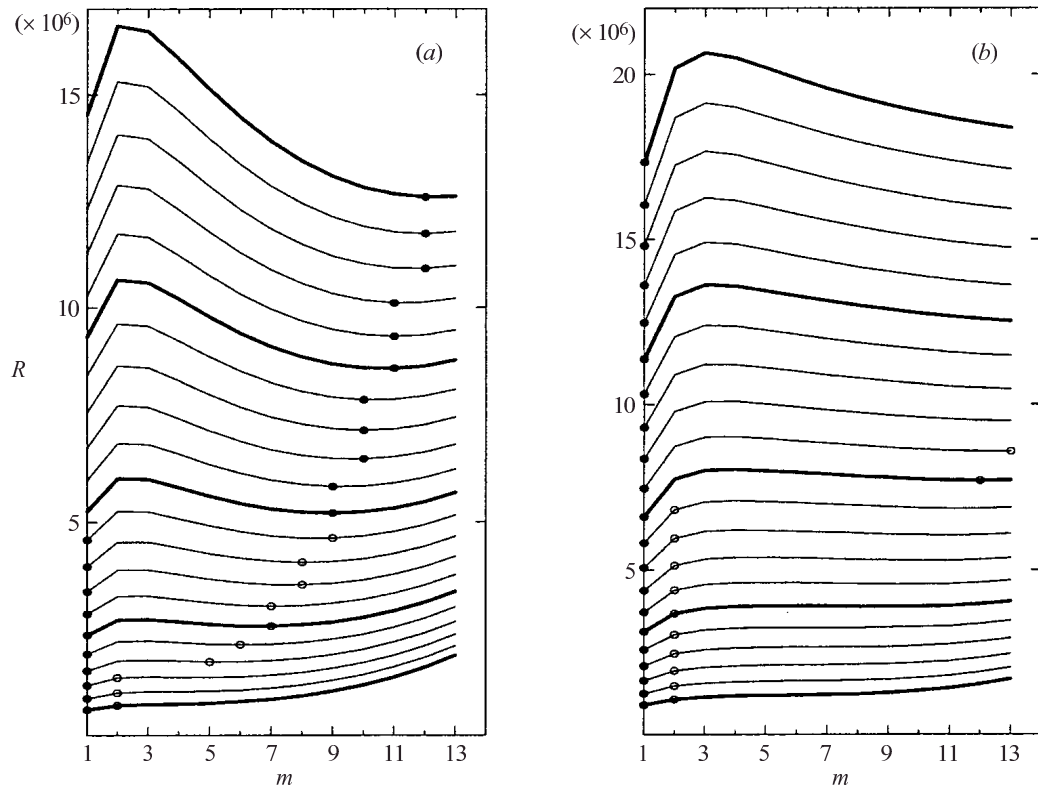
FIGURE 2. The Rayleigh number R as a function of m for $2 \times 10^3 \leqslant \tau P \leqslant 10^4$ (from bottom to top). The lines are equidistant with a step of $\Delta(\tau P) = 400$. The filed circles indicate the preferred values of m. The open circles correspond to the preferred value of m in the case when $m = 1$ is not included in the competition. (*a*) Case A, fixed temperature boundary conditions. (*b*) Case B, insulating thermal boundary conditions.

determination of the Rayleigh number. Zhang neglected the ($m = 1$)-mode and thus arrived at a different criterion for the preferred mode. His preferred values of m are indicated by open circles in figure 2. The ($m = 1$)-mode could indeed be suppressed by the presence of an inner concentric spherical boundary. A rough estimate indicates that inertial convection with azimuthal wavenumber m will be affected significantly when the radius η of the inner boundary exceeds a value of the order $(1 - m^{-1})$. Unfortunately, an analytical theory of inertial waves in rotating spherical fluid shells does not exist and it is thus not possible to extend the analysis of this paper to the case when an inner boundary is present. For a numerical study of inertial convection in rotating spherical fluid shells and its finite-amplitude properties we refer to Simitev & Busse (2003).

The two transitions between modes of different types mentioned in the preceding section illuminate some of the puzzling findings of Zhang & Busse (1987) and Ardes *et al.* (1997). The transition labeled I in figure 17 of Zhang & Busse (1987) can now be clearly identified with the transition from retrograde to prograde inertial convection. The main result of our analysis is that this transition depends primarily on the parameter combination τP with only a minor dependence on the wavenumber m. The second transition (1997). The second transition from inertial to columnar convection cannot be pinned down equally well because of the lack of a sufficiently accurate analytical theory for thermal Rossby waves in the low Prandtl number

30   *F. H. Busse and R. Simitev*

regime. According to the numerical results of Ardes *et al.* (1997) (see their figures 4 and 5) there exists a broad transition range involving perhaps several transitions where the onset of convection occurs in the form of multi-cellular modes. An illumination of this regime should be the goal of future research.

REFERENCES

ARDES, M., BUSSE, F. H. & WICHT, J. 1997 Thermal convection in rotating spherical shells. *Phys. Earth Planet. Inter.* **99**, 55–67.

BUSSE, F. H. 1970 Thermal instabilities in rapidly rotating systems. *J. Fluid Mech.* **44**, 441–460.

CHANDRASEKHAR, S. 1961 *Hydrodynamic and Hydromagnetic Stability.* Clarendon.

SIMITEV, R. & BUSSE, F. H. 2003 Patterns of convection in rotating spherical shells. *New J. Phys.* **5**, 1.1–1.20.

ZHANG, K. 1993 On equatorially trapped boundary inertial waves. *J. Fluid Mech.* **248**, 203–217.

ZHANG, K. 1994 On coupling between the Poincaré equation and the heat equation. *J. Fluid Mech.* **268**, 211–229.

ZHANG, K. 1995 On coupling between the Poincaré equation and the heat equation: non-slip boundary condition. *J. Fluid Mech.* **284**, 239–256.

ZHANG, K. & BUSSE, F. H. 1987 On the onset of convection in rotating spherical shells. *Geophys. Astrophys. Fluid Dyn.* **39**, 119–147.

ZHANG, K., EARNSHAW, P., LIAO, X. & BUSSE, F. H. 2001 On inertial waves in a rotating fluid sphere. *J. Fluid Mech.* **437**, 103–119.

Additional comments.

page 25, line 5 from bottom: The heat equation (2.1c) in the limit $\tau P \omega_0 \longrightarrow 0$ can alternatively be solved with the help of the more general Green's function method presented in section 4 of the article.

page 27, line 1 from top: Evaluations of the integrals (4.4) for an arbitrary wavenumber m yields,

$$h(r) = -m(m+1)(F_1 + F_2 + F_3), \tag{5.15}$$

where, in case A,

$$
\begin{aligned}
F_1 =&\ \left(\frac{y_m(\mu r)}{2} - \frac{j_m(\mu r)y_m(\mu)}{j_m(\mu)}\right)\sqrt{2\pi r}\, r^m \Big[(\mu^3 r^3 - (\mu^3 + (6+4m)\mu)r)J_{m-1/2}(\mu r)\\
&+\Big(((-2m-3)r^2 + 2m+1)\mu^2 + 8m^2 + 16m + 6)J_{m+1/2}(\mu r)\Big)\Big]\mu^{-(7/2)}
\end{aligned}
$$

$$
\begin{aligned}
F_2 =&\ -\frac{\sqrt{2\pi}}{2}y_m(\mu)j_m(\mu r)((16m + 8m^2 - 2\mu^2 + 6)r^3 J_{m+1/2}(\mu) - (6+4m)r^3\mu J_{m-1/2}(\mu)\\
&+((2m+3)\mu^2 r^{(11/2)} + ((-1-2m)\mu^2 - 16m - 8m^2 - 6)r^{(7/2)})r^m J_{m+1/2}(\mu r)\\
&+r^m(-r^{(13/2)}\mu^3 + (\mu^3 + (6+4m)\mu)r^{(9/2)})J_{m-1/2}(\mu r))\Big(\mu^{(7/2)}j_m(\mu)r^3\Big)^{-1}
\end{aligned}
\tag{5.16}
$$

$$
\begin{aligned}
F_3 =&\ \frac{1}{2}j_m(\mu r)\sqrt{2\pi}(-(-1)^m r^m(\mu^3 r^{(11/2)} + (-4m - \mu^2 - 6)\mu r^{(7/2)})J_{-m+1/2}(\mu r)\\
&+(-1)^m r^m((-2m-3)\mu^2 r^{(9/2)} + (8m^2 + 16m + 6 + 2m\mu^2 + \mu^2)r^{(5/2)})J_{-m-1/2}(\mu r)\\
&-(4m+6)\mu r^2(-1)^m J_{-m+1/2}(\mu) + (-8m^2 - 6 - 16m + 2\mu^2)r^2(-1)^m J_{-m-1/2}(\mu))\mu^{-(7/2)}r^{-2}.
\end{aligned}
$$

A similar expression exists for case B but will not be listed here. This general solution of the heat equation (2.1c) might be useful in attempts to derive approximate analytical expressions for R_c for an arbitrary value of m (see below). The expression (5.15) reduces to (4.5) for $m = 1$.

page 27, line 6 from top: No exact general expression for R_c for arbitrary wavenumbers m was found. However, for any fixed value of $m = 1, 2, ...$ an exact expression for R_c may be obtained. Expressions (4.6) for $m = 1$ are the shortest examples of these. Using the general solution (5.15) of the heat equation various approximations of R_c for arbitrary values of m might be obtained. For example the spherical and the ordinary Bessel functions $j_n(z)$, $y_n(z)$, $J_n(z)$, $Y_n(z)$, can be approximated by ascending series in z using formulas (10.1.2) and (10.1.3) of [1]. The solution (5.15) of the heat equation then transforms into a polynomial in r and may be easily integrated as required by the solvability condition (2.10) to obtain an approximation of R_c. Using this approach,

$$R_c^{appr.} = T_1 \Re\{T_2 + T_3\}^{-1}, \tag{5.17}$$

$$T_1 = -\frac{4(m+2)(5+2m)}{m(m+1)} \left(1 + \frac{((1+m)^2-1)^2}{(\omega_0(1+m)(m+2)-m)(3+2m)}\right) \left(\prod_{k=0}^{m}(2k+1)\right)$$

$$T_2 = 16(-1)^{(3+m)} \left(\mu^6(9+2m)(7+2m)^2(5+2m)(3+2m)\left(\prod_{k=-m}^{m}(2k+1)\right)\right)^{-1}$$

$$\cdot\left((4m+6)\mu^4 + (160m+72+32m^2)\mu^2 - 32m^5 - 304m^4 - 880m^3 - 680m^2 + 222m + 189\right)$$

$$T_3 = \sqrt{2\pi}\mu^{-5/2+m}\left(2(-1)^{m+1}J_{-m+1/2}(\mu) + 2J_{m-1/2}(\mu)y_m(\mu)j_m(\mu)^{-1}\right.$$

$$\left. -2\left(y_m(\mu)j_m(\mu)^{-1}J_{m+1/2}(\mu) + (-1)^m J_{-m-1/2}\right)(4m^2 + 8m - \mu^2 + 3)((3+2m)\mu)^{-1}\right)$$

if only the first term in the ascending series has been used. Despite the availability of approximations of R_c for an arbitrary value of m we have chosen to publish expressions (4.6) which are valid for a single m, but are exact and more informative.
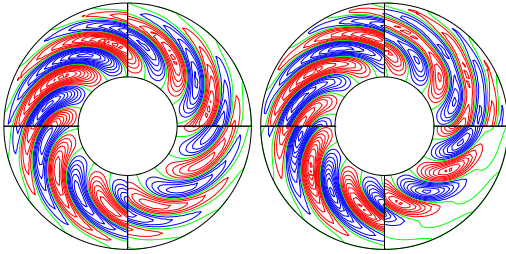
6. Finite-Amplitude Convection in Rotating Spherical Fluid Shells

6.1 Introduction

Topic and motivation. In this chapter we continue the exploration of the properties of non-magnetic convection in rotating spherical fluid shells. In contrast to the previous chapter, here we drop the restriction to linear governing equations and discuss convection at finite amplitudes in which the nonlinear effects cannot be neglected. As often argued in the preceding chapters, rotating convection is fundamental to a variety of geophysical and astrophysical processes. Of particular importance, in the frame of this dissertation, is the fact that convective flow is the type of motion most probably realized in the Earth's fluid core and for this reason responsible for the generation and sustainment of the geomagnetic field.

The problem of finite-amplitude convection is orders of magnitude more difficult than the problem of the onset of convection in rotating spherical shells. In addition to all difficulties native to the linear case (see sec. 5.1), the full set of governing equations described in chapter 3 exhibit the phenomena of turbulence and chaos in space and time. Since no general theory of turbulence exists, it is likely that the exploration of the properties of nonlinear convection will continue to receive attention in the future.

Outline of contents. The chapter is a logical continuation of the numerical studies of the linear onset of convection described in chapter 5 and is influenced by the earlier works of Tilgner & Busse [114] and Grote & Busse [59]. The results may be roughly organized into two strongly interrelated groups. The first group represents an attempt to describe the spatial and time dependence of the supercritical nonlinear convective flow. Since soon after onset convection becomes chaotic, there is no simple method of achieving this objective. Here the intuition gained from the linear studies proves valuable, since the evolution of many of the patterns present at onset may be followed into the nonlinear regime. Furthermore, despite the complicated spatial and time dependences, certain patterns seem to reappear and play a significant role. Following this approach a number of states leading to chaotic convection as well as coherent structures such as localized convection and relaxation oscillations have been described in [59]. However, the results of this work are mostly restricted to values of the Coriolis number near $\tau = 10^4$ and Prandtl numbers near unity and leave open questions such as how the scenario reported in [59] is modified at other values of these parameters and whether particular structures and states exist far from the values used. In particular, the linear studies of the previous chapter indicate that the inertial type of convection, being rather distinct, will not follow the same transitions towards a chaotic regime as described in [59]. The same holds for the convection at high values of the Prandtl number where thermal wind structures rather than geostrophic balance seem to prevail. These questions provide the motivation to explore in more detail the parameter space. Section 6.2 summarizes our results on the time and spatial patterns of finite-amplitude convection at small, moderate and high values of the Prandtl number. The second group of results concerns the averaged properties of finite-amplitude convection. Undoubtedly, the averaging process waists information about the system under observation. However, in view of the lack of a general theory of turbulence, the

Fig. 6.1. *Equatorial streamlines $r\partial_\varphi v$=const. for $P = 0.1$, $\tau = 3\times10^4$, $R = 3\times10^5$ (left) and $R = 3.5 \times 10^5$ (right). The four sections are a quarter of a vacillation period $\Delta t = 0.0864$ (left) and $\Delta t = 0.0124$ (right) apart with time progressing in the clockwise sense.*

averaged properties of the flow complement the detailed observations of its local spatial and temporal structure. Moreover, the experimental studies will normally provide measurements, while the theoretical approaches, as far as they exist, can give estimates or bounds only on averaged quantities. In section 6.3 we consider the time and longitudinal averages of the velocity and temperature fields, the local heat transport and global quantities such as the Nusselt number and the various components of the kinetic energies as functions of the parameters. We also determine averaged values of the helicity since it is of fundamental importance to some theories of magnetic field generation.

Parts of this chapter have been published in references [29, 109, 32].
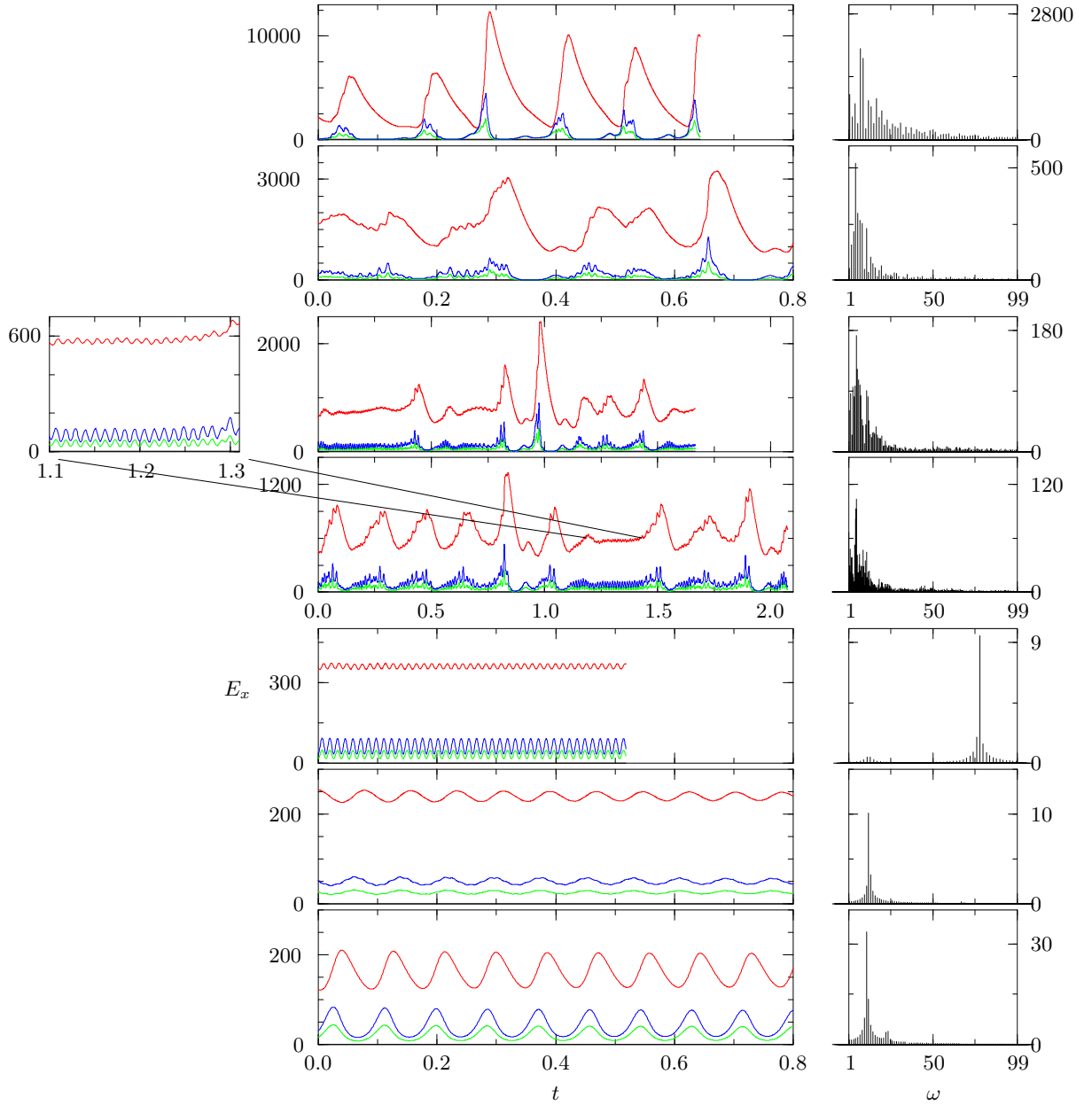
Assumptions. In the introductory chapter 2 we stressed that it is too early for attempts to create realistic models of the geodynamo. Instead we try to investigate the simplest versions of the relevant processes retaining only the most important first order physical effects. In the case of the systematic parameter studies of the present chapter we consider non-magnetic convection of a single component fluid in the Boussinesq approximation described by (3.65) in the case of homogeneous distribution of internal heat sources ($R_e = 0$). We use stress-free boundary conditions for the velocity field (3.66b), fixed-temperature thermal boundary conditions (3.66c) and a radius ratio $\eta = 0.4$. Assumptions other than those will be explicitly stated in the text.

6.2 Structure and spatio-temporal patterns of finite-amplitude convection

Due to the lack of more general and convenient methods to specify the spatial and time dependence of chaotic flows, in this section we follow and extend the work of [59] and describe various flow patterns observed for a wide range of parameter values. Guided by the linear studies of chapter 5 we separate the parameter space into the region of small and moderate and the region of large values of the Prandtl number where distinct types of convection should be observed. As suggested by figure 5.7 high values of τ are more readily accessible at small values of P. Equatorially-attached convection flows appear at small values of the Prandtl number. Their properties at finite amplitudes are studied here for the first time. Because of the required high numerical resolution in time as well as in space the low Prandtl number regime of fully nonlinear convection has posed a significant computational challenge until now. As will be shown the continuity of the convection heat flux requires that equatorially attached convection must be joined by columnar convection as the Rayleigh number increases significantly above its critical value.

6.2.1 Finite-amplitude inertial convection and convection at moderate Prandtl numbers
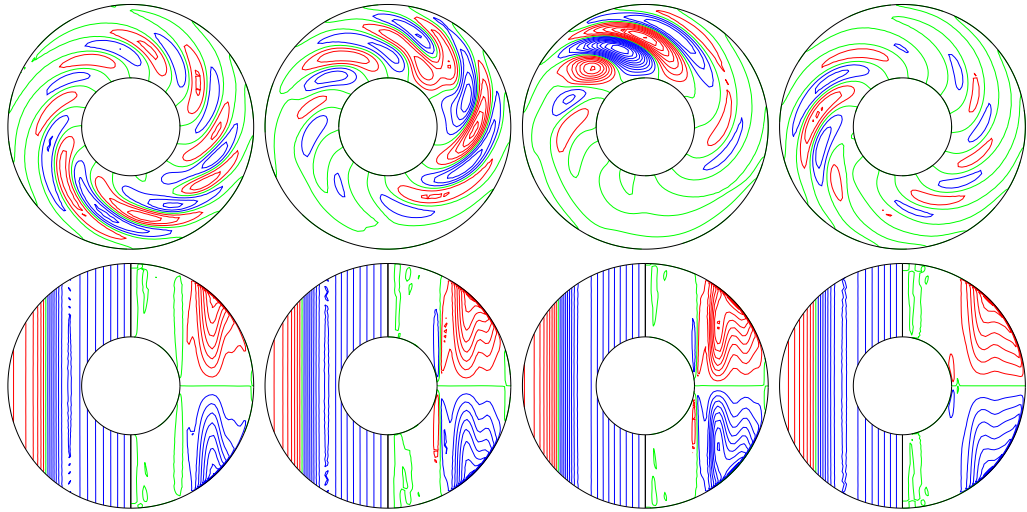
The main body of results concerning the spatial and time patterns of finite-amplitude convection at small and moderate values of the Prandtl number along with other results has
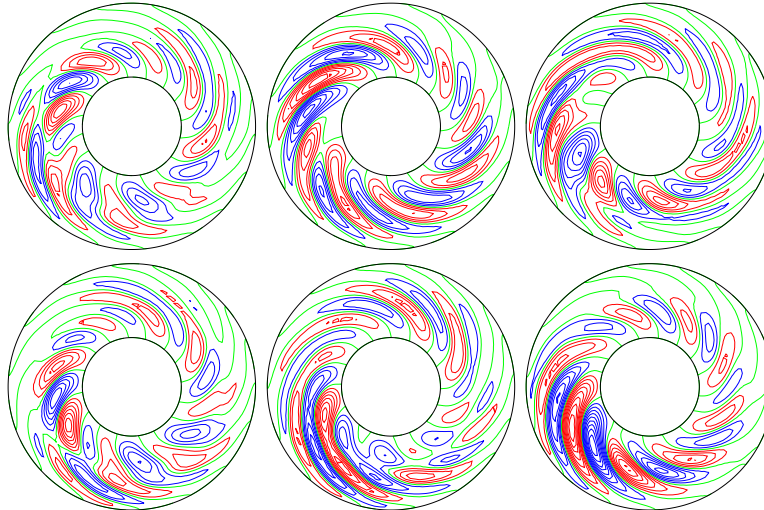
Fig. 6.2. *Time series of energy densities of convection in the case $P = 0.1$, $\tau = 3 \times 10^4$, and $R = 3 \times 10^5$, 3.3×10^5, 3.5×10^5, 3.8×10^5, 4×10^5, 4.5×10^5, 5×10^5 (from bottom to top). Red, blue and green lines indicate $\overline{E}_t$, $\check{E}_t$, and $\check{E}_p$, respectively. The critical Rayleigh number for onset of convection is $R_c = 222518$. The density $\overline{E}_p$ is more than an order of magnitude smaller than the other energy densities and has not been plotted for this reason. The Fourier transforms of $\overline{E}_t$ versus the frequency ω are plotted in the right column.*

been published in reference [109]. Here we reproduce the main results in a reduced form and refer to [109] for further details and discussion.

Evolution of convection columns at moderate Prandtl numbers. In general the on-set of convection in rotating fluid spheres occurs supercritically. As long as the convection assumes the form of shape preserving travelling thermal Rossby waves as described by the linear theory, its azimuthally averaged properties are time independent. In fact, as seen from
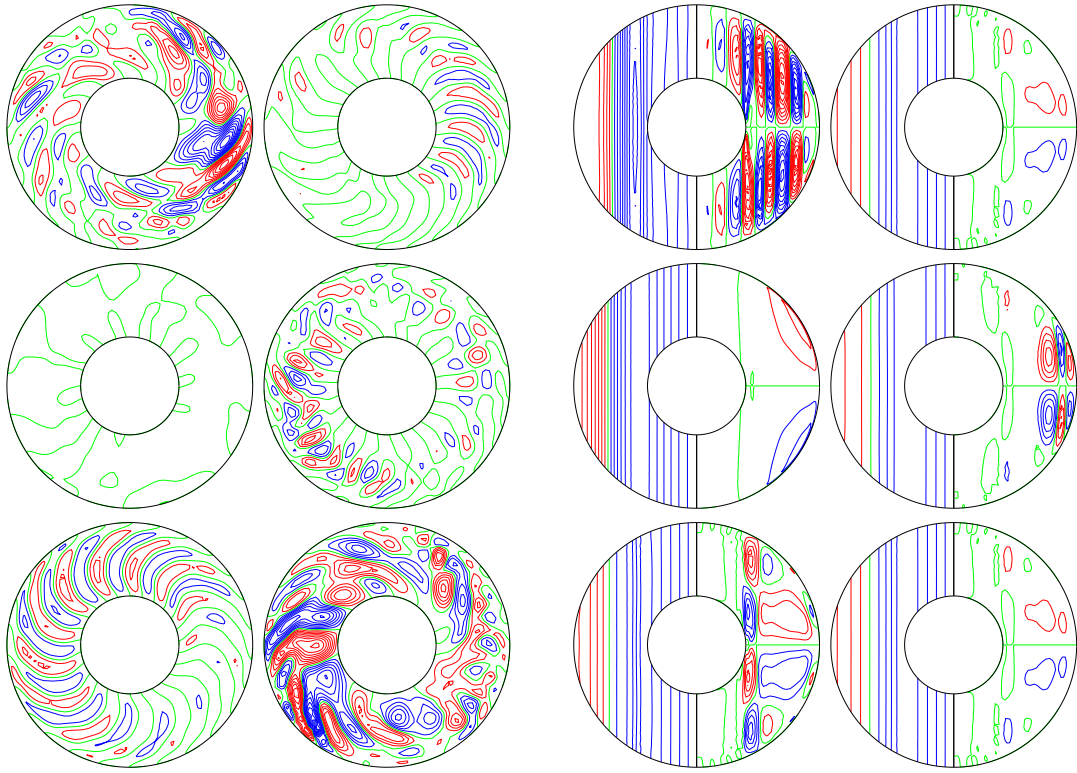
Fig. 6.3. *Sequence of plots equidistant in time (from left to right with $\Delta t = 0.05$) for $P = 0.1$, $\tau = 3 \times 10^4$, $R = 3.8 \times 10^5$. The upper row shows streamlines, $r\partial_\varphi v = \text{const.}$ in the equatorial plane. The left halves of the circles of the lower row show lines of constant $\overline{u_\varphi}$ which is the azimuthally averaged azimuthal component of the velocity field. The right halves show streamlines $r\sin\theta\partial_\theta\overline{v}$ of the axisymmetric meridional circulation.*

Fig. 6.4. *Modulated shape vacillations of convection for $R = 4 \times 10^5$, $\tau = 3 \times 10^4$, $P = 0.1$. The sequence of plots equidistant in time ($\Delta t = 0.00376$), starting at the upper left and continuing clockwise, shows equatorial streamlines $r\partial_\varphi v = \text{const.}$ Since the modulation period is $t_p = 0.0188$, the last plot closely resembles the first plot except for a shift in azimuth.*

a frame of reference drifting together with the convection columns the entire pattern is steady. A differential rotation is generated through the action of the Reynolds stress. The latter is caused by the spiralling cross section of the columns which persists as a dominant feature at moderate Prandtl numbers far into the turbulent regime. The plots of the streamlines $r\partial_\varphi v = \text{const.}$ in the equatorial plane shown in figure 6.1 give a good impression of the spiralling nature of the columns.
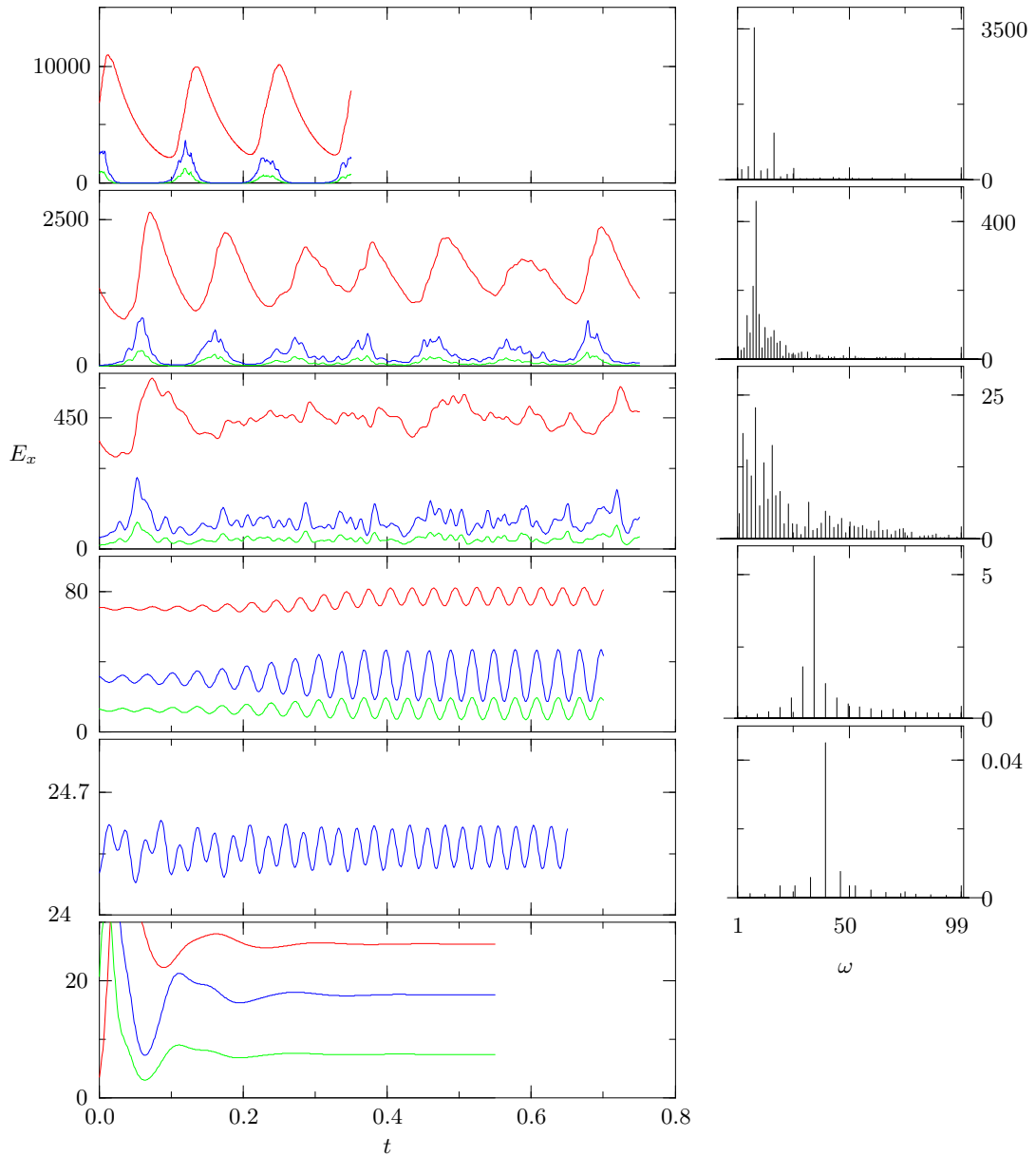
A true time dependence of convection develops in the form of vacillations after a subsequent bifurcation. First the transition to amplitude vacillations occurs in which case just the amplitude of convection varies periodically in time as exhibited in the left plot of figure 6.1. At a somewhat higher Rayleigh number shape vacillations become noticeable which are characterized by periodic changes in the structure of the columns as shown in the right plot of figure 6.1. The outer part of the columns is stretched out, breaks off and decays. The tendency towards breakup is caused by the fact that the local frequency of propagation varies

Fig. 6.5. *Relaxation oscillations of convection for $P = 0.1$, $\tau = 3 \times 10^4$, $R = 5 \times 10^5$. The left six plots show a time sequence (first, then second column) of streamlines $r\partial_\varphi v = const.$ in the equatorial plane. The corresponding six plots to the right show lines of constant $\overline{u_\varphi}$ in the left halves of the circles and of the meridional circulation $r\sin\theta\partial_\theta\overline{v}$ in the right halves. The separation in time is 0.0378 for the first four plots and 0.0126 for the last three plots.*

with distance from the axis according to expression (5.13c) after θ_m has been replaced by the local colatitude θ. The two types of vacillations also differ significantly in their frequencies of oscillation. This is evident from the time records of the energy densities of convection and their Fourier transforms which have been plotted in figure 6.2. The various components of the energy densities are defined by (4.37).
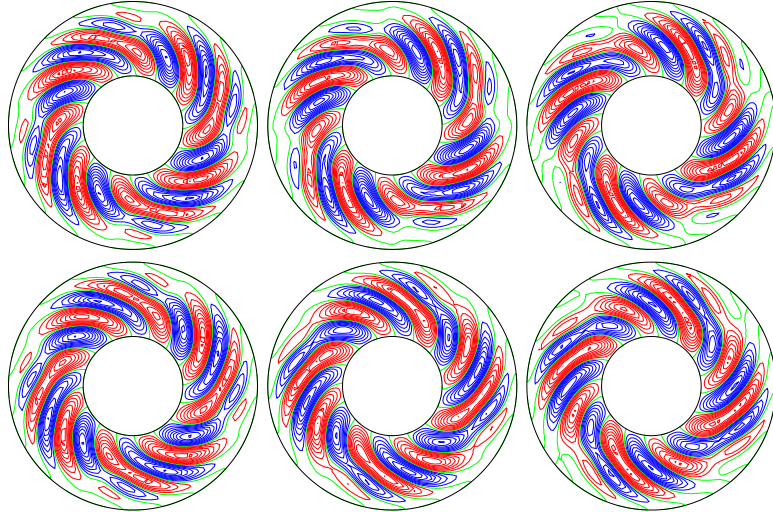
As the Rayleigh number is increased further a fairly sudden transition into a chaotic regime occurs where convection has become strongly inhomogeneous in space and in time. A typical sequence of plots is shown in figure 6.3 which covers about one period of the relaxation cycles seen in the time record for $R = 3.8 \times 10^5$ in figure 6.2. In contrast to the more common relaxation oscillations encountered at higher Rayleigh numbers, see, for example, the time record for $R = 5 \times 10^5$ in figure 6.2, convection does not die off entirely at any time during the cycle. But the interaction between convection and differential rotation appears to be similar. As the amplitude of convection as measured by $\check{E}_p$ and $\check{E}_t$ grows the differential rotation generated by the Reynolds stress grows as well with just a small delay in time. When the differential rotation reaches a critical level the convection columns become disrupted and their amplitude decays. Subsequently the differential rotation decays as well on the time scale of viscous diffusion. It is typical for this type of relaxation cycles that the viscous decay is shorter than the growth time of the differential rotation in contrast to the relaxation oscillations at higher values of the Rayleigh number R. The regime of relaxation oscillations is interrupted once in a while by a return to the more regular regime of shape

Fig. 6.6. *Time series of energy densities of convection for $P = 0.5$, $\tau = 1.5 \times 10^4$ and $R = 3 \times 10^5$, 3.2×10^5, 3.45×10^5, 5×10^5, 7×10^5, 10^6, (from bottom to top). Red, blue and green lines indicate $\overline{E}_t$, $\check{E}_t$, and $\check{E}_p$, respectively. The Fourier transforms of $\overline{E}_t$ versus the frequency ω are plotted in the second column. The critical Rayleigh number for onset is $R_c = 215142$.*

vacillations as shown in the inserted enlargement of the time record for $R = 3.8 \times 10^5$ in figure 6.2. But in contrast to the vacillation of the right plot figure 6.1 the pattern is now strongly modulated. The component with the azimuthal wavenumber $m = 1$ plays a dominant role in this modulation. As can be seen in figure 6.4 the pattern recurs nearly periodically in time in spite of the modulation. Figure 6.4 corresponds to the slightly higher Rayleigh number of 4×10^5 where convection changes intermittently between relaxation cycles and vacillation oscillations.

As the Rayleigh number R is further increased the spatio-temporal structure of convection becomes more irregular as can be seen in the time series for $R = 4.5 \times 10^5$ in figure 6.2. But

Fig. 6.7. *Modulated shape vacillations of convection for $P = 0.5$, $\tau = 1.5 \times 10^4$, $R = 3.2 \times 10^5$. The sequence of plots equidistant in time ($\Delta t = 0.005$), starting at the upper left and continuing clockwise, shows streamlines $r\partial_\varphi v = const.$ in the equatorial plane. Since the modulation period is about 0.025, the last plot resembles the first plot except for a shift in azimuth.*
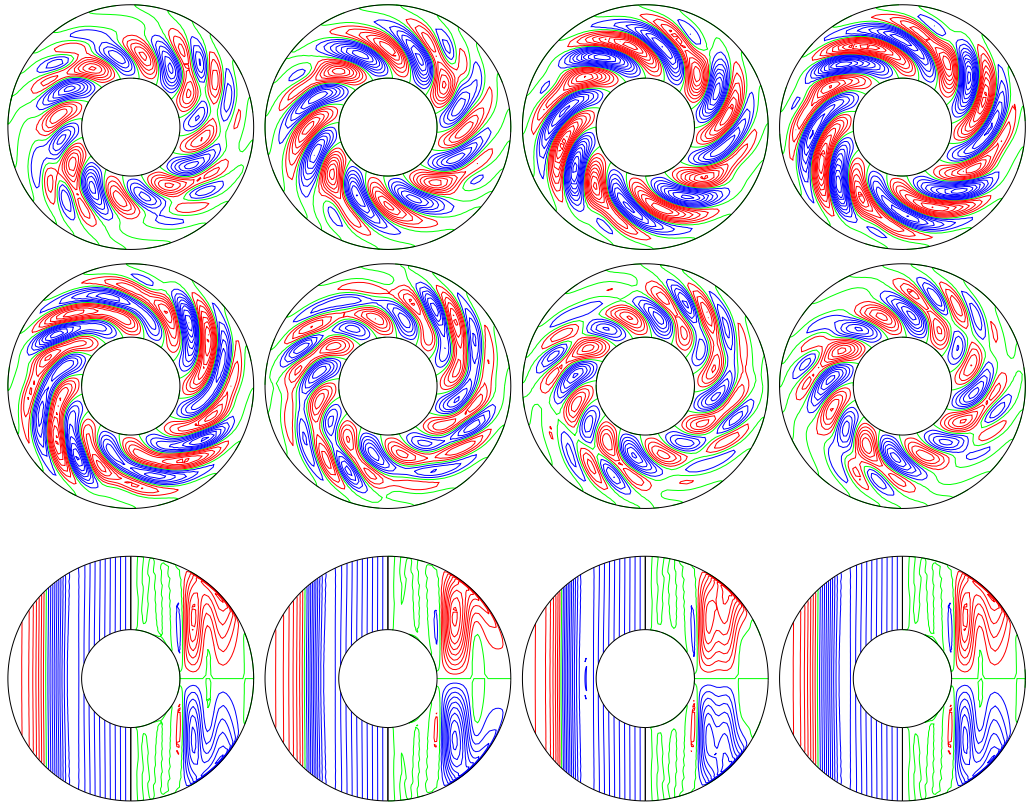
at $R = 5 \times 10^5$ the relaxation oscillations with only intermittent convection become firmly established and they continue to persist up to Rayleigh numbers of the order 10^6. They are basically the same phenomenon as found by Grote & Busse [59] at $P = 1$ and even the period is the same, about 0.1, which corresponds to the viscous decay time of the differential rotation. The only difference that can be noted is the small precursor hump before the burst of convection. In figure 6.5 the third plot shows convection appearing in a fairly regular pattern. Afterwards it decays again as shown in the fourth plot before it erupts in a chaotic fashion as the differential rotation has reached its minimum amplitude. Since this latter part of the cycle occurs on a rather short time scale, smaller intervals between the plots have been used for this part in figure 6.5.

The main difference between convection at $P = 0.1$ and Prandtl numbers of the order unity occurs at the transition between regular and irregular patterns. A typical scenario is shown in figure 6.6. After convection has set in in the form of eight drifting column pairs the usual amplitude vacillations occur as the Rayleigh number is increased. The shape vacillations, however, exhibit a modulation with wavenumber $m = 4$ as shown in figure 6.7. Only every second pair of columns gets stretched until the outer part separates, a little earlier for the cyclonic column than for the anticyclonic one. Then the same process is repeated for the other pairs of columns such that the sequence shown in figure 6.7 exhibits only half a period of the oscillation. In addition, of course, the column pattern drifts in the prograde direction.
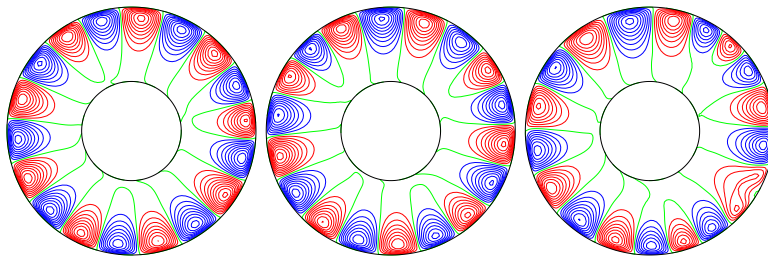
With increasing Rayleigh number the stretching process gets out of phase and an $m = 1$-modulation enters as shown in figure 6.8. The time dependence is still periodic, but has become more complex in that some of the separated outer parts become attached to the preceding column pair. To show this process in more detail some extra plots have been added to the time sequence of figure 6.8. While the amplitude of convection varies considerably throughout the cycle, the differential rotation exhibits only small oscillations as can be seen from the corresponding section of figure 6.6.

By the time when the Rayleigh number R has reached 3.5×10^5 the modulated vacillations have become aperiodic and with increasing Rayleigh number convection becomes more and more chaotic. Regularity reappears only in the form relaxation oscillations as shown in the section for $R = 7 \times 10^5$ of figure 6.6. Remainders of the vacillations can still be seen in this time record. But at $R = 10^6$ the relaxation oscillations have become fully established with convection occurring only in a intermittent fashion.

Convection at small Prandtl numbers. The linear and nonlinear properties of low Prandtl number convection in rotating spherical shells are of special interest for applications to prob-
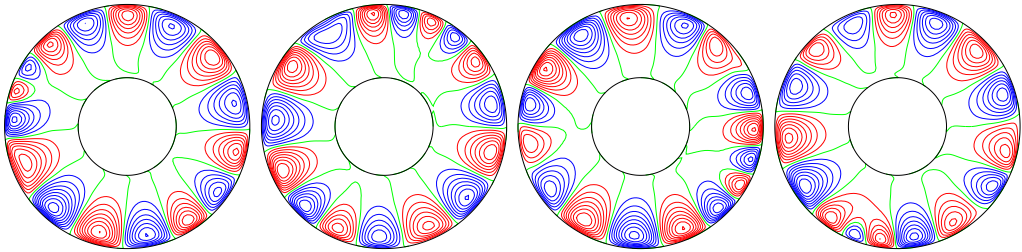
Fig. 6.8. *Modulated shape vacillations of convection for $P = 0.5$, $\tau = 1.5 \times 10^4$, $R = 3.45 \times 10^5$. The first and second rows show equatorial streamlines $r\partial_\varphi v = const.$, the third row shows lines of constant $\overline{u_\varphi}$ in the left halves of the circles and $r\sin\theta\partial_\theta\overline{v} = const.$ in the right halves. The first and the third rows show plots at the times $t = (n-1)\cdot 0.01$ for $n = 1, 2, 3, 4$, the second row shows plots at the intermediate times $t = (n-1)\cdot 0.005$.*
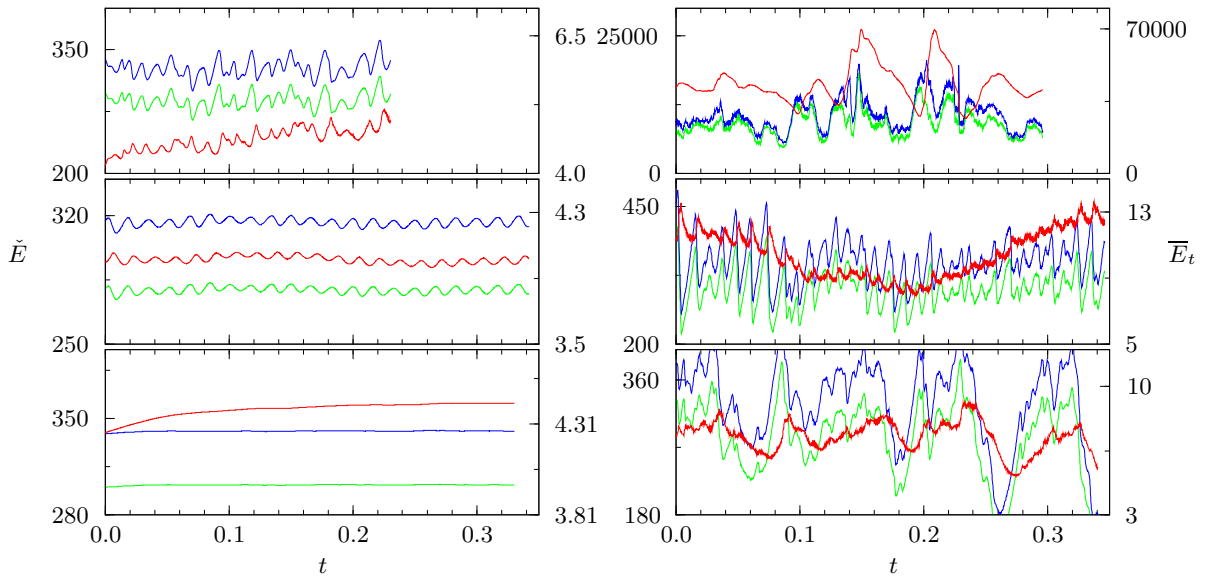
Fig. 6.9. *Equatorial stream-lines $r\partial_\varphi v = const.$ in the case $P = 0.025$, $\tau = 10^5$ and $R = 3.2 \times 10^5$, 3.4×10^5, 3.8×10^5 (from left to right).*

lems of convection in planetary and stellar interiors. Since planetary cores often consist of liquid metal or of metallic hydrogen as in the case of Jupiter and Saturn, their Prandtl numbers are rather low. Moreover, because of high temperatures radiative heat transport is no longer negligible which tends to lower the Prandtl number even more. The latter effect dominates in stellar interiors. On the other hand, turbulence owing to small scale motions which remain unresolved in numerical simulations will tend to equalize all effective diffusivities. But this tendency is not likely to erase entirely the differences in the subgrid scale transports of heat and momentum.

For an analysis of nonlinear properties of equatorially attached convection we focus on the case $P = 0.025$ with $\tau = 10^5$. The critical Rayleigh number for this case is $R_c = 283000$ corresponding to $m = 10$. As the Rayleigh number R is increased beyond the critical value other values of m from 7 to 12 can be realized, but $m = 10$ and lower values are usually
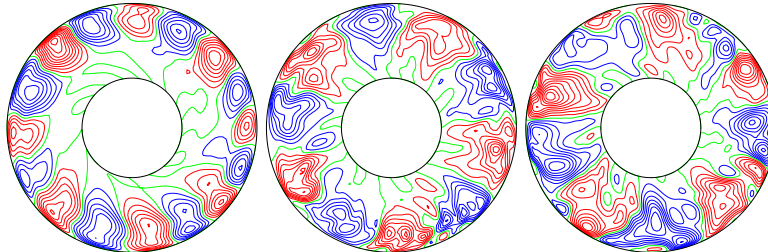
Fig. 6.10. *Equatorial streamlines $r\partial_\varphi v = const.$ in the case $P = 0.025$, $\tau = 10^5$, $R = 4 \times 10^5$. Time increases by $\Delta t = 8 \times 10^{-3}$ from one plot to the next. A fifth plot will be similar to the first one except for a shift in azimuth.*
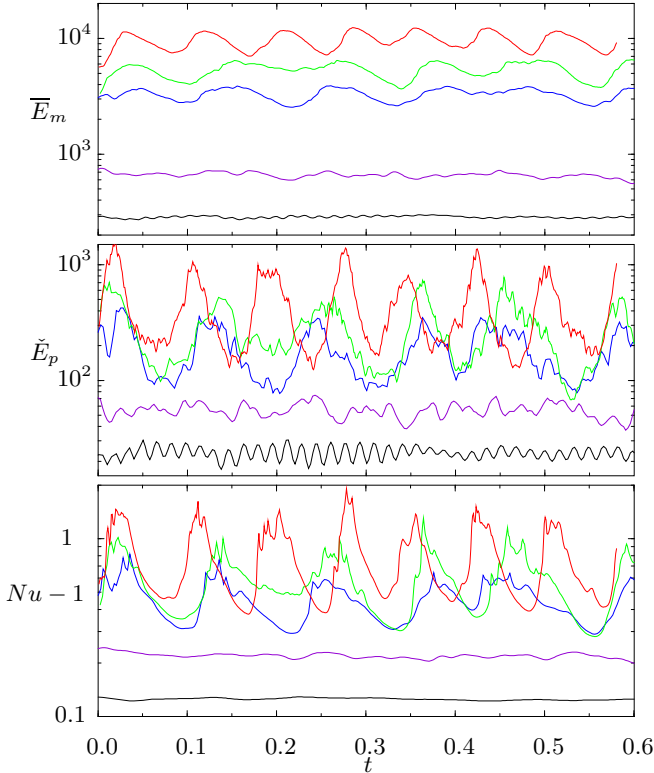
Fig. 6.11. *Time series of energy densities of convection in the case $P = 0.025$, $\tau = 10^5$, for $R = 3.1 \times 10^5$, 3.2×10^5, 3.4×10^5, (from bottom to top, left side) and 3.8×10^5, 4×10^5, 8×10^5 (from bottom to top, right side). The red, blue and green lines correspond to $\overline{E}_t$, $\check{E}_t$, $\check{E}_p$, respectively. $\overline{E}_t$ is measured on the right ordinate and $R_c = 283000$.*

preferred. An asymptotic perfectly periodic solution with $m = 10$ or $m = 9$ can be found only for Rayleigh numbers close to the critical value when computations are started from arbitrary initial conditions. On the other hand, perfect periodic patterns appear to be stable with respect to small disturbances over a more extended regime of supercritical Rayleigh numbers. Distinct transitions like the transition to amplitude vacillations and to structure vacillations do not seem to exist for equatorially attached convection. Instead modulated patterns are typically already observed when R exceeds the critical value by 10% as can be seen in the plots of figure 6.9. These modulations are basically caused by the interaction of two modes with neighboring values of the azimuthal wavenumber m as indicated in figure 6.10. Here the region of small amplitude drifts in the retrograde direction with the difference of the drift rates for $m = 7$ and $m = 8$. The time series of energy densities shown in figure 6.11 indicate that more than two modes usually contribute to the dynamics of the pattern since the time dependence is not periodic as one would expect if only two modes interact. The computations of the time series require a high spatial resolution together with a small time step. The time spans indicated in figure 6.11 are sufficient for reaching a statistically steady
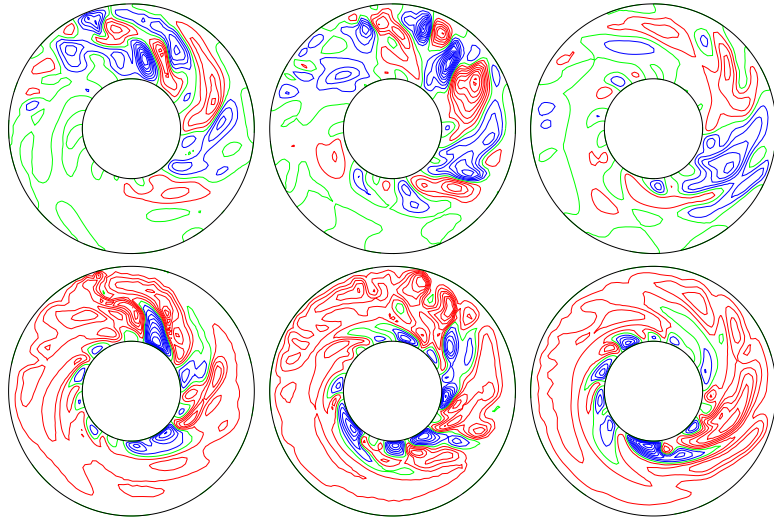
Fig. 6.12. *Equatorial stream-lines $r\partial_\varphi v = const.$ in the case $P = 0.025$, $\tau = 10^5$ and $R = 6 \times 10^5$, 8×10^5, 10^6 (from left to right).*


Fig. 6.13. *Time series of the energy densities of the axisymmetric toroidal component $\overline{E}_t$ (upper plot) and of the non-axisymmetric poloidal component $\check{E}_p$ of motion (middle plot) and of the Nusselt number Nu_i (lower plot) in the case $P = 1$, $\tau = 10^4$, $R_i = 0$ for $R_e = 6 \times 10^5$ (black lines), 8×10^5 (violet lines), 10^6 (blue lines), 1.4×10^6 (green lines) and 1.7×10^6 (red lines).*

state of the fluctuating components of motion since these equilibrate on the fast thermal time scale of the order P^{-1}. Only close to R_c the adjustment process takes longer as can be seen in the case $R = 3.1 \times 10^5$ where a $m = 10$ - pattern approaches its equilibrium state. The pattern corresponding to the other cases of figure 6.11 are the ones shown in figures 6.9, 6.10 and 6.12. The differential rotation represented by $\overline{E}_t$ relaxes on the viscous time scale and thus takes a long time to reach its asymptotic regime in the examples shown in figure 6.11. But the differential rotation is quite weak such that it has a negligible effect on the other components of motion except in the case of the highest Rayleigh number of figure 6.11. Even smaller is the axisymmetric part of the poloidal component of motion which is not shown in the plots of figure 6.11. At higher Rayleigh numbers the equatorially attached eddies spread farther into the interior and in some cases become detached from the equator as can be seen in the plots of figure 6.12. In this way the convection eddies contribute to the heat transport from the inner boundary. But at the same time they acquire the properties of the convection columns which are characteristic for convection at higher Prandtl numbers. Accordingly the differential rotation is steeply increased at $R = 10^6$ and a tendency towards relaxation oscillation can be noticed in the upper right time series of figure 6.11.

Transitions in the case $R_e \neq 0$ and $R_i = 0$. Localized convection. For the purpose of an eventual comparison with experimental observations the computations have been repeated for the case of convection driven only by finite-temperature difference imposed at the boundaries
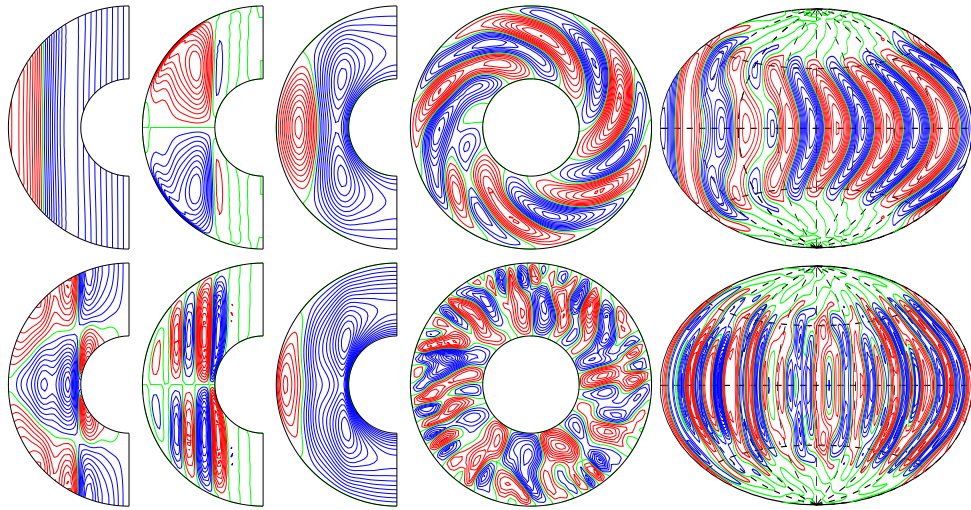
Fig. 6.14. *Localized convection for $P = 1$, $\tau = 10^4$, $R_e = 1.4 \times 10^6$. The streamlines, $r\partial_\varphi v = const.$ (top) and the isotherms, $\Theta = const.$ (bottom), are shown in the equatorial plane for equidistant times (from left to right) with $\Delta t = 0.02$.*

and without distribution of internal heat sources, i.e. for $R_e \neq 0$ and $R_i = 0$. It is found that when R_e is used as a parameter instead of R_i rather similar phenomena are observed. An overview of the time dependence of convection on R_e is provided by figure 6.13 for moderate values of the Prandtl number $P = 1$ and for $\tau = 10^4$. After onset of convection a transition to a quasi-periodic form occurs rather quickly with increasing Rayleigh number. In the absence of internal heating, $R_i = 0$, the temperature gradient near the inner boundary is especially strong and the amplitude of the spiralling convection columns decays more strongly with increasing r than in the case $R_e = 0$. For this reason the disruption of the convection columns and their subsequent reconnection occurs more rapidly after onset. At $R_e = 8 \times 10^5$ convection flow has become chaotic as can be seen from the energy of the fluctuating poloidal component of motion. We take the opportunity to demonstrate the appearance of localized convection, another coherent structure of turbulent convection which was first reported by Grote & Busse [59] in the case of $R_e = 0$, $R_i \neq 0$. Localized convection precedes the state of relaxation oscillations at slightly lower values of R and is characterized by intermittency in space but unlike the relaxation oscillations not in time. In the canonical cases reported in [59] (figure 3 of [59]) the differential rotation becomes so strong that its shearing action inhibits convection in most parts of the spherical shell. Only in a certain small region of longitude convection is strong enough to overcome the shearing action of differential rotation. In the quiet zone the basic temperature profile recovers towards purely conducting state and thus enhances the buoyancy in the interior of the shell. This helps to sustain the localized convection as the temperature field is recirculated into the active zone by the differential rotation. Localized convection is found in the externally heated case, $R_i = 0$, as shown in figure 6.14 for $R_e = 1.4 \times 10^6$, although this feature does not seem to develop as dramatically as in the case exhibited in [59]. Above $R_e = 1.4 \times 10^6$ the relaxation oscillation begins to set in and becomes fully developed as the highest Rayleigh number $R_e = 1.7 \times 10^6$ of figure 6.13 is reached. The amplitude of the oscillation of the differential rotation is not quite as large as in the case internally heated case $R_e = 0$ and the period is slightly shorter. But the phenomenon itself does not depend on the detailed form of the basic temperature distribution.

6.2.2 High Prandtl number convection

Planetary cores often consist of liquid metals (the Earth) or metallic hydrogen (Jupiter, Saturn) and radiative heat transport is huge in stellar interiors and thus the values of their Prandtl numbers are rather small. However, convection at high values of the Prandtl num-

Fig. 6.15. *Convection in rotating spherical fluid shells for $\tau = 5 \times 10^3$ and $R = 2.7 \times R_c$ in the cases $P = 0.5$, $R = 1.5 \times 10^5$ (upper row) and $P = 20$, $R = 4 \times 10^5$ (lower row). Lines of constant mean azimuthal velocity $\overline{u_\varphi}$, streamlines of the meridional circulation and isotherms of $\overline{\Theta}$ are shown in first three columns. The plots in the fourth column show streamlines, $r\partial_\varphi v = const.$ in the equatorial plane. The oval plots indicate lines of constant u_r on the spherical surface $r = r_i + 0.5$. For values of R_c see table 6.1.*
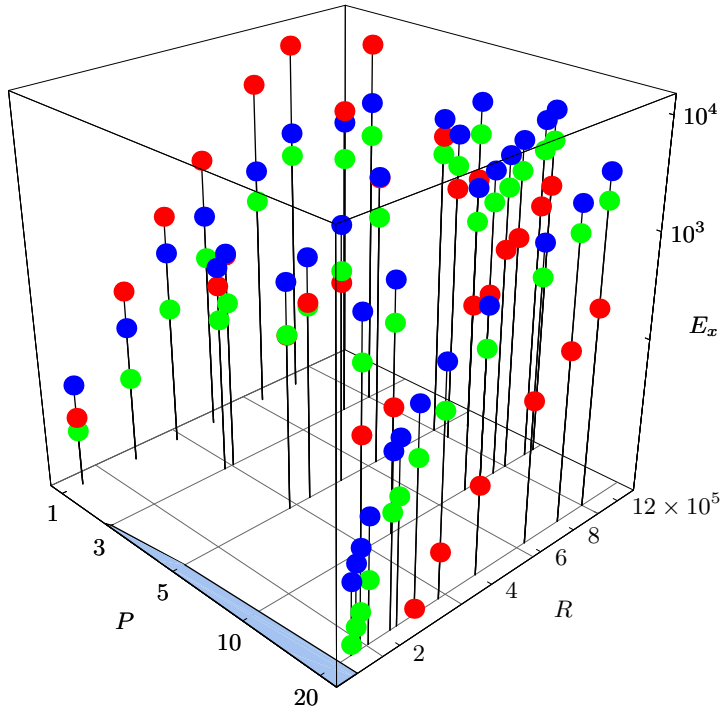
ber should not be left without consideration. First, the strong turbulence exhibited in these celestial bodies will tend to equalize the effective diffusivities which has lead to the common belief that the value of the Prandtl number should be of order unity [40, 62, 80, 82, 59]. But even values of P much higher than unity cannot be dismissed in view of the fact that concentration gradients are probably a very significant source of buoyancy [25]. The double-diffusive convection can, of course, be studied by the introduction of the equation for the concentration (3.65d) in the model. However, it is possible to mimic the effects of composi-

Table 6.1. *Values of the critical Rayleigh number R_c and wavenumber m of the convection cases presented in the chapter.*

P	$\tau \times 10^{-4}$	R_c	m
0.025	5.0	87000.0	7
0.025	10.0	283000.0	10
0.1	0.5	18058.9	4
0.1	1.0	55685.5	7
0.1	1.5	88695.3	7
0.1	3.0	235000.0	10
0.1	5.0	438237.0	10
0.1	10.0	1050000.0	11
0.5	0.5	55631.8	8
0.5	1.0	128940.0	9
0.5	1.5	215142.0	10
1.0	0.5	80296.3	8
1.0	1.0	190000.0	10
3.0	0.5	119983.0	9
5.0	0.5	131776.0	10
10.0	0.5	141308.0	11
20.0	0.5	146119.0	12

Table 6.2. *Values of the Rayleigh number R_{pc} at which the amplitude of the radial velocity u_r at $r = (r_i + r_o)/2$ of the polar convection has reached at least 10%, 5% of the amplitude of the radial velocity of convection outside the tangent cylinder.*

| P	$\tau \times 10^{-4}$	$R_{pc}^{10\%}$	$R_{pc}^{5\%}$
		$\times 10^{-4}$	
0.025	10.0	33	32
0.1	3.0	60	50
0.5	1.0	42	40
0.5	1.5	90	85
1.0	0.5	50	40
1.0	1.0	90	80
20.0	0.5	70	60

PSfrag replacements

Fig. 6.16. *Dependences of energy densities $\overline{E}_t$ (red), $\breve{E}_t$ (blue) and $\breve{E}_p$ (green) on R and P in the case of $\tau = 5 \times 10^3$. The energy densities have been multiplied by P^2 and thus are measured in terms of the thermal scaling. The mean poloidal energy density $\overline{E}_p$ is omitted since its value is about 100 times smaller than these of the other energy densities. The shaded region is below the onset of convection.*
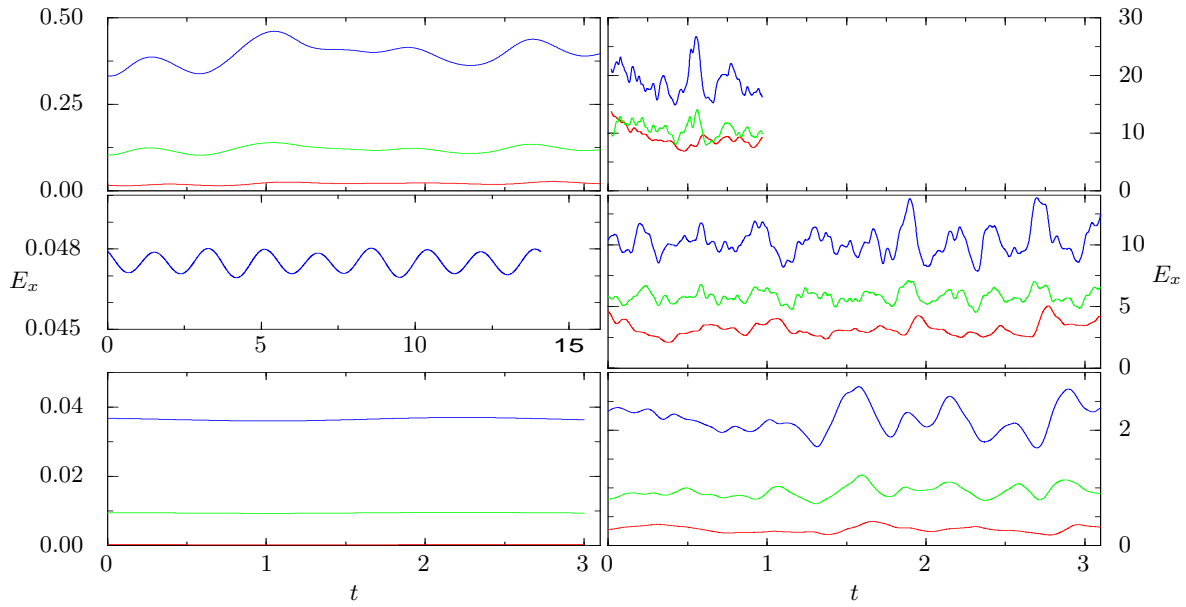
tional convection by simply using higher values of P. This approach offers, perhaps, a better insight since the model is kept as simple as possible and comparisons with earlier linear and non-linear results and other regimes can readily be made.

Characteristic features. Having provided an extensive discussion of the spatio-temporal behavior of finite-amplitude convection at small and moderate values of the Prandtl number, the most natural way to obtain an idea of the flows at higher values of the Prandtl number is to compare the two regimes. The differences between convection at small and moderate values and convection at large values of the Prandtl number are demonstrated in figure 6.15 where the typical flow structures for $P = 0.5$ and $P = 20$ are compared at fixed values of $\tau = 5 \times 10^3$ and $R = 2.7 \times R_c$. The values of the critical Rayleigh number are given in table 6.1. Two main differences between the two regimes may be noticed. The first one is the difference in the profiles of the differential rotation $\overline{u_\varphi}$. While the mean zonal flow takes nearly constant values as a function of the distance from the axis of rotation in the case $P = 0.5$, a strong deviation from such a profile is observed in the high Prandtl number case $P = 20$. The change in the profile of the differential rotation as $P = \nu/\kappa$ increases from 0.5 to 20 at constant viscosity ν is due to the decrease of the value of the thermal diffusivity κ. The approximate form of the differential rotation profile $\overline{u_\varphi}$ may be derived from the leading balance of forces in the momentum equation (3.12). At small values of the Prandtl number and high rotation rate the Coriolis force is balanced only by the pressure gradient and the Taylor-Proudman theorem (5.12) holds, which leads to the geostrophic relationship

$$\hat{\boldsymbol{k}} \cdot \nabla \overline{u_\varphi} = 0, \tag{6.1}$$
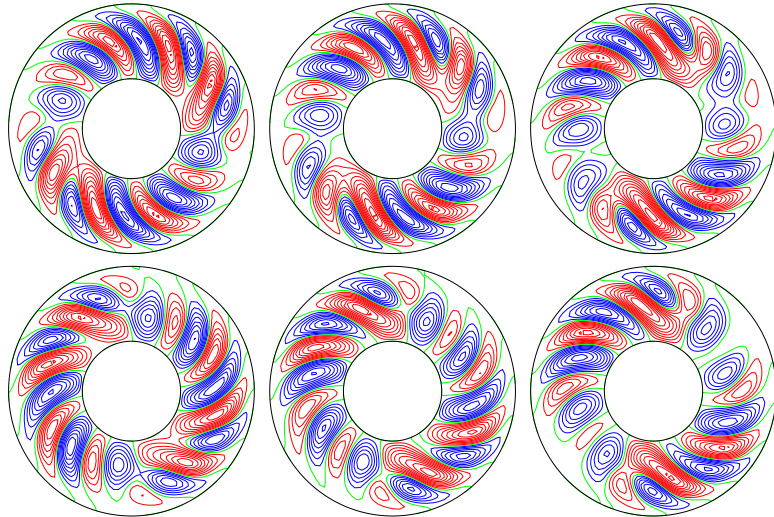
where $\hat{\boldsymbol{k}}$ is the unit vector in the direction of the axis of rotation. On the other hand, due to the small diffusion of heat at high values of the Prandtl number the buoyancy force $\Theta \boldsymbol{r}$ becomes significant and enters the leading balance of the momentum equation. Taking the azimuthal average of the φ-component of its curl yields the thermal wind relationship

$$\tau \hat{\boldsymbol{k}} \cdot \nabla \overline{u_\varphi} = \partial_\theta \overline{\Theta} \tag{6.2}$$
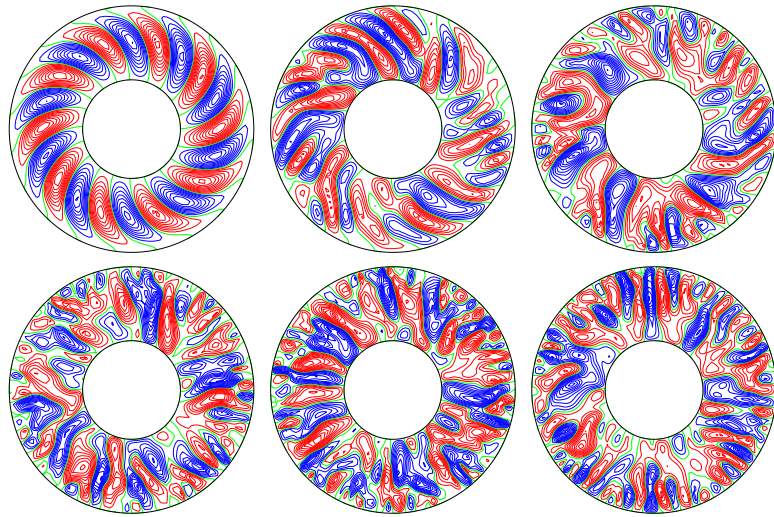
Fig. 6.17. *Time series of energy densities of convection in the case $P = 20$, $\tau = 5 \times 10^3$, for $R = 1.6 \times 10^5$, 1.65×10^5, 2.5×10^5, (from bottom to top, left side) and 4×10^5, 10^6, 1.5×10^6 (from bottom to top, right side). The red, blue and green lines correspond to $\overline{E}_t$ (multiplied by a factor 5), $\check{E}_t$, $\check{E}_p$, respectively.*

in the limit of large values of the Prandtl number P. The right-hand side of (6.2) will be non-zero since $\overline{\Theta}$ deviates from a spherical profile as long as the influence of rotation is significant. Indeed, a comparison of $\overline{u_\varphi}$ and $\overline{\Theta}$ in the case $P = 20$ confirms these arguments. Perhaps more important than the observed change in the profiles of the mean zonal flow with increasing Prandtl number is the fact that simultaneously the differential rotation decreases significantly in amplitude. This decrease cannot, of course, be inferred from the contour plots shown in figure 6.15. It is, however, a typical feature which persists throughout the entire high Prandtl number region as may be seen in figure 6.16, which in addition provides an overview of the simulations of non-magnetic convection performed for $P > 1$ and $\tau = 5 \times 10^3$ and shows the trends in the variations of the time averaged densities of the various energy components versus the Prandtl number and the Rayleigh number. Another trend evident in figure 6.16 is that above some value of P of the order 10 the energy densities become less and less dependent on the Prandtl number P when the thermal time scale instead of the viscous one is used. These observations will be revisited in more detail in section 6.3. The change in the profile of the differential rotation from geostrophic to thermal wind type as well as the decrease in the amplitude lead to a weaker influence of the mean zonal flow on the convection columns. In particular, they loose their spiralling nature and become more and more radially oriented as the Prandtl number increases in accordance with the linear results of chapter 5. An impression of this effect may be gained from a comparison of the plots of the streamlines $r\partial_\varphi v = \text{const.}$ in the equatorial plane for the cases $P = 0.5$ and $P = 20$ shown in figure 6.15. But since the mean zonal flow is amplified through a feedback mechanism when the convection columns are tilted, as was discussed in section 5.4, the decreasing spirality of the columns in turn leads to a weaker generation of differential rotation. The thermal wind profile, the diminishing amplitude of $\overline{u_\varphi}$ and of the tilt of the convection columns with the increase of the Prandtl number P are the basic characteristics of the high Prandtl number convection and affect significantly the temporal and spatial structure of the flow.
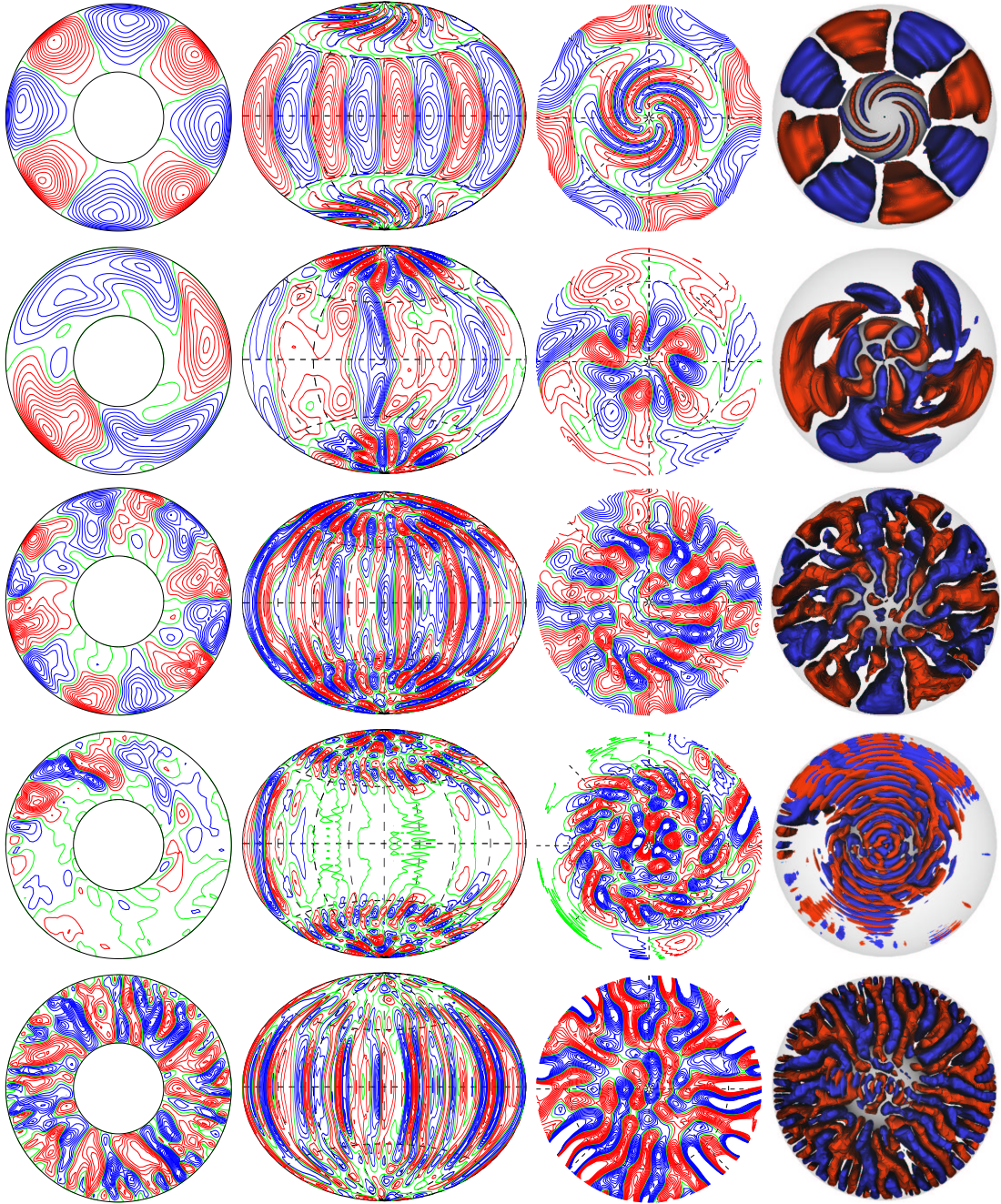
Fig. 6.18. *Equatorial stream-lines $r\partial_\varphi v = const.$ in the case $P = 20$, $\tau = 5 \times 10^3$, $R = 1.75 \times 10^5$. Time increases by $\Delta t = 0.32$ from one plot to the next. The plots follow in a clockwise sense, the lower left one is similar to the upper left one except for a shift in azimuth.*


Fig. 6.19. *Equatorial stream-lines $r\partial_\varphi v = const.$ in the case $P = 20$, $\tau = 5 \times 10^3$ and $R = 1.6 \times 10^5, 2.5 \times 10^5, 4 \times 10^5$ (from left to right, upper row) and $R = 8 \times 10^5, 10^6, 1.5 \times 10^6$ (from left to right, lower row).*

Spatio-temporal structures and transitions. For a brief discussion of the evolution of convection towards its chaotic states we focus on a sequence of cases with $P = 20$, $\tau = 5 \times 10^3$ and with increasing Rayleigh number as shown in figure 6.17. The transition from the state of steadily drifting rolls to a true time dependence has been investigated by Zhang [119] in the case of infinite Prandtl number, who identified two possible mechanisms – amplitude vacillations and shape modulations. Both of these mechanisms are not unique to the high Prandtl number convection and we already demonstrated some of their manifestations at small and moderate values of P. The amplitude vacillations and shape modulations may be understood on the basis of the linear analysis. At any set of parameter values various competing modes can be identified. The critical Rayleigh numbers of those modes change as functions of the parameters and it is possible to locate a Prandtl number or a Coriolis number at which two modes have the same critical Rayleigh number. The closer P or τ are to such a point, the stronger the interaction between the competing modes would be. As the Rayleigh number is increased above the critical R at which a second competing mode will become excited, the time dependence of the flow will be determined by the interaction between the two excited modes. A weak interaction introduces a new frequency into the system leading to a time dependent convection in which only the amplitude of the primary

Fig. 6.20. *Polar convection in the cases,* $\bullet P = 0.025$, $\tau = 5 \times 10^4$, $R = 2 \times 10^5$; $\bullet P = 0.1$, $\tau = 10^4$, $R = 1.9 \times 10^5$; $\bullet P = 0.1$, $\tau = 3 \times 10^4$, $R = 7.5 \times 10^5$; $\bullet P = 1$, $\tau = 10^4$, $R = 1.4 \times 10^6$ *and* $\bullet P = 20$, $\tau = 5 \times 10^3$, $R = 10^6$ *(from top to bottom). The plots in the first column show streamlines* $r\partial_\varphi v = const.$ *in the equatorial plane. The plots in the second, third and fourth columns exhibit lines of constant* u_r *at the surface* $r = r_i + 0.5$, *viewed from the front, from the North pole and in three dimensions, respectively.*
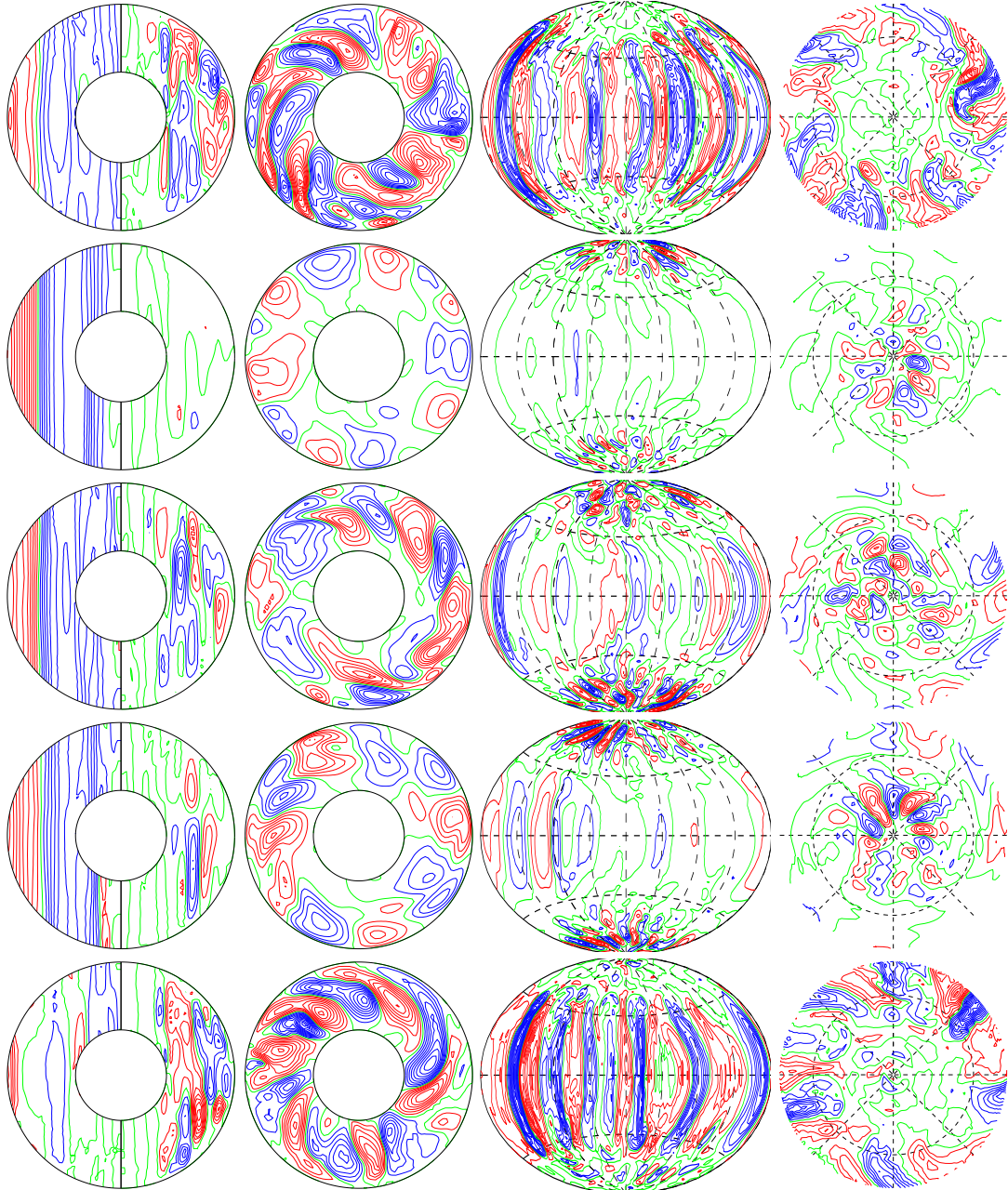
mode vacillates without a substantial spatial modulation. A stronger interaction may result in both vacillations in the amplitude and modulations in the shape of the primary pattern. The transition to time dependence at the chosen parameter values $P = 20$, $\tau = 5 \times 10^3$ occurs through shape modulations as may be seen from the plots of the streamlines $r\partial_\varphi v =$

const. in figure 6.18. The shape modulation of the basic $m = 10$ pattern is caused obviously by a competition with a pattern with similar value of the wavenumber. The amplitude of two pairs of rolls, situated diametrically across the shell, gradually increase. The tilt of the leading one increases while that of the second one decreases until they touch and connect in their lower parts near the inner spherical surface assuming the form of a pair of scissors. Soon after that the second roll gets weaker and decays while the leading one attaches to the roll in front of it. This mechanism of interaction results in a large scale $m = 2$ pattern which more easily reaches throughout the spherical shell and leads to an increased transport of heat. This mechanism is a very characteristic and persistent feature of the dynamics of high Prandtl number convection and continues to operate far into the chaotic regime even to Rayleigh numbers as high as $15 \times R_c$ as is evident from the snapshots in figure 6.19. The interaction between modes and the connection of rolls in scissors-like form can be observed in various stages and variations in all plots of the figure.

The mean toroidal energy remains about three times smaller than the fluctuating energy densities in figure 6.17. Since the differential rotation is much weaker than that at small and moderate values of the Prandtl number P coherent structures such as localized convection and relaxation oscillations have never been observed for $P \geq 3$.

6.2.3 Polar convection

Structure. Another phenomenon, which does not occur at onset of convection in rotating spherical shells, but always sets in as the Rayleigh number is increased to sufficiently large values, is the convection in the regions situated below and above the inner spherical surface. At low values of the Rayleigh number close to the critical the polar regions are nearly stagnant while convection in the equatorial region has already set in. The reason for this is that the axis of rotation and the vector of gravity are parallel in the polar regions. Thus, while hot rising plumes would normally move in a direction opposite to the vector of gravity, they are suppressed from doing so by the Coriolis force which suppresses motions parallel to the axis of rotation. However, as the Rayleigh number is increased polar convection also sets in. Its onset does not occur at a particular critical value of R, since the polar regions are not perfectly isolated from the rest of the shell and are exposed to non-linear disturbances coming from the convection in the equatorial region. Approximate values of R for which the polar convection becomes significant and the amplitude of its radial velocity u_r reaches at least a few percent of amplitude of the radial velocity of the equatorial convection are given in table 6.2. According to the thin shell analysis of [28] the preferred mode of polar convection should be in the form of rolls oriented in the radial direction outward from the poles. Some evidence of this may be observed in the plots of figure 6.20. But in general the polar convection almost never exhibits a regular pattern. The reason for this is that it interacts with the convection in the equatorial regions which, by the time the polar convection has grown to significant amplitudes, is already strongly chaotic. A remarkable exception is represented by the first case shown in figure 6.20 for $P = 0.025$ and $\tau = 5 \times 10^4$. In the small Prandtl number region the polar convection sets in shortly after the equatorial convection, which is still rather regular. In addition, at these values of the Prandtl number P the convection outside the tangent cylinder is of inertial type and is strongly attached to the outer surface and thus has little effect on the polar regions. The third and the fourth case in figure 6.20 show that the polar convection in some cases might develop in the form of concentric rings around the pole. The last case presented in the figure clearly demonstrate that equatorial convection structures may influence each other even when they are situated at the opposite sides of the inner core, since they interact and reconnect with the help of the flow over the polar regions.

Fig. 6.21. *Time sequence of equidistant plots (top to bottom) with $\Delta t = 0.09$ (between last two rows $\Delta t = 0.135$) for $P = 0.1$, $\tau = 3 \times 10^4$, $R = 8.5 \times 10^5$, $Pm = 1$. The left half of the first circle in each row shows $\overline{u}_\varphi = const.$ while the right half displays meridional streamlines, $r \sin \theta \partial_\theta v = const.$ The second column shows equatorial streamlines $r \partial_\varphi v = const.$ The second and third columns exhibit lines of constant u_r at the surface $r = r_i + 0.5$, viewed from the front and from the North pole, respectively.*

Dynamics. A noteworthy feature of the dynamics of polar convection is that it is nearly unaffected by the differential rotation which is rather weak near the poles, as may be seen in figures 6.26, 6.28(a) and 6.31(a) where time-averaged profiles of $\langle \overline{u}_\varphi \rangle_t$ are presented as well as in figure 6.21 where a period of relaxation oscillations at $P = 0.1$ and $\tau = 3 \times 10^4$ is shown. While the familiar bursts and decays of convection outside the tangent cylinder are

clearly observed, the polar convection preserves approximately the same amplitude. Polar convection remains invisible compared to the equatorial one in the first and the last plot of figure 6.21 because of its relatively smaller amplitude at these instants. In this way even when convection decays outside the tangent cylinder during the relaxation oscillation cycle heat is still transported near the poles. Figure 6.21 demonstrates another interesting feature, namely the interplay between the columnar and inertial modes. The differential rotation provides another mechanism for transition between the two types of convection. The inertial convection does not generate much differential rotation since it is not spiralling. On the other hand it cannot be destroyed by the mean zonal flow because its cells are thick and closely attached to the outer wall. However, when the differential rotation grows it extends the inertial convection cells and transforms them into spiralling convection columns. The spiralling columns are sheared off once the differential rotation grows sufficiently and are replaced again by the more robust inertial convection structures.
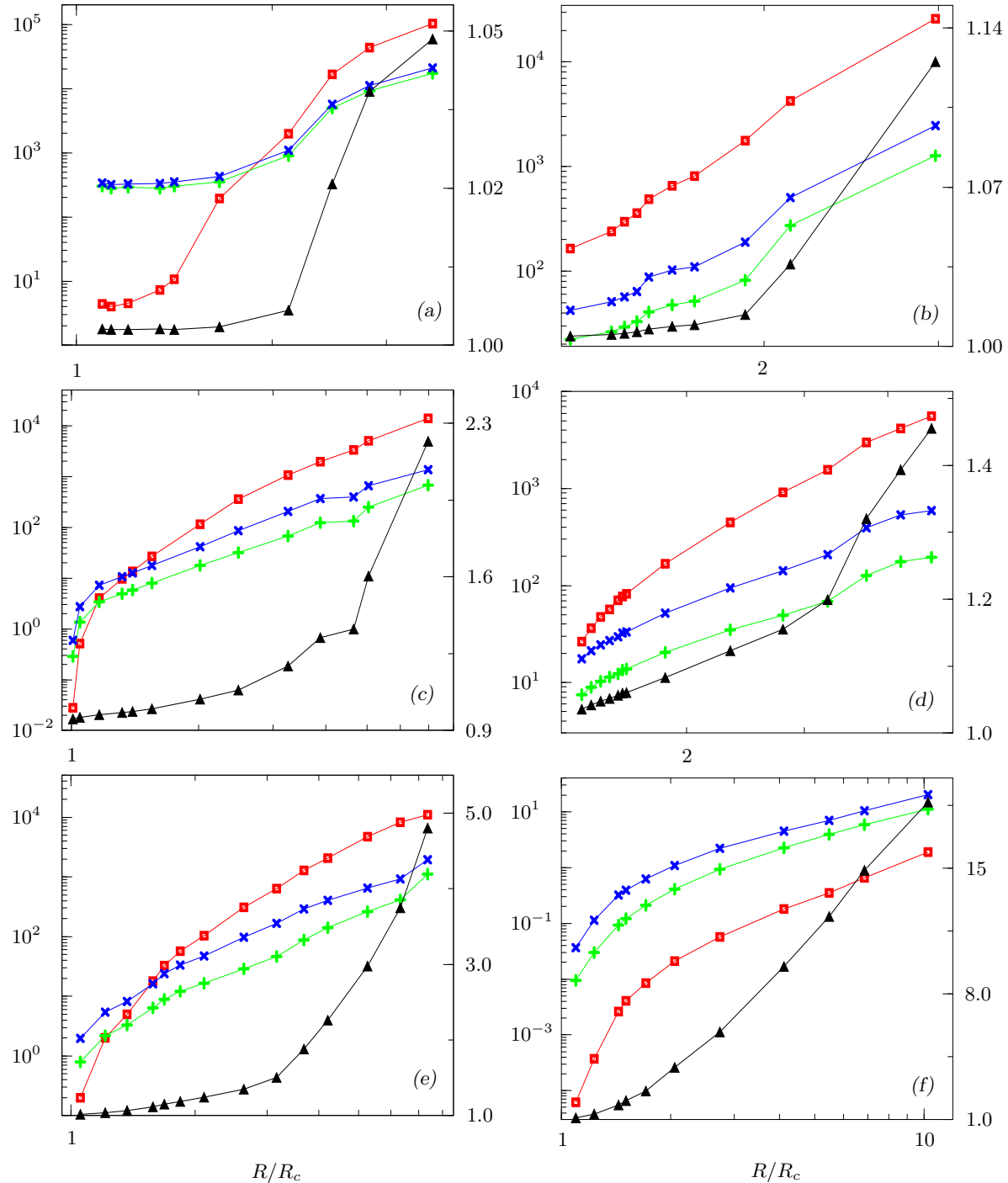
6.3 Averaged properties of finite-amplitude convection. Parameter dependences

The preceding sections of the chapter have focused the attention on various spatial and temporal patterns of convection throughout the parameter space. The hope has been to demonstrate, that although at geophysically interesting parameter values convection is chaotic, many mechanisms and structures of its dynamics can be identified and understood. Although some of these features are quite robust and occur frequently in the reported examples, it must be clearly realized that they constitute only a small subset of all phenomena which might take place in a non-linear turbulent flow. Following too closely the local dynamics of the flow we run into the danger of overlooking the general trends and parameter dependences. For these reasons, we now consider some global and averaged properties of finite-amplitude convection. Of particular interest are the values of the time-averaged energy densities, the profiles of the differential rotation and the heat transport. Other quantities such as the helicity, viscous dissipation, energy spectra can also be explored.

We continue to keep fixed the radius ratio of the shell, the velocity and temperature boundary conditions and the basic reference state. Thus three basic parameters are in control of the flow, namely the Rayleigh, Prandtl and Coriolis numbers. Even now the computational effort required for a complete exploration of the space spanned by these parameters is substantial. For every triple of parameter values (R, P, τ) the evolution of the system is followed by integration of equations (3.65a) in time. The computation is interrupted only when approximate equilibration of the system is achieved where the time series of the kinetic energy densities and other observable quantities appear to remain statistically stationary and meaningful averages may be determined. This procedure may require several hundred to million time steps and it is obvious that reconstruction of hypersurfaces and determining precisely transitions points, as was done in the linear case, is impossible. Therefore, we have tried to isolate the effects of the variation of a given parameter by keeping the values of the rest fixed.
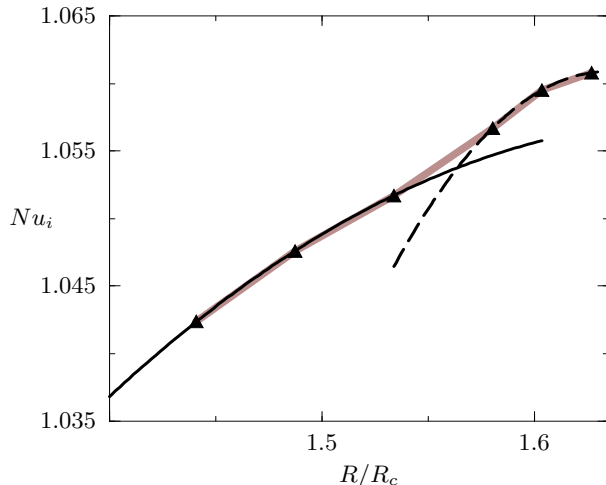
6.3.1 Dependence on the Rayleigh number

In the linear case the critical Rayleigh number is determined as a function of the Prandtl and Coriolis numbers. In the non-linear case R is a new independent parameter which characterizes finite-amplitude convection. Therefore, more effort has been devoted to the investigation of the R-dependence. We analyze six different sequences of cases for which P and τ are kept fixed while the Rayleigh number R is gradually varied as shown in figure 6.22 and table 6.1.

Fig. 6.22. *Time-averaged energy densities $\overline{E}_t$ (red squares), $\check{E}_p$ (green plus-signs), $\check{E}_t$ (blue crosses) and Nusselt number Nu_i (filled triangles, right ordinates) as functions of R/R_c for (a) $P = 0.025$, $\tau = 10^5$, (b) $P = 0.1$, $\tau = 3 \times 10^4$, (c) $P = 0.5$, $\tau = 10^4$, (d) $P = 0.5$, $\tau = 1.5 \times 10^4$, (e) $P = 1$, $\tau = 10^4$, and (f) $P = 20$, $\tau = 5 \times 10^3$. The values of R_c for these cases are listed in table 6.1. The mean poloidal energy component $\overline{E}_p$ has been omitted since it is by factor 10^3–10^2 smaller than the other components. For an additional set of curves see figure 6.16.*
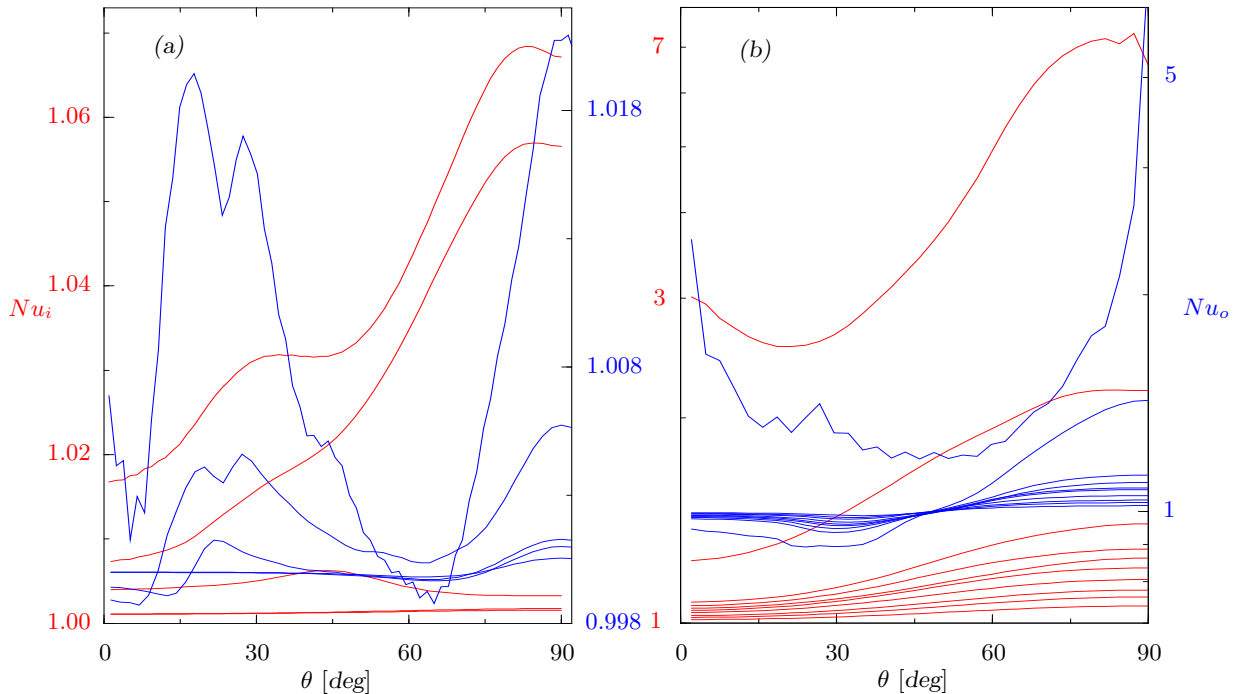
Several other sequences have already been presented in figure 6.16 where the effects of the simultaneous variation of the Rayleigh number and the Prandtl number may be observed.

Fig. 6.23. *The Nusselt number Nu_i versus the Rayleigh number R demonstrating the transition between the states of amplitude (solid line) and shape vacillations (dashed line) in the case $P = 0.5$, $\tau = 1.5 \times 10^4$, $R_c = 215142$. The thick brown line is a segment of the corresponding curve shown in figure 6.22(d), illustrating the lack of points in that figure.*
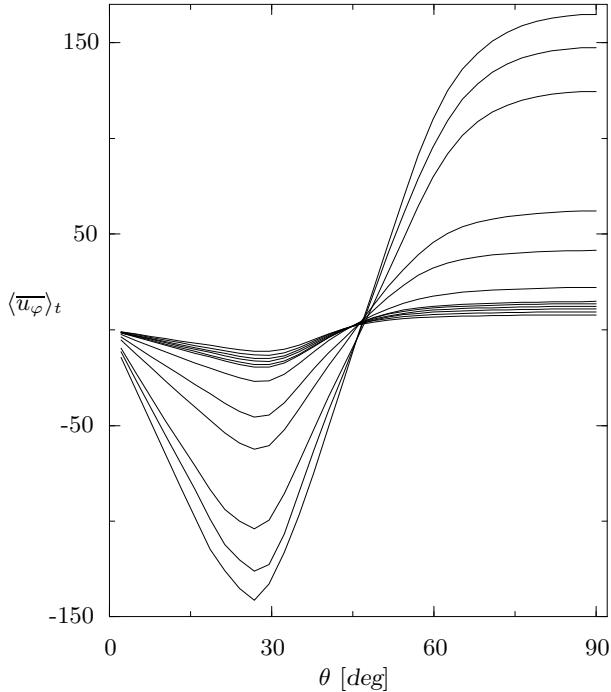
Global properties. In figure 6.22 the time-averaged values of the kinetic energy densities and the heat transport at the inner spherical boundary have been plotted as functions of the Rayleigh number. The mean toroidal energy $\overline{E}_t$ is the energy contained in the differential rotation. In the cases *(a)* to *(e)* in figure 6.22, which are characterized by small and moderate Prandtl numbers, its time-averaged value is initially lower than that of the other components but exhibit the fastest rate of growth with R. $\overline{E}_t$ exceeds the other energy components at about values of R for which the time-periodic convection is replaced by chaotic states. An exception is case *(b)* for $P = 0.1$ and $\tau = 3 \times 10^4$ which is close to the boundary between inertial and columnar convection where the spiralling of the columns is rather strong and differential rotation is more easily generated so that even the time-periodic states of convection exhibit a large mean zonal flow. Only when the value of the Prandtl number is increased above unity as in case *(f)* of figure 6.22 the differential rotation becomes less significant than the other components. The mean poloidal energy $\overline{E}_p$ is the energy contained in the mean meridional circulation. Since the effects of rotation strongly suppress the fluid motion in the direction of the axis of rotation, this component is orders of magnitude smaller than the other components in all cases in figure 6.22 and has been omitted. The fluctuating toroidal and poloidal energies appear to have very similar dependence on R in the sense that they have almost the same shape in all six cases. It may be observed that in the cases *(b)* to *(f)*, which are dominated by columnar convection, the approximate relation $\langle \check{E}_p \rangle_t = 0.4 \langle \check{E}_t \rangle_t$ is almost always satisfied regardless of the value of R. In case *(a)* of inertial convection the time-average of the fluctuating poloidal energy is about 85% of the value of the fluctuating toroidal component. Since the toroidal fluid motions do not have a radial component, it is the poloidal motions which are directly associated with the transport of heat between the boundaries. However, the toroidal motions may also be indirectly related to the heat transport, since they are capable of moving the fluid particles in azimuthal direction into or away from regions of vigorous poloidal motions. For these reasons, a good correlation between the fluctuating energy components and the Nusselt number Nu_i may be observed.

It would be of interest to extract some analytical relationships from the numerical data presented in figure 6.22. For instance, estimation of asymptotic laws for the energy components and the Nusselt number as R goes to large values might be attempted. However, such attempts would hardly succeed for a number of reasons. The values of the Rayleigh number presented in the plots are not asymptotically high. For example, we are uncertain whether the state of relaxation oscillations is the ultimate state of convection as R increases. It is more probable that at values of the Rayleigh number higher than those of the relaxation oscillations these coherent structures cease to exist and a small-scale turbulent state is reached.
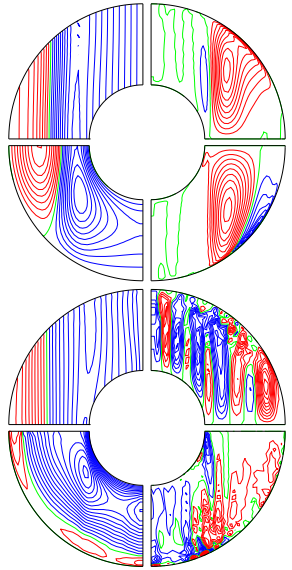
Fig. 6.24. *The time- and azimuthally-averaged local Nusselt numbers at the inner spherical boundary Nu_i (red lines, left ordinate) and at the outer spherical boundary Nu_o (blue lines, right ordinate) as functions of the colatitude θ for (a) $P = 0.025$, $\tau = 10^5$ and $R = 3.8 \times 10^5$, 4×10^5, 6×10^5, 8×10^5, 10^6 (from bottom to top at $45°$) and (b) $P = 1$, $\tau = 10^4$ and $R = 2.3 \times 10^5$, 2.6×10^5, 2.8×10^5, 3×10^5, 3.3×10^5, 3.4×10^5, 3.5×10^5, 4×10^5, 7×10^5, 1.4×10^6 (from bottom to top at $90°$).*

This expectation is justified by the results published by Christensen [39], who reports reaching Rayleigh numbers as high as $134 \times R_c$ for $P = 1$ and $\tau = 6.7 \times 10^4$ and by our high Prandtl number convection cases, in which the differential rotation never grows enough to lead to coherent structures. On the other hand, in the region of intermittent values of R the features of the curves shown in figure 6.22 are better understood on the basis of qualitative arguments. To illustrate this point we present figure 6.23, which shows how the transition between the states of amplitude and shape vacillations for $P = 0.5$ and $\tau = 1.5 \times 10^4$ is reflected in the corresponding Nu_i curve. Any convection regime, e.g. the amplitude vacillations, has a limited ability to transfer heat. With the increase of the Rayleigh number, the Nusselt number which this regime can provide, saturates to its maximum and a point occurs where the heat transport provided by the flow cannot match the energy input. If a competing flow with a higher rate of heat transfer exists, e.g. the shape vacillations in figure 6.23, it becomes preferred over the initial flow. The global Nu_i curve has a kink at the value of R where the transition occurs. Similar arguments hold for the explanation of the structure of the curves of the energy densities and the Nusselt number presented in figure 6.22. However, it is impossible to construct figures similar to 6.23 for most of the higher transitions. Apart from the computational restrictions to obtain a large number of points dense enough to identify the transition point, a distinct possibility exists that such a transition point is not sharply defined since the higher transitions involve nonlinear interactions between many modes and the system may even have several basins of attraction for a fixed set of parameter values. An example of such a case which shows a long intermittent periods of regular and chaotic convection was already presented in figure 6.2 for $P = 0.1$, $\tau = 3 \times 10^4$ and $R = 3.8 \times 10^5$.

PSfrag replacements
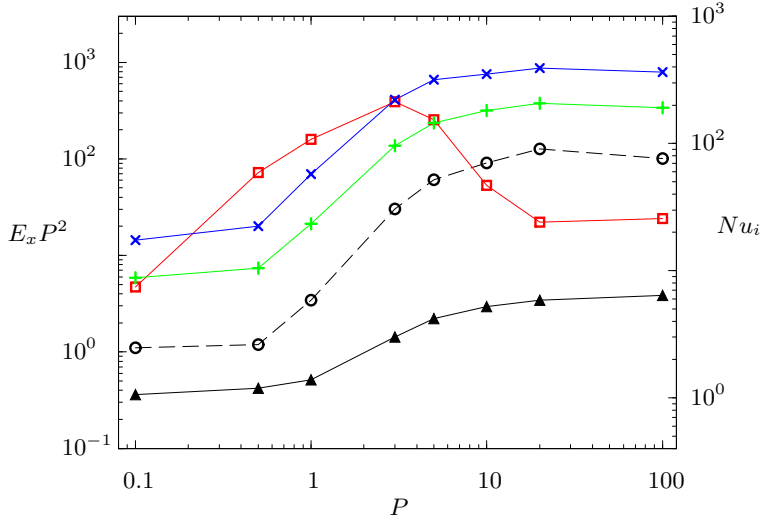
Fig. 6.25. *The time-averaged differential rotation $\langle\overline{u_\varphi}\rangle_t$ at the outer spherical boundary as a function of the colatitude θ for $P = 0.5$, $\tau = 1.5 \times 10^4$ and R taking values between 3×10^5 and 10^6 (from bottom to top at $90°$).*


Fig. 6.26. *The time- and azimuthally-averaged differential rotation $\langle\overline{u_\varphi}\rangle_t$ (upper left quarter), meridional circulation (upper right quarter), temperature perturbation $\langle\overline{\Theta}\rangle_t$ (lower left quarter) and helicity $\langle\overline{H}\rangle_t$ (lower right quarter) for $P = 1$, $\tau = 10^4$ and $R = 2.8 \times 10^5$ (upper circle) and 1.4×10^6 (lower circle).*
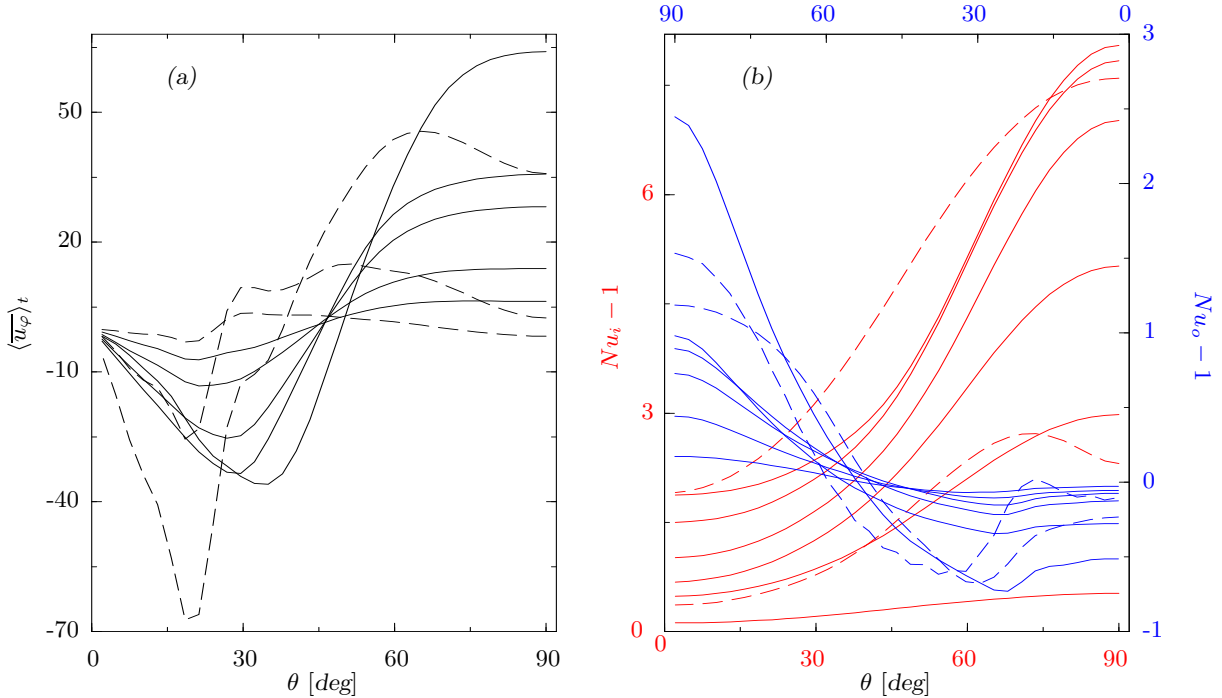
Azimuthal averages. It is of interest to consider the latitudinal distribution of the heat transport with increasing Rayleigh number. The dependence of the Nusselt number on the colatitude θ is rather similar for all six cases discussed in figure 6.22. Therefore, we demonstrate this dependence in figure 6.24 only for the cases $P = 1$, $\tau = 10^4$ and $P = 0.025$, $\tau = 10^5$, which alongside the typical, exhibit some additional interesting features. The values of the Nusselt numbers at both the inner and the outer spherical surface have been plotted in figure 6.24. They have similar behavior except that Nu_o reflects more closely the latitudinal structure of the convection but is always smaller than Nu_i. At low values of the Rayleigh number convection increases the heat transport mainly in the equatorial region and only by an insignificant amount in the polar regions. In fact, at higher latitudes, the Nu_o-curves show even a slight decrease in the heat transport to the outer boundary compared to the case of pure conduction. A possible explanation of this surprising observation might be that at about $30°$ ($150°$) the upper and lower parts of the convection columns touch the colder outer surface while the geostrophic constraint prevents them from reaching the hotter interior. Thus at this latitude colder fluid coming from the outer surface rather than hot fluid from the interior is transported. A sudden increase of both Nu_i and Nu_o can be noticed at $R = 1.4 \times 10^6$ owing to the fully developed polar convection. As already discussed the polar convection is strongly inhibited by the action of the Coriolis force and sets in at much higher values of R. But once it has set in, it encounters less geometric constraints than the convection in the equatorial region and seams to grow faster with R. These features are typical for all cases of various P and τ and are well represented by the case of $P = 1$, $\tau = 10^4$ in figure 6.24(a). The low Prandtl number case $P = 0.025$, $\tau = 10^5$ shown in figure 6.24(b) exhibits an extraordinary third peak of the heat transport measured by Nu_o at about $\theta = 25°$ to
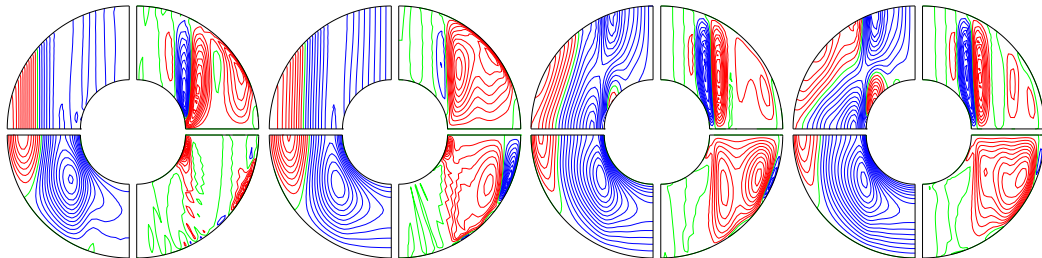
Fig. 6.27. *The time-averaged energy densities $\overline{E}_t P^2$ (red squares), $\check{E}_p P^2$ (green plus-signs), $\check{E}_t P^2$ (blue crosses), $\overline{E}_p P^2$ (circles, multiplied by factor 500) and Nusselt number $Nu_i P^2$ (filled triangles, right ordinate) as functions of P for $\tau = 5 \times 10^3$, $R = 2.7 \times R_c$. The values of R_c are listed in table 6.1.*

$30°$, which is comparable with the peak in the equatorial region and much higher than the peak at the poles. This peak which is especially significant at the largest values of R is again due to the polar convection. The polar convection at low Prandtl numbers develops at much lower values of R than the polar convection at values of P of the order unity and higher so by the time R is increased above 6×10^5 it is capable of transporting as much heat as is transported near the equator. In addition to that the equatorial convection is not very efficient in transporting heat since it is attached very closely to the outer surface and hardly reaches the hotter interior. The polar and the equatorially attached convection almost do not interact with each other as may be seen in figure 6.20 which we used for the discussion of the structure of polar convection. This figure shows that polar convection at low values of P develops in concentric circles around the poles which is the reason for the peak being situated at $\theta = 25°$ to $30°$ in figure 6.24(b). In fact, a similar peak may be noticed in the case of $P = 1$, $\tau = 10^4$ and $R = 1.4 \times 10^6$ in figure 6.24(a) but is much smaller than the peaks at the poles and at the equator, which also may be explained with the help of the plots in figure 6.20.

In view of the importance of differential rotation, we present figure 6.25 which shows the time-averaged mean zonal flow as a function of θ for the case $P = 0.5$, $\tau = 1.5 \times 10^4$. All of the other six sequences of fixed P and τ except the case of $P = 20$ and $\tau = 5 \times 10^3$ have qualitatively the same profile of the differential rotation. It has long been known [12], that convection tends to generate a prograde differential rotation near the equator and retrograde one near the inner spherical shell and in the polar region. This prediction is remarkably well satisfied as can be seen in the profiles in figure 6.25 as well as in the upper right quarter of the plots in figure 6.26. The time-averaged profiles of the differential rotation show remarkable regularity which is due to the strong effects of rotation. The profiles have a maximum of the prograde rotation at the equator, a maximum of the retrograde rotation at $27°$ and approach a vanishing value at the poles. A cylindrical surface of vanishing mean zonal flow exists in the interior of the shell which intersects the surface at nearly the same latitude of $\theta \approx 47°$ regardless of the value of R. At the smaller values of the Rayleigh number the absolute value of $\overline{u_\varphi}$ is relatively small, but significantly increases with R. The states of localized convection and relaxation oscillations are separated by a visible gap from the rest of the profiles in figure 6.25. Although relatively small in amplitude the mean meridional circulation reflects the structure of the flow and might serve as another evidence for polar convection. At lower R the polar regions do not convect, while a significant circulation can be observed there at $R = 1.4 \times 10^6$. The profile of the axisymmetric component of the temperature perturbation is shaped both

Fig. 6.28. *The time- and azimuthally- averaged differential rotation $\langle \overline{u_\varphi} \rangle_t$ at the outer spherical boundary in (a) and local Nusselt numbers Nu_i (red lines, left ordinate, lower abscissa) and Nu_o (blue lines, right ordinate, upper abscissa) in (b) as functions of the colatitude θ for $\tau = 5 \times 10^3$, $R = 2.7 \times R_c$. The values of the Prandtl numbers and the critical Rayleigh numbers are the same as in figure 6.27 and increase from top to bottom in (a) and from bottom to top in (b) near $90°$. The dashed curves are multiplied by factor 30 and belong to $P = 10$, 20 and 100 in (a) and $P = 0.1$ and 0.5 in (b).*
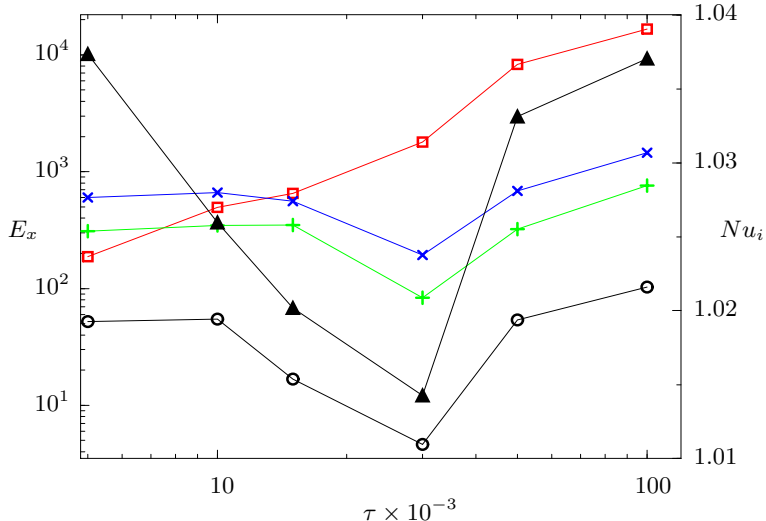
Fig. 6.29. *The time- and azimuthally- averaged differential rotation $\langle \overline{u_\varphi} \rangle_t$ (upper left quarter), meridional circulation (upper right quarter), temperature perturbation $\langle \overline{\Theta} \rangle_t$ (lower left quarter) and helicity $\langle \overline{H} \rangle_t$ (lower right quarter) for $\tau = 5 \times 10^3$, $R = 2.7 \times R_c$ (for values of R_c see table 6.1) and $P = 0.1$, 1, 10, 20 (from left to right).*

by the meridional circulation and the non-axisymmetric components of convection. While significant amplitudes of $\overline{\Theta}$ are confined to the equatorial region for low values of the Rayleigh number R, a more spherical distribution develops at higher values.

6.3.2 Dependence on the Prandtl number

As already discussed, the properties of convection should become independent of the Prandtl number as its value increases if the thermal timescale is used instead of the viscous one. This

Fig. 6.30. *The time-averaged energy densities $\overline{E}_t$ (red squares), $\check{E}_p$ (green plus-signs), $\check{E}_t$ (blue crosses), $\overline{E}_p$ (black circles, multiplied by factor 10^3) and Nusselt number Nu_i (filled triangles, right ordinate) as functions of the Coriolis number τ for $P = 0.1$, $R = 2 \times R_c$. The values of the critical Rayleigh numbers R_c are listed in table 6.1.*
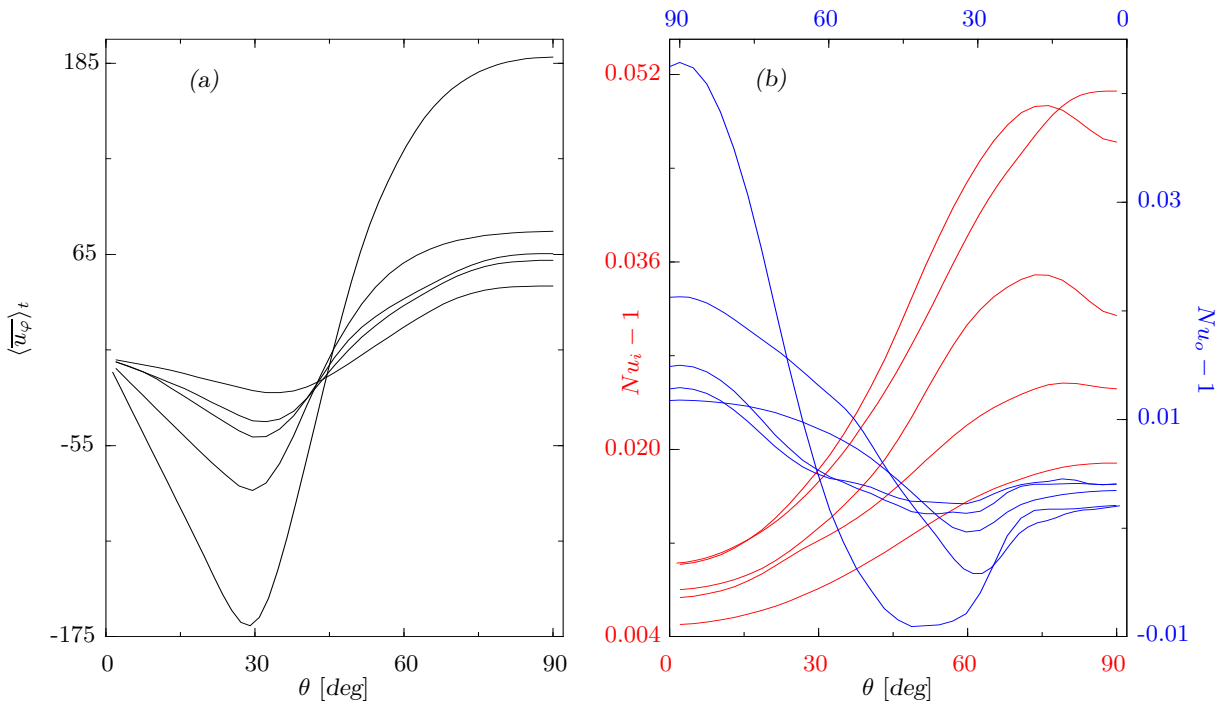
is well illustrated by figure 6.27 where the time-averaged kinetic energy densities as well as the Nusselt number at the inner spherical boundary are plotted for a sequence with a fixed value of $\tau = 5 \times 10^3$ and $R = 2.7 \times R_c$. Additional sequences are presented in figure 6.16. To demonstrate the independence of P in the thermal scaling the values are multiplied by P^2 and indeed show a tendency to approach a constant value above $P = 10$. The mean toroidal energy density corresponding to the differential rotation approaches its constant value more slowly than the other components but there is little doubt that it will too scale as P^{-2}. Using the usual viscous time scaling one may observe that at small values of P the energy densities have higher value while the heat transport has lower ones than the corresponding quantities at high P. This is explained by the fact that at comparable values of the thermal diffusivities the viscosity will be less significant at low Prandtl numbers than at high Prandtl numbers or alternatively at comparable viscosities the thermal diffusivity is smaller at high values of P.

The most significant change in the latitudinal dependences of convection as the value of the Prandtl number is increased is the change from geostrophic to thermal wind structure of the differential rotation. This change may be observed both in the projections of the mean zonal flow on the meridional plane presented in figure 6.29 as well as in its profile as a function of the colatitude θ in figure 6.28(a). The differential rotation changes its geostrophic structure significantly only at values of $P = 10$ and above. The maximum of the prograde differential rotation moves from the equator to lower latitudes of about 65°. The maximum of the retrograde rotation moves closer to the polar regions. The amplitude of the differential rotation decreases gradually.

The heat transport preserves its form with increasing Prandtl number. It is stronger at the equatorial region in figure 6.28(b). No peaks at the polar region are observed since at $R = 2.7 \times R_c$ and $\tau = 5 \times 10^3$ the polar convection has insufficient vigor. A weak minimum where the heat transport is smaller than the pure conductive heat transport is noticed in the Nu_o curves at about 25° away from the poles and may be again be attributed to the fact that the top and bottom of the convection columns reach more easily the colder outer surface than the hotter interior.
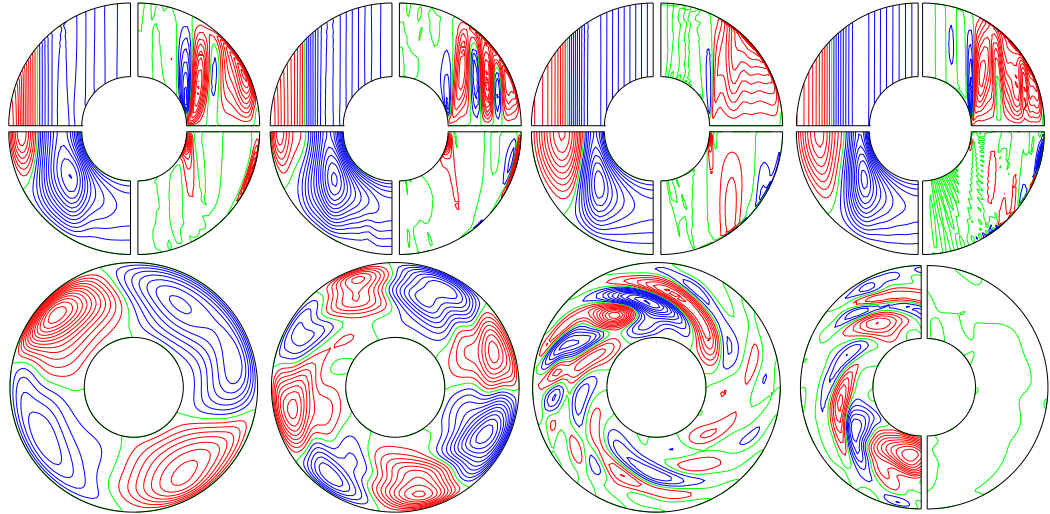
6.3.3 Dependence on the Coriolis number

Finally, we report the results on the variation of the averaged properties of convection with the Coriolis number τ at fixed value of $P = 0.1$ and $R = 2 \times R_c$. Figure 6.30 shows the time averages of the energy densities and the Nusselt number Nu_i while figure 6.31 shows the latitudinal profiles of $\langle \overline{u_\varphi} \rangle_t$, $\langle \overline{Nu_i} \rangle_t$ and $\langle \overline{Nu_o} \rangle_t$. The time- and the azimuthally-averaged

Fig. 6.31. *The time- and azimuthally-averaged differential rotation $\langle \overline{u_\varphi} \rangle_t$ at the outer spherical boundary in (a) and local Nusselt numbers Nu_i (red lines, left ordinate, lower abscissa) and Nu_o (blue lines, right ordinate, upper abscissa) in (b) as functions of the colatitude θ for $P = 0.1$, $R = 2 \times R_c$. The values of the Coriolis numbers and the critical Rayleigh numbers are the same as in figure 6.30 and near 90° increase from bottom to top in (a) while in (b) from top to bottom $\tau = 5 \times 10^4$, 5×10^3, 10^4, 1.5×10^4, 3×10^4 for Nu_i and $\tau = 5 \times 10^3$, 5×10^4, 10^4, 1.5×10^4, 3×10^4 for Nu_i.*

profiles exhibit the shape and characteristics familiar from the similar plots discussed in connection with the R- and the P-dependence and their behavior can be explained having in mind that the main effects of rotation are the increase of the amplitude of differential rotation and the tendency towards geostrophic motions due to the action of the Taylor-Proudman theorem. However, both figures 6.30 and 6.31 show a very surprising feature – a non-monotonic behavior as the rotation rate is increased. The averaged energy densities and the Nusselt number Nu_i presented in figure 6.30, for instance, all show a minimum at intermediate values of τ. In order to explain this unexpected result, we show in figure 6.32 the streamlines of convection in the equatorial plane along with isolines of $\langle \overline{u_\varphi} \rangle_t$, $\langle \overline{\Theta} \rangle_t$, $\langle r \sin\theta \partial_\theta \overline{v} \rangle_t$ and $\langle \overline{H} \rangle_t$ in the meridional plane. In agreement with the linear analysis, the preferred form of convection at $\tau = 5 \times 10^3$ and Prandtl numbers as small as $P = 0.1$ is inertial convection with a small value of the wavenumber determined by the competition between $m = 2$ and $m = 3$ modes. The convection cells, although strongly attached to the outer surface at the equatorial region, are capable of reaching the hotter inner sphere because of their large dimensions due to the small wavenumbers and thus secure a certain amount of heat transport between the interior and the outer surface. As was found in the linear study, an increase of the rotation rate leads to an increase in the preferred wavenumber of inertial convection. The nonlinear solution roughly follows this dependence and increases its wavenumber from $m = 2$ to $m = 4$ at $\tau = 1.5 \times 10^4$ as seen in the lower row of figure 6.32. But the increase of the wavenumber, necessarily leads to a decrease in the spatial dimensions of the equatorially attached rolls which, now do not extend far enough in radial direction so as

Fig. 6.32. *The time- and azimuthally-averaged differential rotation $\langle\overline{u_\varphi}\rangle_t$ (upper left quarter), meridional circulation (upper right quarter), temperature perturbation $\langle\overline{\Theta}\rangle_t$ (lower left quarter) and helicity $\langle\overline{H}\rangle_t$ (lower right quarter) for $P = 0.1$, $R = 2 \times R_c$ (for values of R_c see table 6.1) and $\tau = 5 \times 10^3$, 1.5×10^4, 3×10^4, 5×10^4 (from left to right, upper row). The lower row shows lines of constant $r\partial_\varphi v$ in the equatorial plane at a particular moment in time.*

to reach the inner sphere. For this reason, the transport of heat decreases significantly. Since the chosen value of the Prandtl number $P = 0.1$ is near the border between the inertial and columnar convection, a further increase of the rotation rate leads to a major change in the type of convection. The drifting convection vortices of the columnar convection are also not very well suited to transport heat towards the outer surface. The streamlines are strongly extended in spiral fashion and the drift may reverse the motion of a fluid parcel before it has reached the outer surface. However, the increase of τ and the strong spiralling of the columns lead to a corresponding increase of the differential rotation and ultimately to the state of relaxation oscillations presented in the last column of figure 6.32 for $\tau = 5 \times 10^4$. Although at such a high rotation rate the inhibiting effect of the Taylor-Proudman theorem should be quite significant, it seems that the strong intermittency in time and space and the development of small scale turbulent structures finds a way to increase the heat transport which reaches the size it has exhibited at much smaller rotation rates of $\tau = 5 \times 10^3$. From this we conclude that the effects of rotation do not necessarily lead to a decrease in the heat transported by convection. As we have demonstrated, the Coriolis force may actually suppress motions which exhibit lower values of the Nusselt number than some motions allowed under the constraint of the Taylor-Proudman theorem.

7. Convection-Driven Spherical Dynamos. Basic Properties, Types and Parameter Regions
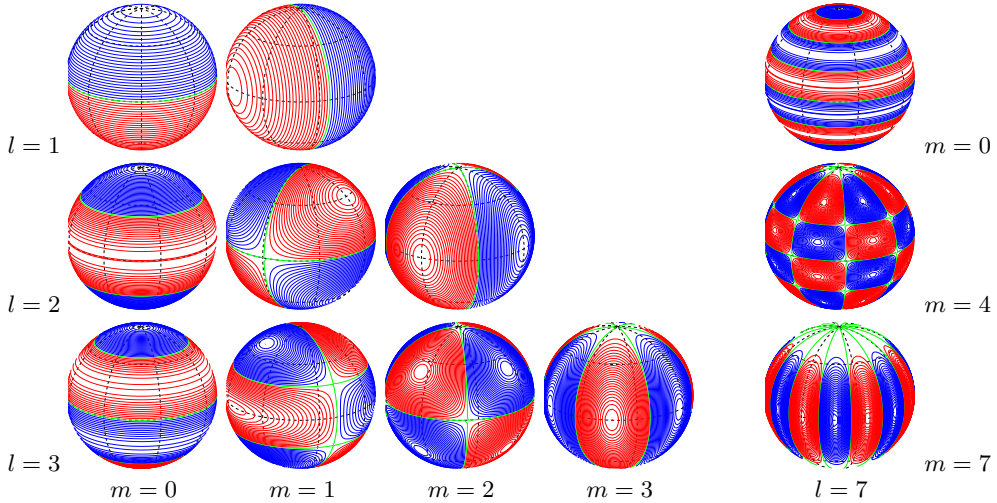
7.1 Introduction

Topic and motivation. The remaining part of the report describes our three-dimensional self-consistent numerical simulations of convection-driven dynamos in rotating spherical fluid shells. Being the only self-consistent method of solving the dynamo problem, numerical simulations are now clarifying the physical processes on which the generation of magnetic fields in conducting fluids depends. If the present rate of progress is sustained we may hope to gain soon a basic understanding of the magnetism of the Earth as well as of those of the planets and satellites of the Solar system. Dynamo simulations provide a new and unparalleled opportunity of interpreting in the frame of a physical theory the features of the geomagnetic field observed by geomagnetic and paleomagnetic techniques. It must be pointed out that the data available from simulations is much more detailed both as time series and as distributions over the Earth's surface than those which actual observations can provide. However, the limitations of numerical simulations should always be kept in mind. Often numerical solutions are too chaotic and very difficult to interpret and understand. They should be regarded as a method to gain insight into the general physical mechanisms, rather than as an explanation of the magnetic activity of any particular cosmical object such as the Earth. Further details on the role of self-consistent numerical simulations among the vast number of topics and branches which constitute dynamo theory have been outlined in chapter 2.

Contents. The prime aims of dynamo simulations are to understand **(a)** the mechanisms leading to the generation and equilibration of magnetic fields and **(b)** their variation in space and time. A sharp border between these two topics does not exist but for clarity we shall attempt to describe them separately. In chapter 8 we focus the attention on the time- and spatially-averaged properties of our dynamo solutions in dependence of the parameters as well as on the interaction and the equilibration of magnetic fields and convection. In chapter 9 we discuss the spatio-temporal variations of our dynamos and attempt to compare them with actually observed geomagnetic features. This chapter provides an overview of our most important dynamo results. Here describe the robust features with respect to which any dynamo solution can be classified. Such features are the types of symmetry and time dependence of solutions. We also provide an overview of the regions in the parameter space which have been investigated. Those topics constitute a necessary frame in which the more subtle properties described in the following chapters may be conveniently understood.

Our results on dynamo action have been or will be published in references [29, 60, 108, 33].

Assumptions. The magnetic induction equation (3.64g) is introduced into the problem of finite-amplitude convection. It is coupled to the equations governing convective flow through the Lorentz force which is included in the momentum equation (3.64b). More precisely, we consider the full problem defined by the Boussinesq equations (3.65) in the case of a homogeneous distribution of internal heat sources ($R_i \neq 0$, $R_e = 0$). We use stress-free boundary conditions for the velocity field (3.66b), fixed-temperature thermal boundary conditions (3.66c) and a radius ratio $\eta = 0.4$. The thermal buoyancy is again the only driving force in

Fig. 7.1. *Various symmetries demonstrated on the examples of spherical harmonics Y_l^m of degree l and order m as indicated in the plot.*

our model. Assumptions other than these will be explicitly stated in the text. In particular, we consider the influence of non-slip boundary conditions (3.66a) for the velocity field and the possibility of a finitely or a perfectly conductive inner core.

7.2 Symmetries

The majority of the finite-amplitude convection solutions demonstrated in chapter 6 show a very complex, often chaotic structure. Geophysically interesting dynamo simulations exhibit similar or stronger chaos, since at small values of the magnetic Prandtl number Pm vigorous velocity fields are required for dynamo action. A general tool providing insight into such complicated solutions is the theory of groups. As in other problems, symmetry methods applied to differential equations enable **(a)** rigorous finding of their symmetries; **(b)** algorithmic reduction of the number of independent variables and derivation of invariant solutions; **(c)** decision whether a nonlinear PDE may be transformed to a linear one and whether a non-constant coefficient linear PDE may be transformed to a constant coefficient one; **(d)** derivation of conservation laws. Unfortunately, the governing equations of the geodynamo are of the type which does not allow such major simplifications. However, the symmetry properties of the geodynamo are important at least from a numerical viewpoint because **(i)** they provide a classification of the strongly chaotic solutions of the problem according to their "approximate" symmetry, **(ii)** in a sufficiently laminar regime, various "assumed" or actual symmetries of the solutions may be used to greatly decrease the computational cost.

Symmetries of the geodynamo. We define a *physical system* as a combination of the geometrical configuration in which some physical process is embedded and the equations governing it. *Symmetry* is a transformation $\mathcal{K}$ which transforms the system or any of its solutions into an equivalent, indistinguishable one. A solution of any system has a symmetry that is either the same as, or lower than that of, the system itself. The symmetries of the system are, in principle, known. Suppose, in addition, that a solution is also known. By application of the symmetry $\mathcal{K}$ onto it, further solutions may be sought. Similarly, knowledge of some part of a solution may lead to conclusions about the unknown part. Let us illustrate these remarks on the example of dynamos in a rotating spherical shells.

Symmetries of the geometrical configuration. The geometrical setting of the problem considered in the thesis is described in section 3.1. Its most important ingredients are its spherical form and its rotation. A non-rotating sphere has a spherical symmetry, i.e. it may be rotated at any angle about any axis as well as reflected in any plane passing through its center. But rotation provides a preferred direction and a rotating sphere loses its spherical symmetry. However, transformations which take the rotating sphere into itself are the identity $\mathcal{I}$, the reflection in the equatorial plane $\mathcal{E}$ and the rotation about the polar axis $\mathcal{P}_M$ by an angle $2\pi/M$, with an integer M. The transformations $\mathcal{I}$, $\mathcal{E}$ and $\mathcal{P}_M$ form an infinite Abelian group. The last two of them may be written in spherical polar coordinates (r,θ,φ) as

$$\mathcal{E} : (r,\theta,\varphi) \longrightarrow (r,\pi-\theta,\varphi), \qquad \mathcal{P}_M : (r,\theta,\varphi) \longrightarrow (r,\theta,\varphi+2\pi/M). \tag{7.1}$$

Symmetries of the governing equations. For simplicity we consider equations (3.64) with boundary conditions which have a spherical symmetry. Apart from the identity $\mathcal{I}$, the group of transformations which preserves the governing equations (3.64) unchanged consists of [65] **(a)** the rotation $\mathcal{P}_M$, **(b)** magnetic field reversal $\mathcal{B}$, **(c)** inversion $\mathcal{U}$ of $\boldsymbol{r}$ and $\boldsymbol{u}$ and **(d)** translation in time $\mathcal{T}_a$ by a time period a, respectively defined as

$$\mathcal{B} : \boldsymbol{B} \longrightarrow -\boldsymbol{B}, \qquad \mathcal{U} : (\boldsymbol{r},\boldsymbol{u}) \longrightarrow -(\boldsymbol{r},\boldsymbol{u}), \qquad \mathcal{T}_a : t \longrightarrow t+a. \tag{7.2}$$

Implications for the solutions. A physical system is invariant under the group of transformations consisting of the two subgroups which leave its geometrical configuration and its governing equations unchanged. We consider how the solutions $(\boldsymbol{u},\boldsymbol{B},p,\Theta,\Gamma)$ of our system classify with respect to those transformations and how the symmetries can be used to constrain the form of the solutions.

First, not all symmetries are equally important, e.g. the transformation $\mathcal{U}$ comes into play only when experiments are constructed and justifies the argument that in a laboratory the centrifugal force may replace the gravity force if the temperature gradient is simultaneously reversed. With respect to the translation in time the solutions may be *periodic* if $\mathcal{T}_a\,y(t) = y(t)$ or *non-periodic* otherwise, where $y(x)$ represents any of the fields forming the solution of equations (3.64). $\mathcal{T}_a$ is very important and even in the most turbulent simulations, we attempt to identify processes which repeat in time even if only in some approximate sense $\mathcal{T}_a\,y(t) \approx y(t)$ or over a finite part of the simulation. However, we do not discuss $\mathcal{U}$ and $\mathcal{T}_a$ further and concentrate on the polar rotation $\mathcal{P}_M$ and the equatorial reflection $\mathcal{E}$.

A transformation $\mathcal{K}$ may transform a field $y(x)$ in many ways. However, here we distinguish three important cases **(a)** $\mathcal{K}\,y = y$, **(b)** $\mathcal{K}\,y = -y$ and **(c)** $\mathcal{K}\,y \neq \pm y$. In the first case we shall call the field $y(x)$ *symmetric* or *even* with respect to $\mathcal{K}$ and denote it by $y^{\mathcal{K}:s}$, in the second case – *antisymmetric* or *odd* with respect to $\mathcal{K}$ and denote it by $y^{\mathcal{K}:a}$, while in the third case – *mixed* and use $y^{\mathcal{K}:m}$. A trivial linear algebraic result states that $y^{\mathcal{K}:m}$ can always be represented as a sum $y^{\mathcal{K}:m} = y_s^{\mathcal{K}:m} + y_a^{\mathcal{K}:m}$ of a symmetric $y_s^{\mathcal{K}:m} = 1/2(1+\mathcal{K})y^{\mathcal{K}:m}$ and an antisymmetric part $y_a^{\mathcal{K}:m} = 1/2(1-\mathcal{K})y^{\mathcal{K}:m}$.

Using those definitions, and for simplicity assuming that the equatorial symmetry of the velocity field is known, it is a simple exercise to determine the equatorial symmetry which is allowed by the governing equations for the rest of the unknowns:

- the induction equation (3.64g):

$$\boldsymbol{u}^{\mathcal{E}:s} \Longrightarrow \boldsymbol{B}^{\mathcal{E}:s} \vee \boldsymbol{B}^{\mathcal{E}:a}, \quad \textit{(quadrupole, dipole)} \tag{7.3a}$$

$$\boldsymbol{u}^{\mathcal{E}:m} \Longrightarrow \boldsymbol{B}^{\mathcal{E}:m}, \tag{7.3b}$$

- the heat equation (3.64d) and the concentration equation (3.64e):

$$\boldsymbol{u}^{\mathcal{E}:s} \Longrightarrow \Theta^{\mathcal{E}:s}, \tag{7.4a}$$

$$\boldsymbol{u}^{\mathcal{E}:m} \Longrightarrow \text{further assumptions are required,} \tag{7.4b}$$

and similarly for the concentration perturbation Γ,

• the momentum equation (3.64b):

$$\boldsymbol{u}^{\mathcal{E}:s} \Longrightarrow p^{\mathcal{E}:s} \wedge \Theta^{\mathcal{E}:s} \wedge \Gamma^{\mathcal{E}:s} \wedge (\boldsymbol{B}^{\mathcal{E}:s} \vee \boldsymbol{B}^{\mathcal{E}:a}), \tag{7.5a}$$
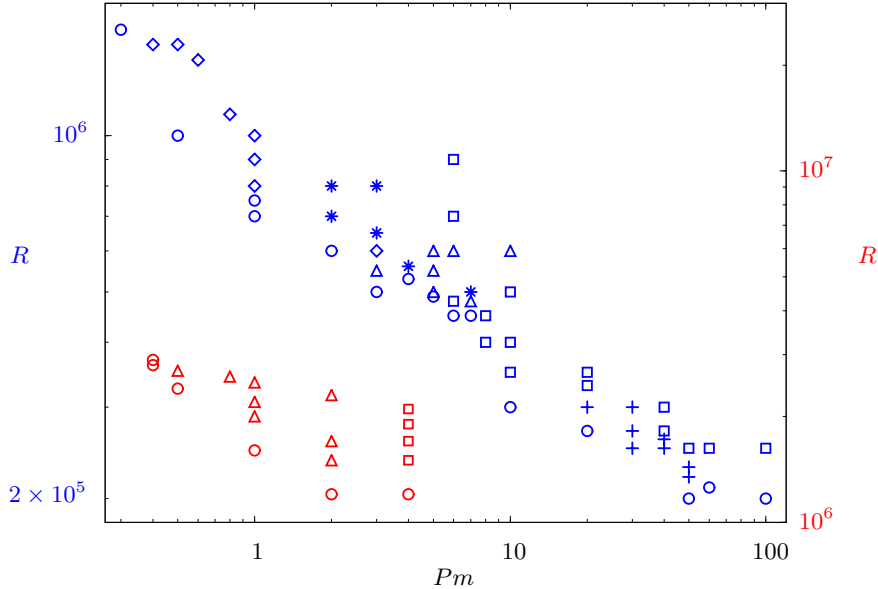
$$\boldsymbol{u}^{\mathcal{E}:m} \Longrightarrow \text{further assumptions are required.} \tag{7.5b}$$

Only velocities of the types $\boldsymbol{u}^{\mathcal{E}:s}$ and $\boldsymbol{u}^{\mathcal{E}:m}$ have been considered, since purely antisymmetric velocity $\boldsymbol{u}^{\mathcal{E}:a}$ is not allowed by the simplest case of the momentum equation $\mathrm{D}_t \boldsymbol{u} = -\nabla p$. In case, the symmetry of any other field is known, a similar analysis may be performed to find the symmetries of the remaining fields. The above expressions do not guarantee that any solutions exist. Formula (7.3a), for instance, should be understand to mean that if the velocity field $\boldsymbol{u}$ is equatorially symmetric, i.e. $\boldsymbol{u}^{\mathcal{E}:s}$ then, in order to satisfy the symmetry properties of the induction equation (3.64g), the magnetic field $\boldsymbol{B}$ must be either equatorially symmetric $\boldsymbol{B}^{\mathcal{E}:s}$ (quadrupole solution) or equatorially antisymmetric $\boldsymbol{B}^{\mathcal{E}:a}$ (dipole solution). However, for the given velocity field $\boldsymbol{u}^{\mathcal{E}:s}$ the induction equation may or may not have any nontrivial solutions $\boldsymbol{B}$ altogether. Finally, since a solution of the physical system must obey all governing equations, the classes of solutions of the self-consistent dynamo problem in a rotating spherical shell with spherically symmetric boundary conditions are determined as an intersection of formulas (7.3) (7.4) and (7.5). This intersection is actually equivalent to expressions (7.5). Analytical [13], experimental [27] as well as the majority of our numerical studies (chapters 5 and 6) yield a "cartridge belt" roll configuration such as that shown in figures 2.2 and 5.1 as a rough approximation for the velocity field $\boldsymbol{u}$. It is thus very likely that the preferred solution for the velocity is equatorially symmetric $\boldsymbol{u}^{\mathcal{E}:s}$ which indicates that to first order the structure of the magnetic field will be either dipolar $\boldsymbol{B}^{\mathcal{E}:a}$ or quadrupolar $\boldsymbol{B}^{\mathcal{E}:s}$. Of course, no symmetry in the strict sense of the word may be expected in a turbulent solution. Therefore, it is more precise to state that in a turbulent situation the equatorially symmetric part $\boldsymbol{u}_s^{\mathcal{E}:m}$ of the velocity will be much larger than its equatorially antisymmetric part and as a consequence either the dipolar $\boldsymbol{B}_a^{\mathcal{E}:m}$ or the quadrupolar part $\boldsymbol{B}_s^{\mathcal{E}:m}$ of the magnetic field will be dominant. The "cartridge belt" roll structure of $\boldsymbol{u}$ implies that the rotational symmetry $\mathcal{P}_M$ with M equal to the number of pairs of rolls is also of importance. This is indeed true especially for the more laminar solutions. Analysis similar to those just outlined may be straightforwardly performed in the case of the $\mathcal{P}_M$ symmetry as well.

Toroidal-poloidal scalars, the spherical harmonics and symmetries. Toroidal-poloidal representations of the type (A.11) and expansions in spherical harmonics similar to (4.1) are widely used in both numerical and analytical studies of the problem. It is again very easy to show that, say, with respect to the reflection $\mathcal{E}$ equatorially symmetric and antisymmetric solenoidal vectors transform according to

$$\mathcal{E} : (T, P)^{\mathcal{E}:s} \longrightarrow (-T, P)^{\mathcal{E}:s}, \qquad \mathcal{E} : (T, P)^{\mathcal{E}:a} \longrightarrow (T, -P)^{\mathcal{E}:a}, \tag{7.6}$$

where the pairs (T, P) with the appropriate superscript represent the toroidal and poloidal scalars defining the vectors by expression (A.11). Similar relations with respect to the rest of the symmetries can be obtained. The symmetry properties of the Legendre functions $P_l^m(\cos\theta)$ and the spherical harmonics $Y_l^m(\theta, \varphi)$ may easily be found in the reference literature, e.g. in [1], and will not be repeated here. However, since we often discuss the visual appearance of the solutions, we only note that the expansion of an equatorially symmetric field $y^{\mathcal{E}:s}$ contains only terms for which $(l + m)$ is even, while that of an antisymmetric field $y^{\mathcal{E}:a}$ contains only terms for which $(l + m)$ is odd. In addition, the spherical harmonic Y_l^M is invariant under the rotation $\mathcal{P}_M$. Some visual examples are shown in figure 7.1.
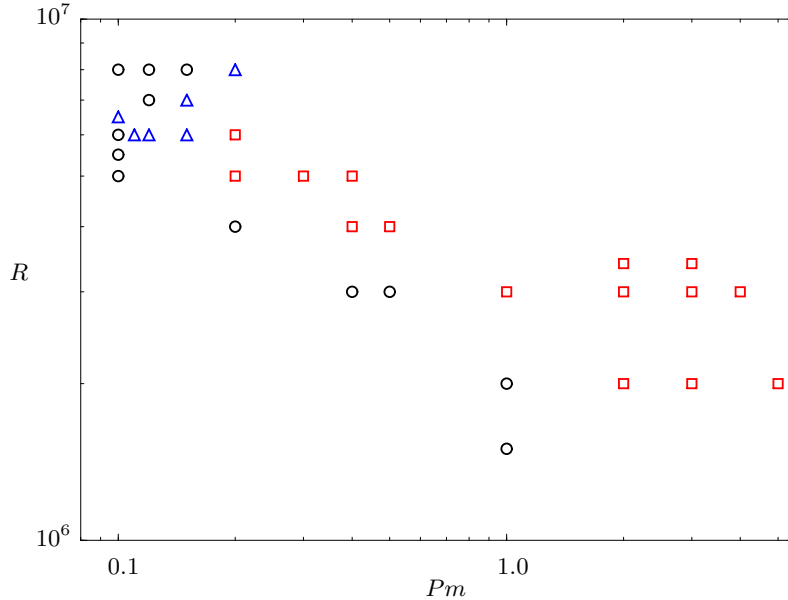
Fig. 7.2. *Convection-driven dynamos as a function of R and Pm in the cases* • $P = 1$, $\tau = 10^4$ *(left ordinate, blue symbols) and* • $P = 1$, $\tau = 3 \times 10^4$ *(right ordinate, red symbols). The symbols indicate regular (plus signs) and chaotic dipolar (squares), hemispherical (triangles), mixed (stars), quadrupolar (diamonds) and decaying dynamos (circles).*

7.3 Overview of major parameter regions

A major goal of the research reported in this dissertation is to illuminate the dependence of convection-driven spherical dynamos on the parameters of the problem. Because of the lack of knowledge of the properties of the Earth's core this research is necessary in order to provide the tools for an extrapolation to realistic models of the geodynamo. Our investigation of the parameter space has resulted in a great number of dynamo solutions obtained at various values of the basic parameters, spanning the computationally accessible range. In this section we provide a view to the parameter regions which have been investigated and the most basic dynamo features observed there. Since the Prandtl and the Coriolis numbers P and τ are the parameters which are most difficult to vary, we have roughly divided the parameter space into three regions according to the value of P. It has been already noted that the values of P and τ are dependent, in the sense that when P is increased τ must be decreased for computational reasons. This behavior has been demonstrated and explained in the linear case in figure 5.7. Therefore, for instance, when referring to "a large Prandtl number region" one may alternatively think of "a small Coriolis number region".

The region of moderate Prandtl and Coriolis numbers. Figure 7.2 shows an overview of a part of the dynamo computations performed at moderate values of P and τ. Apart from the cases shown in the figure many other dynamo solutions in this region have also been obtained. Those include cases at $P = 0.5$, $P = 0.8$, $P = 2$, $\tau = 1.5 \times 10^4$, $\tau = 2 \times 10^4$, and at various values of R and Pm, which are not included in the figure since we aim to present the results in dependence only on two parameters. However, the results emerging from figure 7.2 have been found to be of general validity not only for the region of moderate Prandtl and Coriolis numbers, but as is demonstrated by figures 7.3 and 7.5, for the regions of small and large P as well. An early version of figure 7.2 has been published in [62]. In our studies the figure has been updated and extended to include the dynamos at $\tau = 3 \times 10^4$ as well as all solutions at $Pm < 1$. The critical values of the Rayleigh number R_c and the wavenumber for
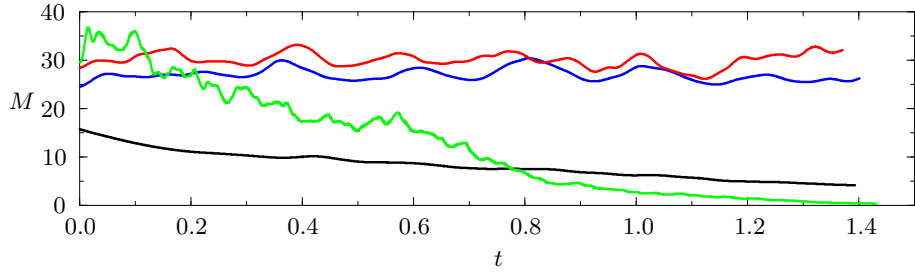
Fig. 7.3. *Convection-driven dynamos as a function of the Rayleigh number R and the magnetic Prandtl number Pm for $P = 0.1$, $\tau = 10^5$. The symbols indicate chaotic dipolar (red squares), hemispherical (blue triangles), and decaying dynamos (black circles).*

the onset the convection are $R_c = 1.9 \times 10^5$ and $m_c = 10$, respectively in the case of $\tau = 10^4$. The corresponding values for the case $\tau = 3 \times 10^4$ are $R_c = 7.8 \times 10^5$ and $m_c = 13$.

When the amplitude of convection is increased by the increase of R beyond R_c, the possibility of magnetic field generation occurs. The bifurcation into a magnetic state first occurs for high values of Pm. For sufficiently large values of Pm, even steadily-drifting and regular time-periodic convection is capable of dynamo action. Such laminar flows generate magnetic fields which in turn also have regular spatio-temporal structure. The regular dynamos exhibit a strong dominance of the dipolar component with $l = 1$, while the expansion coefficients corresponding to spherical harmonics of higher degree $l > 1$ are relatively weak. When R is increased in this region the magnetic field follows to some extent the bifurcation sequence of convection as described in chapter 6, i.e. periodic oscillations of both velocity and magnetic field occur, which are replaced by chaotic solutions in time and space as R is increased further. As will be demonstrated in the next chapter, the presence of magnetic field suppresses coherent structures of convection such as localized convection and relaxation oscillations. However, because of numerical convergence problems, R cannot be increased very far into the turbulent regime and only the stripe-like region shown in the figure has been explored.

At smaller values of Pm ohmic dissipation causes a stronger decay of small scale magnetic features. Thus, R must be increased to reach a magnetic Reynolds number large enough for generation of magnetic field. As a result the velocity field becomes increasingly chaotic as does the generated magnetic field. The dipolar character of the dynamos remains dominant.

At much lower values of Pm of order unity or less the preferred type of dynamo symmetry is quadrupolar with the quadrupolar dominance increasing steadily as Pm is decreased. Although, strictly speaking the quadrupolar dynamos are chaotic in space and time, their mean azimuthal features such as $\overline{B}_\varphi$ and $r \sin\theta \partial_\theta \overline{h}$ as well as the coefficients $H_2^0(r,t)$ and $G_1^0(r,t)$ show oscillating behavior. This property of quadrupolar dynamos will be addressed in detail in chapter 9. It must be noted that in order to reach sufficiently large Reynolds number, R must be increased simultaneously with the decrease of Pm. For instance, in order to obtain a self-sustaining magnetic field at $P = 1$, a Rayleigh number larger than 8×10^5 is
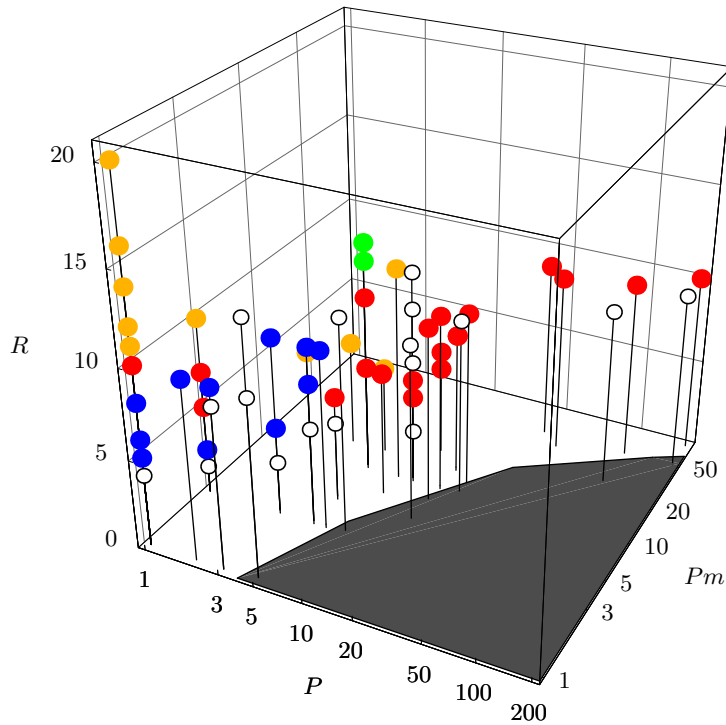
Fig. 7.4. *Total magnetic energies in the cases $P = Pm = 10$, $\tau = 5 \times 10^5$ and $R = 3 \times 10^5$ (black line), 5×10^5 (blue line), 6×10^5 (red line), 7×10^5 (green line). The abscissa of the case $R = 3 \times 10^5$ is multiplied by 0.65 and in the case $R = 7 \times 10^5$ by 0.286.*

required at $\tau = 10^4$ and $R > 2 \times 10^6$ at $\tau = 3 \times 10^3$. For this reason the dynamo simulations are inhibited by numerical problems from reaching very small values of Pm, too. The smallest value of Pm attained so far will be discussed in connection with figure 7.3.

At intermediate values of Pm situated between those of the dipolar and quadrupolar regions, a variety of solutions exhibiting a mixture of expansion coefficients corresponding to higher spherical harmonics degrees l are observed. A special class of solutions are the hemispherical dynamos for which the dipolar and quadrupolar components are roughly equal and cancel each other in one of the hemispheres so that the magnetic flux concentrates almost entirely in the other one [62]. However, various dynamos corresponding to intermediate configurations between the dipolar and quadrupolar components are also found in the region.

The regions of dipolar, quadrupolar and mixed dynamos are not separated in any strict sense. As will be demonstrated below there are even examples in which a single dynamo shows multiple types of symmetry in the course of a single simulation. Generally, as R is increased the dynamos become both increasingly filamentary and more dipolar. This is due to the fact that polar convection develops at higher values of R and introduces an additional asymmetry favoring the global dipolar dominance. Finally we note that in the case of no-slip velocity boundary conditions other groups [40] report mainly dipolar dynamos throughout the entire region discussed in connection with figure 7.2.

The region of small Prandtl and large Coriolis numbers. In the small Prandtl number region a systematic exploration of the onset of dynamo action and the types of dynamo symmetry has been done in the case $P = 0.1$. The results are shown in figure 7.3 and are qualitatively similar to those discussed above. The property that for larger values of Pm dipolar dynamos are realized while for lower values a transition to hemispherical dynamos occurs also agrees with the results obtained for $P = 1$. A remarkable feature of figure 7.3 is the observation that dynamo action may decay as the Rayleigh number is increased. This phenomenon is observed for the values of $Pm = 0.1$, 0.12 and 0.15, for which we have found that non-decaying dynamos exist at $R = 6.5 \times 10^6$ and 6×10^6 but the magnetic field decays at $R = 8 \times 10^6$ and 7.5×10^6. The same behavior is expected to occur at larger values of Pm if R is increased further. But problems of numerical resolution have prevented us from reaching Rayleigh numbers beyond 10^7 so far. The effect is due to the increasingly small-scale structure of convection, leading in turn to small-scale magnetic features which correspondingly decay easier as well as to increased differential rotation. Thus, for a given value of Pm regions in R of no dynamo action are found both below and above the region of active dynamos. It is remarkable, that a dynamo at Pm as low as 0.1 could be attained which is considerably lower than the lowest value attainable in the case $P = 1$. However, as Pm is decreased below 0.1 the upper and lower regions of no dynamo action connect and no quadrupolar dynamos
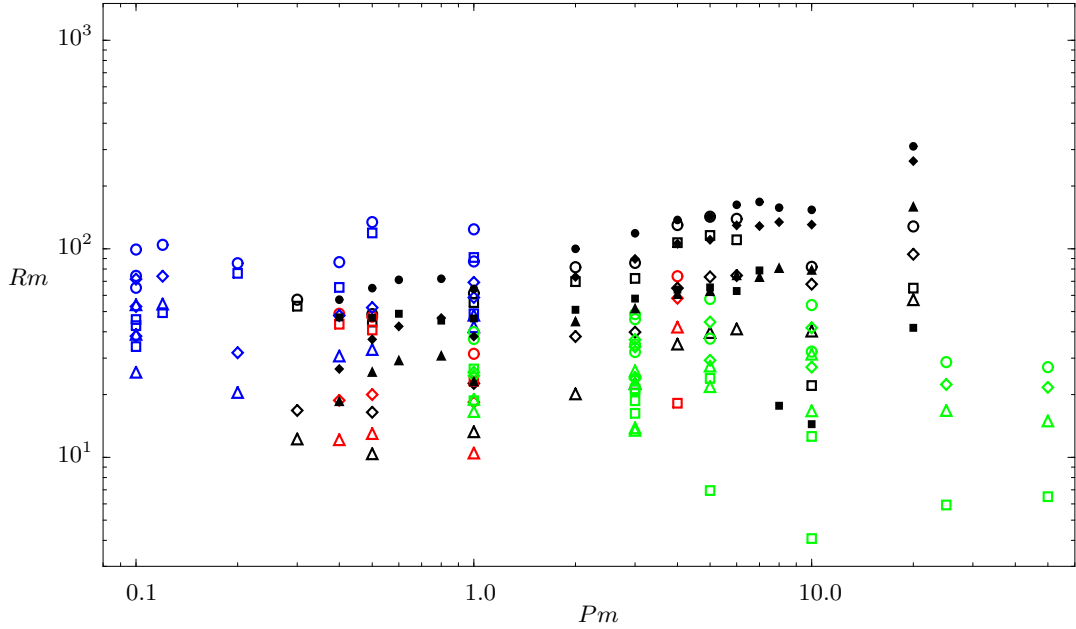
Fig. 7.5. *Convection-driven dynamos as a function of the Rayleigh number R, the Prandtl number P and the magnetic Prandtl number Pm for $\tau = 5 \times 10^3$. The symbols indicate chaotic dipolar (red), hemispherical (green), quadrupolar (blue), mixed (yellow) and decaying dynamos (empty circles).*

can be found. In this respect figure 7.3 is in strong contrast to figure 7.2, where quadrupolar dynamos are found at the lowest values of Pm. As in the case of figure 7.2 additional dynamos have been simulated but have not been included in figure 7.3.

The region of large Prandtl and intermediate Coriolis numbers. That convection amplitudes in an intermediate range are most suitable for the generation of a global magnetic field appears to be a general property of spherical dynamos. This phenomenon is exhibited again in figure 7.5 where convection-driven dynamos in the region of large Prandtl numbers are indicated in the $R - P - Pm-$space. In the particular case of $P = Pm = 10$, it was found that the magnetic field decays for $R = 3 \times 10^5$ and 7×10^5 while sustained dynamo action appears to exist for $R = 5 \times 10^5$ and 6×10^5 as shown in figure 7.4. The Elsasser number for these latter cases is 0.12. It appears that at such a value of R the magnetic Reynolds number is high enough to permit dynamo action, but is not so high that flux expulsion from the convection eddies becomes a dominant effect.

The results displayed in figure 7.5 have been obtained for the particular value 5×10^3 of the Coriolis parameter τ. But from the results presented above and from several computations carried out for $\tau = 10^4$ we expect that these results are representative for a fairly large range of the parameter τ. Figure 7.5 supports the observations made in figures 7.2 and 7.3 that quadrupolar dynamos are found for lower values of Pm while dipolar dynamos predominate at higher values of Pm. Here, however, a clear distinction can often no longer be made in that components of both symmetries contribute about equally to the magnetic energy. This is especially pronounced at large convection amplitudes in the quadrupolar region, i.e. at high R and relatively low Pm. In this region the onset of polar convection results in magnetic fields which exhibit a mixture of dipolar and quadrupolar components.
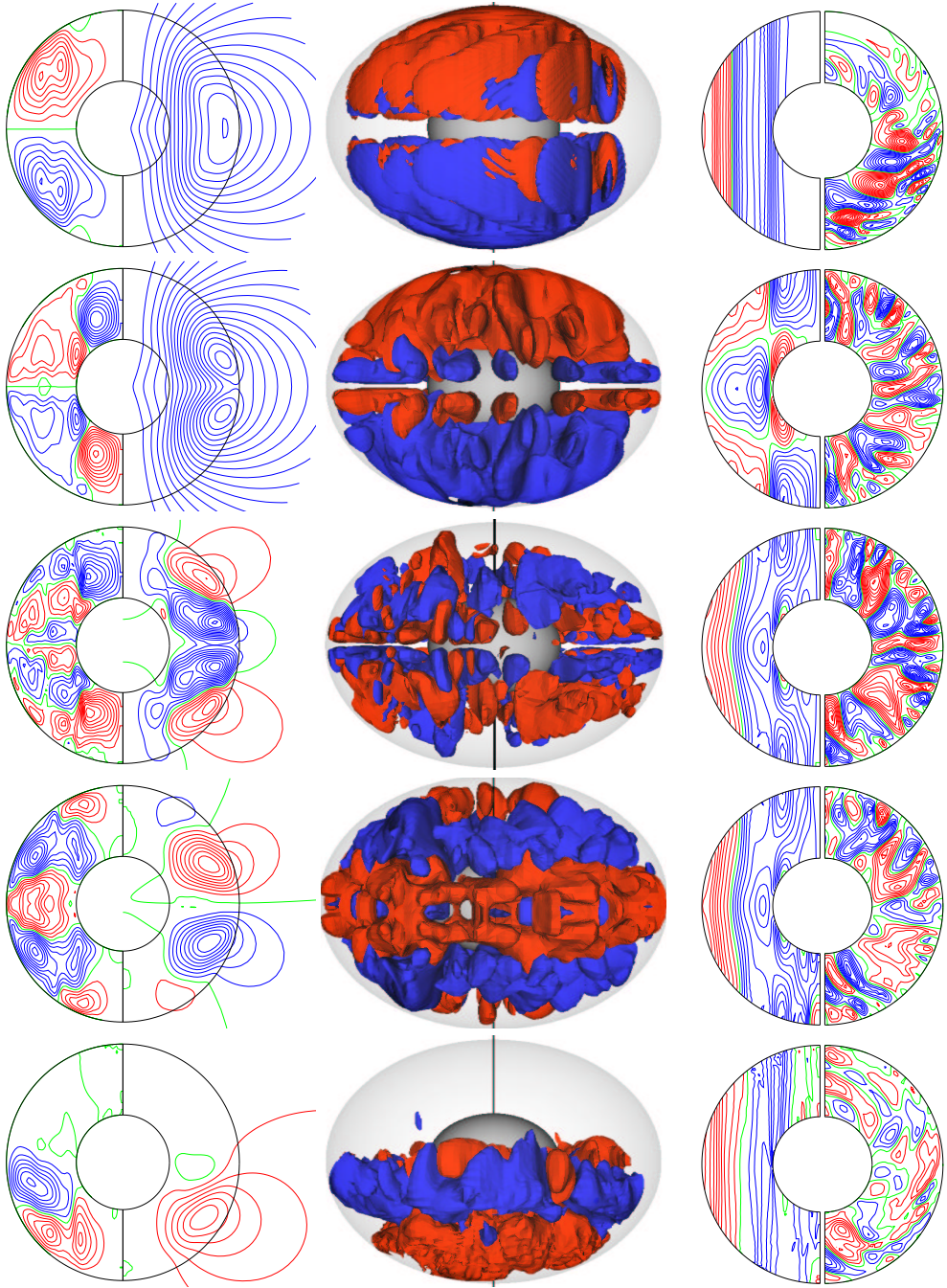
Onset of dynamo action. An important goal of numerical dynamo simulations is to determine the conditions which separate active from decaying dynamos in the parameter space.

Fig. 7.6. *Magnetic Reynolds number $Rm \equiv Pm\sqrt{2E_x}$ for the onset of dynamo action, as a function of Pm, where E_x denotes the densities of the total kinetic energy (circles), $\overline{E}_t$ (squares), $\check{E}_t$ (diamonds), $\check{E}_p$ (triangles), in the cases $P = 1$, $\tau = 10^4$ (black), $P = 1$, $\tau = 3 \times 10^4$ (red), $P = 0.1$, $\tau = 10^5$ (blue) and $P \geq 1$, $\tau = 5 \times 10^3$ (green). The empty symbols are based on decaying dynamos, the full symbols are based on the lowest non-decaying solutions.*

This question is of particular interest to dynamo theory in general and much of the kinematic theory is devoted to finding the conditions for dynamo action by establishing antidynamo theorems or my means of a linear analysis of the induction equation (see section 2.2.2). The onset of dynamo action is equally important but it is much more difficult to determine in self-consistent simulations. Because magnetic solutions bifurcate from non-magnetic convection at finite amplitudes, a sharp border between decaying and active dynamos is unlikely to exist. For example, it is observed, e.g. in figure 8.3, that a dynamo is sustained for several magnetic decay times and then suddenly decays because of the nonlinear interaction between magnetic field and convection. Furthermore, a precise border of dynamo action in the parameter space is very expensive to determine because each point in that space require a three dimensional integration for a sufficiently large time period to find whether magnetic field is sustained. Thus only a limited number of cases may be investigated. However, figures 7.2, 7.3 and 7.5 already provide many valuable observations in this respect. In figures 7.2 and 7.3 the regions of decaying and active dynamos may be separated by approximate lines of the type $(R - R_c)^{c_1}/Pm = c_2$. Similarly in the case of figure 7.5 the border may be approximated by the relation $Pm = c_3 \ln(c_4 P)$. The constants c_i, $i = 1, 2, 3, 4$ may be easily fitted from the data but their precise values are not very meaningful. Furthermore, such relations cannot describe important effects such as the decay of dynamo action at very large values of R as shown in figures 7.3 and 7.4, nor the borders in the limits of large and small values of Pm.

A more physically meaningful condition for dynamo action can be related to the velocity of the convective flow and the electric conductivity of the fluid. They may be combined to form the magnetic Reynolds number $Rm \equiv Pm\sqrt{2E_x}$. In figure 7.6 Rm as a function of Pm is shown for all decaying dynamos presented in figures 7.2, 7.3 and 7.5. Since magnetic fields modify convection as will be shown in section 8.2, values of Rm based on the kinetic energy densities of the lowest active dynamos in the case $P = 1$, $\tau = 10^4$ are also shown in the

Fig. 7.7. *Various types of dynamo symmetry. From top to bottom: dipolar dynamos for* •
P = 0.1, τ = 10⁵, R = 2 × 10⁶, Pm = 1; • P = 10, τ = 5 × 10³, R = 5 × 10⁵, Pm = 10; and
• P = 5, τ = 5 × 10³, R = 6 × 10⁵, Pm = 10; • Quadrupolar dynamo for P = 5, τ = 5 × 10³,
R = 8 × 10⁵, Pm = 3 and • Hemispherical dynamo for P = 0.1, τ = 10⁵, R = 6 × 10⁶,
Pm = 0.11. The left column shows lines of $\overline{B}_\varphi$ = const. (left half) and $r\sin\theta\,\partial_\theta\overline{h}$ = const.
(right half). The middle column shows surfaces of B_r = const. The right column shows lines of
$\overline{u}_\varphi$ = const. (left half) and $r\partial_\varphi v$ = const. in the equatorial plane (right half).

figure with filled symbols, but no significant difference is found. From figure 7.6 it appears
that the magnetic Reynolds number based on the total energy of convection must exceed a
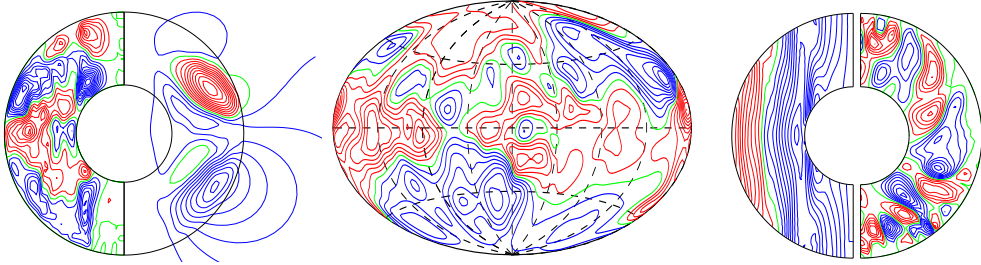
value between 100 and 200 for magnetic fields to be generated and sustained. The critical value of Rm appears to be distinctly lower for the dynamos in the high P region and higher for those of the moderate and low P region. We would like to suggest that this distinction may be due to the role of the differential rotation in these regions. At lower values of P and higher values of τ differential rotation is strong and the dynamos appear to be of $\alpha\omega$-type. At higher values of P and lower values of τ differential rotation is weak and dynamos are more likely of α^2-type. It would not be surprising if the well-defined difference in the critical value of Rm is due to type of dynamo solution. Of course, the nomenclature of turbulent mean-field magnetohydrodynamics is not used in its strict sense here. A sort of large scale more laminar α- and ω-effects are envisaged here, instead.

7.4 Basic properties of dynamo solutions

Above, we have discussed the general structure of dynamo solutions expected on the basis of symmetry considerations. We have provided an overview of the parameter regions where numerical simulations have been carried out and confirmed that quadrupolar and dipolar solutions are observed indeed. Here we will discuss the differences between mathematical and numerical symmetry properties and present typical dynamo solutions in order to demonstrate their actual numerical features and time dependence.

Typical spatial structures. In figure 7.7 five different dynamo solutions have been plotted each at a fixed moment in time. The first three rows of the figure show examples of dipolar magnetic fields. The first example is a small Prandtl number dynamo at $P = 0.1$ with spiraling columnar convection and strong differential rotation in a geostrophic balance, while the second one at $P = 10$ belongs to the large Prandtl number region and features radially oriented convection and a weak mean azimuthal flow with a thermal-wind profile. Despite these large differences in the values of P and the dynamical regime of convection, the structures of the magnetic fields of these cases look almost identical when observed at some distance away from the core-mantle boundary. Indeed, the azimuthally-averaged magnetic field lines start in one of the hemispheres and end in the other one. The two cases look very similar to the idealized plot illustrating dipolar symmetry in figure 7.1 which indicates a strong dominance of the H_1^0 coefficient in the expansion of the magnetic field in spherical harmonics. A few differences in the magnetic fields of the two solutions exist which, however, are undetectable from outside. The first one is the existence, in the large Prandtl number case, of thin layers parallel to the equatorial plane and with polarity opposite to the polarity in the corresponding hemisphere. The layers are due to weak contributions of higher degree coefficients H_l^0. However, even these equatorial structures preserve the perfect dipolar antisymmetry. A more important difference, between the large and small P dynamos, is observed in the structure of the mean azimuthal magnetic field component $\overline{B}_\varphi$. The small P case exhibits a pair of large-scale fluxes of opposite polarity situated at mid-latitudes and each confined to one of the hemispheres, while the large P dynamo also shows a pair of flux tubes which, however, are much more intensive and concentrated in the polar regions. In this case fluxes of $\overline{B}_\varphi$ are also observed outside the tangent cylinder but these are much weaker than the polar fluxes. Such a structure of the mean azimuthal field is a direct consequence of the profile of the differential rotation and is typical for both Prandtl number regions.

Although again dipolar, the third dynamo at $P = 5$, $\tau = 5 \times 10^3$, $R = 6 \times 10^5$, $Pm = 10$ in figure 7.7 is quite different. The regions of positive and negative polarity are not concentrated in one of the hemispheres but are located in relatively small localized patches all over the globe. However, it still preserves it perfect equatorial antisymmetry, since a patch of a given polarity in one of the hemispheres has an exactly corresponding patch of the opposite polarity

Fig. 7.8. *A chaotic dynamo with dipolar and quadrupolar components of roughly equal strength in the case $P = 1$, $\tau = 10^4$, $R = 8 \times 10^5$, $Pm = 3$. The left plot shows lines of constant $\overline{B}_\varphi$ (left half) and $r \sin\theta \partial_\theta \overline{h} = const.$ (right half). The middle plot shows isolines of B_r at $r = 1.7 \times r_0$. The right plot shows lines of $\overline{u}_\varphi = const.$ (left half) and $r \partial_\varphi v = const.$ in the equatorial plane (right half).*
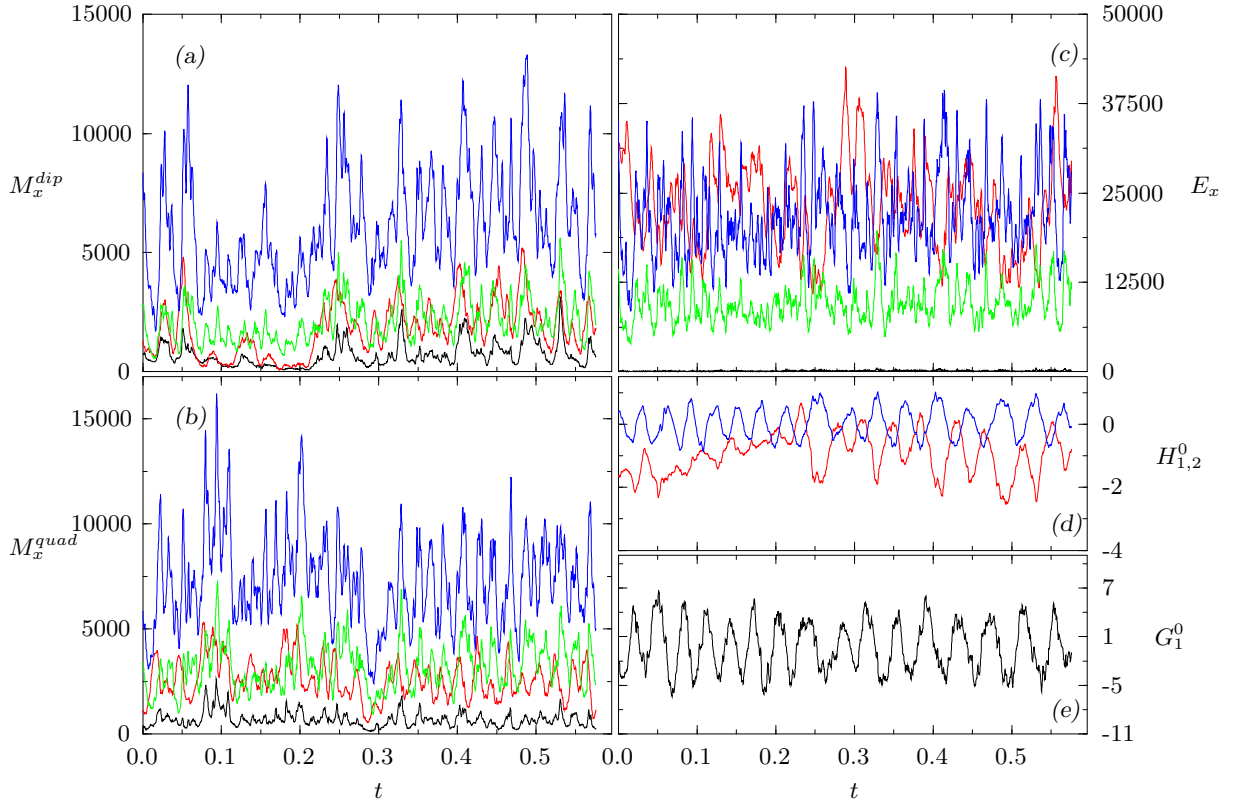
in the other hemisphere. As has been discussed above in section 7.2, such a patchy structure is due to the fact that the coefficients of degree and order $(l + m) =$ odd are dominant in the spherical harmonic expansion of the field, but no single coefficient is much larger than the others as is the case with the H_1^0-dominance of the first two examples. We note once again that such a structure of the magnetic field cannot be predicted solely from observing the structure of convection. The flow is, indeed, typical for the particular parameter region.

The fourth case in figure 7.7 demonstrates a large P quadrupolar dynamo. Magnetic fluxes of opposite polarity appear in broad alternating tubes parallel to the equator and are similar to the perfect symmetry, due to the H_2^0 expansion coefficient (see also figure 7.1). However, contributions from terms of higher order and degree are also noticeable. The most characteristic feature of those fluxes is that they are not stationary but propagate from the equator to the poles in a periodic fashion. The quadrupolar oscillations are of paramount importance to understanding the temporal behavior of dynamos and will be discussed in chapter 9. The alternating-flux-tube pattern is not the only pattern in which equatorially symmetric dynamos appear. A patchy structure similar to that shown for the third dipolar dynamo but with symmetric flux polarities, due to the dominance of a mixture of $(l + m) =$ even expansion coefficients have also been observed in our simulations.

The last example, shown in figure 7.7, represents a hemispherical dynamo [62], obtained in the small P region. At a value of $Pm = 0.11$ it is, in fact, also one of the smallest magnetic Prandtl numbers reached so far. In this particular case the dipolar and quadrupolar contributions are almost exactly equal and the magnetic fluxes neutralize in the northern hemisphere, while they add up in the southern one. This is rather remarkable in view of the fact that the time series are in fact chaotic. Like the quadrupolar dynamos, the hemispherical cases always oscillate.

In all cases of figure 7.7 we observe that the velocity field is equatorially symmetric. This justifies the assertion made in section 7.2 that the velocity field is typically of $\boldsymbol{u}^{\mathcal{E};s}$ type and enables the separation of the various classes of symmetry of the magnetic field. Only in the example of the hemispherical dynamo, minor deviations from equatorial symmetry of $\boldsymbol{u}$ can be seen. It will be argued that this is an effect of the interaction of the magnetic field and convection, and in the case of an absence or a more uniform distribution of the magnetic field, the weak asymmetry of $\boldsymbol{u}$ would disappear.
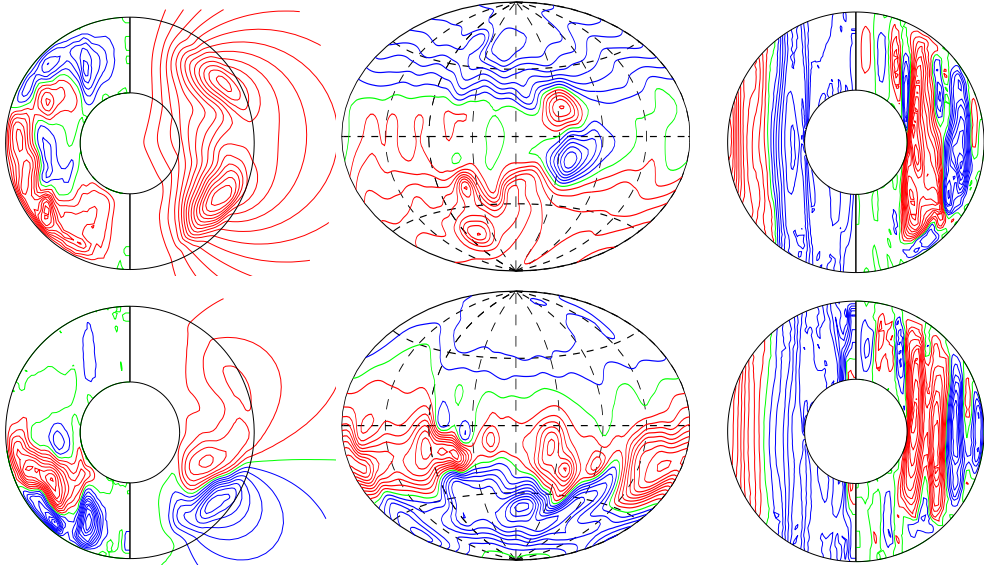
The dynamos presented in the last figure are examples in which the dominating symmetry is well exhibited, similarly to the illustrations of perfect symmetry in figure 7.1. In this, they are rather different from the geodynamo, however, since its symmetry properties are less

Fig. 7.9. *Time series of energy densities and selected coefficients in expression* (4.1) *of a chaotic dynamo in the case* $P = 0.1$, $\tau = 3 \times 10^4$, $R = 1.2 \times 10^6$, $Pm = 0.5$. *Plots (a) and (b) show energy densities of dipolar and quadrupolar components of the magnetic field, while plot (c) shows energy densities of the velocity field. Red, blue, green and black lines indicate* $\overline{E}_t$, $\check{E}_t$, $\overline{E}_p$, $\check{E}_p$, *respectively. Plots (d) and (e) show the values of the coefficients* $H_1^0(r,t)$ *(red line),* $H_2^0(r,t)$ *(blue line) and* $G_1^0(r,t)$, *respectively at* $r = (r_i + r_o)/2$.

evident. This is especially true for the dipolar cases in figure 7.7, which require geophysically unrealistic large value of Pm in order to attain their dipolar dominance. Once the value of Pm is decreased those dynamos cannot persist and are replaced by the much more frequently observed cases in which dipolar and quadrupolar symmetries are mixed. One such example is shown in figure 7.8. It is interesting to observe that the magnetic fluxes have a dipolar symmetry near the poles while a quadrupolar one close to the equator, which is exhibited both in the mean azimuthal component as well as in the radial component of the field. We once again emphasize the important fact that in both figures 7.7 and 7.8 the presence of magnetic field, sometimes, rather strong does not seem to influence convection strongly. The structure of convection shown in the last columns of these figures appears to be much the same as in the simulations of non-magnetic convection. We only point the attention to the effect of the field on differential rotation in figure 7.8. The profile of $\overline{u}_\varphi$ shows a slight tendency towards a thermal wind structure in the presence of the magnetic field, while it would be purely geostrophic in its absence.
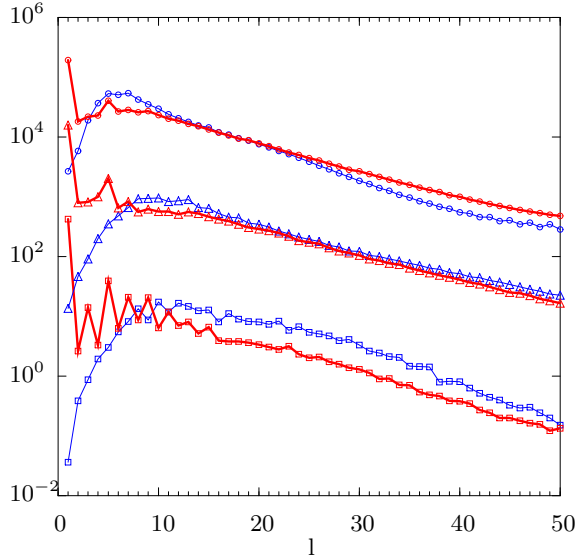
Typical time dependence. So far we have demonstrated some typical spatial and symmetry properties of numerical dynamos. Figure 7.9 presents an example of the time dependence of dynamos illustrated by the time series of the magnetic and kinetic energy densities in the case $P = 0.1$, $\tau = 3 \times 10^4$, $R = 1.2 \times 10^6$ and $Pm = 0.5$. The relatively small value of Pm requires

Fig. 7.10. *The chaotic dynamo of figure 7.9 shown in a predominantly dipolar (upper row, t = 0.02) and a hemispherical state (lower row , t = 0.36). The left column shows lines of constant $\overline{B}_{\varphi}$ (left half) and meridional streamlines $r \sin\theta \partial_\theta \overline{h} = const.$ (right half). The middle column shows isolines of B_r at $r = 1.7 \times r_0$. The right column shows lines of $\overline{u}_\varphi = const.$ (left half) and meridional streamlines $r \sin\theta \partial_\theta v = const.$ (right half).*

a rather large value of R in order to sustain a non-decaying magnetic field. The resulting velocity and magnetic fields are highly chaotic in time as can be seen in the figure. The total magnetic energy which is a sum of the dipolar and quadrupolar components shown in 7.9(a) and 7.9(b), respectively is of the same order as the total kinetic energy, the components of which are exhibited in 7.9(c). Although the equilibration of energies will be addressed in much detail in the next chapter we note several important observations. Firstly, it appears that the dipolar and quadrupolar energy densities are anticorrelated in the sense that when the former are comparatively larger the later are small and vice versa. This feature can be roughly explained by the argument that for a particular energy input measured by the value of R, the total magnetic energy equilibrates to some average value given by the sum of the quadrupolar and the dipolar components. Therefore, when one of them grows the other one must decrease in order to sustain the approximately constant average total energy allowed by the energy input. Secondly, the mean poloidal density $\overline{M}_p$ and the fluctuating densities $\check{M}_p$ and $\check{M}_t$ are well-correlated both for the dipolar and quadrupolar components. The correlation with the mean toroidal energy density $\overline{M}_t$ is not so clearly evident. Both periods during which it is anticorrelated to the other densities as well as periods during which it is correlated with some finite tag can be observed. This behavior of $\overline{M}_t$ is due to the fact that it is generated from the rest of the magnetic energy components by the action of the differential rotation which are in a complex interplay and competition. Indeed, the main effect of the magnetic field on the differential rotation may be seen in 7.9(c). The mean azimuthal flow is strongly reduced and is compatible to $\check{E}_p$ and $\check{E}_t$ in the presence of the field, while it would be much larger than the latter energies in a non-magnetic case.

An important aid in assessing general features of dynamo solutions such as their symmetry and periodicity are the expansion coefficients of the toroidal and poloidal scalar functions defined by (4.1). In figure 7.9(d) and 7.9(e) the most easily interpreted coefficients are shown. $H_1^0(t)$ and $H_2^0(t)$ are the poloidal dipolar and quadrupolar coefficients, respectively. They are

PSfrag replacements

Fig. 7.11. *Time-averaged magnetic (thick red lines) and kinetic (thin blue lines) power spectra integrated over the radial and longitudinal directions in the cases ● $P = 0.1$, $\tau = 3 \times 10^4$, $R = 8.5 \times 10^5$, $Pm = 1$ (circles), ● $P = 0.1$, $\tau = 10^5$, $R = 5 \times 10^6$, $Pm = 0.3$ (triangles) and ● $P = 10$, $\tau = 5 \times 10^3$, $R = 6 \times 10^5$, $Pm = 10$ (squares).*

usually the largest in the expansion, and since only the poloidal part of the field can be observed from outside the spherical shell, they are also the most important ones. Comparing the absolute values of $H_1^0(t)$ and $H_2^0(t)$ the predominant dynamo symmetry can be easily determined. In the particular example of figure 7.9, it is observed that the field is predominantly dipolar for $t < 0.15$, because $|H_1^0| > |H_2^0|$, and with mixed contributions for $t > 0.15$. The fact, the two poloidal coefficients are anticorrelated in the later period indicates that a southern hemispherical dynamo is realized. Indeed, these conclusions are confirmed by figure 7.10 showing plots of the field structure in the two time intervals. It is remarkable that in a single computation the dynamo solution may reside in different states such as a hemispherical and a dipolar one. The toroidal coefficient G_1^0 characterizes the mean toroidal magnetic field component. In the present example, it features a very clear periodic time dependence which is not evident in the chaotic time series of the energy densities. The periodicity in G_1^0 is an indication of a dynamo oscillation typical for all quadrupolar and hemispherical solutions as well as for many dipolar dominated ones. Dynamo oscillations will be a major topic of discussion in chapter 9.

Typical magnetic and kinetic power spectra. Finally, we wish to present examples of typical kinetic and magnetic power spectra of our numerical dynamo solutions. Since the quadrupolar and hemispherical dynamos are less geophysically relevant, we have selected three dipolar dynamos from across the Prandtl number regions as illustrations in figure 7.11. The figure may be used for comparison with actual geomagnetic observations such as in [93], and thus the geophysical relevance of our solutions may be estimated. However, the spectra shown in figure 7.11 are integrated in r and φ directions and in this differ from the observational spectra which are usually given at the core-mantle boundary or at the Earth's surface. The spectra in figure 7.11 have been truncated to degree $l = 50$ in order to show in more detail the contribution from the leading terms, but the numerical simulations have been carried out with a resolution of $l = 96$ in all three cases. An important argument for the geophysical relevance of our dipolar solutions is that the decay of the magnetic power with the spherical degree l is compatible with that reported from observations [93]. Another interesting feature is that the magnetic power has a tendency to drop sharply at $l = 2$ indicating a weak quadrupole and to recover at $l \geq 3$. Such a feature is also observed for the Earth's magnetic field [93]. The amplitude of the power spectra, however, does not always agree well with the geomagnetic values. The discrepancies are not surprising in view of the fact that the parameter values are very different from those estimated for the Earth.

8. Equilibration and Parameter Dependences of Convection-Driven Spherical Dynamos
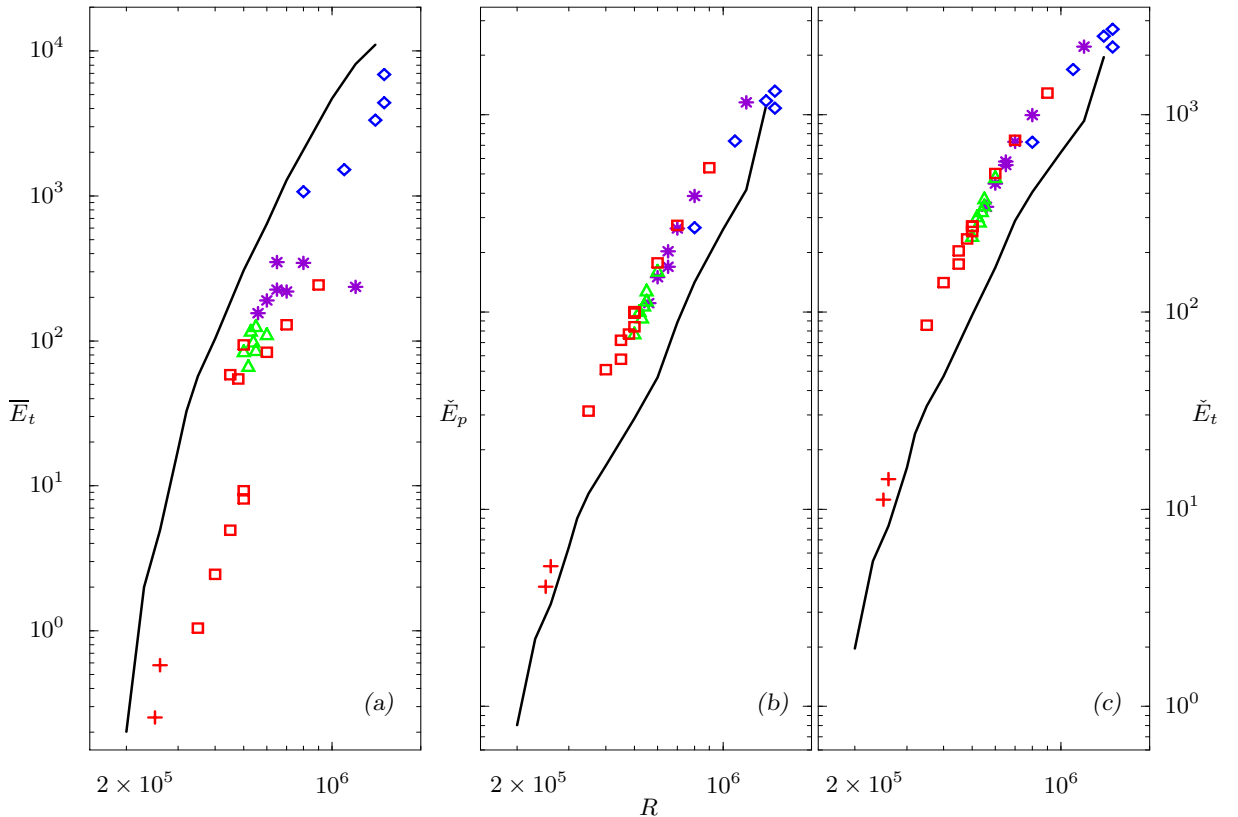
8.1 Introduction

Topic and motivation. In earlier work [56, 76, 80, 30, 94, 59] often particular parameter values have been chosen which seemed to provide the optimal compromise between applicability to the Earth's core and computational efficiency. It now appears that extrapolations to conditions of planetary cores are best obtained on the basis of known dynamo properties over an extended domain in the parameter space. In this chapter we thus analyze the dependence of convection-driven dynamos on the parameters of the problem.

Contents. Our observations of the interaction between self-generated magnetic fields and convection flows are discussed in section 8.2 and the influence of various boundary conditions is outlined in section 8.3. Results on the equilibration of magnetic and kinetic energies and other global properties of the dynamo solutions are presented in section 8.4. One of the major goals of studying parameter dependences is the possible discovery of approximate scaling relationships which would permit the elimination of one or more parameters from the problem. In the magnetostrophic approximation the Prandtl number dependence is dropped which is justified in the case of large P [56]. For large Pm the magnetostrophic approximation can also be expected to hold as we shall discuss in subsection 8.4.3.

8.2 Interaction between magnetic fields and convection

Mechanisms of magnetic field generation. Some basic results on conditions necessary for dynamo action and antidynamo theorems as well as the mechanisms of generation of a toroidal field from a poloidal one and vise versa by α- and ω-effects have already been outlined in section 2.2.2. Although those concepts are kinematic and essentially linear, it has been demonstrated that in some modified form they apply to the self-consistent generation of magnetic fields by convection [77, 94, 71]. Kageyama and Sato [77] have argued that their model is of $\alpha\omega$-type in which the toroidal field is generated from the poloidal one by the ω-effect of the mean zonal flow while the generation of the poloidal field from the toroidal one is due to a large-scale α-effect in which the toroidal field lines are drawn between two neighboring convection columns and subsequently stretched in vertical direction by the meridional motions within the columns. A very similar process of transformation of the toroidal into poloidal filed lines has been reported by Olson *et al.* [94] in a magnetoconvection study, but the ω-effect is rather weak due to the no-slip velocity boundary conditions and thus their model is more likely an α^2-dynamo. Our simulations with stress-free boundary conditions exhibit strong differential rotation and certainly support the idea that the ω-effect is an important field generation mechanism. The correlation between the mean azimuthal magnetic and velocity fields will be discussed shortly. However, the detailed processes by which the generation and amplification of the magnetic field occur are very difficult to visualize or explain in terms of simple relations with the flow structures. This task becomes impossible as we strive to reach more realistic parameter values and necessarily increase the value of
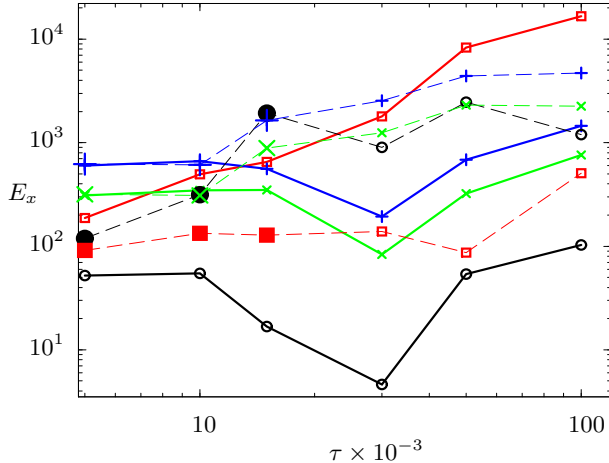
Fig. 8.1. *Time-averaged kinetic energy densities of non-magnetic convection (thick lines) and of quadrupolar (blue diamonds), mixed (violet stars), hemispherical (green triangles), chaotic dipolar (red squares), and regular dipolar dynamo solutions (red plus signs). Both non-magnetic convection and dynamo solutions are in the case $P = 1$ and $\tau = 10^4$. Values of Pm of the dynamo cases may be obtained by comparison with figure 7.2. The densities $\overline{E}_t$, $\check{E}_p$, and $\check{E}_t$ are shown in (a), (b), (c), respectively. $\overline{E}_p$ is relatively small and is omitted.*

the Rayleigh number and as the resulting flows become filamentary and turbulent. In fact, dynamos very close to the onset of convection and unrealistically large values of Pm have been used in [77, 94], and [71] to explain the magnetic field generation mechanism. Even then it has been only possible to illustrate it by cartoons such as figures 5 of [77] and [94].

Interaction between magnetic fields and convection. The problem of rotating magnetoconvection, i.e. convection in rotating systems in the presence of an imposed magnetic field has a long history [36]. It can be formulated as a linear problem when the conditions for the onset of convection are of primary interest. It has been demonstrated that the stabilizing effect of the Coriolis force on the onset of convection in a horizontal fluid layer heated from below and rotating about a vertical axis can be partly released when a vertical magnetic field is imposed leading to a reduction of the critical Rayleigh number R_c [36]. The optimal strength B_0 of the imposed magnetic field for lowering R_c is usually given by an Elsasser number Λ of the order unity where Λ is defined by

$$\Lambda = \frac{B_0^2}{\Omega \varrho \mu \lambda}.$$
(8.1)

In the rotating cylindrical annulus an axisymmetric azimuthal magnetic field also leads to a reduction of R_c if the parameter τ is high enough [17]. The same result has been obtained for
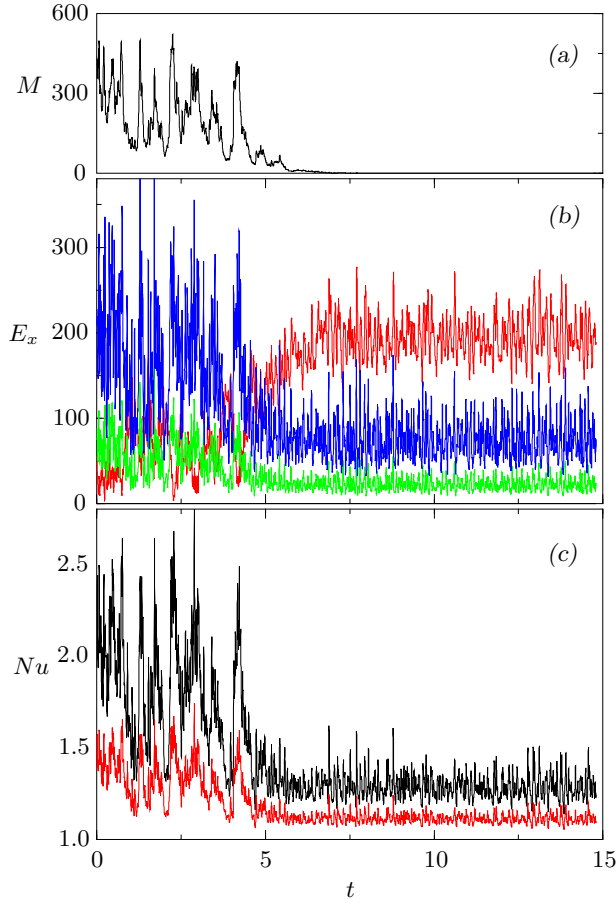
Fig. 8.2. *Time-averaged energy densities $\overline{E}_t$ (red squares), $\check{E}_p$ (blue crosses), $\check{E}_t$ (green plus-signs), $\overline{E}_p$ (black circles, multiplied by factor 10^3) as functions of the Coriolis number τ for the non-magnetic cases $P = 0.1$, $R = 2 \times R_c$ (thick solid lines) and for the corresponding dynamo cases (broken lines) with $Pm = 5$ (open symbols) and $Pm = 10$ (large filled symbols). The values of the critical Rayleigh numbers R_c are listed in table 6.1.*

an axisymmetric radial field and for the case of convection in the presence of an azimuthal magnetic field in a rotating sphere [50]. Whenever inhomogeneous magnetic fields are imposed such as a curved azimuthal one in the case of the sphere, the possibility of magnetic instability must be taken into account. Except for this latter possibility the optimal field strength for the reduction of R_c corresponds to an Elsasser number of the order unity and the characteristic wavenumber m of convection is reduced in comparison to the non-magnetic case. Nonlinear properties of convection subject to both, the effects of rotation and of an imposed azimuthal magnetic field, have also been studied [95, 123].

The interaction of convection with a magnetic field generated by its own dynamo action appears to be quite different from that with an imposed magnetic field. The fundamental reason for this is, of course, the nonlinear feedback between the magnetic and the velocity fields. As the magnetic field is amplified by the convective flow, the Lorentz force eventually becomes important, its back-reaction on the flow modifies the velocity field and leads to the saturation of the magnetic field and a new equilibrium of the velocity field. Much of this chapter reports results on those processes throughout the parameter space. However, because of their essential nonlinear nature straightforward conclusions are difficult to make. Therefore, we approach the topic in steps and in the rest of this section we consider explicitly how the generated magnetic field modifies the convection flow and leads to its new equilibrium.
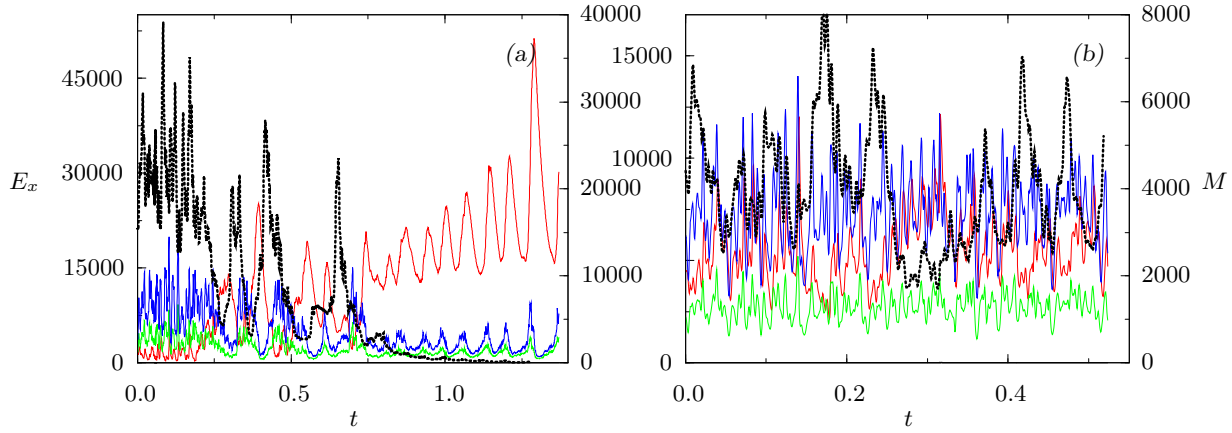
Compared to magnetoconvection, no reduction of the critical Rayleigh number R_c for onset of convection has yet been found in the case of convection-driven dynamos. The decrease in the value of the characteristic azimuthal wavenumber m of columns is also insignificant in our simulations. The major effects of self-generated magnetic fields on convection in fluids with P of the order unity are illustrated in figure 8.1 which presents a comparison between the time-averaged kinetic energy densities of non-magnetic convection solutions and those of dynamo solutions with equilibrated magnetic fields. Breaking of the differential rotation is the most important effect of the magnetic field on convection. As it can be observed in figure 8.1(a), the energy density of the mean zonal flow $\overline{E}_t^{dyn}$ of all dynamo cases is significantly weaker than the corresponding energy density $\overline{E}_t^{conv}$ of the non-magnetic cases. In chapter 6 the suppression of radial and fluctuating motions and the resulting decrease of all other energy densities has been identified as the major effect of the differential rotation on the convective flow. Now because the magnetic field weakens the differential rotation, it relaxes the inhibiting effect imposed by the mean zonal flow on all other convection components. Indeed, the increase in the values of the fluctuating poloidal and toroidal kinetic energy densities can now be readily seen in figures 8.1(b) and (c),

$$\check{E}_p^{dyn} \approx 2.8 \times \check{E}_p^{conv}, \qquad \check{E}_t^{dyn} \approx 2.8 \times \check{E}_t^{conv}. \tag{8.2}$$

PSfrag replacements

0

Fig. 8.3. *Decay of a dynamo for $P = 1$, $\tau = 10^4$, $R = 4.5 \times 10^5$, $Pm = 7$. The total magnetic M (in (a)), the mean toroidal $\overline{E}_t$ (red line), the fluctuating poloidal $\check{E}_p$ (green line), the fluctuating toroidal $\check{E}_t$ (blue line) kinetic energy densities (in (b)), and Nusselt numbers Nu_i (black line) at the inner and Nu_o (red line) at the outer spherical boundary (in (c)) are plotted as functions of time t.*

A further remarkable observation is that these effects appear to be almost independent of the values of Pm and the type of symmetry of the dynamo solutions. Indeed, note that in figure 8.1 the values $P = 1$ and $\tau = 10$ are kept fixed but various values of Pm are allowed in an attempt to include the majority of the equilibrated dynamo solutions obtained in this region. The value of Pm varies by two orders of magnitude from 50, for the regular dipolar dynamos simulated near the onset of convection, to 0.4, for the highly chaotic quadrupolar dynamos. In all these cases which feature immensely different magnetic and velocity fields, the values of the fluctuating components seem to change by a roughly equal amount given by expressions (8.2). Only minor deviations can be observed due to the effects of the variation of R rather than of Pm or the type of dynamo solutions. Indeed, $\check{E}_p^{dyn}$ and $\check{E}_t^{dyn}$ disobey approximation (8.2) only towards the smallest and the largest values of R. These several cases are marginal in the sense that they have been obtained near the borders of dynamo action. Those marginal cases have been simulated in order to reach a value of Pm as small as possible or to obtain steadily-drifting and periodic magnetic fields in the case of the quadrupolar and regular dipolar dynamos, respectively. The reduction of $\overline{E}_t$, however, is not as uniform for all dynamo cases as the increase in the fluctuating components, and it may again be argued, that this effect is due to the variation of the Rayleigh number R. At small values of R of the order 2×10^5 the differential rotation is very weak even in the absence of a magnetic field, since this is the regime of steadily-drifting and periodic convection. At values of R about 5×10^5 the transition from chaotic to localized convection and relaxation oscillations occur in the case of non-magnetic convection. It is interesting to observe that near this value of R the differential rotation seems to saturate in the presence of a magnetic field. However, with the further increase of the Rayleigh number the saturation cannot persist. Unlike in
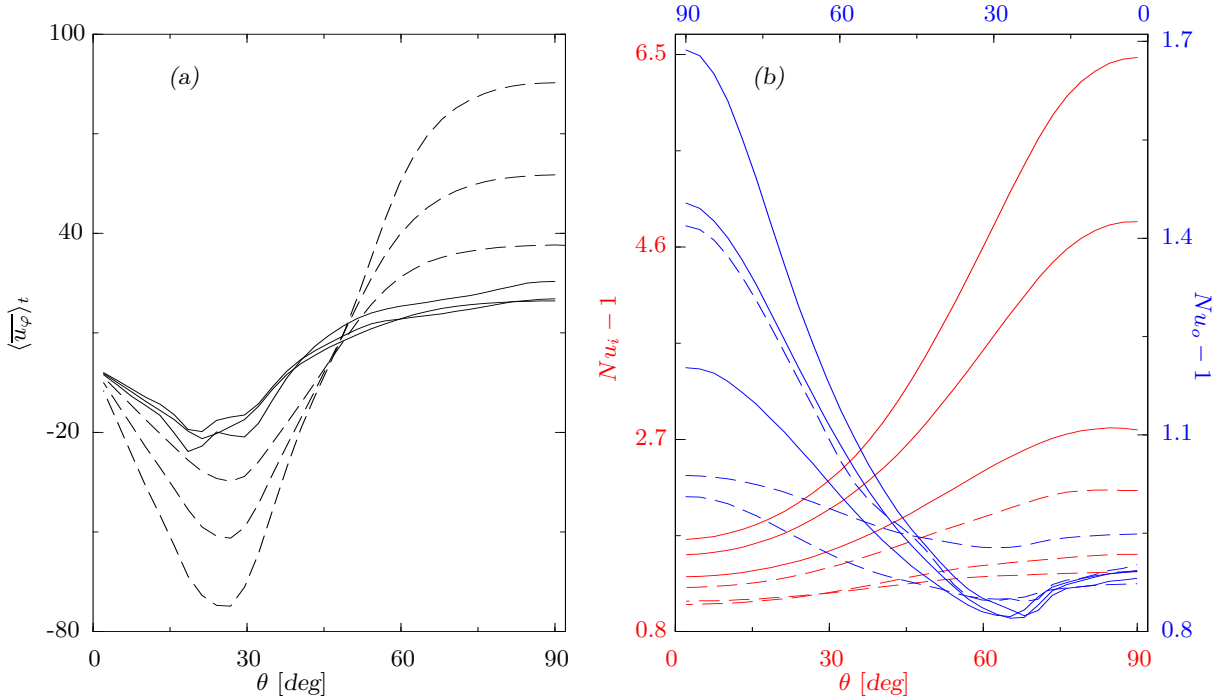
Fig. 8.4. *(a) Transition from a dynamo state to a state of relaxation oscillations for stress-free boundary conditions compared to (b) a stable dynamo state for no-slip boundary conditions both at $P = 0.1$, $\tau = 3 \times 10^4$, $R = 8 \times 10^5$, $Pm = 1$. The total magnetic energy densities M are shown as thick dotted black lines using the right ordinates and the kinetic energy densities are shown in the color code of figure 7.9 using the left ordinates.*

non-magnetic convection, the states of localized convection and relaxation oscillations have never been observed in dynamo simulations.
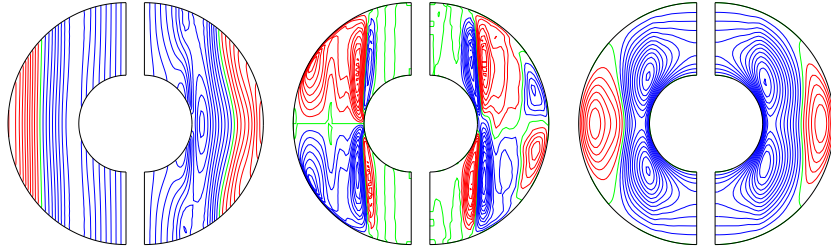
In order to explore the influence of magnetic fields on convection in dependence of the Coriolis number we present figure 8.2 where non-magnetic convection and dynamo cases at the same parameter values are shown. The similar figure 6.30 showing only the non-magnetic cases has been discussed in section 6.3.3. The surprising decrease of the energy densities at intermediate values of τ has been attributed to the transition from inertial to columnar convection and the simultaneous increase of differential rotation. As the magnetic field relaxes the inhibiting action of the differential rotation, the remaining energy density components increase in figure 8.2 both from their non-magnetic values and as functions of τ.

The reduction of differential rotation in the presence of magnetic fields is strikingly demonstrated in marginal cases, where the magnetic field is on a sensitive equilibrium and may decay as a result of a significantly large fluctuation of the velocity field. Figure 8.3 shows a typical example for which the value of the magnetic Reynolds number is close to the critical value for dynamo action. The dynamo operates with a magnetic energy compatible to the kinetic one for several magnetic diffusion times but later suddenly decays. In this process the differential rotation which has been strongly suppressed in the presence of the field has an opportunity to grow. Once it increases to its convective equilibrium it suppresses the fluctuating poloidal and toroidal components of motion. As can be seen in figure 8.3(c), this leads to a strong decrease in the heat transport measured by the Nusselt number.

Figure 8.4 emphasizes two further points. Its left panel *(a)* presents a dynamo solution with stress-free boundary conditions for the velocity field. After a decay of the magnetic field very similar to the one just described in connection with figure 8.3, the differential rotation recovers to its non-magnetic size. However, in this case it is so strong that convection enters the state of relaxation oscillations. Thus, the presence of self-sustained magnetic fields not only reduces differential rotation but may lead to a very different dynamical regime by inhibiting the coherent structures of non-magnetic convection. The second observation concerns a comparison with a dynamo solutions at the same values of the basic parameters but with no-slip velocity boundary conditions which is shown in panel *(b)* of the same figure. The no-slip boundary conditions lead to a much weaker differential rotation in comparison with the stress-free ones. For this reason the mean zonal flow of the case shown in figure
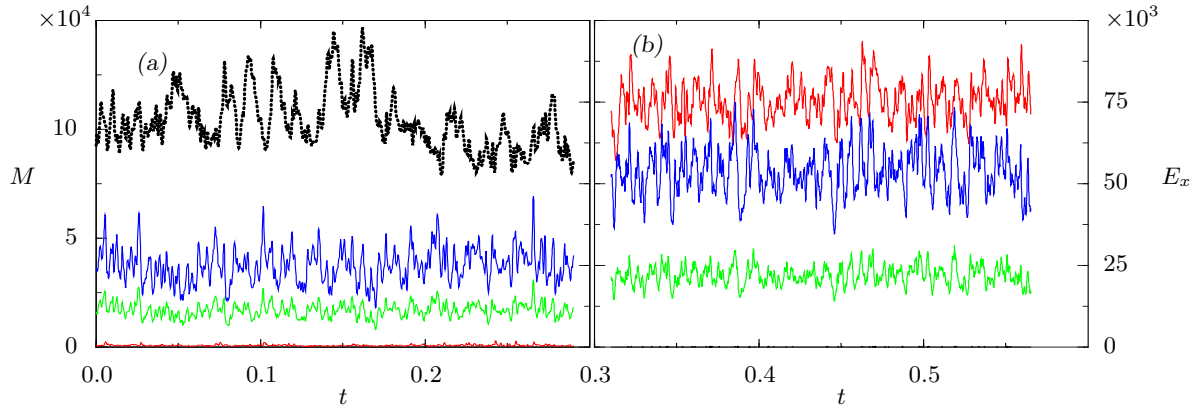
Fig. 8.5. *Time- and azimuthally-averaged* $\langle\overline{u_\varphi}\rangle_t$ *at the outer spherical boundary in (a) and local* Nu_i *(red lines, left ordinate, lower abscissa) and* Nu_o *(blue lines, right ordinate, upper abscissa) in (b) as functions of the colatitude* θ *for* $P = 1$, $\tau = 10^4$*. From bottom to top at* $\theta = 90°$ *the values of* R *are* $R = 5 \times 10^5$, 6×10^5 *and* 7×10^5 *for both non-magnetic convection (dashed lines) and dynamo solutions with* $Pm = 6$ *(solid lines).*


Fig. 8.6. *Effects of magnetic fields on convection. All left halves show non-magnetic convection for* $P = 1$, $\tau = 10^4$, $R = 7 \times 10^5$ *and all right halves show the dynamo solution at the same parameters and* $Pm = 6$*. The first, second and third pair of plots show the time- and azimuthally-averaged* $\langle\overline{u_\varphi}\rangle_t$*, meridional circulation, and* $\langle\overline{\Theta}\rangle_t$*, respectively.*

8.4(b) never increases sufficiently to cause a decay of the magnetic field as in the case of stress-free boundary conditions in 8.4(a).

We finally present in figures 8.5 and 8.6 time- and azimuthally-averaged profiles of differential rotation, Nusselt number and contour lines of meridional circulation and temperature perturbation. The results may once again be explained with the decrease of the differential rotation in the presence of magnetic fields. It is interesting to notice in figure 8.5(a) that the profiles of $\langle\overline{u_\varphi}\rangle_t$ become almost identical for the three dynamo solutions while they differ significantly in amplitude in the corresponding non-magnetic cases. This effect has already been pointed out in connection with the saturation of the differential rotation at intermediate values of R in figure 8.1. Apart from the effects evident in figure 8.6, we draw the attention

Fig. 8.7. *Decrease of all kinetic energy densities in the presence of magnetic field in the dynamo case $P = 0.1$, $\tau = 10^5$, $R = 4 \times 10^6$, $Pm = 0.5$ in (a) compared to the corresponding non-magnetic convection in (b), both at no-slip boundary conditions. The total magnetic density M is shown as thick black lines using the right ordinates and the kinetic densities are shown in the color code of figure 7.9 using the left ordinates.*

to the fact that the presence of a magnetic field may lead to equatorial asymmetry in the velocity field as may be seen in figure 7.7, where a hemispherical dynamo solution is shown.

8.3 Effects of boundary conditions on dynamo solutions
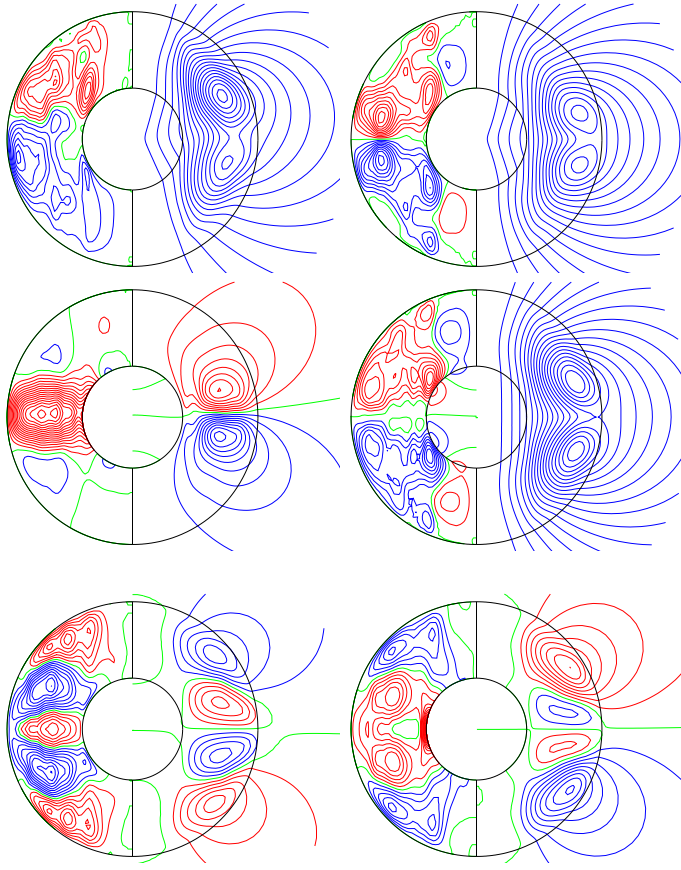
Because published dynamo solutions utilize different parameter values and mechanical, thermal and magnetic boundary conditions, a systematic comparison between various models is difficult to conduct. Attempts to investigate the differences between numerical models based on various assumptions have most recently been made by Kutzner and Christensen [81, 82]. Both studies focus of the mechanisms driving the system and consider thermal and compositional driving with internal or external distribution of energy sources and a variety of thermal boundary conditions. Here we complement their studies with a few brief remarks outlining the possible effects of various velocity and magnetic boundary conditions. Such comparisons have not been pursued in detail, because it is neither possible nor reasonable for a single workgroup to repeat all of its simulations in the entire parameter space for all combinations of boundary conditions. Therefore, we have adopted the following strategy. In the major part of the dissertation we focus on electrically insulating inner and outer regions with stress-free velocity boundary conditions and fixed-temperature thermal boundary conditions. In this section, we have selected two dynamo solutions which, when computed using our standard assumptions, belong to the two main types of dynamo symmetry. Furthermore, in order to simultaneously assess the influence of the parameter values, one of the cases is situated in the small P region while the other one in the large P region. The dynamo at parameter values $P = 0.1$, $\tau = 10^5$, $R = 4 \times 10^6$, $Pm = 0.5$ has a dipolar symmetry while the solution at $P = 5$, $\tau = 5 \times 10^3$, $R = 8 \times 10^5$, $Pm = 3$ has a quadrupolar one. We have repeated the simulations of these two cases for four types of models with various combinations between boundary conditions as follows. Type **A** uses stress-free boundary conditions for the velocity and insulating boundary conditions for the magnetic filed, type **B** adopts no-slip and insulating conditions, type **C** – no-slip conditions and a finitely-conducting inner core and finally type **D** has stress-free velocity boundary conditions and a perfectly-conducting inner core. Our normal assumption of a temperature gradient due to homogeneously distributed heat

Table 8.1. *Time-averaged global properties of dynamos with various velocity and magnetic boundary conditions as follows.* **A***: stress-free and insulating,* **B***: no-slip and insulating,* **C***: no-slip and a finitely-conducting inner core and* **D***: stress-free and a perfectly-conducting inner core. The predominant symmetry type is indicated with "D" if dipolar, "Q" if quadrupolar and "–" if the dynamo is decaying.*

	$P = 0.1,\ \tau = 10^5,\ R = 4 \times 10^6,\ Pm = 0.5$				$P = 5,\ \tau = 5 \times 10^3,\ R = 8 \times 10^5,\ Pm = 3$			
	A	B	C	D	A	B	C	D
Type	D	D	D	Q	Q	–	–	Q
$\overline{E}_p$	$.286{\times}10^2$	$.112{\times}10^2$	$.108{\times}10^2$	$.299{\times}10^2$	$.157$	$.611$	$.523$	$.147$
$\overline{E}_t$	$.599{\times}10^4$	$.647{\times}10^3$	$.807{\times}10^3$	$.764{\times}10^4$	$.533{\times}10^2$	$.105{\times}10^2$	$.106{\times}10^2$	$.528{\times}10^2$
$\check{E}_p$	$.142{\times}10^5$	$.115{\times}10^5$	$.121{\times}10^5$	$.138{\times}10^5$	$.574{\times}10^2$	$.614{\times}10^2$	$.611{\times}10^2$	$.566{\times}10^2$
$\check{E}_t$	$.336{\times}10^5$	$.257{\times}10^5$	$.273{\times}10^5$	$.247{\times}10^5$	$.119{\times}10^3$	$.983{\times}10^2$	$.952{\times}10^2$	$.119{\times}10^3$
$\overline{M}_p$	$.129{\times}10^5$	$.392{\times}10^5$	$.355{\times}10^5$	$.768{\times}10^3$	$.487{\times}10$	–	–	$.466{\times}10$
$\overline{M}_t$	$.133{\times}10^5$	$.879{\times}10^4$	$.716{\times}10^4$	$.538{\times}10^5$	$.325{\times}10$	–	–	$.336{\times}10$
$\check{M}_p$	$.136{\times}10^5$	$.169{\times}10^5$	$.147{\times}10^5$	$.148{\times}10^5$	$.818{\times}10$	–	–	$.837{\times}10$
$\check{M}_t$	$.307{\times}10^5$	$.345{\times}10^5$	$.327{\times}10^5$	$.448{\times}10^4$	$.109{\times}10^2$	–	–	$.110{\times}10^2$
$\overline{V}_p$	$.643{\times}10^5$	$.104{\times}10^6$	$.122{\times}10^6$	$.462{\times}10^5$	$.151{\times}10^3$	$.111{\times}10^4$	$.686{\times}10^3$	$.140{\times}10^3$
$\overline{V}_t$	$.584{\times}10^6$	$.366{\times}10^6$	$.348{\times}10^6$	$.709{\times}10^6$	$.182{\times}10^4$	$.342{\times}10^4$	$.245{\times}10^4$	$.179{\times}10^4$
$\check{V}_p$	$.133{\times}10^8$	$.179{\times}10^8$	$.191{\times}10^8$	$.125{\times}10^8$	$.414{\times}10^5$	$.524{\times}10^5$	$.528{\times}10^5$	$.406{\times}10^5$
$\check{V}_t$	$.229{\times}10^8$	$.354{\times}10^8$	$.372{\times}10^8$	$.171{\times}10^8$	$.455{\times}10^5$	$.580{\times}10^5$	$.568{\times}10^5$	$.450{\times}10^5$
$\overline{O}_p$	$.626{\times}10^6$	$.129{\times}10^7$	$.120{\times}10^7$	$.874{\times}10^5$	$.544{\times}10^3$	–	–	$.520{\times}10^3$
$\overline{O}_t$	$.148{\times}10^7$	$.944{\times}10^6$	$.890{\times}10^6$	$.222{\times}10^7$	$.359{\times}10^3$	–	–	$.372{\times}10^3$
$\check{O}_p$	$.125{\times}10^8$	$.138{\times}10^8$	$.133{\times}10^8$	$.106{\times}10^8$	$.468{\times}10^4$	–	–	$.488{\times}10^4$
$\check{O}_t$	$.253{\times}10^8$	$.268{\times}10^8$	$.276{\times}10^8$	$.362{\times}10^7$	$.600{\times}10^4$	–	–	$.587{\times}10^4$
Λ	$.707$	$.995$	$.902$	$.740$	$.032$	–	–	$.032$
Rm	164	138	142	152	64	55	55	64
Nu_i	2.125	2.275	2.316	1.563	11.285	12.968	12.729	11.194

sources and fixed-temperature thermal boundary conditions are used in all four models. A detailed comparison between the most important global observables characterizing the eight dynamos is presented in table 8.1 and snapshots of the spatial structure of the corresponding solutions for the magnetic field are shown in figures 8.8 and 8.9.
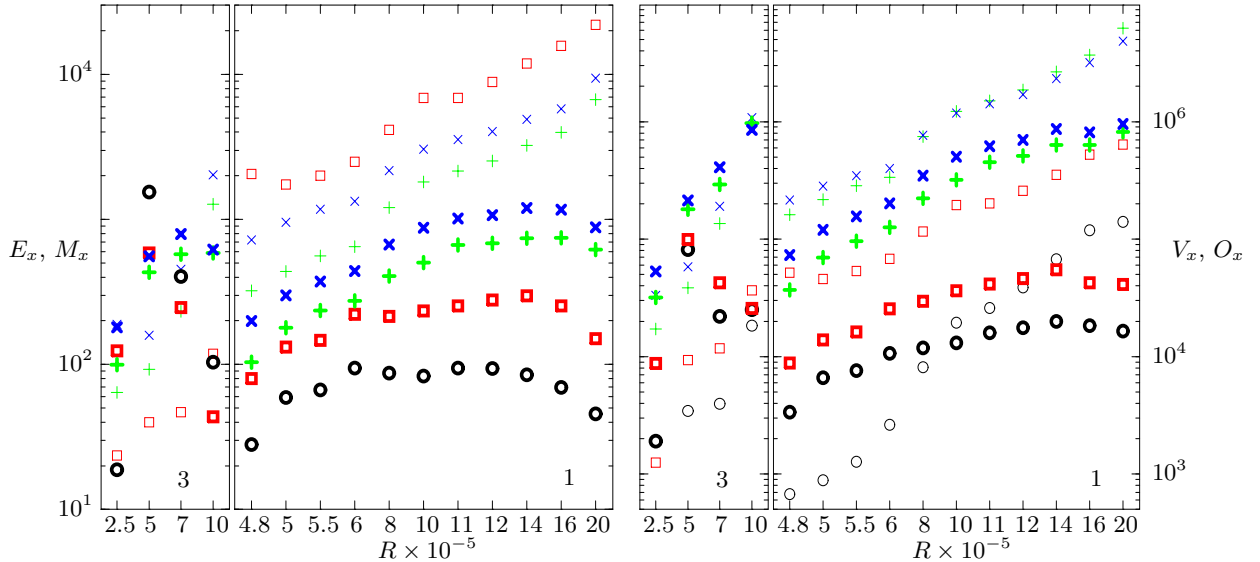
The change of the velocity boundary conditions has a most direct effect on the convection flow which in turn modifies the magnetic field. The major effect of the replacement of stress-free boundary conditions by no-slip ones in non-magnetic convection simulations is a decrease of all energy densities which is most significant for the differential rotation. This effect is not unexpected because the velocity field is forced to be zero on the boundary in the later case while it may have a finite value in the former. One important consequence is, in particular, that the differential rotation cannot become sufficiently strong to cause a significant suppression of the convective motions and to generate coherent structures such as localized convection and relaxation oscillations. Indeed, these phenomena have not been observed in our no-slip simulations. Because of those effects of the no-slip boundary conditions on convection, a major difference between the stress-free and the no-slip dynamo solutions is found in the way magnetic fields affect convective flows. Figure 8.1 has convincingly demonstrated that in the case of stress-free conditions magnetic fields enhance radial and fluctuating motions and increase their energy densities and the heat transport. In order

Fig. 8.8. *Effects of various boundary conditions on dynamo solutions for $P = 0.1$, $\tau = 10^5$, $R = 4 \times 10^6$, $Pm = 0.5$ and in clockwise direction cases* **A**, **B**, **C** *and* **D** *as described in the caption of table 8.1. The left halves of each plot show lines of constant zonal component of the magnetic field $\overline{B}_\varphi$ and the right halves show meridional field lines of the axisymmetric component of $\boldsymbol{B}$, $r \sin\theta \partial_\theta h = const.$ at particular moments in time.*

Fig. 8.9. *Same as figure 8.8 but for cases* **A** *and* **D** *at values of the parameters $P = 5$, $\tau = 5 \times 10^3$, $R = 8 \times 10^5$, $Pm = 3$.*

to assess the effect of the magnetic field in the case of no-slip conditions we have simulated a dynamo solution, the magnetic field of which has been later removed and the case continued as a non-magnetic convection case. The results are presented in figure 8.7. Surprisingly and contrary to the results shown in figure 8.1, all energy densities including $\check{E}_p$ and $\check{E}_t$ increase from the values they exhibited in the presence of the magnetic field. This behavior can be explained as follows. When the magnetic field is artificially removed, the energy which the dynamo action has consumed becomes available to the convective flow. Since differential rotation in the case of no-slip boundary conditions is much less significant and cannot act to suppress convection, the release of additional energy is distributed between all components of the flow. Therefore the main effect which a self-sustained magnetic field has on no-slip convection, is not to relax the inhibiting action of the differential rotation, which is small altogether, but rather to suppress the vigor of all convection components by draining their energies. Based on these observations the results presented in table 8.1 are easy to explain. Indeed, as expected, the kinetic energy densities of the no-slip dynamos are smaller than the corresponding stress-free ones. The differential rotation shows the largest decrease, leading to the surprising result that although the kinetic energy of the no-slip dynamos is smaller than that of the stress-free dynamos, the heat transport measured by the Nusselt number is larger for the former. The same effect is observed for the energy densities of the magnetic field. Except for the mean toroidal magnetic energy density $\overline{M}_t$ which is most dependent on differential rotation, all other magnetic energy components increase in the case of no-slip boundary conditions, because they are disturbed little by the differential rotation and the vigorous velocity fluctuations. However, in the second group of dynamo solutions shown in the right-hand side of table 8.1 just the opposite effect is observed. Not only does the magnetic energy not increase when no-slip conditions are used but the magnetic fields entirely
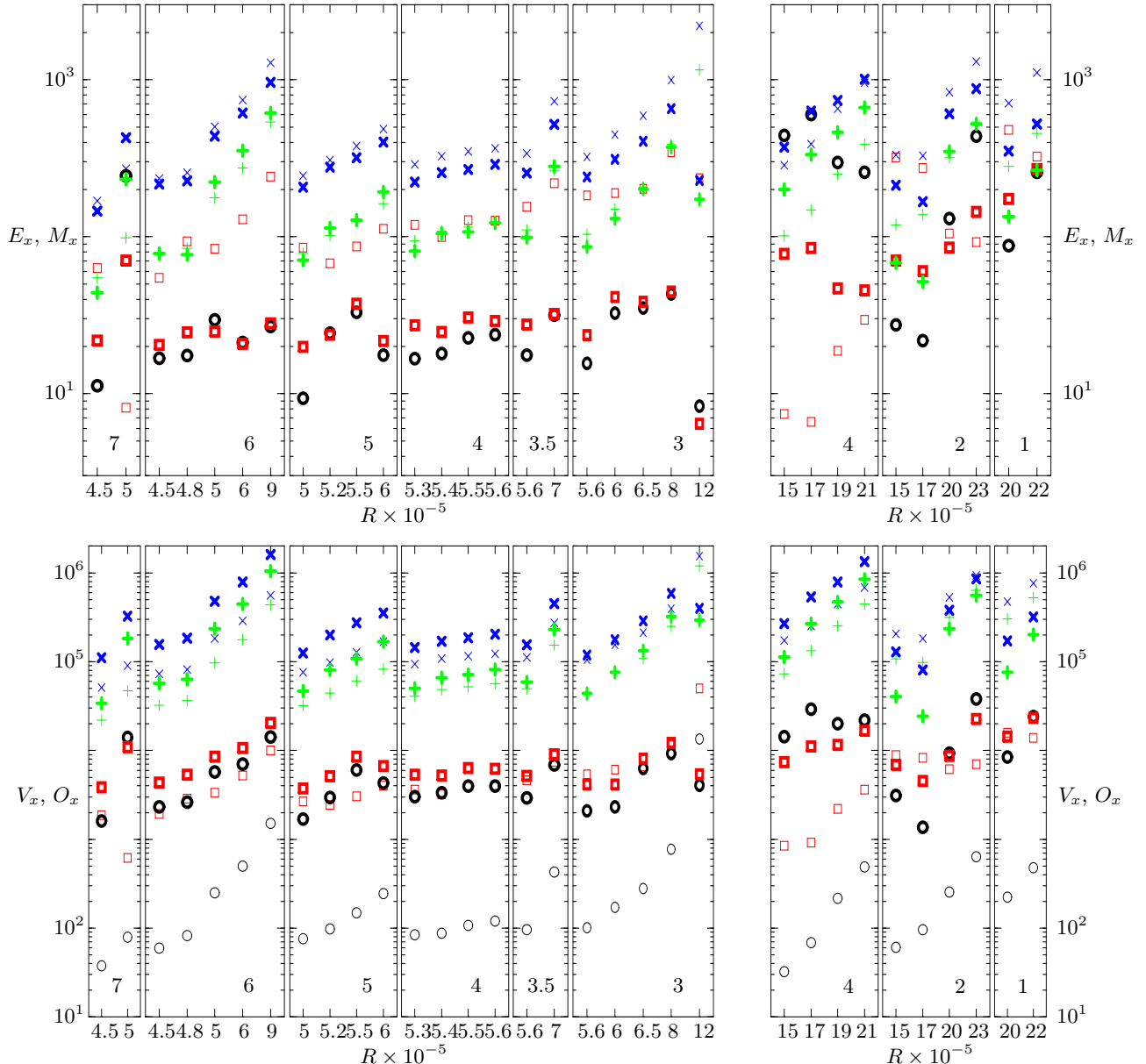
Fig. 8.10. *Kinetic E_x and magnetic energy densities M_x (left plot) and viscous V_x and Ohmic dissipations O_x (right plot) as functions of R for convection-driven dynamos in the case $P = 1$, $\tau = 5 \times 10^3$ and Pm as indicated at the bottom of the plots. The components $\overline{X}_p$, $\overline{X}_t$, $\check{X}_p$, $\check{X}_t$, where $X = E, M, V, O$, are represented by black circles, red squares, green plus-signs and blue crosses, respectively. Kinetic energy densities and viscous dissipations are shown with light symbols, magnetic energy densities and Ohmic dissipations are shown with heavy symbols.*

decay. This illustrates a situation when the vigor of the flow decreased due to the no-slip conditions is just not sufficient to support dynamo action. Indeed, this may be observed in the values of the magnetic Reynolds number Rm in the table. A fact which is not evident in table 8.1 but may be seen in figure 8.8 is that the no-slip conditions strongly increase the dominance of the dipolar magnetic components for the cases shown in the left-hand side of table 8.1. While the dipole oscillates when the stress-free conditions are used and quadrupolar components become significant for short periods during simulation the imposition of no-slip conditions stabilizes the dipole and leads to a perfect dipolar symmetry.

The effects of magnetic boundary conditions on dynamo solutions are equally dramatic. The perfectly conducting inner core appears to increase significantly the preference for quadrupolar solutions and the regions where they are obtained. The replacement of the electrically insulating inner core with a perfectly conducting one, for instance, leads to a change in the type of dynamo symmetry, as can be observed in figure 8.8. The quadrupolar dynamo found in the case $P = 0.1$, $\tau = 10^5$, $R = 4 \times 10^6$, $Pm = 0.5$ and boundary conditions of type **D** is most extraordinary. As will be discussed in the following chapter all quadrupolar dynamos are oscillatory in nature. This case, however, does not change significantly its appearance in time.

The effect of the introduction of an inner core with a finite conductivity equal to that of the fluid is minor. Indeed, a comparison between the models **B** and **C**, for both the dipolar small P dynamos and the quadrupolar large P ones, shows that they are almost identical. The convection energy components differ insignificantly, with the most important difference being a slightly larger differential rotation in the case of a conducting inner core. This is due to the fact that once the inner core is spun by the viscous and Lorentz torques (3.41) the velocity at the inner boundary does not have to vanish with respect to the outer boundary as in the case of insulating inner and outer regions which are motionless relative to each other. The magnetic field penetrates into the conducting inner core only very weakly. The effects
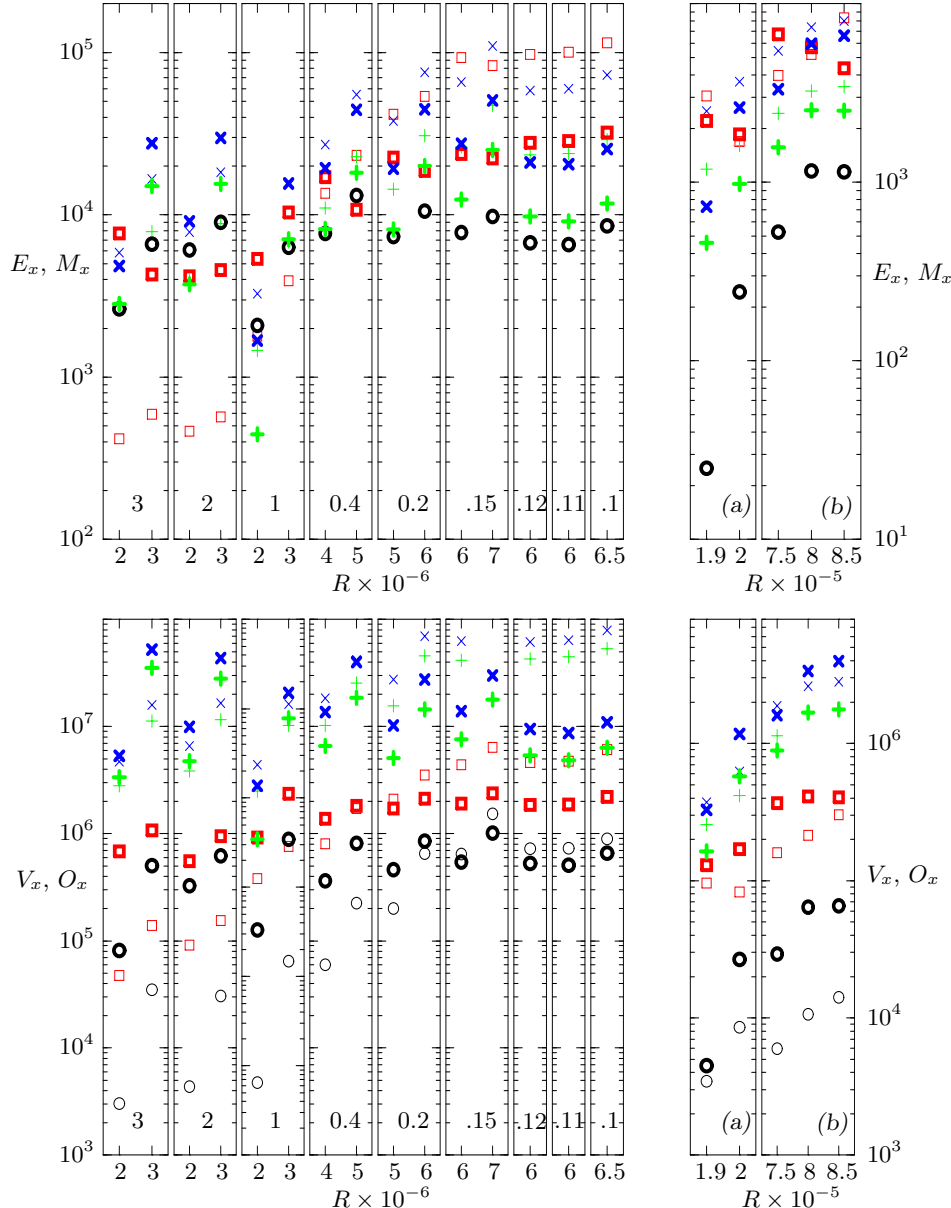
Fig. 8.11. *Same as figure 8.10 but in the case $P = 1$, $\tau = 10^4$ (left column) and $\tau = 3 \times 10^4$ (right column).*

due to a conducting inner core suggested by [69] have not been observed in our simulations. In accordance with the results of [116], we generally find that once the solution is chaotic, the magnetic field cannot penetrate deep into the inner core which adjusts on a longer timescale to the magnetic changes. Therefore, the inclusion of the inner core conductivity into the simulations has no effect on reversals or on the general structure of the solution.

8.4 Parameter dependences
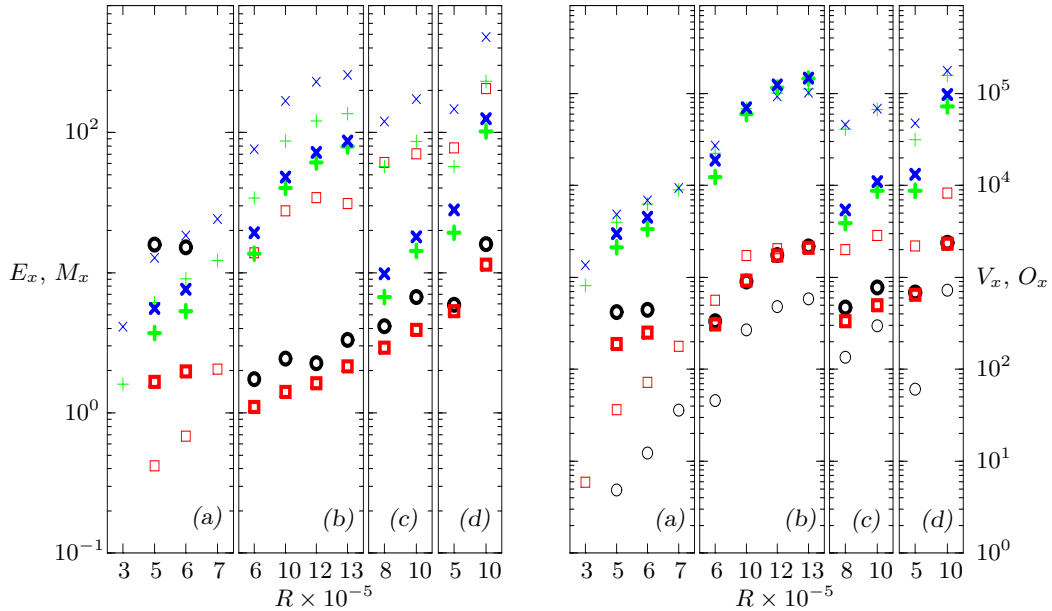
Having discussed how convective flows are modified by the magnetic fields generated by their dynamo action, we proceed to address the main question of the equilibration of spherical dynamos, namely the question of the mean amplitude of magnetic and velocity fields. With

Fig. 8.12. *Same as figure 8.10 but in the case $P = 0.1$, $\tau = 10^5$ (left column) and $P = 0.1$ and (a) $\tau = 10^4$, $Pm = 2$, (b) $\tau = 3 \times 10^4$, $Pm = 1$ (right column).*

this in mind extensive computations have been performed to produce the dependences of the energies of the various components of magnetic and velocity fields as well as of the viscous and ohmic dissipations on the basic parameters of the problem.

In order to study the dependence on the parameters we present a number of solutions in the moderate, small and large Prandtl number regions. The solutions are collected in sequences in which three of the parameters are fixed and the last one is allowed to vary. Some sequences, however, are rather short and consist only of two or three cases. There are two reasons for this. The main one is, as often discussed so far, of computational character. For the values of three parameters fixed, it is often impossible to vary the last one outside some limited interval, and when possible the simulations are time and resource consuming. Thus we have been restricted to constructing one or two main longer sequences. The second

Fig. 8.13. *Same as figure 8.10 but in the cases $\tau = 5 \times 10^3$ and (a) $P = 10$, $Pm = 10$, (b) $P = 5$, $Pm = 10$, (c) $P = 5$, $Pm = 3$ and (d) $P = 3$, $Pm = 3$.*

reason is the desire to carry out simulations in regions which are as close as possible to the conditions estimated for the Earth's core, e.g. to reach very small values of Pm and large values of τ. However, it has been impossible to achieve this by variation of just one parameter while all three others are kept fixed. Usually more than one parameter value has to be adjusted simultaneously. Proceeding in this fashion we have explored "stripes" in the parameter space, rather than "straight line cuts". Furthermore, it has been impossible to, fit or approximate the results by any reasonable expression which would be valid for the majority of sequences. Therefore, in order to represent those "stripes" in the parameters space we have grouped the sequences into "super-sequences", in which now the values of two parameters vary and those of the other two are kept fixed.

Although the energies are obtained from averages over several Ohmic or viscous decay times, the influence of the statistical fluctuations cannot be eliminated entirely and the curves shown in the following figures are not as smooth as can be expected if computations would be continued over much longer periods in time. However, each average is taken over time period sufficient to represent a meaningful value of the corresponding quantity.

8.4.1 Dependence on the Rayleigh number
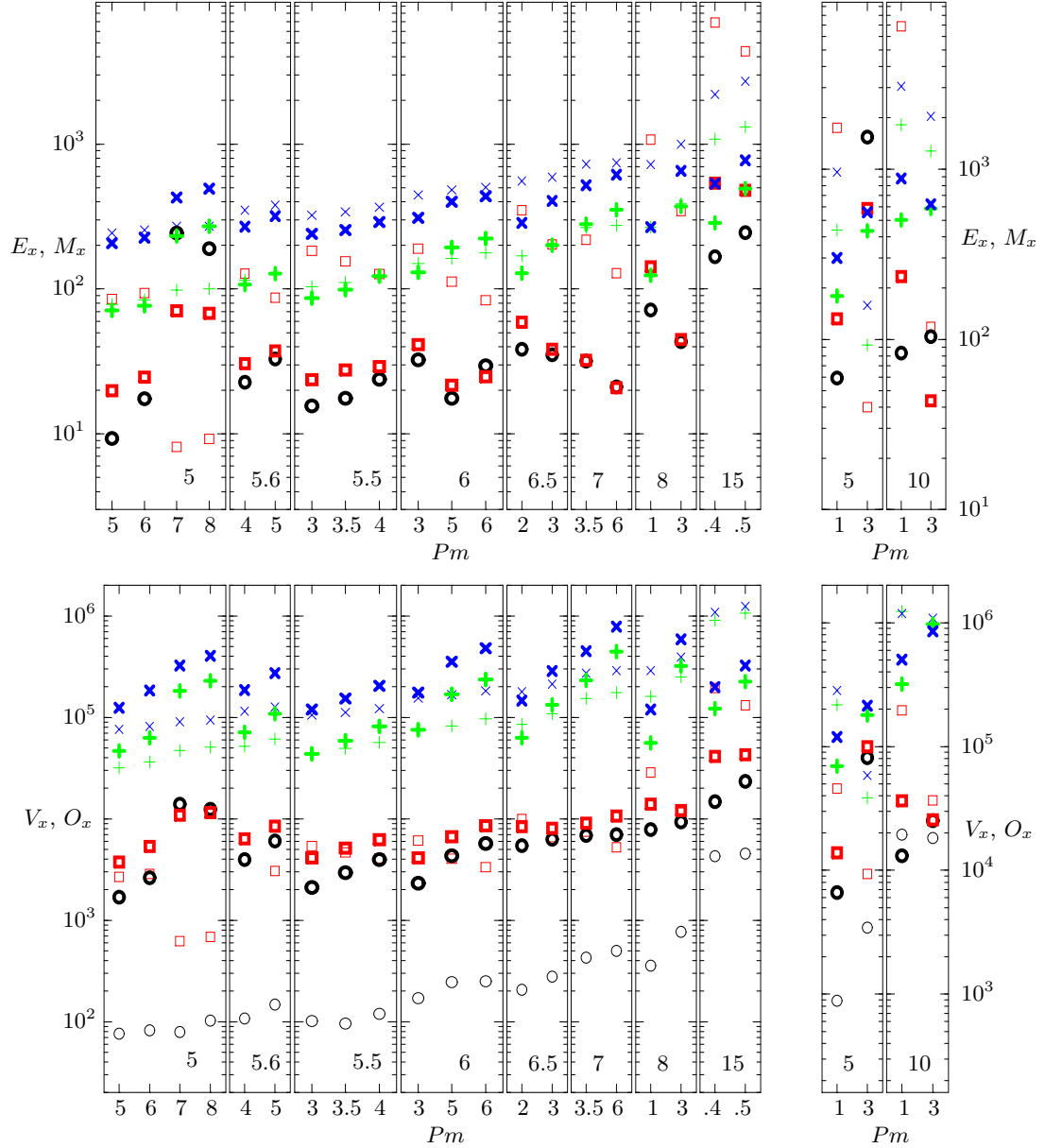
At moderate values of the Prandtl number. Kinetic and magnetic energies as functions of R at moderate values of P have been plotted in figures 8.10 and 8.11. The first figure shows cases for which $\tau = 5 \times 10^3$ while the second one shows cases for which $\tau = 10^4$ and $\tau = 3 \times 10^4$. The value of R is allowed to vary within each sequence while the value of Pm varies in the "super-sequences" and is indicated in the plots.

The longest and the most important sequence is the one for $P = 1$, $\tau = 5 \times 10^3$ and $Pm = 1$, shown in figure 8.10. The Elsasser number Λ approaches unity for the maximum value of the magnetic energy which is achieved at Rayleigh numbers in the neighborhood of 1.4×10^5. Flux expulsion and an increasingly filamentary structure of the magnetic field cause a decrease of the energy for higher values of R, while the Ohmic dissipation continues to increase. For the

same reason axisymmetric components of the fields decay faster with increasing R than the fluctuating non-axisymmetric components. That convection amplitudes in an intermediate range are most suitable for the generation of a global magnetic field has already been noticed in figures 7.5 and 7.4. At small R the dynamos are almost purely quadrupolar. However, since the critical value R_c is only about 8.03×10^4, convection in the polar region has set in at about $R \approx 5 \times 10^5$ and dipolar components grow at higher latitudes. Finally for $R \geq 10^6$ dipolar and the quadrupolar components of the field contribute about equal amounts to the magnetic energy. A feature which distinguishes the sequence shown in figure 8.10 for $Pm = 1$ from all other dynamo sequences is that the differential rotation is still the largest component of the kinetic energy density. As an explanation of this it may be argued that at $Pm = 1$ the dynamo action is near its onset and the magnetic fields are rather week and unable to suppress the mean zonal flow as much as in all other cases. Indeed, the magnetic energy densities in this case are smaller than the kinetic ones, while in all subsequent figures they are at least of the same order. The fluctuating toroidal followed by the fluctuating poloidal magnetic and kinetic energy densities and dissipations have usually the largest values compared to the rest of the components. Those two components are well-correlated. This feature is typical in all parameter regimes presented on the following pages.
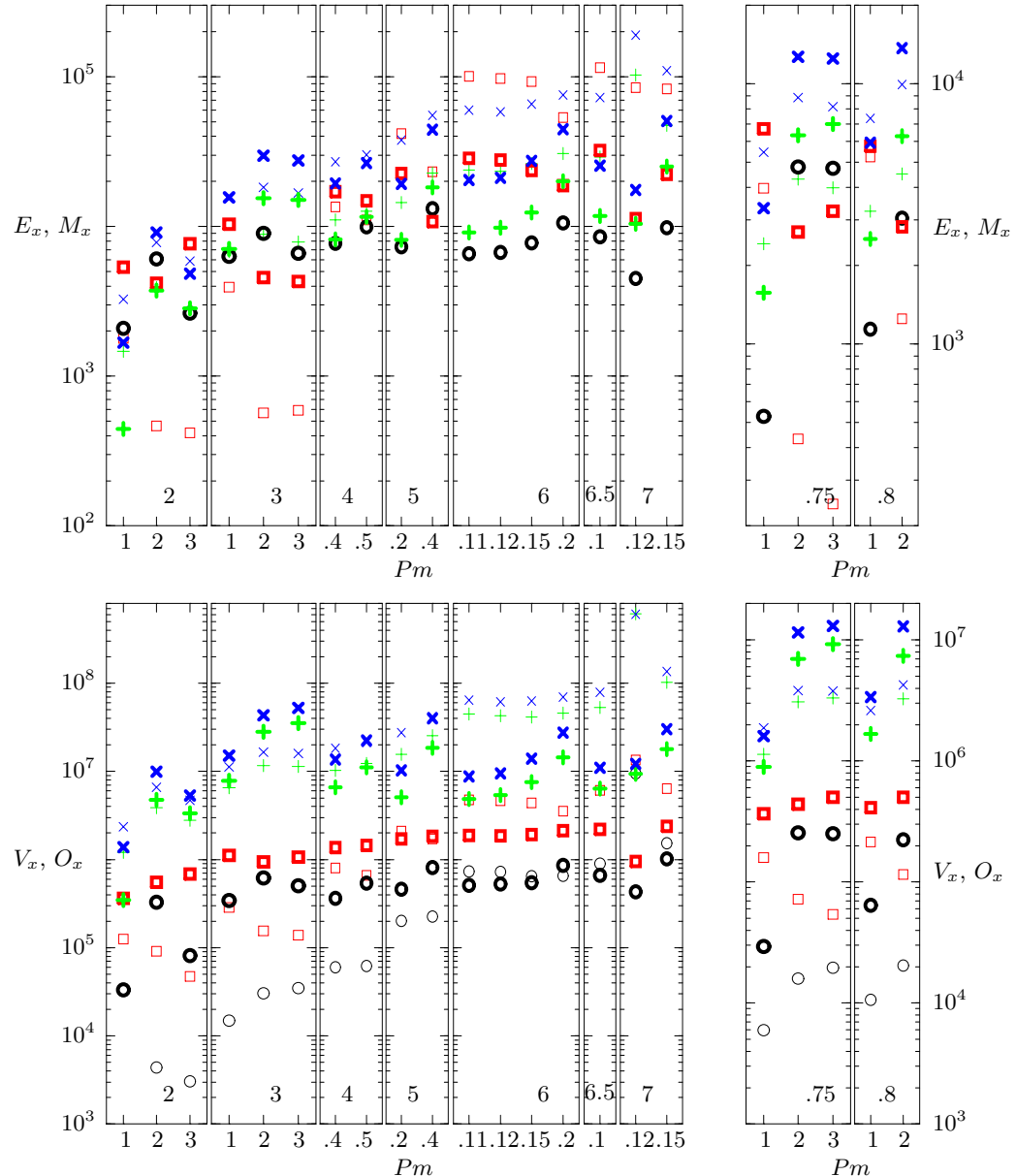
As the Coriolis number τ is increased in figure 8.11 the kinetic energy densities decrease by an order of magnitude as may be expected because of the constraints of rotation. The magnetic energy densities remain of the same size as those shown in figure 8.10 and thus their influence on convection becomes relatively more profound. The immediate consequence is that the differential rotation is no more the largest kinetic energy component. Both the energies and the dissipations continue to grow as the Rayleigh number R is increased. The one exception is the sequence for $\tau = 10^4$ and $Pm = 3$ in which the magnetic energies start to decrease at the highest value of $R = 1.2 \times 10^6$ for the same reasons as discussed above. However, in this sequence the Ohmic dissipations exhibit a decrease, as well. **At small values of the Prandtl number.** The dependence on R at small values of $P = 0.1$ is presented in figure 8.12. The main objective for the simulations shown in this figure has been to reduce the value of Pm as much as possible. Since the average values of the energy densities and the dissipations increase with the decrease of P, this parameter regime appears to be the most appropriate for reaching very small values of Pm. Indeed, a value as small as $Pm = 0.1$ has been achieved, for which a non-decaying dynamo is found to operate. If an attempt is made to reduce the value of P even further, the regime of inertial convection is reached, the dynamo action of which is not very efficient. The important goal of reducing the value of Pm has prevented us from constructing long sequences in which only the value of R is varied in this region. Both the variations in R and in Pm are done in small steps which provides a nice "super-sequence" illustrating the dependence on these parameters. In figure 8.12 it can be observed that the magnetic energy densities remain almost constant as R is increased but Pm is decreased simultaneously while the kinetic energy grows steadily with R. Ultimately, this leads to a differential rotation so strong that it cannot be suppressed by the presence of the magnetic fields as can be seen in the cases for $P = 0.1$, $\tau = 10^5$ and $Pm = 0.12, 0.11, 0.1$. When either R is increased or Pm is decreased further, any relatively strong fluctuation of the small-scaled velocity field causes the magnetic field to decay. Perhaps, the most important observation to be made in figure 8.12 is that the mean toroidal magnetic energy density $\overline{M}_t$ is correlated with the differential rotation. Towards small values of R the fluctuating components of the magnetic field become larger than $\overline{M}_t$, as is typical for the majority of dynamo solutions, but as $\overline{E}_t$ increases with increasing R the mean toroidal magnetic component is the one that grows fastest and ultimately exceeds both $\check{M}_t$ and $\check{M}_p$. The fluctuating components, however, are still the major contributors to the Ohmic dissipation of the magnetic field.

Fig. 8.14. *Kinetic E_x and magnetic energy densities M_x (upper row) and viscous V_x and Ohmic dissipations O_x (lower row) as functions of Pm for dynamos in the case $P = 1$, $\tau = 10^4$ (left column) and $\tau = 5 \times 10^3$ (right column) and $R \times 10^{-5}$ as denoted at the bottom of the plots. The various components are indicated as in figure 8.10.*

At large values of the Prandtl number. Exploration of the Rayleigh number R dependence has not been the main reason for performing simulations also in the large Prandtl number region. By increasing the Prandtl number P we have aimed at understanding the dependence on the Prandtl number. As a result the sequences shown in figure 8.13 are also not very long. However they are sufficient to demonstrate that for intermediate values of the Rayleigh number R both magnetic and kinetic energies increase with the Rayleigh number R. We once again point the attention at cases near the onset of dynamo action such as the sequence at $P = Pm = 10$ where dynamos decay both at insufficiently large values of the Rayleigh number R and at values for which the convection is too vigorous and filamentary.
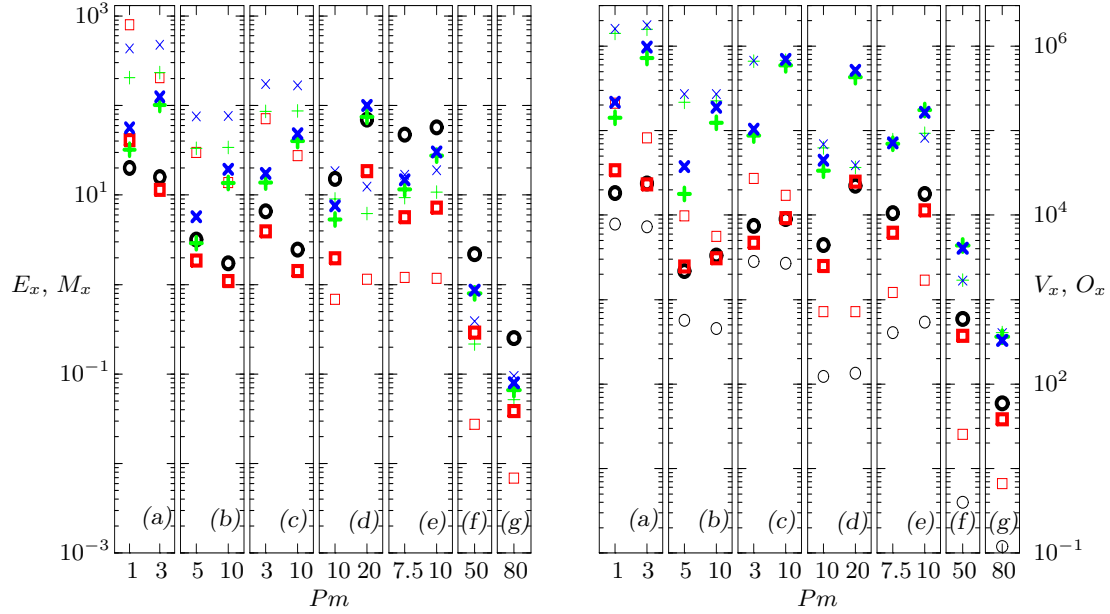
Fig. 8.15. *Same as figure 8.14 but in the case $P = 0.1$, $\tau = 10^5$ (left column) and $\tau = 3 \times 10^4$ (right column). $R \times 10^{-6}$ is denoted at the bottom of the plots.*

8.4.2 Dependence on the magnetic Prandtl number

The magnetic Prandtl number along with the Rayleigh number are those parameters, the values of which are most easily varied. The variation of one of them is usually accompanied by a variation of the other. For this reason our results on the dependence of the time-averaged energy densities and dissipations of spherical dynamos on Pm may be viewed as complimentary to the results on the dependence on R. However, we hope that the rearrangement of the dynamo solutions in sequences where R is also kept fixed may be illuminating.

Figures 8.14, 8.15 8.16, therefore, present dependence on the magnetic Prandtl number Pm of dynamo solutions at moderate, small and large values of P. As might be expected the increase of the magnetic Prandtl number Pm leads to an increase in the magnetic energy densities and subsequent decrease in the size of the differential rotation. When the mean zonal
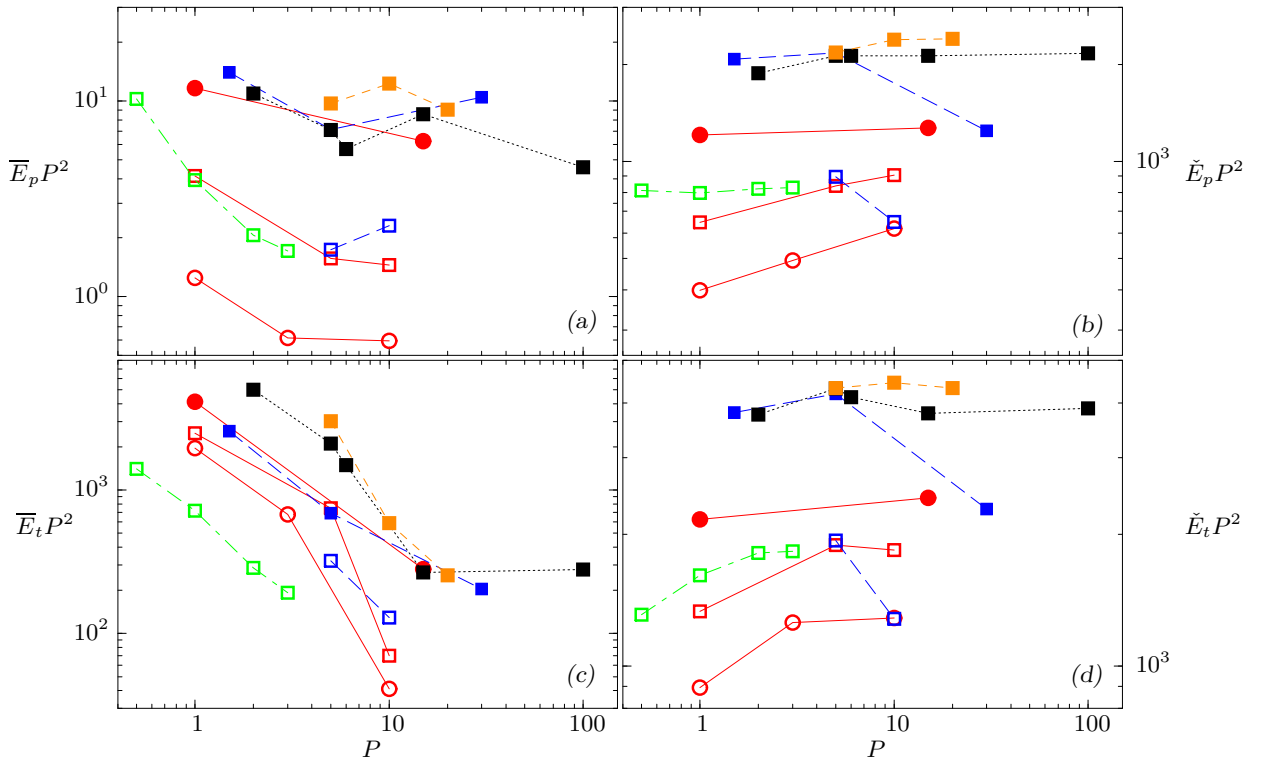
Fig. 8.16. *Same as figure 8.14 but in the cases $\tau = 5 \times 10^3$ and (a) $P = 3$, $R = 10^6$, (b) $P = 5$, $R = 6 \times 10^5$, (c) $P = 5$, $R = 10^6$, (d) $P = 10$, $R = 6 \times 10^5$, (e) $P = 15$, $R = 10^6$, (f) $P = 100$, $R = 10^6$, (g) $P = 200$, $R = 10^6$.*

flow is reduced, the convection becomes more efficient. Curiously, because of this mechanism the kinetic energy densities $\overline{E}_p$, $\check{E}_p$ and $\check{E}_t$ also increase when Pm is increased. The decrease of the differential rotation may be so significant as to lead to a related decrease in the mean toroidal magnetic energy density $\overline{M}_t$ as can be seen in some sequences in figures 8.14 and 8.15. This, however, does not lead to a significant saturation of the magnetic field at least for the values of Pm used, since the fluctuating components of the magnetic energy continue to grow with the magnetic Prandtl number Pm. The Ohmic dissipations grow much faster than the viscous ones.

8.4.3 Dependence on the Prandtl number. Validity of the magnetostrophic approximation

The magnetostrophic approximation. The fact that convection-driven dynamos in rotating systems depend on a rather large number of parameters has led to numerous attempts to eliminate one or more parameters through reductions of the basic equations. The most important among these reductions is the *magnetostrophic approximation* in which the acceleration of fluid particles is neglected in comparison to the Coriolis force and the Lorentz force. Indeed, among the various advection terms in the basic equations (3.64) for convection-driven dynamos the advection of momentum appears to be the least important. The advection of temperature provides the essential nonlinearity in the dependence of the convection amplitude on the Rayleigh number and the advection of the magnetic flux density represents an intrinsic part of the equation of magnetic induction. But in the equation of motion the Coriolis force term usually exceeds by far the other inertial terms and it is not surprising that this property is used as an argument for the neglection of the term $\partial \boldsymbol{u}/\partial t + \boldsymbol{u} \cdot \nabla \boldsymbol{u}$. This is known as the *magnetostrophic approximation*. It is formally justified in the limit of large Prandtl numbers. Using the thermal time scale d^2/κ instead of the viscous one and scaling the magnetic flux density with $\sqrt{\rho\mu_0\kappa\nu}/d$, the basic dimensionless equations become

Fig. 8.17. *Kinetic energy densities $\overline{E}_p$ (in (a)), $\check{E}_p$ (in (b)), $\overline{E}_t$ (in (c)) and $\check{E}_t$ (in (d)) all multiplied by P^2 as functions of P in the case $\tau = 5 \times 10^3$. The dynamos corresponding to fixed ratios $\kappa/\lambda = 1, 2, 5, 0.5$ are indicated by red solid, blue long-dashed, green dash-dotted and black dotted lines, respectively, and cases of non-magnetic convection by an orange short-dashed line. The values $R = 5 \times 10^5, 6 \times 10^5, 8 \times 10^5, 10^6$ are denoted by empty circles and squares and full circles and squares, respectively.*

$$P^{-1}D_t\boldsymbol{u} + \tau\hat{\boldsymbol{e}}_{\boldsymbol{z}} \times \boldsymbol{u} = -\nabla\pi + \Theta\boldsymbol{r} + \nabla^2\boldsymbol{u} + (\nabla \times \boldsymbol{B}) \times \boldsymbol{B} \tag{8.3a}$$

$$D_t\Theta = R\boldsymbol{u} \cdot \boldsymbol{r} + \nabla^2\Theta \tag{8.3b}$$

$$\frac{\kappa}{\lambda}(D_t\boldsymbol{B} - \boldsymbol{B} \cdot \nabla\boldsymbol{u}) = \nabla^2\boldsymbol{B} \tag{8.3c}$$

where $D_t = \partial_t + \boldsymbol{u} \cdot \nabla$ is the material derivative. The temperature has been scaled by β_0/R in this case. In the magnetostrophic approximation the term $P^{-1}D_t\boldsymbol{u}$ is neglected and thus one of the dimensionless parameters of the problem disappears.
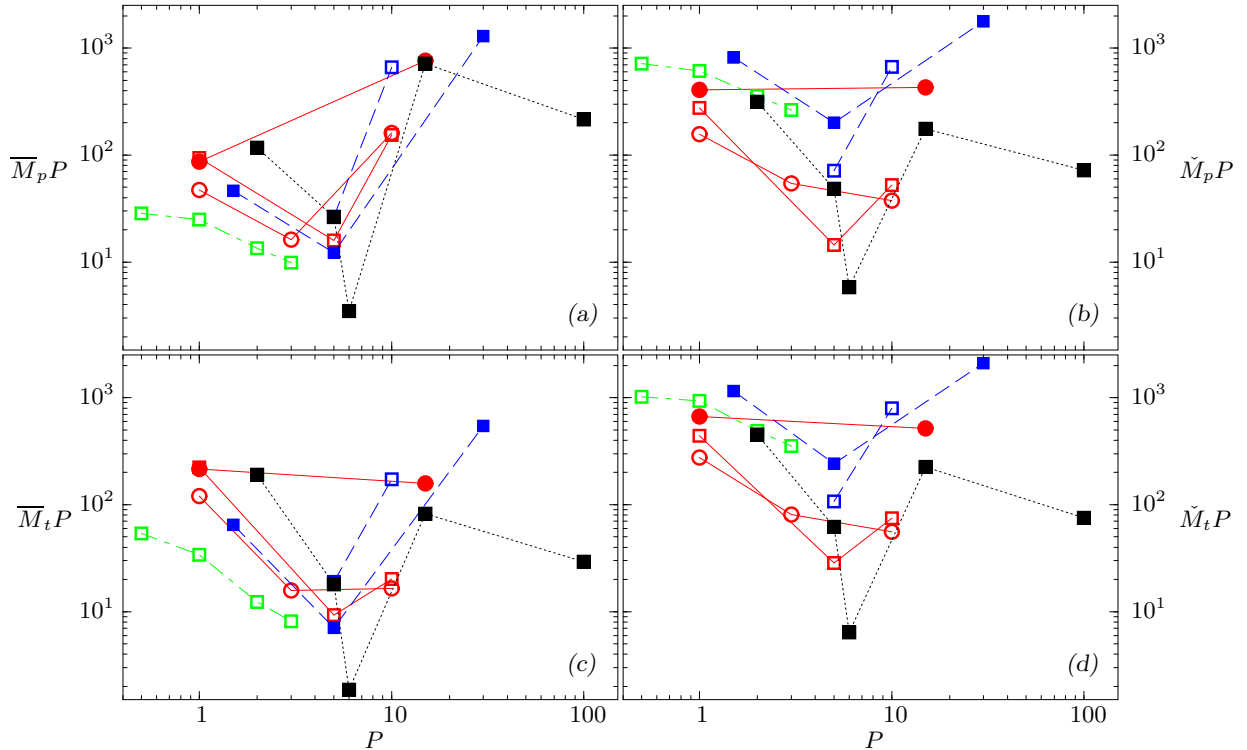
An alternative formulation. The magnetostrophic approximation can also be obtained in another way. Using the magnetic diffusion time scale, d^2/λ, and the scale $\sqrt{\varrho\mu_0\lambda\nu}/d$ for the magnetic flux density the basic equation can be transformed into

$$Pm^{-1}D_t\boldsymbol{u} + \tau\hat{\boldsymbol{e}}_{\boldsymbol{z}} \times \boldsymbol{u} = -\nabla\pi + \Theta\boldsymbol{r} + \nabla^2\boldsymbol{u} + (\nabla \times \boldsymbol{B}) \times \boldsymbol{B} \tag{8.4a}$$

$$\frac{\lambda}{\kappa}D_t\Theta = R\boldsymbol{u} \cdot \boldsymbol{r} + \nabla^2\Theta \tag{8.4b}$$

$$D_t\boldsymbol{B} - \boldsymbol{B} \cdot \nabla\boldsymbol{u} = \nabla^2\boldsymbol{B} \tag{8.4c}$$

For large magnetic Prandtl numbers Pm it appears to be justified to drop $Pm^{-1}D_t$ from equation (8.4a) whereby a magnetostrophic approximation is obtained with one parameter less than in the original equations. Dynamo solution should then become independent for $Pm \longrightarrow \infty$ and the ratio of magnetic to kinetic energy would grow in proportion to Pm.
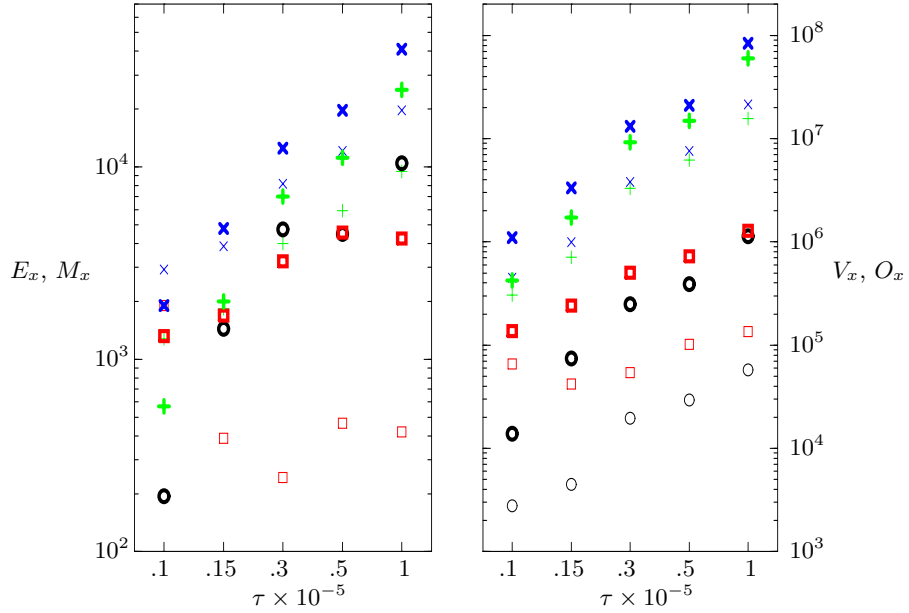
Fig. 8.18. *Same as figure 8.17 but for the magnetic energy densities $\overline{M}_p$ (in (a)), $\check{M}_p$ (in (b)), $\overline{M}_t$ (in (c)) and $\check{M}_t$ (in (d)) all multiplied by P.*

Validity of the magnetostrophic approximation. From the form of equations (8.3) it is clear that the magnetostrophic approximation should certainly be valid in the limit $P \longrightarrow \infty$. For values of P of the order unity or less the question of the validity of the magnetostrophic approximation is less obvious since the generation of differential rotation by the Reynolds stresses of convection is not represented in that approximation. Also, inertial oscillations which play a role in low Prandtl number convection cannot be represented in the magnetostrophic approximation. For this reason we have attempted to increase the value of P as far as computationally reasonable and assess the validity of the magnetostrophic approximation. In figures 8.17 and 8.18 the kinetic and magnetic energy densities have been plotted for fixed values of κ/λ. It can be seen that the kinetic energies tend to become independent of P with increasing P in accordance with the magnetostrophic assumption. The energy $\overline{E}_t$, representing the differential rotation, is the only exception as expected. No indication of an approach towards the validity of the magnetostrophic approximation is found, however, when the magnetic energy densities are considered. As already mentioned, the dynamo process is very sensitive to the presence of differential rotation. Therefore, the failure of the differential rotation to satisfy the magnetostrophic approximation is the reason for the large deviation of the magnetic energy densities from it. It appears that much higher values of P may be needed before the magnetostrophic regime is approached.

8.4.4 Dependence on the Coriolis number

Finally, we discuss the equilibration of magnetic and kinetic energies and dissipations in dependence on the Coriolis number. Although last in our discussion this dependence is by far not the least important. Understanding of the τ dependence is crucial for several reasons.

Fig. 8.19. *Kinetic E_x and magnetic energy densities M_x (left plot) and viscous V_x and Ohmic dissipations O_x (right plot) as functions of τ for dynamos in the case $P = 0.1$, $R = 3.2 \times R_c$ and $Pm = 3$. The various components are indicated as in figure 8.10. The values of the critical Rayleigh number R_c are listed in table 6.1.*

First, the Coriolis force term exceeds by far the other inertial terms. Second, the variation of τ leads to a qualitatively distinct convective regimes. Finally, one of the main restrictions on the numerical simulations, which we would like to overcome, is the computational restriction to small rotation rates.

However, we have devoted only limited effort to study explicitly the equilibration of magnetic and kinetic energies as a function of τ, since a considerable range of rotation rates has already been covered by the results reported so far. Figure 8.19 presents a sequence of dynamo solutions for $P = 0.1$, $Pm = 3$, and $R = 3.2 \times R_c$ and varying values of τ. Although a short sequence, it already contains a remarkable result. Contrary to the expectation that rotation would inhibit convective motions, an effect which has been demonstrated long ago [36], figure 8.19 exhibits a definite increase of the fluctuating and the mean poloidal kinetic energy densities and all magnetic energy densities. This surprising result can be explained with the fact that the presence of the self-generated magnetic field suppresses the differential rotation more than the increasing rotation rate promotes it. Released from the inhibiting effect of the mean zonal flow, the amplitude of convection appears to increase as the system rotates faster. The vigor of convection, on its turn, leads to an increase in the magnetic energy densities. Interestingly, the latter increase even faster than the kinetic ones. However, such situation probably occurs only at intermediately large values of τ. Although we have no evidence, we would like to speculate that when τ is increased to sufficiently large values the magnetic field would not be able to suppress the ever growing differential rotation and the convective motions would again be strongly inhibited by rotation.

9. Structure and Spatio-Temporal Patterns of Convection-Driven Spherical Dynamos

9.1 Introduction
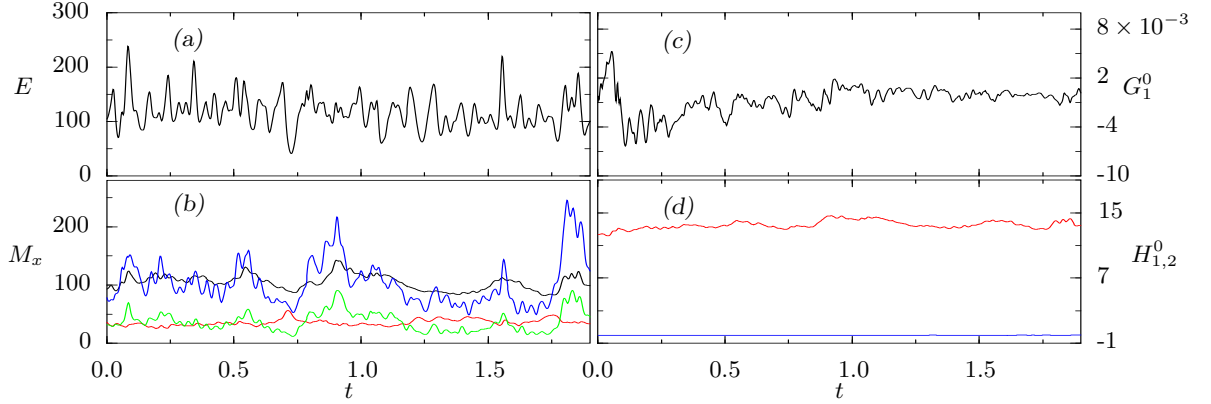
Topic and motivation. Considerable attention has been paid in the preceding couple of chapters to the global and time-averaged properties of convection-driven dynamos, in order to understand the mechanisms of equilibration and interaction between convection and the magnetic fields generated by it as well as the most characteristic features and symmetries of the solutions in dependence on the parameters of the problem. In this section we focus the attention on a second, equally important group of questions, concerning the spatial and temporal structure of dynamos which has been neglected in the averaging procedures.

Similar to finite-amplitude convection, geophysically interesting dynamos have a very complex, often chaotic spatio-temporal behavior. Unfortunately, it cannot be described by simple relations and we will need, once again, to retreat to illustrative examples and simplifying assumptions. As demonstrated in chapter 7, even when the dynamo solutions are highly chaotic, a predominant component of the expansion in spherical harmonics (4.1) or a combination of such, may still be identified. The dominant component contains a major part of the energy available to the magnetic field as shown by the power spectra in figure 7.11. The rest of the terms play an important role through the process of nonlinear coupling but to a large extent they depend on the dominant one. A similar situation is observed when the field is separated into mean and fluctuating parts. The fluctuating energy densities often exceed the mean ones. However, they exhibit rapid fluctuations about some average values which correlate and follow the trends featured by the mean energy densities. Therefore, it is reasonable to focus the attention on the mean features of the dominant expansion components of dynamo solutions in order to study their behavior in space and time. In this way, a necessary and useful simplification is achieved and the most important physical effects are captured. For these reasons, the discussion in this chapter is most often illustrated by plots of the mean toroidal and poloidal components of the magnetic field $\overline{B}_\varphi$ and $r\sin\theta\,\partial_\theta\overline{h}$, respectively.
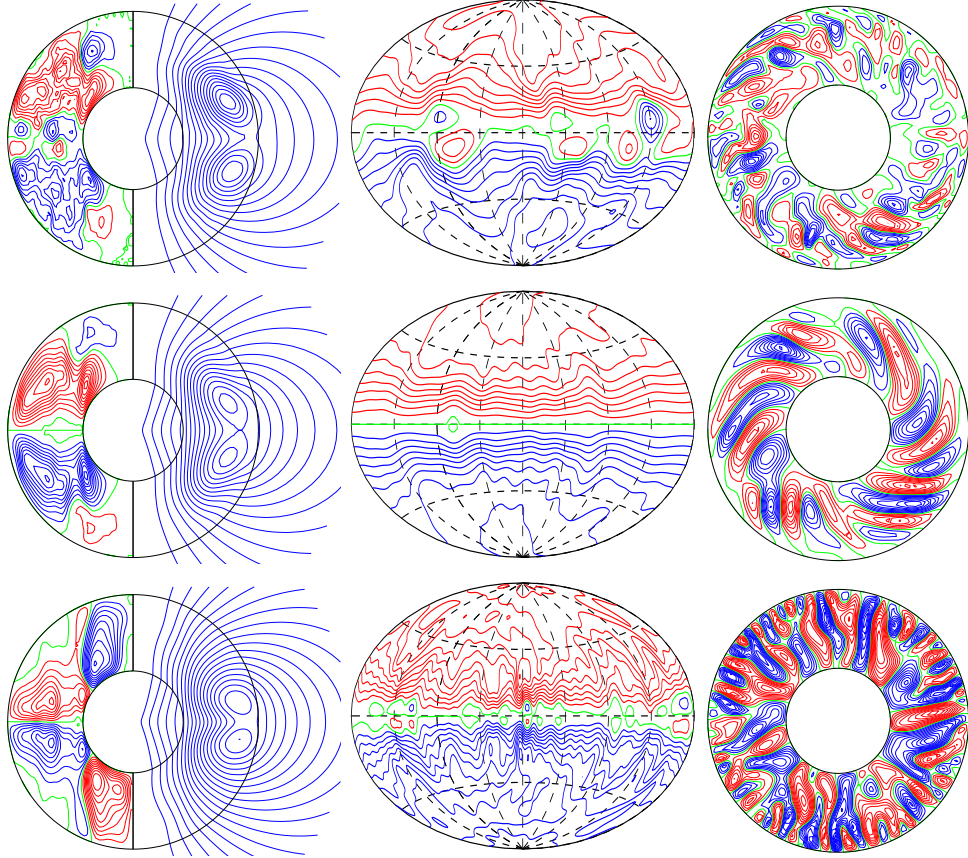
Contents. Careful observations of our numerous dynamo solutions have revealed typical and repeatable patterns of dynamo behavior. Most notable among them are the various dynamo oscillations which we discuss in detail in section 9.2. In sections 9.3, 9.4 and 9.5 we apply their properties in order to address the issues of dynamo intermittency, geomagnetic polarity reversals and secular variation impulses, respectively. These latter topics are of considerable interest since they link our theoretical and numerical results to the observations of actual features of the Earth's magnetic field. The majority of our results on dynamo oscillations have been published in references [29, 60, 108, 33].

9.2 Dynamo oscillations

The basic elements of our understanding of the chaotic temporal and spatial behavior of convection-driven spherical dynamos are *the dynamo oscillations*. Despite the fact that the fluctuating components of the generated fields are rather turbulent, the axisymmetric ones
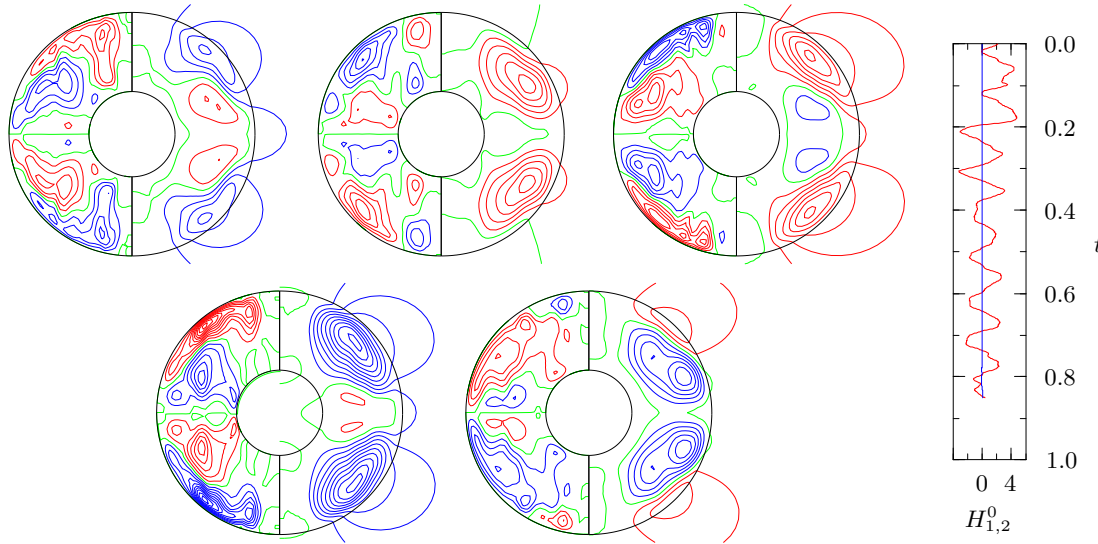
Fig. 9.1. *Time series of energy densities and selected coefficients of a non-oscillatory dipolar chaotic dynamo for $P = 1$, $\tau = 10^4$, $R = 3.5 \times 10^5$, $Pm = 10$. Plot (a) shows the total kinetic energy density E, plot (b) shows energy densities of the dipolar components while plots (c) and (d) show the values of the coefficients $H_1^0(r,t)$, $H_2^0(r,t)$ and $G_1^0(r,t)$, respectively at $r = (r_i + r_o)/2$. The color code is explained in the caption of figure 7.9.*


Fig. 9.2. *Non-oscillatory chaotic dipolar dynamos in the cases • $P = 0.1$, $\tau = 10^5$, $R = 3 \times 10^6$, $Pm = 2$ (upper row); • $P = 1$, $\tau = 10^4$, $R = 3.5 \times 10^5$, $Pm = 10$ (middle row); and • $P = 200$, $\tau = 5 \times 10^3$, $R = 10^6$, $Pm = 80$ (lower row). The left column shows meridional isolines of $\overline{B}_\varphi$ (left half) and of $r \sin\theta \partial_\theta \overline{h} =$ (right half). The middle column shows lines $B_r = const.$ at $r = 1.7 \times r_0$. The right column shows equatorial streamlines $r\partial_\varphi v = const.$*

often exhibit well-defined coherent structures which repeat themselves in an almost periodic fashion and reoccur in a large number of different dynamo cases.
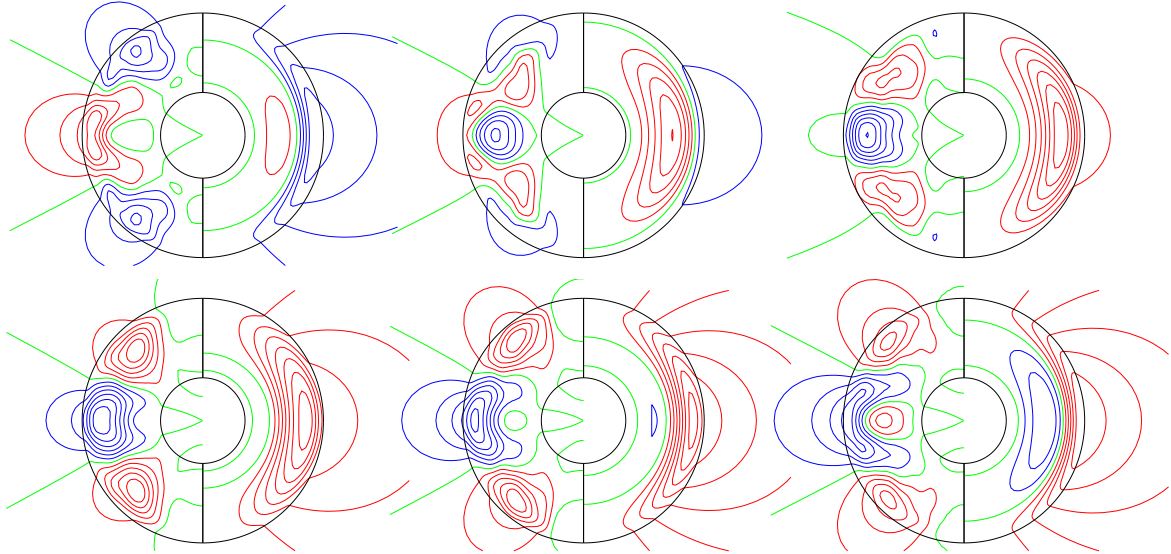
Fig. 9.3. *Perfectly oscillating dipolar dynamo in the case $P = 1$, $\tau = 3 \times 10^3$, $R = 3 \times 10^5$ and $Pm = 3$. The plots (left part) cover a bit less than a period (clockwise with $\Delta t = 0.02$) and show meridional lines of constant $\overline{B_\varphi}$ in the left half and of $r \sin\theta \partial_\theta \overline{h}$ in the right half of each circle. In the right part a time series of the coefficients H_1^0 (red) and H_2^0 (blue) is shown.*

9.2.1 Stationary and periodic dynamos

Before we dive into the variety of dynamo oscillations, we mention, for completeness, simpler types of dynamo behavior. As noted in chapter 7, for sufficiently large values of the magnetic Prandtl number Pm magnetic fields can be generated by regular or steadily drifting convection near onset. These dynamos represent the simplest examples of time dependence. Magnetic fields with steadily-drifting structures similar to the columnar convection rolls and with constant energy densities are easily obtained [23]. Time-periodic dynamos at $P = 1$, $\tau = 10^4$ and $Pm \geq 50$ have also been reported [62]. These solutions are obtained both with stress-free and no-slip boundary conditions as well as in the presence of a conducting inner core. They exhibit a strong dipolar dominance. Because of their simplicity, regularity and low computational cost they have been extensively studied. But since the geodynamo does not operate in such a regular fashion, more strongly-driven chaotic cases need to be analyzed.

9.2.2 Non-oscillatory chaotic dynamos

Apart from the regular and periodic dynamos, chaotic solutions with a spatial structure showing very little variation in time also exist. These dynamos are almost exclusively of dipolar character as may be seen in the plots of figure 9.2. They appear throughout the parameter space and the only condition for obtaining such a solution seems to be the requirement that the ratio Pm/P should be sufficiently large. This requirement may be easily explained with the results presented in figures 7.2, 7.3 and 7.5 where chaotic non-oscillatory dipolar dynamos are found towards large values of Pm. The non-oscillatory dipoles show little dependence on the regime of convection. Figure 9.2 shows, for example, three different types of convection – a chaotic small P case, a columnar type convection at $P = 1$ and a large P case with radially oriented sells. All these flows generate dipolar magnetic fields of rather similar appearance. Although the structure of the fields shown in the figure exhibits only minor variations with time, the dynamo solutions are far from regular. This may be illustrated with the help of

Fig. 9.4. *Half a period of the oscillations shown in figure 9.3. The plots (first row, then second row) show meridional field lines $r \sin\theta \partial_\theta \overline{h} = const.$ with H_1^0 in the right half and H_l^0 in the left half and a time step of $\Delta t = 0.01$.*
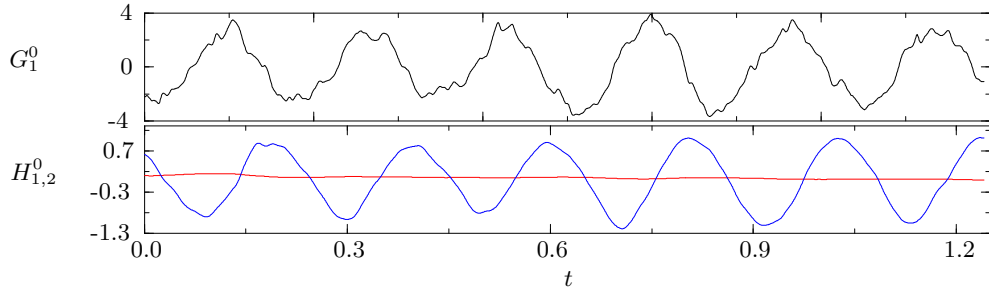
figure 9.1 where the energy densities of one of the cases presented in figure 9.2 is shown. The main feature of the figure apart from the highly irregular time series is the large dominance of the axial dipole coefficient H_1^0 in (d).

Non-oscillatory examples of predominantly quadrupolar dynamos are extremely rare, even exceptional. One such solution have already been demonstrated in figure 8.8. Such cases have been found, so far, only when perfectly conducting boundary conditions for the magnetic field at the inner core boundary are used.
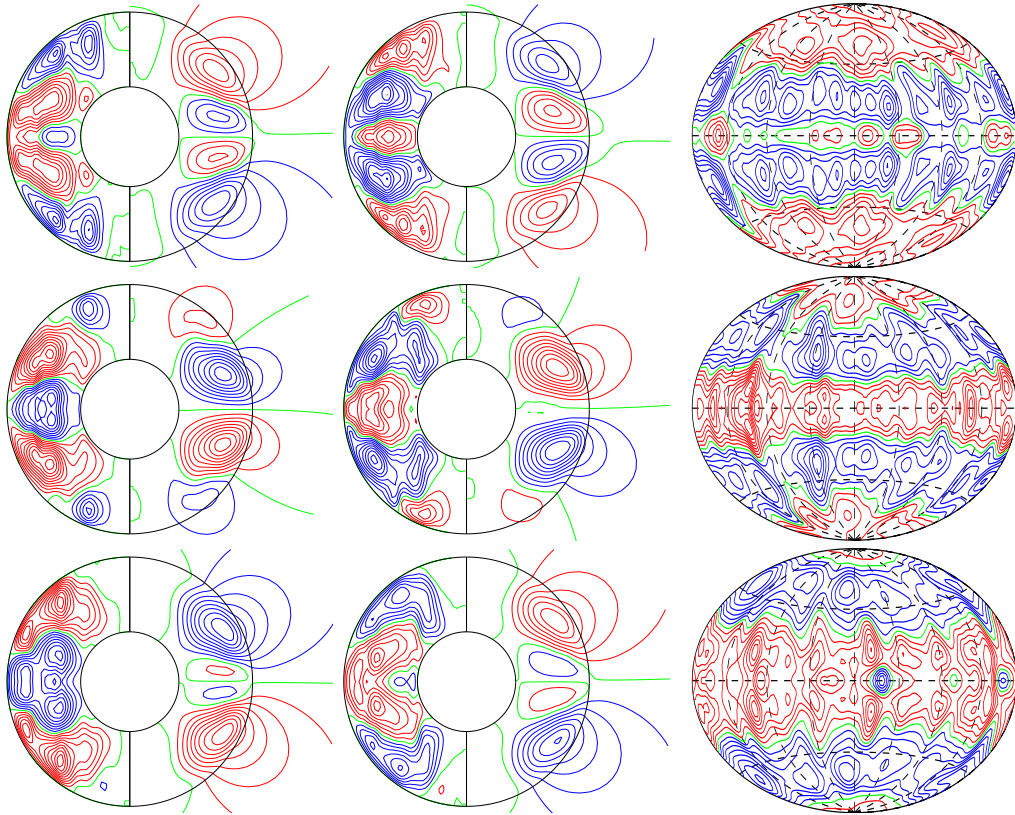
9.2.3 Prototypical dynamo oscillations

The motivation behind most of our numerical simulations have been to explore the parameter space of the problem and in particular to obtain dynamo solutions at values of the magnetic Prandtl number Pm as small as possible. This has required the use of relatively large values of the Rayleigh number, for which the solutions become highly turbulent and filamentary. Nevertheless, a variety of coherent oscillations may be identified and followed in time. In most cases a number of expansion coefficients contribute to the oscillations which makes it difficult to understand those oscillations. Thus, we try to decompose and isolate the effects due to the various coefficients. More precisely we select dynamo solutions in which one of the coefficients is dominant. It is then possible to separate its contribution from the contributions of the rest of the components. In this manner a clear idea may be obtained of how the axial dipole H_1^0, the quadrupole H_2^0 and the higher l components oscillate. It is then relatively straightforward to understand the more complex composite oscillations.

In general, strongly dipolar dynamos are non-oscillatory as discussed in the preceding section. However, as the energy available to the axial dipole decreases while the energy available to the other components grows but they do not yet dominate, the dipolar dynamos eventually begin to oscillate. An example of an oscillating dipole is shown in figure 9.3. The time series of the poloidal coefficients H_1^0 and H_2^0 in the right part of the figure show that the quadrupolar component is negligible in this case while the dipolar one has an almost periodic time dependence. The left part of the figure suggests, however, that the axial dipole is not the
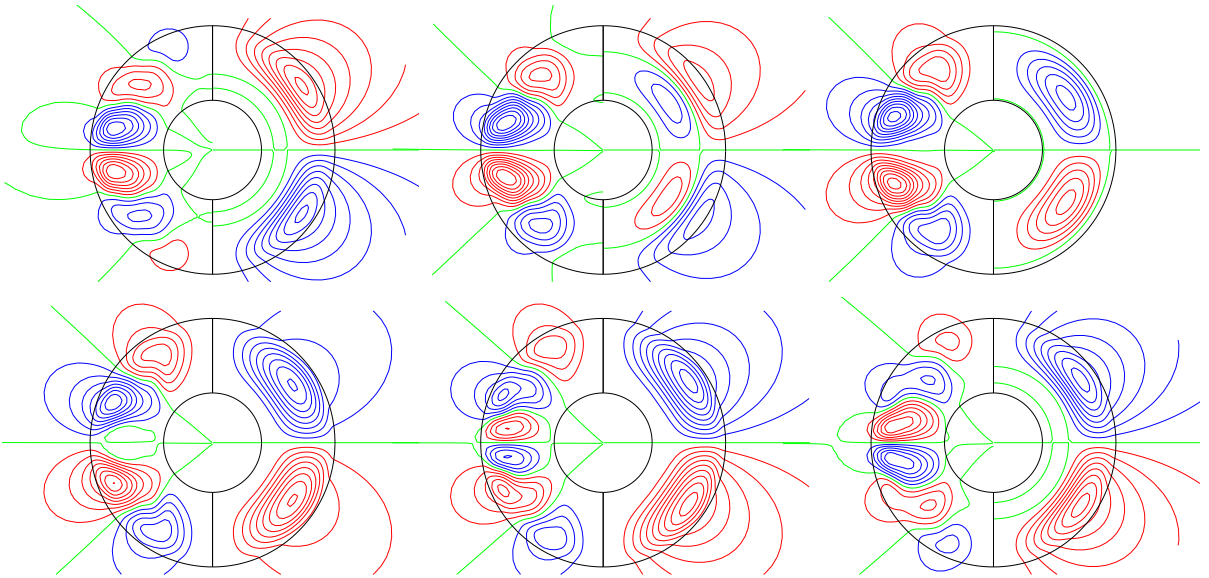
Fig. 9.5. *Time series of the coefficients G_1^0 (upper plot) and H_1^0, H_2^0 (lower plot) of an oscillating quadrupolar dynamo in the case $P = 5$, $\tau = 5 \times 10^3$, $R = 8 \cdot 10^5$, $P_m = 3$. The color code is explained in the caption of figure 7.9(d) and (e).*


Fig. 9.6. *A period of quadrupolar dynamo oscillations for the same case as in figure 9.5. The first two columns (from top to bottom, first left, then right starting at $t_0 = 0.961$ with $\Delta t = 0.04$) show meridional lines of constant $\overline{B_\varphi}$ in the left half and $r \sin \vartheta \partial_\theta \overline{h}$ in the right half of each circle. The third column shows lines of constant B_r on the spherical surface $r = 1.4 r_o$. The plots cover only the second half of the period and correspond to the same instants in time as the plots in the second column.*

only component contributing to the oscillation. Indeed, the oscillation may be decomposed to extract its axial dipolar part from the rest as has been done in figure 9.4. The sequence of plots covers half a period of the oscillation. The oscillation of the H_1^0 components, in the right halves of the plots, involves the creation of a new flux of the opposite polarity near the inner boundary in the equatorial plane. The flux gradually grows in magnitude and size pushing the old flux outside the shell. Ultimately the old flux decays while the new one of the opposite
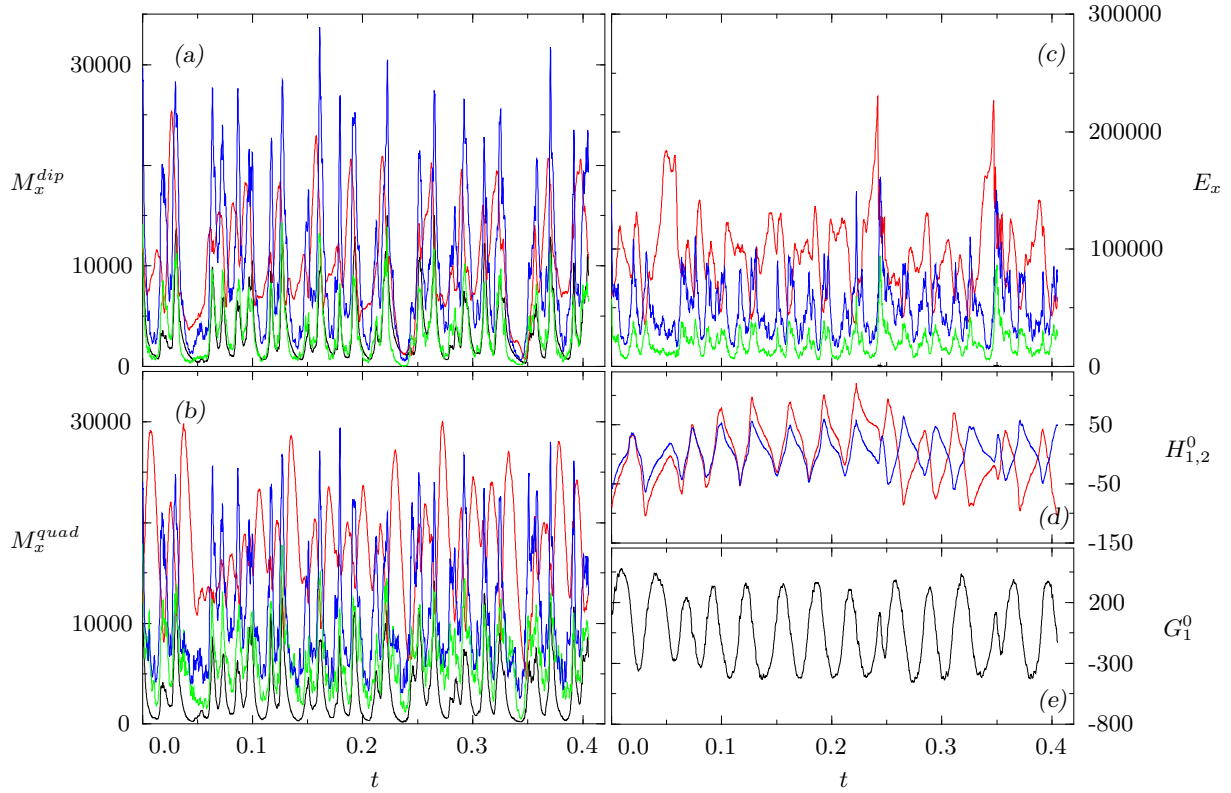
Fig. 9.7. *Half a period of the oscillations shown in figure 9.6. The plots (first row, then second row) show meridional field lines $r \sin \theta \partial_\theta \overline{h} = const.$ with H_2^0 in the right half and H_l^0 in the left half and a time step of $\Delta t = 0.02$.*

polarity replaces it entirely. While this process takes place a third new flux is created and the oscillation continues in a periodic fashion. Simultaneously an oscillation of the remaining expansion components, including the quadrupole, is taking place, as shown in the left halves of figure 9.4. It may be argued that the structure of the higher l components is determined by the predominant $l = 1$ one. It is important to notice that the contribution of the remaining $l > 1$ coefficients is also antisymmetric with respect to the equator. This is always the case when the dipole is dominant and indicates that the even l contributions are negligible. For this reason, there are always an odd number of fluxes in the left halves of the figure. The one situated at the equator is of the opposite polarity with respect to the polarity of the axial dipole. At the beginning of the period a new small flux rope is created close the equatorial plane near the inner boundary. It grows and moves towards the outside but remains strictly in the equatorial plane. In this process it separates the flux which is situated in front of it. The two parts do not decay but propagate toward higher latitudes. Concurrently the pair of fluxes which are initially situated closest to the poles decay gradually. The entire process repeats periodically with alternating polarities.

Contrary to the dipolar solutions, the quadrupolar ones are oscillatory in general. Figures 9.5 and 9.6 illustrate the corresponding oscillations. The same approach is again applied and the quadrupolar oscillation is decomposed with its dominant H_2^0 part separated from the remaining components as shown in figure 9.7. The sequence of events constituting a cycle is similar to the one just described in the case of the pure dipolar oscillations. The most important difference is that the field fluxes are now perfectly symmetric about the equator, indicating l=even dominance. This once again confirms the hypothesis that the dominant component determines the structure due to the higher l coefficients.

Apart from the cases when either the dipolar or the quadrupolar component is solely dominant, there are solutions in which both of them are of equal strength, resulting in a hemispherical dynamo. A snapshot of such a dynamo has already been presented in the last rows of figures 7.7 and 7.10. Hemispherical solutions have been first reported in [62] and various details of their oscillations are described in [59] and [29]. Here we wish to draw the
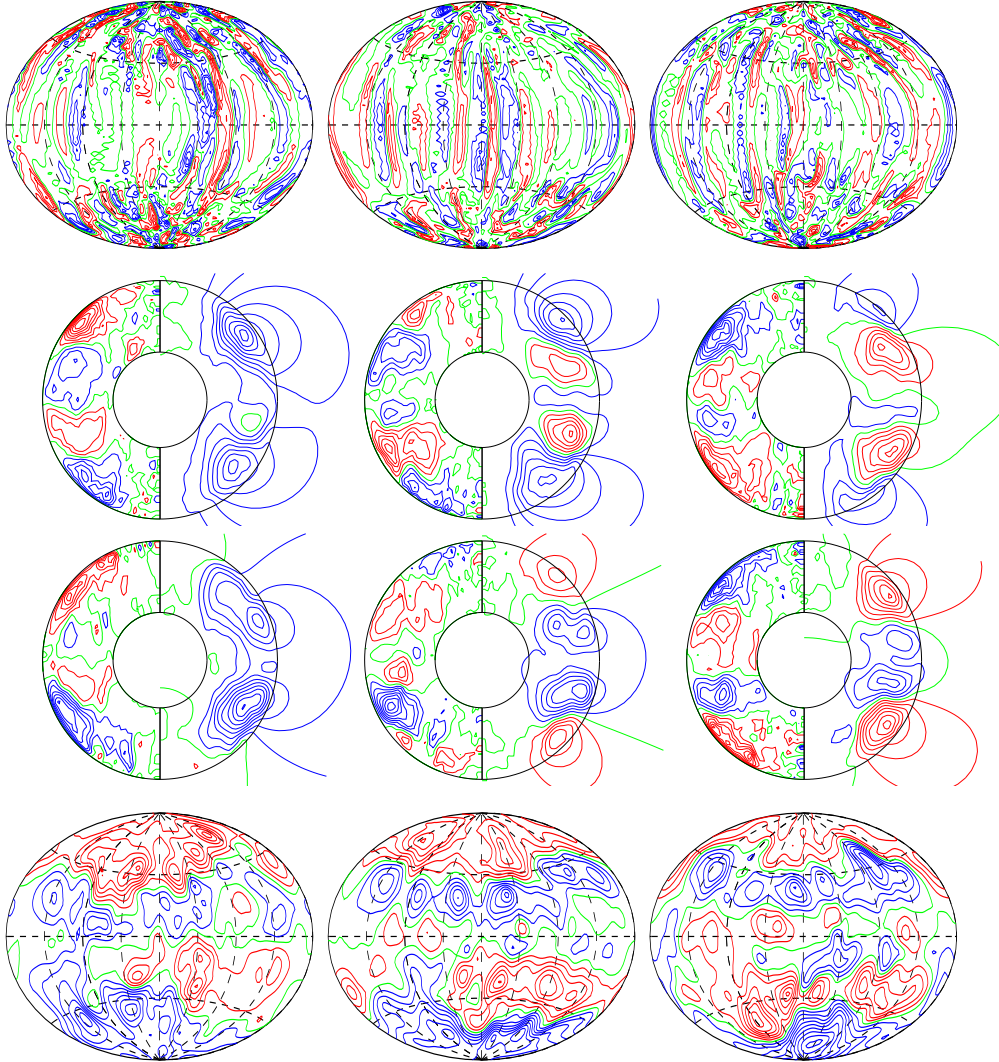
Fig. 9.8. *Same as figure 7.9 for the oscillating hemispherical dynamo in the case $P = 0.1$, $\tau = 10^5$, $R = 6 \times 10^6$, $Pm = 0.12$.*

attention on a further interesting aspect of the time dependence of the hemispherical dynamos illustrated in figure 9.8 on the example of a low P dynamo. The fact that the dynamo is hemispherical is best seen in 9.8(d) where the quadrupolar and the dipolar coefficients H_2^0 and H_1^0 are roughly equal in absolute value at any moment in time. In fact, the case is driven away from its perfect quadrupolar-dipolar balance near the middle of the time series where the solution changes from northern to southern hemispherical. What is more remarkable is that the magnetic energy densities exhibit the same periodicity as the dynamo oscillations. The oscillations of the magnetic energies are so strong and coherent that the magnetic field is able to decrease the strength of the differential rotation almost instantaneously. The decrease of $\overline{E}_t$ leads, in turn, to a strong increase of the fluctuating convection energy densities. The kinetic energy also starts to oscillate with the periodicity of the hemispherical oscillation. In this way the dynamo oscillation controls the time dependence of energy densities. In contrast, such a situation is only rarely observed for quadrupolar dynamos and never for dipolar ones.

9.2.4 Oscillations of dipolar dynamos
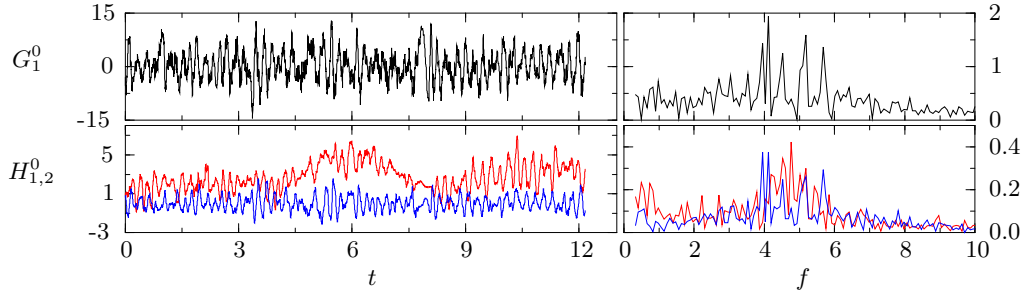
Almost all of the quadrupolar and hemispherical dynamos found in our simulations, regardless of the precise values of their parameters or convective regime, oscillate in a fashion very similar to the perfect oscillations described in the previous subsection. For a long time, the dipolar dynamos have been thought to be non-oscillatory [62], [59] but a wide variety of dipolar oscillations have been found subsequently. Our simulations suggest that, in contrast with the quadrupolar coefficient H_2^0 which oscillates on its own, the axial dipole needs an interaction
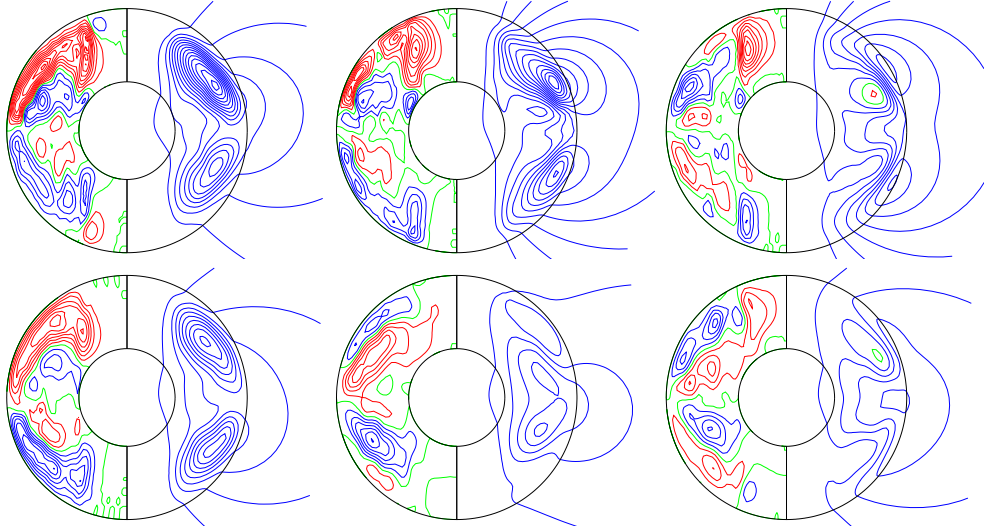
Fig. 9.9. *Oscillating dipolar dynamo in the case $R = 1.4 \times 10^6$, $\tau = 5 \times 10^3$, $P_m = P = 1$. The second and third row cover a period (clockwise with $\Delta t = 0.003$) with the plots displaying lines of constant $\overline{B_\varphi}$ in the left half and meridional field lines $r \sin \theta \partial_\theta \overline{h} = const.$ in the right half of each circle. The first and last rows show lines of constant u_r at $r = 0.5(r_i + r_o)$ and B_r at $r = 1.7 r_o$, respectively, and cover only the first part of the same period.*

with other components in order to be excited. A situation in which the energy of the dipolar component does not exceed by too much the energy of the remaining components seems to be a condition for dipolar oscillations. For such reasons the type of dipolar oscillation appears to be sensitive to the parameter region where the solutions have been obtained.
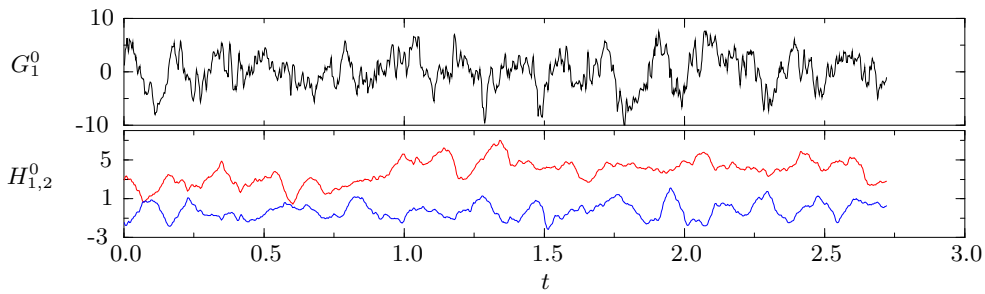
Dipolar oscillations by increasing the Rayleigh number. In order to find a region where the dipole is still dominant but mixed with other components, it is reasonable to start from a quadrupolar dominated region and vary the most easily adjustable parameter – the Rayleigh number. As noted earlier, a clear distinction of dynamos with different symmetry is usually only possible as long as convection occurs predominantly outside the tangent cylinder and still exhibits an approximate symmetry about the equator. Even in the case of hemispherical dynamos only a minor deviation from this symmetry is caused by the action of the Lorentz force. Increasing R leads to the development of polar convection. As soon as the critical

Fig. 9.10. Time series of the coefficients G_1^0 (upper plot) and H_1^0, H_2^0 (lower plot) and their Fourier transforms are shown in the left and right columns, respectively, in the case $P = 1$, $\tau = 10^4$, $R = 5.6 \cdot 10^5$, $P_m = 4$. The color code is the same as in figure 7.9(d) and (e).
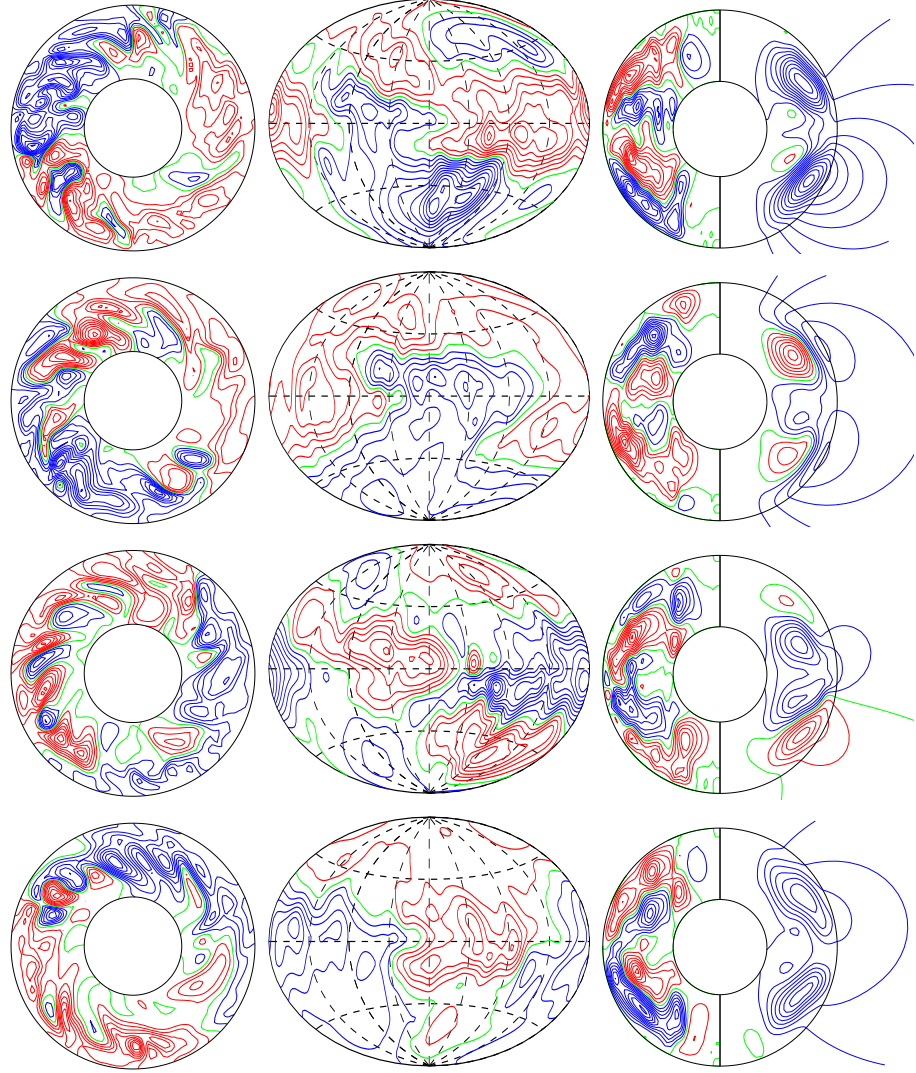
Fig. 9.11. A period of oscillation of the dipolar dynamo of figure 9.10. The plots start at $t_0 = 10.362$, follow in clockwise sense with $\Delta t = 0.005$ and show lines of constant $\overline{B_\varphi}$ in the left half and meridional field lines $r\sin\theta\partial_\theta \overline{h} = const.$ in the right half of each circle.

Fig. 9.12. Same as in figure 9.5 but for an oscillating dipolar dynamo in the case $P = 1$, $\tau = 10^4$, $R = 6 \cdot 10^5$ and $P_m = 6$.
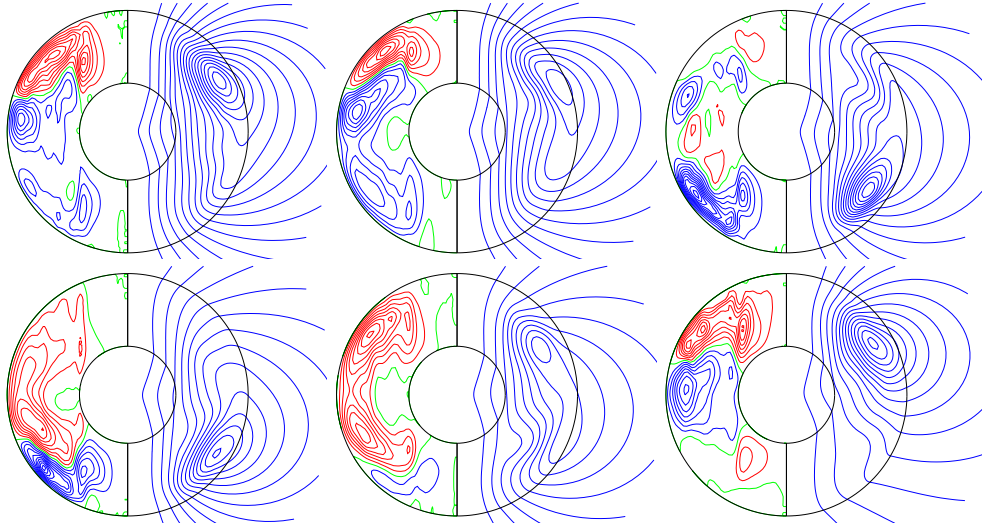
value of R for the onset polar convection is exceeded, the influence of equatorial symmetry diminishes and mixtures of quadrupolar and dipolar components of the magnetic field are generated without the nearly perfect correlation that characterizes hemispherical dynamos, as seen in figure 9.9. Usually, the quadrupolar part of the magnetic field is still stronger outside

**Fig. 9.13.** *An oscillating dipolar dynamo in the case $P = 1$, $\tau = 10^4$, $R = 5.4 \times 10^5$, $P_m = 4$. The sequence of plots equidistant in time (from top to bottom with $\Delta t = 0.08$) shows field lines $r\partial_\varphi h = $ const. in the plane $\theta = 80°$ in the first column, B_r on the spherical surface $r = 1.7r_0$ in the second column, and meridional lines of constant $\overline{B}_\varphi$ in the left halves and $r\sin\theta\partial_\theta\overline{h} = $ const., in the right halves of the plots in the third column.*

the tangent cylinder while the dipolar components appear to be generated primarily in the polar regions. The dipolar fields at large R still exhibit the oscillations which characterize the predominantly quadrupolar fields at lower values of R. The dipolar oscillations obtained in this manner are of interest also because they represent almost periodic reversals of the magnetic polarity. The problem of geomagnetic reversals will be discussed in section 9.4.

Dipolar oscillations by increasing the magnetic Prandtl number. A second approach towards obtaining oscillating dipolar solutions is to increase the value of Pm which is also easily adjustable. As Pm is increased, starting from a predominantly quadrupolar region, the dipolar component becomes stronger. While it is still not much larger than the quadrupolar one, both components actively interact. An example may be seen in figure 9.10 where the poloidal coefficients H_1^0 and H_2^0 together with the toroidal coefficient G_1^0 indicating the periodic behavior of $\overline{B}_\varphi$ are presented. The dipolar component slightly exceeds the quadrupolar

Fig. 9.14. *An oscillating dipolar dynamo in the case $P = 0.1$, $\tau = 10^5$, $R = 4 \times 10^6$ and $P_m = 0.4$. The time sequence of equidistant plots (first row, then second row) with $\Delta t = 0.012$ covers about one period. The left half of each plot shows lines of constant $\overline{B}_\varphi$ while the right half shows meridional field lines, $r \sin \theta \partial_\theta \overline{h} = const.$*
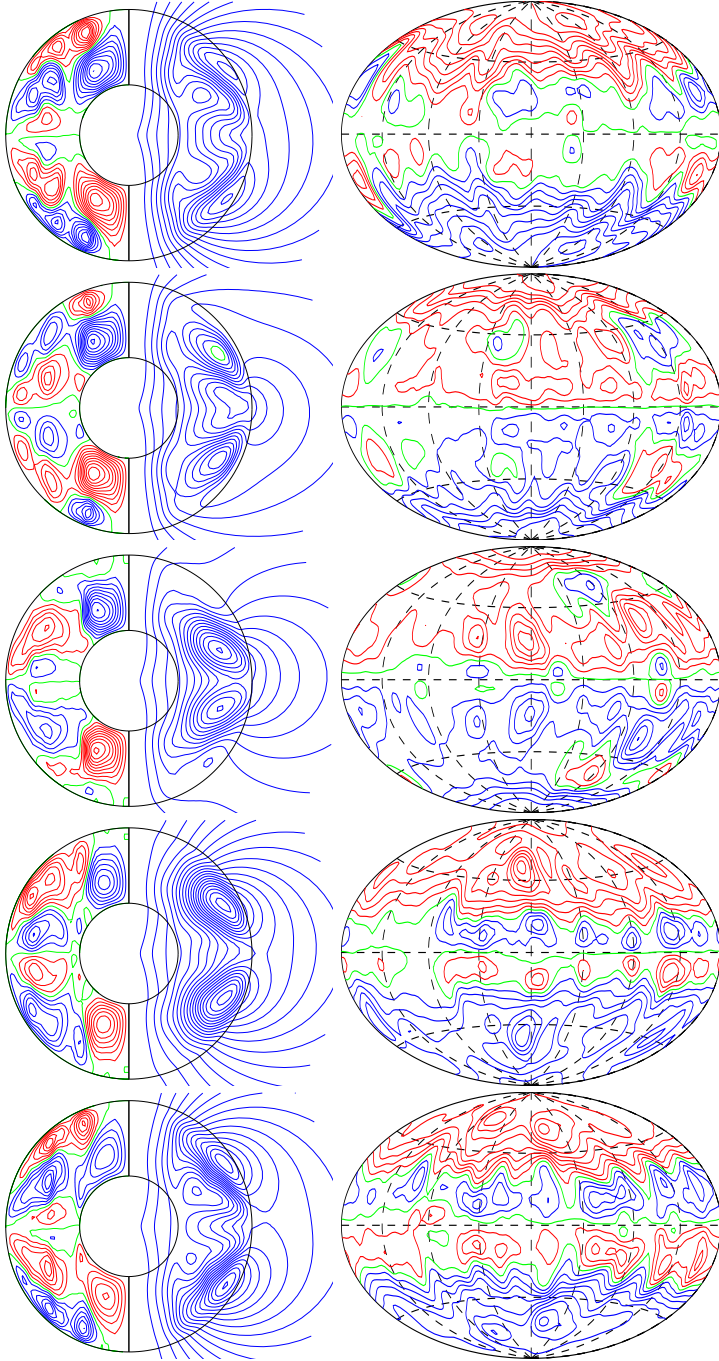
so that at some distance from the core-mantle boundary an oscillating dipole field is observed. A period of the oscillation is shown in figure 9.11. Although the dipolar character of the field is apparent from the figure, the Fourier spectra on the right-hand side of figure 9.10 demonstrate that the oscillation of $\overline{B}_\varphi$ is actually still determined by the oscillation of the quadrupolar component.

As Pm is further increased, the strength of the dipole increases while its interaction with the quadrupole decreases as may be seen in figure 9.12. Ultimately, non-oscillatory solutions with strong dipolar dominance are found in this direction.

$(m = 1)$ dipolar oscillations. Once the regions of oscillatory dipolar dynamos are determined a variety of different oscillations can be observed. The dynamo oscillation of figure 9.13 is indeed quite different from the examples discussed earlier. Although the flux tubes of alternating polarity of the mean azimuthal component $\overline{B}_\varphi$ of the magnetic field propagate towards higher latitude as before, an oscillation can not be detected in the axisymmetric component of the poloidal field outside the sphere. This property is caused by the predominance of the $(m = 1)$ component of the field as shown in the plots of the poloidal field lines in planes parallel to the equator and of B_r in the first and second columns of figure 9.13, respectively. The oscillatory process is nearly 180° out of phase on opposite sides of the sphere. At larger distances from the surface an equatorial dipole slowly drifting relative to the rotating frame of reference will be the main feature of the field.
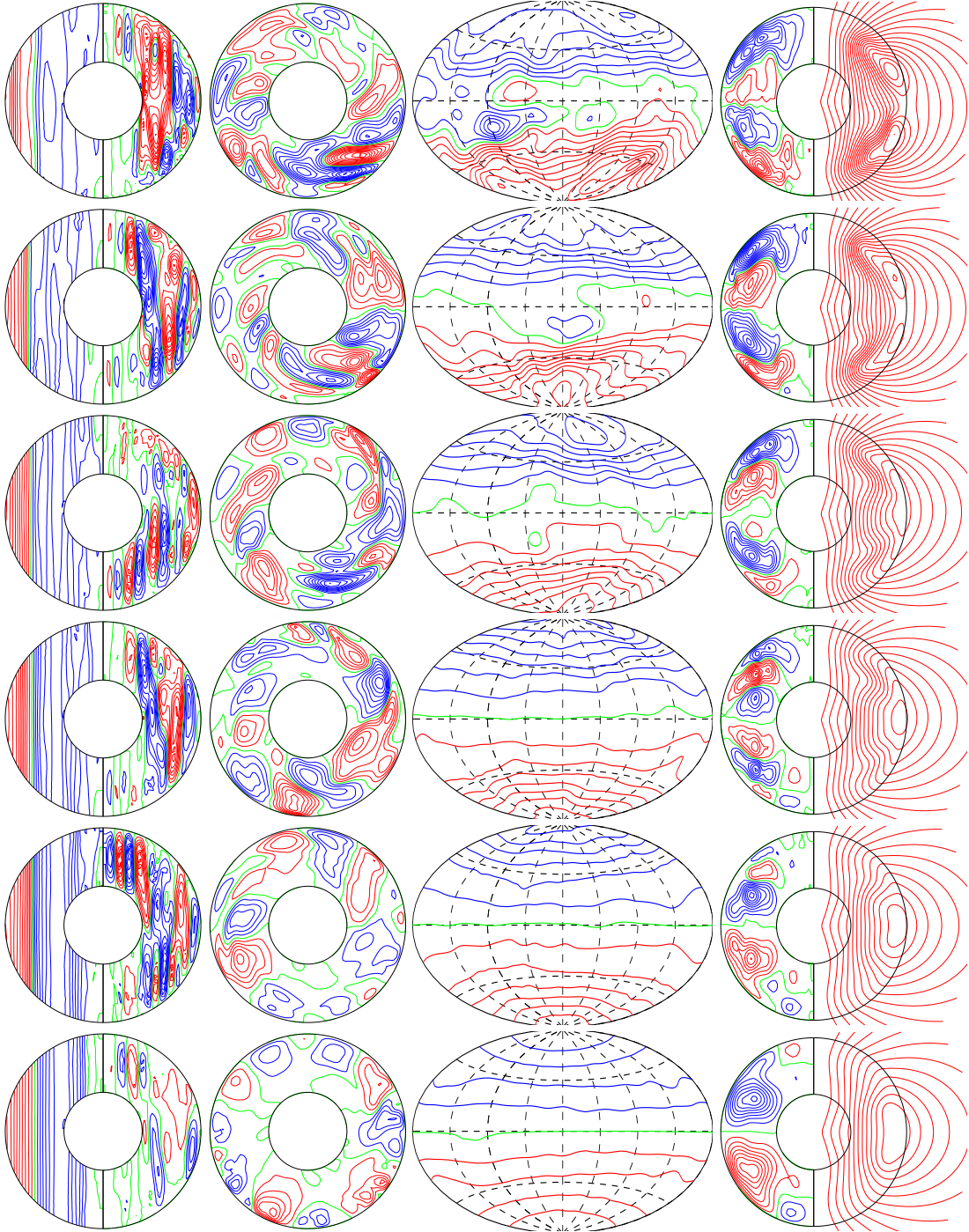
Axial dipolar oscillations. Another type of dipole oscillations which is frequently encountered in low Prandtl number dynamos is shown in figure 9.14. The magnetic field structure is characterized by a strong hemispherical component. But this component switches nearly periodically between the northern and the southern hemisphere. While the mean azimuthal field becomes almost quadrupolar during the switchover (see the 5. plot of figure 9.14) the poloidal field attains its most dipolar structure at this point.

Invisible dipolar oscillations. Another type of oscillatory dynamo is exhibited in figure 9.15. As is typical for dynamos at Prandtl numbers of the order 5 or larger, strong magnetic

Fig. 9.15. An "Invisible" oscillating dynamo with $\Delta t = 0.06$ in the case of $P = P_m = 5$, $\tau = 5 \times 10^3$ and $R = 6 \times 10^5$. The plots in the first column show lines of constant $\overline{B_\varphi}$ in their left halves and meridional field lines, $r \sin\theta \partial_\theta \overline{h} = const.$, in their right halves. The second column exhibits lines of constant B_r on the surface $r = r_o + 0.4$.

flux tubes surround the axis in the polar regions. These flux tubes do not participate in the oscillation. The latter is confined to the region outside the tangent cylinder where $\overline{B}_\varphi$ executes its usual nearly periodic oscillations in the equatorial region as seen in the figure. Although the poloidal field is also located mostly outside the tangent cylinder, the presence of the polar flux tubes prevents its participation in the oscillation except for the small reversal region close to the equator. Thus, little information about this oscillation can be gained by watching the poloidal field from the outside which exhibits a steady dipole with only a minor oscillatory modulation at low latitudes. The occurrence of the strong polar flux tubes is perhaps the most robust feature, found throughout the entire region of high Prandtl number dynamos. These polar fluxes owe their existence to the thermal wind structure of

Fig. 9.16. *Time sequence of equidistant plots (top to bottom) covering the time span from $t = 6.969$ to $t = 7.065$ of the time series of figure 9.17. The left half of the first circle in each row indicates lines of constant $\overline{u_\varphi}$ while the right half displays meridional streamlines, $r \sin \theta \partial_\theta \overline{v} = const.$. The second circle in each row shows streamlines, $r \partial_\varphi v = const.$, in the equatorial plane. The oval plot exhibits lines of constant B_r on the surface $r = r_o + 0.7$. The last circle in each row indicates lines of constant $\overline{B_\varphi}$ in its left half and meridional field lines, $r \sin \theta \partial_\theta \overline{h} = const.$, in its right half.*

the differential rotation at high values of P, which is much stronger in the polar region as has been shown in chapter 6.
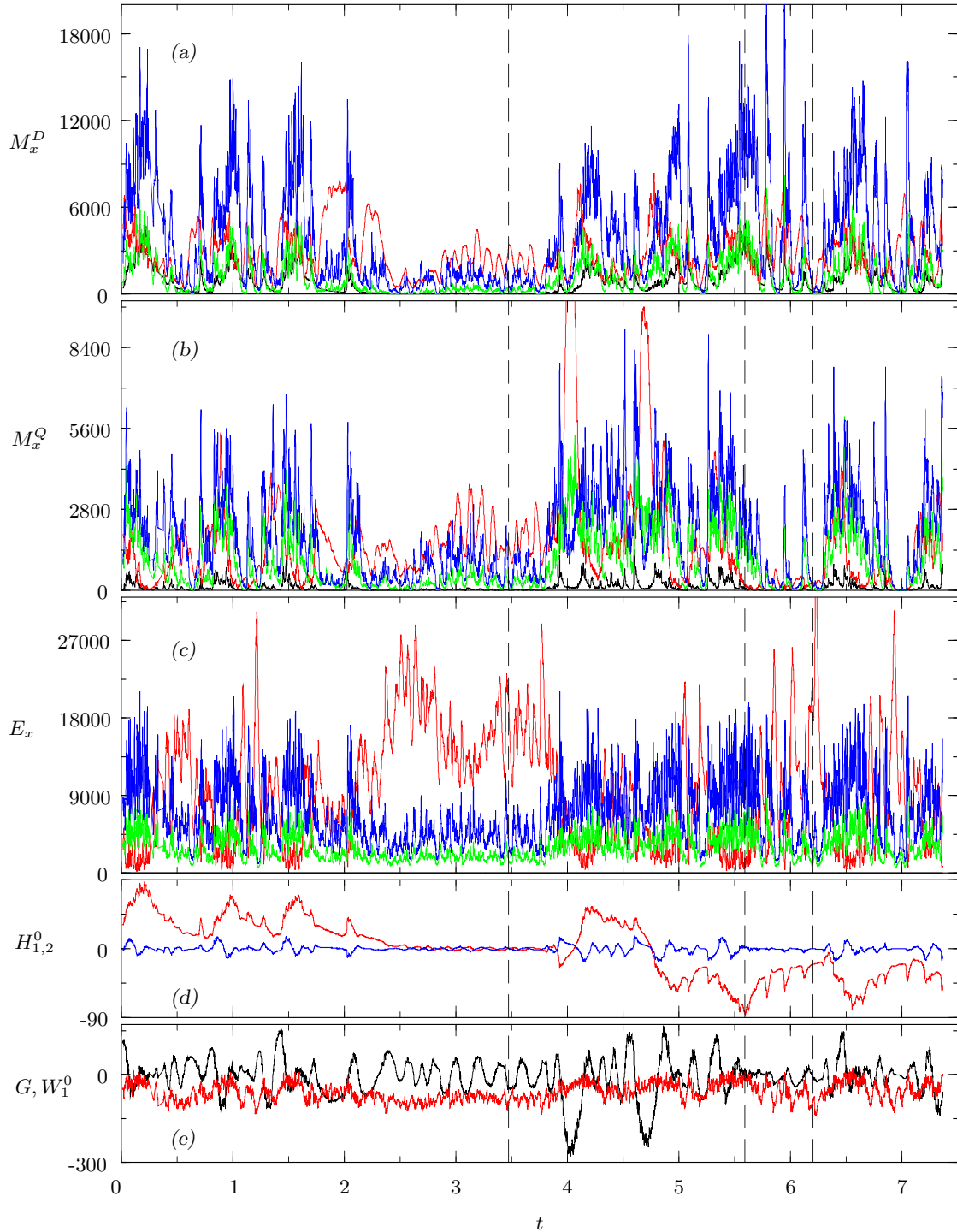
Dipolar oscillations driven by differential rotation. The last typical case of dipolar oscillations which we shall demonstrate differs from the preceding examples in that the dipolar component is strongly dominant and the oscillations are not due to the interaction of the axial dipole $l = 1$ with the higher l components but are rather caused by the competition of the magnetic field and the differential rotation.

This type of oscillation which is presented in figure 9.16 occurs at small values of P and intermediate values of τ and R. At these parameter values the solution is situated near the boundary between inertial and columnar convection. When a self-generated magnetic field is present it breaks the differential rotation and strongly promotes the columnar convection. This effect may be observed in the upper rows of plots in figure 9.16. However, when the differential rotation becomes too small the ω-effect creating toroidal magnetic field from the poloidal one operates less efficiently. As a result, the mean toroidal magnetic field decreases which leads to a further decrease in the poloidal field itself because of a reduced large-scale α-effect. The weakening of the magnetic field allows the differential rotation to grow again, as may be seen in the last two rows of figure 9.16. The increase of differential rotation suppresses the convective motions and destroys the columnar structures. However, because the Rayleigh number is not sufficiently large and because the solution is on the boundary with inertial convection, the flow never dies out completely. It rather crosses the boundary and assumes equatorially-attached cell structure. The equatorially-attached cells are much less affected by the action of the differential rotation as have been shown in chapter 6. Thus the inertial convection helps to preserve the magnetic field from a further decay. Once the differential rotation is strong again it amplifies the mean toroidal magnetic field and thus closes the regenerative cycle of the magnetic field which grows to its initial high intensity and the process starts again. A remarkable property of this type of oscillation is that the creation of new flux, propagating towards higher latitudes, typical for the preceding examples of dipolar oscillations, is now of much less significance. A weak flux may be observed only in the axisymmetric component of the toroidal field. The dipole keeps its strong dominance and form and only changes its strength as the oscillation continues.

The process which this last example illustrates is of special importance not only because it represents a different type of oscillation but also because it leads to a strongly intermittent dynamo action. The dynamo intermittency in turn is a precondition for magnetic field polarity reversals very similar to those actually observed for the geomagnetic field. These topics will be addressed in detail in the following sections of the chapter.
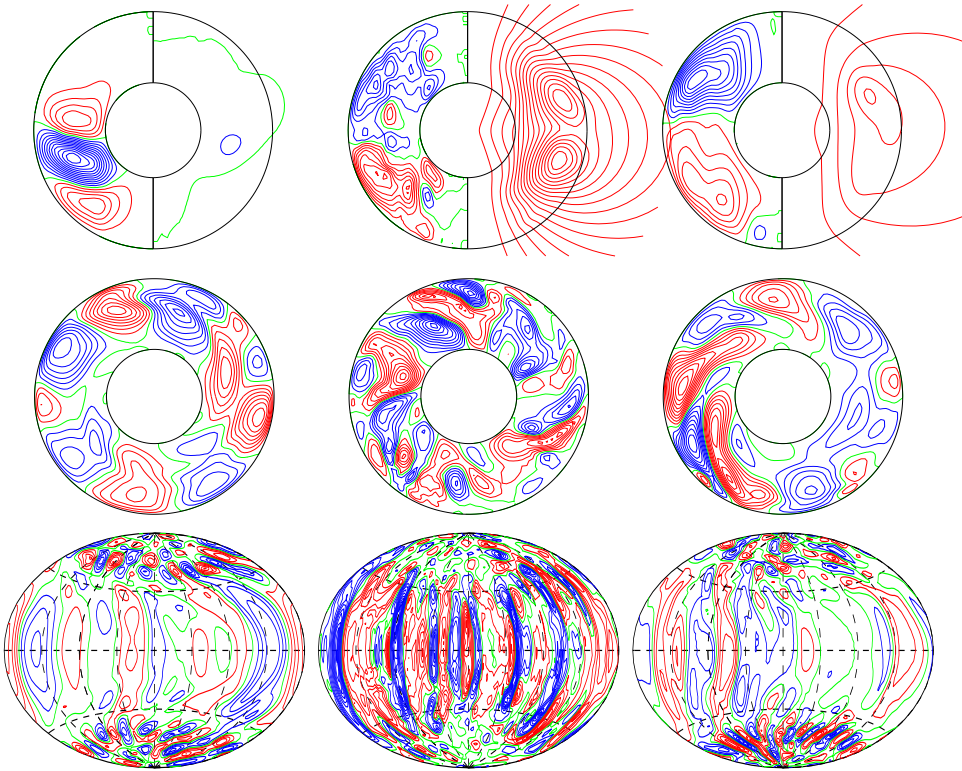
9.3 Intermittency

Despite that the majority of our dynamo and convection solutions are highly turbulent, most of them ultimately equilibrate to well-established average values of their energies. It is also usual to observe that if two different runs are performed for the same parameter values but different initial conditions they converge to the same equilibrium. However, since the governing equations of the dynamo process are nonlinear, the existence of multiple attractors may not be excluded. Indeed, cases with two attractors have already been found and reported in our work [29], but such cases are the exception rather than the rule. In this section we present a case, which is even more remarkable, because it seems to poses two distinct attractors and switch between them aperiodically and without apparent triggering event. The two equilibrium states between which the solution alternates have well-distinguishable average energy values as well as spatial structures. This "intermittent" dynamo solution, obtained at values of the parameters $P = 0.1$, $\tau = 3 \times 10^4$, $R = 8.5 \times 10^5$ and $Pm = 1$, is shown in figure 9.17. At the beginning of the simulation the solution equilibrates at its high energy

Fig. 9.17. *Time series of energy densities and selected coefficients in the case $P = 0.1$, $\tau = 3 \times 10^4$, $R = 8.5 \times 10^5$, $Pm = 1$. The same quantities as in the corresponding panels of figure 7.9 are shown, except in (e) where in addition the coefficient W_1^0 is displayed in red.*

state and remains there for a period of 2 time units when it suddenly switches to its low energy state where it remains for a roughly equal time interval. It ultimately returns to the initial high level at $t = 4$. While in the high energy state, the dynamo frequently performs short-time excursions to the low energy one, implying that the intermittency is a characteristic

Fig. 9.18. *Snapshots of the case presented in figure 9.17 at the moments marked by vertical lines, t = 3.48 (left column), t = 5.58 (middle column) and t = 6.10 (right column). The left half of each plot in the first row shows lines of constant $\overline{B_\varphi}$ while the right half shows meridional field lines, $r \sin \theta \partial_\theta \overline{h} = const$. Equatorial streamlines $r\partial_\varphi v$ and u_r at $r = 0.5(r_i + r_o)$ are plotted from top to bottom in the next rows.*

feature of the solution. Figure 9.18 illustrates the spatial structure of the dynamo in the two states. In the high energy state the dynamo is strongly dominated by its dipolar component while it is perfectly hemispherical in the low energy state. It is not so remarkable that the dynamo switches between two attractors but rather that it is possible to equilibrate on them which, as figure 9.18 shows, means that at the same parameter values it can operate in two distinct dynamical regimes. From the structure of the convection solution in the figure, it may be suggested that this is possible because the case is situated on the border between the regions of inertial and columnar convection. As has been argued in chapter 6, inertial convection is less sensitive to the inhibiting action of the differential rotation than columnar convection. The same holds for polar convection which can also be observed in the figure. The low energy state of the dynamo is strongly dominated by differential rotation which is able to suppress columnar convection but has only little effect on polar and equatorially-attached convection. In turn the latter support magnetic field generation, although not as efficiently as the columnar structures but at sufficient rate to prevent the field from a total decay in the presence of the strong differential rotation. Once the magnetic field recovers to its high values it contributes to the suppression of the differential rotation and promotes the columnar convection. It is worth noting, that the largest contribution to the magnetic energy in the hemispherical state is provided by the mean toroidal energy while in the dipolar state the other energy components dominate. Figure 9.17 suggests that this effect is due to the strong differential rotation in the hemispherical state which stretches the field lines in the

azimuthal direction and creates a strong toroidal magnetic field. The corresponding strong fluxes of $\overline{B}_{\varphi}$ are also observed in figure 9.18. The figure shows another interesting aspect, namely that in its hemispherical state, the dynamo will not be detected from a distance as large as the Earth's surface, since its poloidal component is very weak. The short-term behavior of the solution while in its high energy state has already been described as the last example of dipolar oscillations in the preceding section. While in its lower level the dynamo executes the ordinary hemispherical oscillations.

The significance of this example is two-fold. First, it demonstrates the existence of parameter regions where dynamo solutions may achieve such a delicate balance between various effects so that two or more alternative long-living states become possible. This in turn, seems to provide an appropriate mechanism for a realization of Earth-like polarity reversals of the magnetic field, a topic to be addressed in the following section.

9.4 Geomagnetic polarity reversals

Up to this point in the dissertation we have not attempted to link our results to any actual observations of the geomagnetic field. But the ultimate goal of any theory is to explain the physical reality rather than avoid it. Dynamo theory is no exception and in the present section we use the results of our numerical simulations to offer some insight to what is perhaps the most striking feature of the geomagnetic field – its polarity reversals.

Phenomenology. During most of the time covered by the paleomagnetic record, the Earth's field has been dominated by an axial dipole with either "normal" or "reversed" polarity. *Geomagnetic polarity reversals* are the transitions between these two states.

The attributes common to most polarity reversals, as inferred from a large number of paleomagnetic studies, have been recently summarized in [88]. The major polarity epochs (chrons) have variable duration which during the last 10 Ma is 0.2 – 0.25 Myr. Extremely long polarity epochs have also existed such as the 36-Myr Cretaceous superchron. There is little evidence for polarity bias, implying that normal and reversed fields have the same average structure and are equally probable. The duration of reversals is estimated to be between 1.5 and 5 kyr. The magnetic field intensity is reduced prior to and during the polarity transition typically by a factor 2 – 10 but the field recovers quickly (usually within a few kyr) without dwelling in a low intensity state. Transitional magnetic fields include non-dipole components but retain some large-scale structure. Another not-so-well established attribute is the "sawtooth" intensity variation during polarity epochs where the intensity is highest shortly after polarity change and tends to decrease prior to the next reversal.
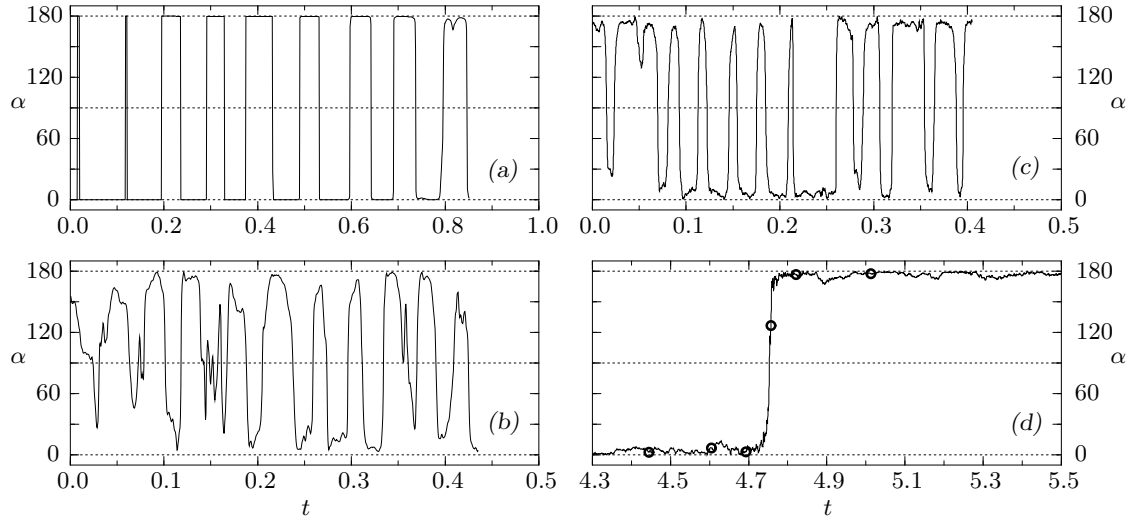
Reversals as a property of chaotic dynamical systems. Among the countless variety of geomagnetic features, the reversals are probably those that most fascinate geophysicists. However, their existence should not be a surprise; it would be more surprising if reversals did not occur. Indeed, since the momentum equation (3.64b) is quadratic in $\boldsymbol{B}$ and the induction equation (3.64g) is homogeneous in $\boldsymbol{B}$, the equations governing the dynamo process are invariant under the symmetry $\mathcal{B} : (\boldsymbol{u}, \boldsymbol{B}) \longrightarrow (\boldsymbol{u}, -\boldsymbol{B})$, which preserves the flow $\boldsymbol{u}$ and changes the sign of the magnetic field $\boldsymbol{B}$. Thus for any solution $(\boldsymbol{u}, \boldsymbol{B})$ of (3.64b) and (3.64g) exist a second solution $(\boldsymbol{u}, -\boldsymbol{B})$ and there is no reason for preferring one polarity over the other. Moreover, it has long been realized that events similar to reversals are not a specific property of the dynamo process but occur in a variety of nonlinear systems. For instance, the statistical properties of reversals can be simulated by low-order dynamical systems such as those describing coupled or shunted disk dynamos. The low-order systems do not exhibit separation of time scales between quasi-steady polarity configurations and rapid reversal

events, but this may be taken into account by invoking more complicated systems containing dynamical structures such as structurally stable heteroclinic cycles. In this sense, the fundamental reason for the existence of reversals may be attributed to the properties of the nonlinear governing equations and the presence of the symmetry $\mathcal{B}$. It may be argued that neither external triggering random process nor symmetry breaking due to inhomogeneity of boundary conditions nor any other influence external to the system is required to give rise to a sequence of aperiodic reversals.

Geophysical questions. Numerical studies. Even though no external influence for the occurrence of reversals is required from a mathematical viewpoint, it is very likely that such influence exists. Furthermore, it is unquestionable that the polarity transitions themselves affect significantly and carry information about other geophysical processes. Thus the issue of reversals is far from closed and adapting from [88] we, state several questions which will guide our discussion. **(1)** What is the character of a reversal as seen from the Earth's surface? From inside? **(2)** Is the geodynamo in a reversing configuration only when it reverses or more often? **(3)** Are reversals triggered by an external reason or may a flow pattern be identified as a reason for reversals? **(4)** What is the mechanism of reversals? Of course, many other questions may be posed, but these are the ones to which numerical simulations may best contribute. The main objectives of previous studies have been to describe the geometry of the external field during transition [55, 75], to explore effects of various patterns of boundary heat flow heterogeneity [54] and of the inner core conductivity [69, 116], to determine a parameter region of "reversing dynamos" and the sensitivity of reversal frequency to model parameters [82]. However, the results are not conclusive and relatively little attention has been paid to the mechanisms that cause the reversals. This is particularly true for the highly chaotic dynamo models where the magnetic field and the flow have high spatial and temporal complexity, and the mechanisms driving the reversal are difficult to isolate. In most early studies hyperdiffusivities have been employed which may alter the dynamo behavior [61]. In the following we describe our attempts to gain insight into the process of polarity transitions.

Types of reversals. Although special efforts have been committed to obtain reversing dynamos in our calculations, only a limited number of realistic dipolar reversals have been found. However, many less appropriate examples have been observed. The easiest method to detect whether a dynamo reverses or not, is to compute the tilt angle of the magnetic field dipole axis relative to the rotation axis. The dynamo is in a quasi-steady polarity configuration if the dipole tilt angle α has a value close to $0°$ or $180°$, and in a period of transition when α switches between these values and crosses the $\alpha = 90°$ line. The value of the poloidal coefficient H_1^0 which describes the axial dipole contribution represents an equivalent indication for a reversal. The dynamo undergoes a polarity transition when H_1^0 changes sign.

The reversals observed in our simulations may be classified into two groups - **(1)** periodic or nearly-periodic reversals and **(2)** aperiodic reversals. Cases *(a)*, *(b)* and *(c)* in figure 9.19 represent examples of the first group while case *(d)* is an example of the second one. The periodic reversals occur as a result of the dynamo oscillations which have been extensively discussed in the previous sections. Of all the various dipolar oscillations only two involve transitions between the normal and the reversed polarity. The "pure" dipolar oscillations illustrated in figures 9.3 and 9.4 reverse in almost perfectly periodic fashion as may be seen in the impulse-like signal shown if figure 9.19*(a)*. The time spent in each of the two polarity states is equal, implying their equal probability. Studying figures 9.3 and 9.4 and 9.19*(a)* we may note that during the reversals the dipole axis remains strictly parallel to the rotation axis and the poles do not wander over the surface. The reversal occurs simply by the process of creation and grow of new fluxes of the opposite polarity near the equator and the gradual decay of the old fluxes carrying the initial polarity. The second type of dipolar oscillation

Fig. 9.19. *The dipole tilt α as a function of time in the cases (a) $P = 1$, $\tau = 3 \times 10^3$, $R = 3 \times 10^5$, $Pm = 3$, (b) $P = 1$, $\tau = 5 \times 10^3$, $R = 1.4 \times 10^6$, $Pm = 1$, (c) $P = 0.1$, $\tau = 10^5$, $R = 6 \times 10^6$, $Pm = 0.12$ and (d) $P = 0.1$, $\tau = 3 \times 10^4$, $R = 8.5 \times 10^5$, $Pm = 1$.*
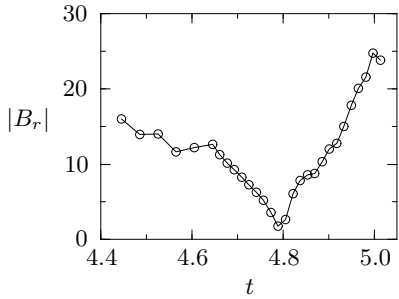
which leads to reversals is the oscillation at increasing Rayleigh number shown in figure 9.9. The reversal mechanism in this case is again obvious from the time sequence of that figure. The value of the dipole tilt corresponding to this case in figure 9.19(b) does not switch between 0° and 180° so neatly. Short events during which the dipole axis briefly crosses the equator but returns to its initial hemisphere are seen. In addition, the figure indicates that the dynamo spends slightly more time in the state of normal polarity.

Figure 9.19(c) illustrates another situation, in which dipolar reversals are observed, namely in the case of oscillating hemispherical dynamos. Since any hemispherical dynamo has a finite dipolar component roughly equal to the quadrupolar one and since these two components oscillate together, the hemispherical dynamos execute dipolar reversals, in principle. Clearly the periodic reversals are not realistic from geomagnetic point of view.

Our numerical simulations also feature several aperiodic polarity transitions. The group of aperiodic reversals may, in turn, also be separated into two subgroups. The first one contains reversals occurring in dynamos with highly chaotic behavior obtained at sufficiently large values of R. In such dynamos, however, field is filamentary, the axial dipole component is no longer dominant and the quadrupolar and the higher degree components are equally strong. But since the axial dipole is finite, the orientation of its axis now assumes all possible tilt angles, often randomly crosses the equator and still shows preference to align with the rotation axis. Such aperiodic reversals probably do not have much geophysical significance because of the relatively small dipolar contribution to the magnetic field. This subgroup of aperiodic reversals has also been observed and extensively studied in [82].

Reversals in the case $P = 0.1$, $\tau = 3 \times 10^4$, $R = 8.5 \times 10^5$, $Pm = 1$. Our second subgroup of aperiodic reversals actually consists of a single example, namely the case at $P = 0.1$, $\tau = 3 \times 10^4$, $R = 8.5 \times 10^5$ and $Pm = 1$, already discussed in connection with dynamo intermittency and oscillations. This remarkable case also exhibits two polarity transitions very much resembling the actual geomagnetic reversals which we analyze in more detail.

Features. Comparison with geomagnetic reversals. Apart from the many periodic reversals while in its hemispherical state the case presented in figures 9.17, 9.19(d), 9.20 and 9.21 features a couple of strongly dipole dominated transitions, occurring as isolated events
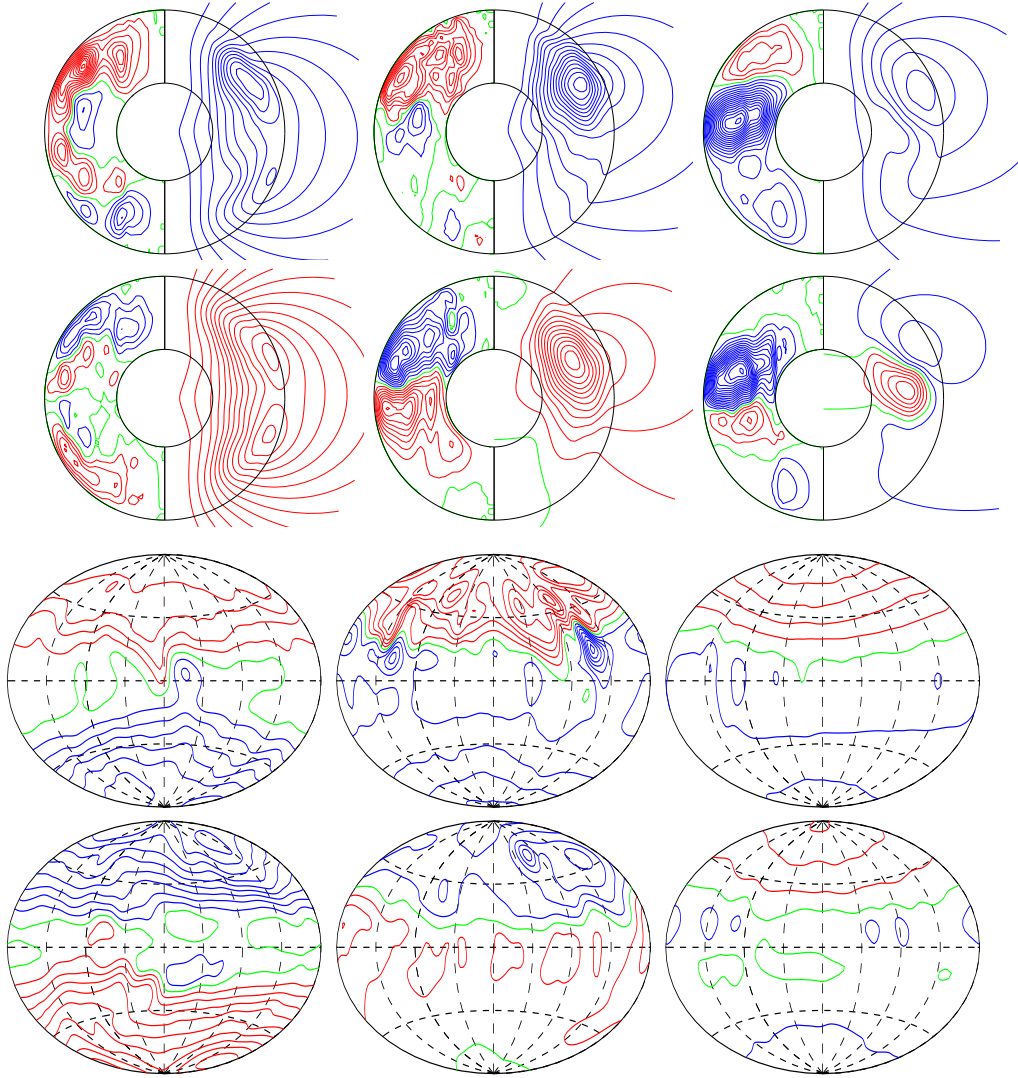
Fig. 9.20. *The averaged value of $|B_r|$ at the surface $r = 2.6r_o$ for the same case as that shown in figure 9.19(d).*

at times $t_1 = 4.07$ and $t_2 = 4.76$. In order to demonstrate the extent to which these reversals resemble actual geomagnetic transitions we compare them with the robust characteristics proposed in [46]. **(1)** It is considered to be a robust observation that the field intensity drops significantly before the reversal, but recovers shortly after its completion. In figure 9.20 the absolute value of the radial magnetic field $|B_r|$ at the surface of the Earth is plotted as a function of time. Indeed, the minimum is observed at the time of the reversal. The same observation can be made in the plots of figure 9.21. It must be noted that the total magnetic energy in the fluid outer core is not at its lower level during the reversals and that there exist other instants in time when it actually has a lower value. However, the total magnetic energy in the fluid outer core is inaccessible for observation. **(2)** A second robust observation is that the duration of reversals is about a few thousand years. With the help of figure 9.19(d) we may easily estimate that in our simulation the transition occurs between $t_1 = 4.7$ and $t_2 = 4.8$ which converted into years gives a duration of 2500 yrs and is well within the range of geomagnetic observations [88]. **(3)** A third robust observation is that the reversal frequency should be a few events per million years. With only two dipolar reversals occurring in a simulation spanning nearly 0.2 Myr it is obvious that this requirement is also met. However, a continuation of this case is necessary to better estimate the frequency of reversals.

The exact sequence of events occurring during the polarity transition may be followed in the plots of figure 9.21. The instants at which the snapshots in the figure are taken are marked by circles in the dipole tilt curve in figure 9.19(d). The particular event, causing the reversal in this case is the oscillation of the $l = 1$ dipolar and $l = 2$ quadrupolar components. At the moment when these components are approaching their minima, a higher l flux is created near the equator. This flux is amplified by the dipolar and quadrupolar components which grow during the second part of their oscillation period. This ultimately results in the reversal of the initial polarity of the magnetic field. Below we speculate on the conditions necessary for an Earth-like reversal and suggest a possible reversal mechanism.

Hypothetical dynamo undergoing Earth-like reversals. Based on the various types of reversals, we wish to suggest a type of dynamo which would exhibit aperiodic reversals similar to those of the geodynamo. Such a dynamo should exhibit a sort of intermittent behavior in which it should feature periods in time during which the axial dipole component H_1^0 is sufficiently dominant, as well as periods during which the axial dipole should become comparable to the "competing" higher l components. During the latter periods possibilities for polarity transitions occur. Such a "condition" is neither too restrictive nor too particular. On the contrary, our numerical results support it as a rather reasonable one. Consider the balance between two dominant components – the axial dipole H_1^0 and say the H_2^0 quadrupole. Several cases are possible: **(A)** the axial dipole is strongly dominant for all times; **(B)** the axial dipole is "intermittently" dominant, i.e. with periods in which it is comparable with the quadrupole. This is our hypothetical reversal case.; **(C)** the two components are nearly equal for all times, or the quadrupolar component is either intermittently of largely dominant. Case **(A)** reminds us of the non-oscillatory dynamo cases which we have observed at

Fig. 9.21. *Magnetic field polarity reversal in the case $P = 0.1$, $\tau = 3 \times 10^4$, $R = 8.5 \times 10^5$, $Pm = 1$. The first pair of rows show $\overline{B_\varphi} = $ const. (left halves) and meridional field lines, $r \sin\theta \partial_\theta \overline{h} = $ const. (right halves). The second pair of rows show $B_r = $ const. at $r = 1.7 r_o$. The plots follow in clockwise sense at times indicated by circles in figure 9.19(d).*

high values of Pm. Since the dipolar component is much larger than the quadrupolar *for all times* it never decreases enough so as to change sign. Indeed, if the dynamo is to reverse, its poloidal coefficient $H_1^0(r,t)$ must change sign which implies that a finite period of time must exist when the axial dipole is comparable to the other components. Case **(C)** describes hemispherical, mixed and purely quadrupolar dynamos which often reverse but in geomagnetically unrealistic fashion. Thus the only reasonable suggestion for an Earth-like reversing dynamo remains the dynamo of case **(B)**. The intermittent dynamo presented in figures 9.17, 9.19(d), 9.20 and 9.21 is exactly of this type. In fact, this demonstrates that such a dynamo is not merely a hypothetical possibility but is a realizable solution of the basic equations.
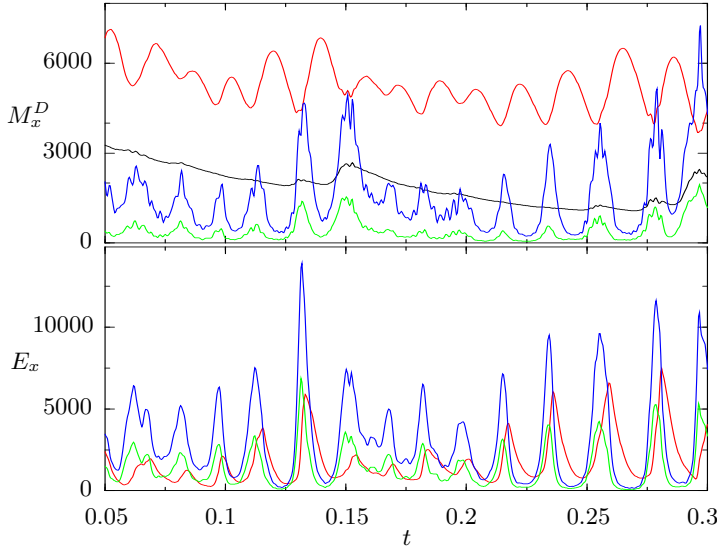
Reversal mechanism. The reversal mechanism of a dynamo of case **(B)** may be most robustly understood in terms of dynamo oscillations and interaction between the dominant axial dipole and the quadrupole and may best be explained with the help of the time series of the poloidal coefficients H_1^0 and H_2^0 as shown in figure 9.17(d). As already discussed, a

dipolar reversal occurs when H_1^0 changes sign while the balance between the absolute values of these coefficients indicates whether the dominant component is the dipolar ($|H_1^0| > |H_2^0|$), or the quadrupolar ($|H_1^0| < |H_2^0|$). Furthermore, an oscillating behavior of the coefficients corresponds to pure dynamo oscillations as shown in figures 9.4 and 9.7.

It may be observed in the time series of figure 9.17(d) that at any instant in time this dynamo is in one of the three distinct states **(i)** "basic" state, **(ii)** "migrative" state or **(iii)** "transitional" state which alternate each other cyclically. In the basic state the dipolar component is significantly larger than the quadrupolar. It seems as if it contains most of the energy available to the magnetic field and no energy is left to excite the higher l components. The dynamo is in a polarity stable configuration which does not reverse. For reasons which are not quite clear, but most probably involve the nonlinear interaction between the differential rotation and the magnetic field, as seen in figure 9.17(a), (b) and (c) and have been discussed in connection with the intermittent behavior, the basic state is sooner or later replaced by the migrative state. In the migrative state the axial dipole $|H_1^0|$ steadily decreases and eventually when it reaches a certain low level, an opportunity arises for the quadrupole $|H_2^0|$ to grow. However, as all numerical results indicate, the quadrupole never increases monotonically but it rather oscillates in its usual fashion. At this stage the dynamo enters its transitional state which is comparatively short. Looking again at figure 9.17(d), we may observe that two distinct scenarios take place. If the quadrupolar component is in phase with the decline of the dipolar one, both coefficients continue to approach zero until they change sign. Plots of the type used in figure 9.4 show that when the dipolar component has a low amplitude it also becomes oscillatory. For this reason once it has changed sign it continues the second half of its oscillation period and recovers towards a basic state of the opposite polarity. A complete reversal has occurred. A second case is much more often observed in figure 9.17(d) in which the quadrupolar component is in antiphase with the decline of the dipolar one. The growing quadrupole seems to block the further decrease of the dipole and repels it backwards. After the repelling impulse the axial dipole starts to increase keeping its initial polarity and the reversal has been avoided. Apart from the low energy hemispherical state, the cycle of alternating basic, migrative and transitional states occurs seven times in the time record of figure 9.17(d). In five of the cases a reversal is avoided and in two cases transitions to the opposite polarity occur. This suggests that this might be a typical reversal mechanism. Even if this is the case, the question of a reversal mechanism is only replaced by more basic ones. In the first place, it is not clear why the basic state looses it approximate stability and the dipolar component starts to decrease, nor what determines the duration of the basic state and its average energy. Concerning the migrative state, one might ask what is the reason for the quadrupole H_2^0 to get excited and to begin oscillating when the axial dipole H_1^0 becomes low in energy. What determines the period of the quadrupolar oscillation? Will it eventually be in phase or antiphase with the dipolar one? Finally, the mechanism of interaction by which the quadrupole repels the axial dipole towards its initial polarity is unclear.

9.5 Torsional oscillations and geomagnetic secular variation impulses
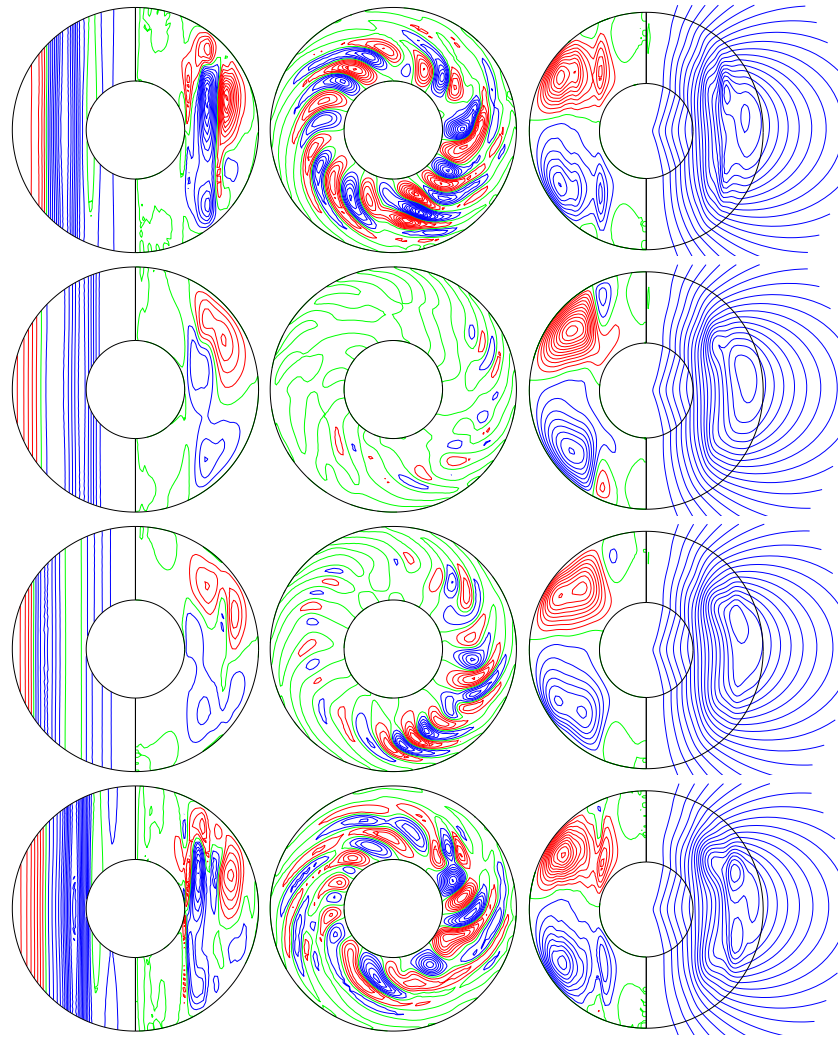
Of special interest to both theory, simulations and observation in geomagnetism are the ideas which could bridge the gap between those branches and provide validity checks of their methods. In this last section we discuss from a numerical point of view one such idea which links some observational phenomena, known as "geomagnetic jerks" or "secular variation impulses" to the theoretical possibility of torsional oscillations in the Earth's fluid core.

Fig. 9.22. *Dipolar magnetic energy densities (upper part) and kinetic energy densities (lower part) as functions of time in the case $P = 0.1$, $\tau = 10^5$, $R = 2\times10^6$, $Pm = 1$. The color code is explained in the caption of figure 7.9.*

The temporal variations of the geomagnetic field cover a wide spectrum which may be roughly divided into higher frequencies due to external sources and lower frequencies of internal origin known as the main field. Until recently the time scale boundary between the external and internal sources has been thought to be at least several years. Changes on such time scales are exhibited mainly by the higher harmonic degrees of the main field, for example degrees 10 to 13 as retrieved by satellite measurements between 1980–2000. Such changes of the smallest features of the main field are clearly local and are to be expected on physical grounds. However, very different global variations of internal origin of the large scales of the main field with time scales of the order of or shorter than one year have been shown to exist [41]. The subsequent examination of the geomagnetic data from observatories across the world reveals that nine such events have occurred during the 20th century, three being unquestionably of global extent (1968, 1978, 1992), three possibly also global (1901, 1913, 1925), two seen only at single locations (1932, 1949) and one just recently detected (1999). Prior to the 20th century the quality of available data is poor to detect such fast occurring events. These variations are the so called *jerks (impulses)*. They are most easily observed as abrupt changes in the secular variation, i.e. in the time derivative of the declination of the geomagnetic field D, or of its East component Y as may be seen in figures 1 and 2 of [87].

Even before observational evidence has first been reported, large scale variations of internal origin exhibiting very short time scales had been theoretically suggested [7] based on the idea of torsional oscillations in the Earth's core. The physical origin of such oscillations is similar to the origin of elastic waves on a string with the magnetic field $\boldsymbol{B}$ playing the part of the string. In a perfect conductor the $\boldsymbol{B}$-field and the fluid are virtually frozen together. If a portion of a field line is swept away by a lateral motion of the fluid, the resulting curvature of the field line r_c gives rise to a restoring force B^2/r_c. As the curvature increases, the restoring force rises and eventually the inertia of the fluid is overcome and the lateral movement is stopped. However, the Lorentz force is still present and so the flow now reverses carrying the field lines back with it. Eventually, the field lines return to their equilibrium positions but now the inertia of the fluid carries the field lines past the neutral point and the process starts in reverse. Oscillations known as *Alfvén waves* develop in this way. When the dynamics of the fluid is dominated by Coriolis and magnetic forces, as in the Earth's core, the Alfvén-type oscillations involve torsional motions on coaxial cylinders. The torsional oscillations play important role in the mathematical theory of core MHD and, therefore are important regardless of whether they lead to phenomena which may be observed. Already in the initial

Fig. 9.23. *Time sequence of equidistant plots (top to bottom) covering the time span from $t = 0.234$ to $t = 0.258$ of figure 9.22. The left half of the first circle in each row indicates lines of constant $\overline{u_\varphi}$ while the right half shows meridional streamlines $r\sin\theta\, \partial_\theta \overline{v} = const.$ The middle circle exhibits streamlines $r\partial_\varphi v = const.$ in the equatorial plane. The right circle shows lines of constant $\overline{B_\varphi}$ in its left half and meridional field lines $r\sin\theta\, \partial_\theta \overline{h} = const.$ in its right half.*

studies of Braginsky [7] the period of torsional oscillations for suitable basic **B**-fields has been determined, the inner core has been allowed for, the boundary layers at the core-mantle and inner-outer core boundaries have been studied as well as the coupling to the mantle has been incorporated. However, much of this has remained only a theoretical analysis until recently when Bloxham *et al.* [6] argued that the regularity of the occurrence of jerks during the last 30 years may be a result of the propagation of Alfvén torsional waves in the Earth's core.
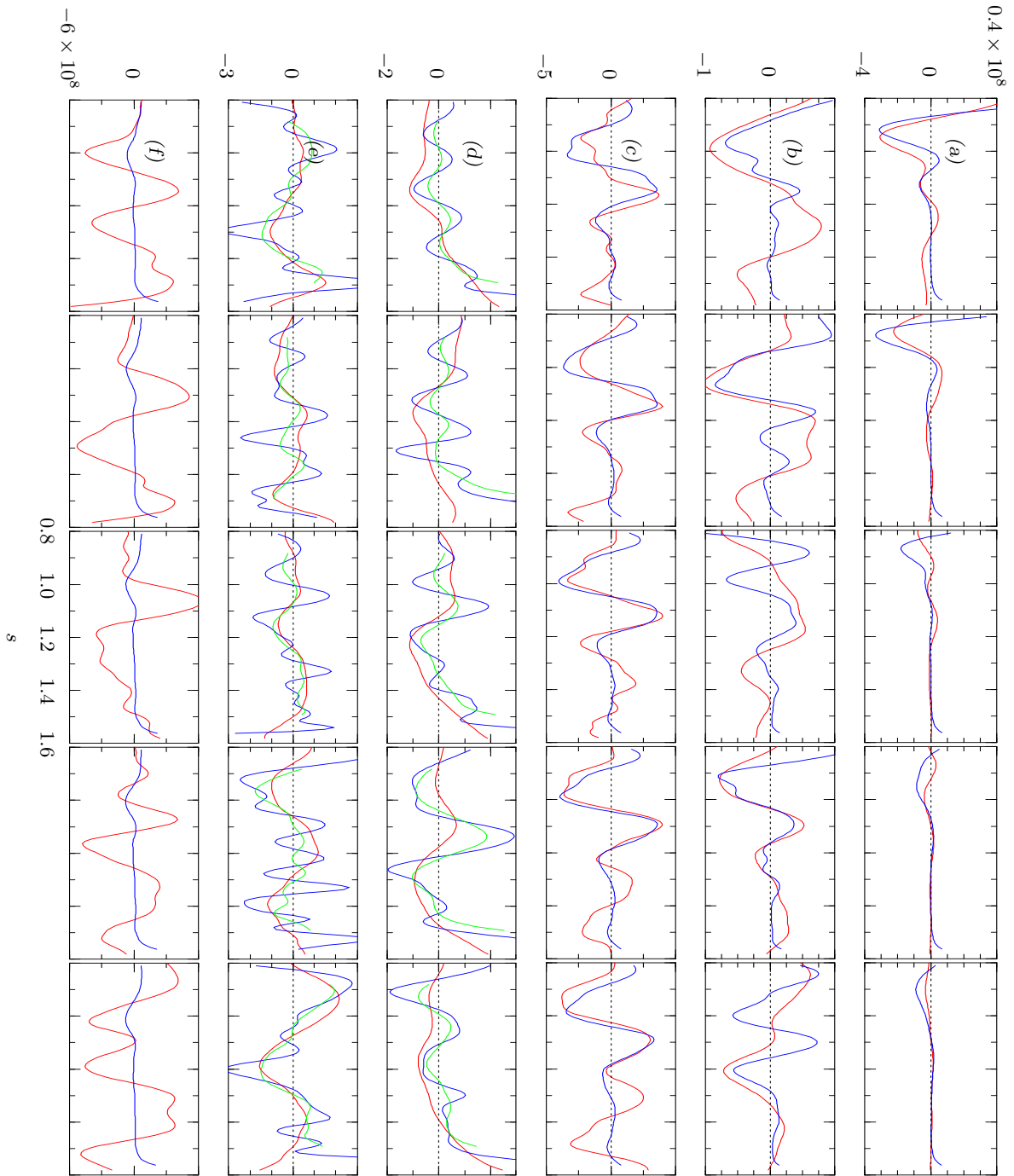
Torsional oscillations have not yet been reported in self-consistent dynamo simulations to present time. Theoretically, the torsional oscillations result from small perturbations of velocity in a situation when the main balance of forces is determined by the Coriolis and Lorenz forces while buoyancy and dissipation effects are negligible. Such a balance is the geostrophic flow which requires large values of τ. However, the rotation parameter cannot be increased drastically due to computing constraints which, in turn, leads to the general difficulty of simulating torsional oscillations in self-consistent dynamo simulations. However,

by carefully increasing the Coriolis number to values $\tau = 10^5$ and adjusting the value of the Prandtl number to $P = 0.1$, we have been able to identify a region in the parameter space where such balance of forces seems to exist. In this region the dynamo oscillations become much more pronounced. In figure 9.22 strong nearly periodic oscillations are clearly seen. They represent a striking coherent structure of a highly turbulent system. The oscillations are similar to the relaxation oscillations of convection in the absence of a magnetic field in that the convection columns can grow in amplitude only if the differential rotation is sufficiently weak. While viscous diffusion leads to the decay of $\overline{E}_t$ in the non-magnetic case, the axisymmetric poloidal component of the magnetic field breaks the differential rotation in the case of figure 9.22. Thus a period of about 0.02 is seen, instead of the period 0.1 resulting from the viscous decay. From figure 9.23 it is apparent that the radial dependence of the differential rotation and not only its amplitude changes throughout the oscillation period. Similarly the distribution of the azimuthal component $\overline{B_\varphi}$ of the magnetic flux density changes owing to the stretching of the meridional field lines by the differential rotation. The shearing action of the differential rotation on the magnetic field may be clearly observed in the plots of $\overline{B_\varphi}$ and the meridional field lines. The period of 0.02 corresponds roughly to that expected for a standing torsional Alfvén wave. There thus appears to be a resonance between the dynamo oscillation of figure 9.22 and a torsional Alfvén wave.

However, to establish more decisively whether or not the observed oscillations really represent torsional Alfvén waves, we check if they obey the corresponding equation. In order to obtain the equation governing torsional waves in the core we consider small perturbations $\boldsymbol{u}$ from an initial Taylor state. The primary state is geostrophic in the s- and z-dimensions where cylindrical coordinates (s, φ, z) are used. We expect that $u_s << u_\varphi$ and $u_z = 0$. The magnetic force contributes significantly to the force balance only in the φ-direction. After neglecting the buoyancy force the viscous dissipation and the magnetic diffusion from the momentum and induction equations (3.64b) and (3.64g), linearizing them to the first order in the perturbations and taking their φ-components as well as averaging over coaxial cylindrical surfaces we obtain a second order equation for u_φ
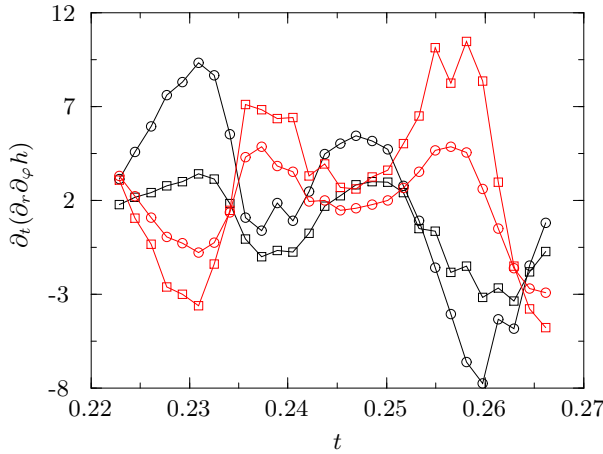
$$\frac{\partial^2}{\partial t^2}\overline{u}_\varphi = \frac{1}{s}\frac{\partial}{\partial s}\left[\frac{s}{z_+ - z_-}\int_{z_+}^{z_-} \overline{B}_s^2 dz \frac{\partial}{\partial s}\overline{u}_\varphi\right], \tag{9.1}$$

where $z_\pm$ denote the values $\pm\sqrt{r_o^2 - s^2}$ where coaxial cylinders with radius s intersect the outer spherical surface. Further details on the derivation of equation (9.1) may be found in [64]. This equation may be solved subject to suitable boundary conditions. However, we do not wish to solve equation (9.1), but only want to estimate its validity in numerical results similar to those presented in figures 9.22 and 9.23. Results for five dynamo cases which appear to satisfy approximately the balance of equation (9.1) are shown in figure 9.24 where the left-hand side and the right-hand side of the equation are compared. The equation is only approximately satisfied. However, this is hardly surprising, since the dynamo calculations are performed on the basis of the full set of nonlinear equations (3.64), including dissipation effects of turbulent convection as well as buoyancy and in addition have probably insufficiently high rotation rate τ. In this sense, the agreement observed in figure 9.24 is remarkably good. The values of the left- and right-hand side of (9.1) averaged over s are roughly equal in each plot in the figure. Despite the existence of intervals in s-direction where the two curves fail to balance, they both follow the same trend and the averaged correlation coefficients for the first five cases in the figure are all larger than 0.5. As the Rayleigh number R is increased the convection becomes increasingly turbulent and small-scaled which leads to seasonal changes in the curves representing the right-hand side of equation (9.1). Even in these cases, however, the trend and the averaged values of the two curves are roughly the same as may be seen after

Fig. 9.24. *Each row represents a time sequence of equidistant plots of the left-hand side (red) and right-hand side (blue) of equation* (9.1) *in the cases (a) $P = 0.1$, $\tau = 10^5$, $R = 2 \times 10^6$, $Pm = 1$, $\Delta t = 0.0016$, (b) $P = 0.1$, $\tau = 10^5$, $R = 2 \times 10^6$, $Pm = 2$, $\Delta t = 0.001$, (c) $P = 0.1$, $\tau = 10^5$, $R = 3 \times 10^6$, $Pm = 1$, $\Delta t = 0.0001$, (d) $P = 0.1$, $\tau = 10^5$, $R = 3 \times 10^6$, $Pm = 1$, $\Delta t = 0.005$, perfectly conducting IC., (e) $P = 0.1$, $\tau = 10^5$, $R = 3.4 \times 10^6$, $Pm = 3$, $\Delta t = 0.0016$, (f) $P = 0.1$, $\tau = 10^5$, $R = 4 \times 10^6$, $Pm = 0.5$, $\Delta t = 0.0001$. The green line in (d) and (e) represent a running average over 20 points of the right-hand side of the equation.*

running averages have been computed to smooth out the fast oscillations in cases *(d)* and *(e)*.

Fig. 9.25. *The secular variation of $\partial_t(\partial_r\partial_\varphi h)$ for the case presented in figure 9.22 at spherical coordinates (r,θ,φ) as follows: $(2.6r_o, 39°, 222°)$ (black line, circles), $(2.6r_o, 67°, 222°)$ (black line, squares), $(2.6r_o, 39°, 297°)$ (red line, circles) and $(2.6r_o, 67°, 297°)$ (red lines, squares).*

in order to show a contrast, the last case *(f)* in figure 9.24 shows a dynamo solution in the same parameter regime for which torsional oscillations are not observed. Here the balance of equation (9.1) is not satisfied, its left- and right-hand sides differ by orders of magnitude and the average coefficient of correlation between them is less than 0.1. Each of the six cases in figure 9.24 is represented by a sequence of plots equidistant in time in order to illustrate that the balance of equation (9.1) is approximately satisfied not only in s-direction but also in time. The two curves show a propagation of a wave as time increases.

After we have gained confidence in the fact that torsional oscillations exist in self-consistent dynamo simulations we wish to verify whether they could be observed in a way similar to the one in which jerks are observed at the surface of the Earth. For this reason the quantity $\partial_t(\partial_r\,\partial_\varphi h)$ which plays a role analogous to the secular variation of the magnetic declination D or of the East magnetic component Y, has been plotted in figure 9.25 at several different locations around the globe at a distance corresponding to the one of the Earth's surface. The plot covers two periods of the torsional oscillations shown in figure 9.22 and as a result two "jerks" should be observed. Indeed the changes in the trend of the curves at times $t_1 = 0235$ and $t_2 = 0.255$ may be interpreted as indications of such events. If this interpretation is correct, a further observation in figure 9.25 may be made. We may note that the secular variation records of the jerks may be correlated for observatories situated at roughly equal longitudes in the way the black curves in the figure are, but anticorrelated with other curves obtained at observatories at different longitudes, in the way the black and the red curves are. It may also be argued that locations could possibly exist where a jerk would not be detected. Figure 9.25 might be qualitatively compared with figures such as figure 1 and 2 of [87].

Future efforts need to focus on finding a parameter regime where the force balance leading to torsional oscillations is even better satisfied than in the cases shown in this section. Once such regime is found a a more detailed comparison with actual geomagnetic observations of the type presented in figure 9.25 might be done.

10. Summary and Discussion

10.1 Summary and discussion of results

Topic of dissertation. Results from numerical and analytical studies of convection and dynamo action in rotating fluid spheres and spherical shells are reported. The research is motivated by the geophysical problem of the origin and properties of the Earth's magnetism.

Extensive numerical simulations are performed in order to advance the understanding of the basic physical components and mechanisms believed to be responsible for the generation and the variations of the main geomagnetic field. Questions such as linear onset and finite-amplitude properties of rotating convection, generation and equilibration of magnetic fields, nonlinear feedback effects of self-sustained magnetic fields on convection, spatio-temporal structures of magnetic and velocity fields, oscillations and coherent processes in turbulent regimes and others are studied in dependence of all basic parameters of the problem, as well as for various choices of the velocity, magnetic and thermal boundary conditions and for some secondary assumptions such as a finitely-conducting inner core and various basic temperature profiles. Apart from clarification and parameter studies of basic physical mechanisms, the dissertation includes an analytical study of rotating inertial convection as well as some comparisons with actually observed geomagnetic features. However, the opportunities for analytical studies and direct geophysical implications are rather limited by the complexity of the self-consistent dynamo problem and by our approach toward its numerical simulation.

Publications. The results of the dissertation have been or will be published in references [29, 31, 32, 33, 34, 60, 107, 108, 109]. In addition the dissertation includes new results, and a large amount of additional details and refinements of those results already published, coupled with a systematic exposition of the methods used in the work.

10.1.1 Mathematical and numerical modeling

The derivation of the *pseudo-anelastic approximation* from first principles represents an original result of the dissertation. The main advantage of this approximation, in comparison with the traditionally used Boussinesq approximation, is that it accounts for compressibility in the basic static state of the model and allows for a radially-dependent static profile of the mass density to be taken into account. It is less general than the anelastic approximation [58] because constant material parameters of the fluid are assumed. However, this is not a major deficiency since the effect of the radially-dependent basic density profile is believed to be of primary importance compared with other effects of compressibility in the Earth's core [57]. This argument coupled with relative mathematical simplicity and ease of numerical implementation make the pseudo-anelastic approximation a gratifying generalization of the Boussinesq equations.

10.1.2 Convection in rotating fluid spheres and spherical shells

The most important physical component of convection-driven dynamos is convection itself. The majority of dynamo features are predetermined by the properties of convection. Thus,

a large part of the report is devoted to studies of non-magnetic convection in rotating fluid spheres and spherical shells under various assumptions and in dependence of the three basic parameters – the Rayleigh number R, the Coriolis number τ and the Prandtl number P.

Linear onset of convection. The two major types of rotating spherical convection – columnar and inertial are studied in extension of earlier works of Zhang and Busse [124], Ardes *et al.* [3], and Zhang [121] from numerical and analytical perspectives. The Prandtl number P_c separating the two types of convection decreases with increasing the Coriolis number τ [3].

Numerical studies on columnar and inertial convection. The numerical studies of the dissertation extend the parameter regions covered by [124] and [3] to values of P and τ in the ranges $10^{-7} \le P \le 10^2$ and $1 \le \tau \le 10^8$. The influence of fixed-flux thermal boundary conditions, which has been neglected in the earlier studies is also clarified.

• Inertial convection. With increasing τ a well-defined transition from a retrograde to a prograde drifting mode occurs. A contribution of the dissertation is that the border between those modes where the transition occurs is determined in the $P - \tau - \eta$ space of the problem for fixed-temperature boundary conditions. It is also tested numerically that the frequencies of both modes of inertial convection are approximately independent on the values of the radius ratio η which, for instance, is satisfied in the range $0.01 < \tau < 0.5$ for $P = 10^{-5}$. The transitions between inertial and columnar convection and between inertial and non-rotating convection are investigated in detail for particular values of the parameters. At asymptotically large τ a transition from single-cellular prograde inertial modes to multi-cellular inertial modes is observed. This phenomenon is reported in [98] in the case of cylindrical annulus. The results have motivated us to undertake an analytical study of inertial convection [34].

• Columnar convection. This is the type of convection believed to occur in the Earth's fluid core. The main contribution of the dissertation is the extension of the results of [124] and [3] to the case of fixed-flux thermal boundary conditions. A significant result is the observation that for values of P above unity and of τ nearly up to 10^4 the preferred wavenumber for the onset of convection is $m = 1$ when fixed-flux thermal boundary conditions are used while m grows monotonically reaching values of the order 15 for $P = 2$ $\tau = 10^4$ in the case of fixed-temperature boundary conditions. This result is important because those are exactly the values of P and τ genuinely accessible for nonlinear finite-amplitude convection and dynamo simulations. It indicates that a simple variation in the thermal boundary conditions may result in a totally different scale of convection and magnetic fields of drastically different dynamical behavior. Similar effect has been suggested in [25] due to a second source of buoyancy with sufficiently different diffusivity. However, shortage of time has prevented us from following this path of investigation and it is suggested as a future research objective. The critical Rayleigh number R_c as a function of the radius ratio of the shell and the competition of modes are also studied. The analytical expressions derived by Busse [13] for R_c on the basis of the annulus model are compared to numerical results in the $P - \tau$ space in the range $10^4 \le \tau \le 10^7$ and $10^{-8} \le P \le 10^{-2}$. These results are essential from a point of view of dynamo simulations. The knowledge of the precise value of R_c helps to predict the finite-amplitude properties of convection and thus avoid expensive three-dimensional computations in the vast parameter space which, for instance, may result in a decay of dynamo action.

Analytical study of inertial convection. The onset of convection in the form of inertial waves is studied through a perturbation analysis. The heat equation which appears in the first order of the perturbation scheme is solved analytically using a Green's function method. Explicit expressions for the dependence of the Rayleigh number of both retrograde and prograde drifting modes on the azimuthal wavenumber and on the product τP are derived and new results for the case of a nearly thermally insulating boundary are obtained. The results allow to make precise analytical predictions of the transition between the retrograde

and prograde drifting inertial modes and of the preferred wavenumber for given value of τP. It is believed that the multi-cellular inertial convection [98, 109] can be treated analytically in a similar way which also remains a topic for future research.

Finite-amplitude convection. Except close to onset finite-amplitude convection exhibits chaotic spatio-temporal behavior which has no simple description. To overcome this difficulty the report discusses both spatio-temporal structures of nonlinear convection and its averaged properties as functions of the parameters of the problem.

Spatio-temporal structures. Along with turbulent states which are of primary interest in planetary and stellar applications but allow limited insight into their spatial and temporal structures, a variety of more regular dynamical features at Rayleigh numbers not far above threshold are reported. Amplitude vacillations and shape modulations of convection columns are common features at moderate and large Prandtl numbers. In the low Prandtl number regime equatorially attached convection evolves differently with increasing Rayleigh number and exhibits an early transition into a chaotic state. The time dependence near onset often appears as a superposition of two or more modes with similar properties. Drifting at different rates they superimpose so that modulations of the their patterns appear.

A remarkable discovery of [62] and [59] has been that coherent structures can reappear in the turbulent regime. Examples are the localized convection and the relaxation oscillations caused by the interaction of differential rotation with the other convection components. Since coherent structures are of special interest for dynamo solutions, we extend the results of [62] and [59] in the parameter space and also for convection driven only by a temperature difference between the inner and outer spherical boundary. For small values of P localized structures and relaxation oscillations of columnar convection are easily found. However, when P is reduced below 0.025 convection enters the inertial regime. The equatorially-attached rolls are less sensitive to differential rotation and coherent structures do not appear. As P is increased beyond values of 3 thermal wind balance is found to dominate. The differential rotation rapidly decreases with P and coherent structures are again not observed. Polar convection develops at several times the critical Rayleigh number in all parameter regions.

Global properties of finite-amplitude convection such as time-averaged energy densities, profiles of the differential rotation and the heat transport are studied in the parameter space. Differential rotation is found to be very important in controlling the flow by suppressing the other convective motions through its shearing action. However, the results do not reveal simple scaling and asymptotic relations and studies reaching even more turbulent regime [39] should be confirmed for the full three-dimensional non-magnetic convection problem.

10.1.3 Convection-driven spherical dynamos

Extensive numerical simulations of convection-driven spherical dynamos are performed, spanning the computationally accessible parameter space and employing several possibilities for the magnetic and mechanical boundary conditions and the conductivity of the inner core. The goals of the computations are to ● outline the regions in the parameter space where dynamo action exists, ● explore the basic physical mechanisms of magnetic field generation and nonlinear saturation, including the effects of self-sustained magnetic fields on convection, ● observe the spatio-temporal structures and behavior of dynamo solutions, ● compare numerical results with actual geomagnetic observations, wherever possible. Because of the lack of knowledge of the properties of the Earth's core this research is necessary in order to provide the tools for extrapolation to realistic models of the geodynamo.

Parameter dependences and physical mechanisms. In addition to the three basic parameters of non-magnetic convection, the magnetic Prandtl number describing the ratio of the ohmic diffusion timescale to the viscous diffusion timescale appears in the problem.

The exploration of the parameter space extends the studies reported in the works of Grote *et al.* [62] and Grote and Busse [59]. Taking as a reference point these studies, the value of the Coriolis number τ is increased by a factor 10 reaching 10^5. The range of values of the Prandtl number which is difficult to change and has been kept fixed to 1 and 0.5 in [62] and [59] is extended both towards smaller values reaching $P = 0.025$ and towards larger values reaching $P = 300$. A main objective of the research is to obtain sustained magnetic fields at values of the magnetic Prandtl number as small as possible and it is a remarkable achievement to do so down to values of $Pm = 0.1$. The values of Pm and R are easier to vary and are often adjusted to the values of the rest of the parameters in order to sustain magnetic fields. However, in the region of large rotation rates ($\tau = 10^5$) the Rayleigh number for onset of convection and dynamo action increases by an order of magnitude from the cases studied in [62] and [59] and values as large as $R = 10^7$ are reached in our simulations.

Many of the dynamo features relate to the general symmetry properties of dynamo solutions. Dynamos of dipolar, quadrupolar, hemispherical and mixed types are reported in [62] and [59]. A major goal is to outline the range of parameters for which convection-driven dynamos can be obtained and the parameter regions where a particular type of dynamo symmetry is dominant. Dynamo action is generally found to occur at values of the magnetic Reynolds number somewhat larger than one hundred. In the moderate and high Prandtl number regions the observation emerges that quadrupolar dynamos are found for lower values of the magnetic Prandtl number Pm while dipolar dynamos predominate at higher values of Pm and also at higher values of the Rayleigh number R. This is in strong contrast to the region of small Prandtl numbers (e.g. $P = 0.1$, $\tau = 10^5$) where only dipolar and hemispherical dynamos exist but no quadrupolar dynamos are found. This is explained by another significant result that dynamo action ceases to operate when the convective motions become too vigorous and small-scaled i.e. no-dynamo regions exist not only for too small values of R but also for too large values of R. At $Pm = 0.1$ and $P = 0.1$, $\tau = 10^5$ a working dynamo of hemispherical type is still found. The reduction of the value of Pm and the simultaneous increase of R in an attempt to obtain a quadrupolar dynamo leads to a decay of the magnetic field for this reason. Thus, no-dynamo regions are found below and above the region of working dynamos for sufficiently small P.

Effects of generated magnetic fields on convection. The main effect of self-sustained magnetic fields on convection is to break and strongly suppress differential rotation and as a consequence to enhance convection and the heat transport. Since imposed magnetic fields have even stronger effect on rotating convection and reduce the value of R_c [36], it is surprising that subcritical finite amplitude convection is not found in dynamo simulations. However, when no-slip boundary conditions are used the opposite effect is found that magnetic fields lead to a decrease in kinetic energy. This is explained with the fact that for no-slip conditions the differential rotation is much weaker already in the non-magnetic case and so does not suppress convection significantly. Thus, in this case magnetic fields do not relax the constraint of differential rotation but rather drain the energy of convection. Furthermore, no-slip conditions have been found to stabilize dipolar magnetic fields while a perfectly conducting inner core promotes quadrupolar dynamos. A finitely conducting inner core has only little effect, altogether, because magnetic fields have insufficient time to penetrate the region. The presence of magnetic fields is also found to inhibit coherent structures of convection such as localized convection and relaxation oscillations except for very low values of P where the oscillations bear certain characteristics of torsional rather than of relaxation oscillations.

Equilibration of averaged global quantities. The nonlinear saturation and equilibration of averaged magnetic and kinetic energies and dissipations of convection-driven spherical dynamos are among the most important questions in nonlinear dynamo theory. In the dis-

sertation those processes are studied on a very large number of cases in dependence of all four basic parameters. • Rayleigh number dependence. A typical example of the equilibration process as a function of R is provided by the case $\tau = 5 \times 10^3$, $Pr = Pm = 1$, where convection driven dynamos are studied for values R up to about 20 times the critical value. The original energy sequence reported in [59] is extended to improve the statistical significance of the average kinetic and magnetic energies. While the onset of dynamo action occurs with quadrupolar symmetry it is found that the dipolar contributions to the magnetic field start with the onset of convection in the polar regions and increase more rapidly with R than the quadrupolar ones. The increasingly filamentary structure of the magnetic field leads to a decrease of the energy of its axisymmetric components while the growth of the non-axisymmetric components approaches saturation at the highest values of R that could be investigated without significant numerical problems. The other sequences constructed to study the R-dependence confirm this general picture that while both kinetic energies and Ohmic and viscous dissipations increase with R the magnetic energy has a maximum at intermediate values of this parameter. • Coriolis number dependence. At intermediate values of τ the presence of magnetic field suppresses differential rotation and enhances the fluctuating components of convection and the kinetic and magnetic energies increase as functions of τ. • Prandtl number dependence, magnetostrophic approximation. The Prandtl number dependence of dynamos poses the very important question about the validity of the magnetostrophic approximation. Special efforts have been devoted to address this question through numerical simulations in the region of large values of P and the magnetostrophic approximation is found to be poorly satisfied at least for values of P below 300. The reason for this is that differential rotation which is an important factor in the dynamo process still depends strongly on the value of the Prandtl number in this region. • Thus, the extensive studies of the equilibration process performed in the accessible parameter space do not reveal any simple scaling relations or asymptotic behavior for the values of the time-averaged energy densities and dissipations as functions of the basic parameters.

Spatio-temporal structures. The cyclical processes are of much importance in view of the parameter range accessible to modern numerical simulations. In the case when parameter values are "mild" the dynamos are steady or periodic. Parameter values which are geophysically realistic are inaccessible computationally [103] but as far as one can reach in this direction increasingly chaotic convection and filamentary small-scale fields without well-defined structure are found. In the intermediate parameter regions genuinely accessible today oscillatory behavior is typical. While the H_2^0 part of the magnetic field is oscillatory in case it is dominant, the axial dipolar part H_1^0 oscillates only when higher degree components have significant contributions as well. As a result the quadrupolar and hemispherical dynamos always oscillate in a very similar manner [59]. Non-oscillatory quadrupolar dynamos are found only when perfectly conducting inner core used. Dipolar dynamos have been originally considered to be non-oscillatory [62, 59] but the six different types of dipolar oscillations reported in the dissertation alter this view. Among other situations, the non-oscillatory dipoles begin to oscillate when Pm is decreased or R is increased. In the first case this is due to the increasing contribution of higher degree components while in the second case to the onset of polar convection. Further typical examples of dipolar oscillations are found in the high Prandtl number dynamos where only the equatorial region of the spherical shell oscillates while strong magnetic flux tubes at the polar regions remain little affected by the oscillation and appear as "invisible oscillations" from the Earth's surface. At small values of P the differential rotation is sufficiently strong and interacts with magnetic fields in ways which result in still different types of dipolar oscillatory behavior. The dynamos found in the small Prandtl number regions are remarkable in even more aspects. Although not typical, these

solutions exhibit dynamo intermittency which is an important manifestation of the nonlinear nature of dynamo solutions. The intermittency leads to a dynamo solution switching aperiodically between several attracting states in which the dynamo may exhibit very different general properties. The dynamo intermittency is found to be a precondition for magnetic field polarity reversals very similar to those believed to have actually occurred in the case of the Earth.

Comparisons with geomagnetic observations. Our approach to geodynamo simulations is to explore basic physical mechanisms and parameter dependences rather than to build a realistic model of the Earth of the sort reported in [57, 56, 103] and others. Thus, the parameter values used here are remote from geophysical ones and no actual claims of realism are made. However, our simulations certainly resemble in many ways the characteristic features of the geomagnetic field and some comparisons between them are both tempting and unavoidable.

Magnetic field polarity transitions. Examples of dipolar magnetic field polarity reversals are found in our simulations. Only a fraction of them are similar to actual geomagnetic polarity transitions. Based on one of them, a typical reversal mechanism is proposed. However, this mechanism is not sufficiently simple since it poses deeper fundamental questions. Nevertheless, it is very useful because it provides insight to questions raised in the literature [88]. In particular, we argue that no triggering effect due to the fluid flow is necessary to cause reversals. The polarity transitions seem to occur because of the delicate balance between energy components and a nonlinear superposition of dipolar and quadrupolar dynamo oscillations. Furthermore, in several instances of its time series the dynamo enters very similar transitional states and yet only in two of them it actually reverses implying that a dynamo may be much more often in a reversing state which is not an excursion in the sense that it can not be detected from the Earth's surface.

Torsional oscillations. Existence of Alfvén torsional waves in three dimensional self-consistent numerical simulations is reported in the dissertation for the first time. The appropriate cases found in the small Prandtl number region are tested against the differential equation governing the oscillation process and are found to be in good agreement. Future efforts need to focus on finding a parameter regime where the force balance leading to torsional oscillations is even better satisfied than in the cases shown in this chapter. Once such regime is found a detailed comparison with actual geomagnetic observations of the type presented in [87] may be done.

10.2 Some future objectives

Many open questions and possible extensions of the research carried out in the dissertation have been pointed out in the text. Here we explicitly mention two important possibilities.

A practical implementation of the pseudo-anelastic approximation and an exploration of the effects of various profiles of radial dependence of the mass density in the core may be performed. The programing implementation is a routine task after the pseudo-anelastic equations and their spectral and time discretizations have been derived.

An important objective for future research is the investigation of double-diffusive convection. Interesting possibility for new dynamical regime in the presence of a second source of buoyancy is suggested by Busse [25]. The equation governing the perturbation of concentration is already implemented in the numerical code in the frame of the current research project and a number of simulations are performed. These are not reported in the dissertation since further improvements of the available results are necessary.

A. Appendices

A.1 Notation

The Appendix provides a key to the notation used in the dissertation. Only the symbols most commonly occurring throughout the text are given. Other symbols are explained in the text.

- $\overline{X}$ – Azimuthal average.
- $\check{X}$ – Fluctuating part: $X - \overline{X}$.
- $\langle X \rangle$ – Volume average.
- $\langle X \rangle_t$ – Time average.
- $\langle X \rangle_{\theta,\varphi}$ – Average over a spherical surface.
- ∂_t – Eulerian time derivative, $\frac{\partial}{\partial t}$.
- α – Alpha pseudo-tensor, dipole axis tilt angle.
- α_C, α_T – Expansion coefficients, $(d\rho/dI)_i/\rho$, $I = C, T$ and $i = T, C$.
- ΔT – Temperature difference between boundaries.
- ε_0, μ_0 – Electric, magnetic permeability.
- ζ, V – Material volume, volume fixed in space.
- η – Ratio of inner to outer radii of the spherical shell.
- κ_C, κ_T, κ'_T – Diffusion coefficients of light elements and heat.
- λ – Magnetic diffusivity.
- Λ – Elsasser number.
- ν – Kinematic viscosity.
- π – "Reduced" pressure, $p/\rho - (\boldsymbol{\Omega} \times \boldsymbol{r})^2/2$.

- ρ, $\delta\rho$ – Density, density perturbation.
- τ – Coriolis number.
- ω – Frequency.
- $\boldsymbol{\Omega}$ – Angular velocity.
- $\boldsymbol{B}$ – Magnetic field.
- C, Γ – Concentration, concentration perturbation.
- d – Length scale; thickness of the spherical shell.
- D_t – Total time derivative (Material, Lagrangian).
- $\hat{\boldsymbol{e}}$ – Unit vector.
- $\boldsymbol{E}$ – Electric field.
- $E, \overline{E}, \check{E}$ – Kinetic energy density; Mean, fluctuating part.
- $\boldsymbol{g}$, g – Gravitational force, acceleration due to gravity.
- g, G – Magnetic field toroidal scalar.
- h, H – Magnetic field poloidal scalar.
- $\boldsymbol{J}$ – Current density.
- $\boldsymbol{m}$ – Linear momentum.
- m – Wavenumber.
- $M, \overline{M}, \check{M}$ – Magnetic energy density; Mean, fluctuating part.

- Nu – Nusselt number.
- O – Ohmic dissipation.
- p – Pressure.
- P – Prandtl number.
- Pm – Magnetic Prandtl number.
- Q – Effective strength of external influences or sources.
- $\boldsymbol{r}$ – Position vector.
- (r, θ, φ) – Spherical polar coordinates.
- r_i, r_o – inner, outer radii of the spherical shell.
- R, R_c – Rayleigh number; Critical Rayleigh number.
- Re – Reynolds number.
- Rm – Magnetic Reynolds number.
- S – Entropy.
- $\hat{\boldsymbol{S}}$ – Stress tensor.
- T, Θ – Temperature, temperature perturbation.
- $\boldsymbol{u}$ – Velocity field.
- v, V – Velocity poloidal scalar.
- V – Viscous dissipation.
- w, W – Velocity toroidal scalar.

A.2 Reynolds' transport theorem

To establish the validity of (3.2) we make use of a parametric representation of the position vector of a fluid particle $\boldsymbol{r} = \boldsymbol{r}(\boldsymbol{\xi}, t)$. The parameter $\boldsymbol{\xi}$ could represent, for example, the initial position of the particle at time $t = 0$. By changing variables, the material volume $\zeta(t)$ can be mapped to a volume ζ_0 in the same way as a particle can be mapped to its initial position. Since the initial volume ζ_0 of the material element is fixed the differentiation and integration commute and the total time derivative is replaced by the material derivative because a material volume is considered [1]

$$\frac{\mathrm{d}}{\mathrm{d}t} \int_{\zeta(t)} Z(\boldsymbol{r}, t)\, \mathrm{d}\zeta = \frac{\mathrm{d}}{\mathrm{d}t} \int_{\zeta_0} Z(\boldsymbol{r}(\boldsymbol{\xi}, t), t) J\, \mathrm{d}\zeta_0 = \int_{\zeta_0} \mathrm{D}_t[Z(\boldsymbol{r}(\boldsymbol{\xi}, t), t) J]\, \mathrm{d}\zeta_0 \tag{A.1}$$

$$= \int_{\zeta_0} J \mathrm{D}_t Z + Z \mathrm{D}_t J\, \mathrm{d}\zeta_0 = \int_{\zeta_0} [\mathrm{D}_t Z + Z\nabla \cdot \boldsymbol{u}] J\, \mathrm{d}\zeta_0 = \int_{\zeta(t)} (\mathrm{D}_t Z + Z\nabla \cdot \boldsymbol{u})\, \mathrm{d}\zeta.$$

The Jacobian J must be non-vanishing for the transformations between $\boldsymbol{r}$ and $\boldsymbol{\xi}$ to exist. The total time derivative of J may be obtained by direct differentiation:

---

[1] In contrast, for a volume fixed in space (Eulerian description) the differentiation and integration immediately commute i.e. $\frac{\mathrm{d}}{\mathrm{d}t} \int_V \mathrm{d}V = \int_V \mathrm{d}V \partial_t$. Then in order to formulate conservation laws, additional fluxes through the surface bounding the fixed volume must be considered.

$$\mathrm{D}_t J = \mathrm{D}_t \frac{\partial(x_1, x_2, x_3)}{\partial(\xi_1, \xi_2, \xi_3)} = \mathrm{D}_t \varepsilon_{ijk} \frac{\partial x_i}{\partial \xi_1} \frac{\partial x_j}{\partial \xi_2} \frac{\partial x_k}{\partial \xi_3}$$

$$= \varepsilon_{ijk} \frac{\partial u_i}{\partial x_m} \frac{\partial x_m}{\partial \xi_1} \frac{\partial x_j}{\partial \xi_2} \frac{\partial x_k}{\partial \xi_3} + \varepsilon_{ijk} \frac{\partial x_i}{\partial \xi_1} \frac{\partial u_j}{\partial x_m} \frac{\partial x_m}{\partial \xi_2} \frac{\partial x_k}{\partial \xi_3} + \varepsilon_{ijk} \frac{\partial x_i}{\partial \xi_1} \frac{\partial x_j}{\partial \xi_2} \frac{\partial u_k}{\partial x_m} \frac{\partial x_m}{\partial \xi_3} \qquad (A.2)$$

$$= J \frac{\partial u_1}{\partial x_1} + J \frac{\partial u_2}{\partial x_2} + J \frac{\partial u_3}{\partial x_3} = J \nabla \cdot \boldsymbol{u}$$

where the fact that a determinant of a matrix with repeating rows is zero is also used. x_i, ξ_i, u_i are Cartesian components of $\boldsymbol{r}$, $\boldsymbol{\xi}$ and $\boldsymbol{u}$, respectively and ε_{ijk} is the Levi-Civita symbol.

A.3 Rotating reference frame

The transformation from an inertial to a rotating reference frame may be done in a number of ways, many of which are described in the standard texts in Mechanics. A most algorithmic method consists of writing the Euler matrix describing the transformation between the reference frames and taking its time derivatives. Here we make use of the operator of infinitesimal rotation.

An infinitesimal transformation of a vector $\boldsymbol{p}$ is given by

$$\boldsymbol{p}' = \hat{A}\boldsymbol{p} = (1 + \hat{e})\boldsymbol{p} \qquad (A.3)$$

where $\hat{e}$ is infinitesimal operator. The inverse of $\hat{A}$ is $1 - \hat{e}$ since

$$\hat{A}\hat{A}^{-1} = (1 + \hat{e})(1 - \hat{e}) = 1 - \hat{e}^2 \approx 1. \qquad (A.4)$$

Furthermore since we are interested in rotations, $\hat{A}$ must be orthogonal and from $\hat{A}^T = \hat{A}^{-1}$ follows that $\hat{e} = -\hat{e}^T$. Therefore

$$\hat{e} = \begin{pmatrix} 0 & \mathrm{d}\phi_3 & -\mathrm{d}\phi_2 \\ -\mathrm{d}\phi_3 & 0 & \mathrm{d}\phi_1 \\ \mathrm{d}\phi_2 & \mathrm{d}\phi_1 & 0 \end{pmatrix}, \qquad \mathrm{d}\boldsymbol{p} = \hat{e}\boldsymbol{p} = \begin{pmatrix} 0 & \mathrm{d}\phi_3 & -\mathrm{d}\phi_2 \\ -\mathrm{d}\phi_3 & 0 & \mathrm{d}\phi_1 \\ \mathrm{d}\phi_2 & \mathrm{d}\phi_1 & 0 \end{pmatrix} \begin{pmatrix} p_1 \\ p_2 \\ p_3 \end{pmatrix} = \boldsymbol{p} \times \mathrm{d}\boldsymbol{\phi} \qquad (A.5)$$

and the transformation of $\boldsymbol{p}$ is given by

$$\boldsymbol{p}' = \boldsymbol{p} + \boldsymbol{p} \times \mathrm{d}\boldsymbol{\phi}, \qquad (A.6)$$

where $\boldsymbol{\phi}$ represents a vector with magnitude equal to the angle of rotation and in direction of the axis of rotation. If we assume that $\boldsymbol{p}'$ corresponds to the vector in the rotating reference frame, and $\boldsymbol{\Omega} = \frac{\mathrm{d}\boldsymbol{\phi}}{\mathrm{d}t}$, its time derivative transforms according to

$$\hat{\Re}\partial_t \boldsymbol{p} = (\partial_{t'} + \boldsymbol{\Omega} \times)\boldsymbol{p}'. \qquad (A.7)$$

At this point one can easily transform the acceleration between inertial and rotating reference frame:

$$\frac{\mathrm{d}\boldsymbol{u}}{\mathrm{d}t} = (\hat{\Re}\partial_t)^2 \boldsymbol{r} = \left(\frac{\mathrm{d}}{\mathrm{d}t'} + \boldsymbol{\Omega} \times \right)^2 \boldsymbol{r} = \frac{\mathrm{d}\boldsymbol{u}'}{\mathrm{d}t'} + 2\boldsymbol{\Omega} \times \boldsymbol{u}' + \boldsymbol{\Omega} \times (\boldsymbol{\Omega} \times \boldsymbol{r}) + \frac{\mathrm{d}\boldsymbol{\Omega}}{\mathrm{d}t'} \times \boldsymbol{r}. \qquad (A.8)$$

A.4 Poloidal-toroidal representation

Definitions and general statements.

Definition A.4.1. *A* **toroidal field** $\boldsymbol{A}_T$ *is any field of the form*

$$\boldsymbol{A}_T = \nabla \times T(\boldsymbol{r})\boldsymbol{r}, \qquad (A.9)$$

where $T(\boldsymbol{r})$ *is any scalar function of position* $\boldsymbol{r}$.

Definition A.4.2. *A* **poloidal field** $\boldsymbol{A}_P$ *is any field of the form*

$$\boldsymbol{A}_P = \nabla \times \nabla \times P(\boldsymbol{r})\boldsymbol{r}, \qquad (A.10)$$

where $P(\boldsymbol{r})$ *is any scalar function of position* $\boldsymbol{r}$.

One may note that addition of any arbitrary function of $|\boldsymbol{r}|$ to T or P has no effect on $\boldsymbol{A}_T$ or $\boldsymbol{A}_P$, respectively. Thus without loss of generality we assume that the averages of T or P vanish.

Theorem A.4.1. *Any solenoidal vector* $\boldsymbol{A}$, *i.e. a vector for which* $\nabla \cdot \boldsymbol{A} = 0$ *is satisfied, may be represented as*

$$\boldsymbol{A} = \boldsymbol{A}_P + \boldsymbol{A}_T = \nabla \times \nabla \times P(\boldsymbol{r})\boldsymbol{r} + \nabla \times T(\boldsymbol{r})\boldsymbol{r}. \qquad (A.11)$$

A proof of this theorem in the spherical case is given by Backus in 1958 [4].

Expressions for P and T.

$$P = (\mathcal{L}_2)^{-1}(\boldsymbol{r} \cdot \boldsymbol{A}), \qquad T = (\mathcal{L}_2)^{-1}\boldsymbol{r} \cdot (\nabla \times \boldsymbol{A}). \tag{A.12}$$

Use (A.18) and (A.19) to prove.

Components of $\boldsymbol{A}_P$ and $\boldsymbol{A}_T$ in spherical polars.

$$\boldsymbol{A}_T^T = \left(0, \; \frac{1}{\sin\theta}\partial_\varphi T, \; -\partial_\theta T\right), \qquad \boldsymbol{A}_P^T = \left(\frac{1}{r}\mathcal{L}_2 P, \; \partial_\theta\frac{1}{r}\partial_r(rP), \; \frac{1}{\sin\theta}\partial_\varphi\frac{1}{r}\partial_r(rP)\right). \tag{A.13}$$

The formulas may be verified by direct evaluation using the definitions (A.9) and (A.10).

Simple properties.

$$\boldsymbol{r} \cdot \boldsymbol{A}_T = 0, \tag{A.14}$$
$$\boldsymbol{r} \cdot \boldsymbol{A}_P = \mathcal{L}_2 P, \tag{A.15}$$
$$\nabla \times \boldsymbol{A}_T = \boldsymbol{C}_P, \tag{A.16}$$
$$\nabla \times \boldsymbol{A}_P = -\nabla \times \boldsymbol{r}\nabla^2 P = \boldsymbol{C}_T, \tag{A.17}$$

where $\boldsymbol{C}_P$ is poloidal and $\boldsymbol{C}_T$ is toroidal,

$$\boldsymbol{r} \cdot \boldsymbol{A} = (\boldsymbol{r} \times \nabla)^2 P = \mathcal{L}_2 P, \tag{A.18}$$
$$\boldsymbol{r} \cdot \nabla \times \boldsymbol{A} = (\boldsymbol{r} \times \nabla)^2 T = \mathcal{L}_2 T, \tag{A.19}$$
$$\boldsymbol{r} \cdot \nabla \times \nabla \times \boldsymbol{A} = -\mathcal{L}_2 \nabla^2 P. \tag{A.20}$$

A.5 Chebyshev polynomials

The Chebyshev polynomials are orthogonal over a weight $\sqrt{1 - x'^2}$ in the interval $-1 \leq x' \leq 1$ and are defined there as

$$T_n(x') = \cos\left(n\arccos(x')\right). \tag{A.21}$$

One may map the interval $-1 \leq x' \leq 1$ onto the interval $0 \leq x \leq 1$ by a change of the variable $x = 1/2(x' + 1)$.

References

1. Abramowitz, M., Stegun, I.A., *Handbook of mathematical functions*, Dover, New York, 1972
2. Ahlers, G., Xu, X., Prandtl-number dependence of heat transport in turbulent Rayleigh-Bénard convection, *Phys. Rev. Lett.*, **86**, 3320–3323, 2001
3. Ardes, M., Busse, F.H., Wicht, J., Thermal convection in rotating spherical shells, *Phys. Earth Planet. Inter.*, **99**, 55–67, 1997
4. Backus, G., A class of self-sustaining dissipative spherical dynamos, *Ann. Phys.*, **4**, 372–447, 1958
5. Batchelor, G.K., *An Introduction to Fluid Dynamics*, Cambridge University Press, Cambridge, 1967
6. Bloxham, J., Zatman, S., Dumberry, M., The origin of geomagnetic jerks, *Nature*, **240**, 65–68, 2002
7. Braginsky, S.I., Torsional magnetohydrodynamic vibrations in the Earth's core and variations in day length, *Geomagn. Aeron.*, **10**, 1–8, 1970
8. Braginsky, S.I., Dynamics of the stably stratified ocean at the top of the core, *Phys. Earth Planet. Inter.*, **111**, 21–34, 1999
9. Braginsky, S.I., Roberts, P.H., Equations governing convection in Earth's core and the geodynamo, *Geophys. Astrophys. Fluid Dyn.*, **79**, 1–97, 1995
10. Bullard, E.C., The magnetic field within the Earth, *Proc. R. Soc. Lond.*, **A197**, 433–453, 1949
11. Bullard, E.C., Gellman, H., Homogeneous dynamos and terrestrial magnetism, *Phil. Trans. R. Soc. Lond.*, **A247**, 213–278, 1954
12. Busse, F.H., Differential rotation in stellar convection zones, *Astrophys. J.*, **159**, 629–639, 1970
13. Busse, F.H., Thermal instabilities in rapidly rotating systems, *J. Fluid. Mech.*, **44**, 441–460, 1970
14. Busse, F.H., Generation of magnetic fields by convection, *J. Fluid Mech.*, **57**, 529–544, 1973
15. Busse, F.H., A model of the geodynamo, *Geophys. J. R. Astron. Soc.*, **42**, 437–459, 1975
16. Busse, F.H., A necessary condition for the geodynamo, *J. Geophys. Res.*, **80**, 278–280, 1975
17. Busse, F.H., Generation of planetary magnetism by convection, *Phys. Earth Planet. Inter.*, **12**, 350–358, 1976
18. Busse, F.H., Mathematical problems of dynamo theory, in *Applications of Bifurcation Theory*, ed. P.H. Rabinowitz, pp. 175–202, Academic Press, 1977
19. Busse, F.H., Magnetohydrodynamics of the Earth's dynamo, *Ann. Rev. Fluid Mech.*, **10**, 435–462, 1978
20. Busse, F.H., Recent developments in the dynamo theory of planetary magnetism, *Ann. Rev. Earth Planet. Sci.*, **11**, 241–268, 1983

21. Busse, F.H., Asymptotic theory of convection in a rotating cylindrical annulus, *J. Fluid Mech.*, **173**, 545–556, 1986

22. Busse, F.H., Fundamentals of thermal convection, in *Mantle Convection, Plate Tectonics and Global Dynamics*, ed. W.R. Peltier, pp. 24–95, Gordon and Breach, 1989

23. Busse, F.H., Homogeneous dynamos in planetary cores and in the laboratory, *Ann. Rev. Fluid Mech.*, **32**, 383–408, 2000

24. Busse, F.H., Convective flows in rapidly rotating spheres and their dynamo action, *Phys. Fluids*, **14**, 1301–1314, 2002

25. Busse, F.H., Is low Rayleigh number convection possible in the Earth's core?, *Geophys. Res. Lett.*, **29**, GLO149597, 2002

26. Busse, F.H., Bénard convection and geophysical applications, in *Dynamics of spatio-temporal structures: Henri-Bénard centenary review*, eds. E. Guyon I. Mutabazi, J.E. Wesfreid, Springer, 2004, *to be published*

27. Busse, F.H., Carrigan, C.R., Laboratory simulation of thermal convection in rotating planets and stars, *Science*, **191**, 81, 1976

28. Busse, F.H., Cuong, P.G., Convection in rapidly rotating spherical fluid shells, *Geophys. Astrophys. Fluid Dyn.*, **8**, 17–41, 1977

29. Busse, F.H., Grote, E., Simitev, R., Convection in rotating spherical shells and its dynamo action, in *Earth's Core and Lower Mantle*, eds. C.A. Jones, A.M. Soward, K. Zhang, pp. 130–152, Taylor & Francis, 2003

30. Busse, F.H., Grote, E., Tilgner, A., On convection driven dynamos in rotating spherical shells, *Studia geoph. et geod.*, **42**, 211–223, 1998

31. Busse, F.H., Simitev, R., Current state and future challenges of the dynamo theory of planetary magnetism, in *Fundamental and Applied MHD, (Proc. 5th Int.* PAMIR *Conference, Ramatuelle)*, pp. L1–L13, LEGI, Grenoble, 2002

32. Busse, F.H., Simitev, R., Convection in rotating spherical fluid shells, in *Mathematical Aspects of Natural Dynamos*, ed. E. Dormy, Caramulo, 2004, *to be published*

33. Busse, F.H., Simitev, R., Convection in rotating spherical fluid shells and its dynamo states, in *Fluid Dynamics and Dynamos in Astrophysics and Geophysics*, eds. A.M. Soward, C.A. Jones, D.W. Hughes, N.O. Weiss, Taylor & Francis, 2004, *to be published*

34. Busse, F.H., Simitev, R., Inertial convection in rotating fluid spheres, *J. Fluid Mech.*, **498**, 23–30, 2004

35. Canuto, C., Hussaini, M.Y., Quarteroni, A., Zang, T.A., *Spectral Methods in Fluid Dynamics*, Springer, New York, 1988

36. Chandrasekhar, S., *Hydrodynamic and Hydromagnetic Stability*, Clarendon Press, Oxford, 1961

37. Childress, S., Soward, A.M., Convection-driven hydromagnetic dynamo, *Phys. Rev. Lett.*, **29**, 837–839, 1972

38. Chossat, P., Armbruster, D., Oprea, I., eds., *Dynamo and Dynamics, a Mathematical Challenge*, Kluwer Academic Publishing, Dodrecht, 2001

39. Christensen, U.R., Zonal flow driven by strongly supercritical convection in rotating spherical shells, *J. Fluid Mech.*, **470**, 115–133, 2002

40. Christensen, U.R., Olson, P., Glatzmaier, G.A., Numerical modeling of the geodynamo: A systematic parameter study, *Geophys. J. Int.*, **138**, 393–409, 1999

41. Courtillot, V., Ducruix, J., Le Mouël, J.-L., Sur une accélération récente de la variation séculaire du champ magnétique terrestre, *C.R. Acad. Sci. D*, **287**, 1095–1098, 1978

42. Courtillot, V., Le Mouël, J.-L., Time variations of the Earth's magnetic field: From daily to secular, *Ann. Rev. Earth Planet. Sci.*, **16**, 389–476, 1988

43. Cowling, T.G., The magnetic field of sunspots, *Mon. Not. R. Astron. Soc.*, **94**, 39–48, 1934

44. Davidson, P.A., *An Introduction to Magnetohydrodynamics*, Cambridge University Press, Cambridge, 2001

45. Dolginov, A.Z., Magnetic field generation in celestial bodies, *Phys. Rep.*, **162**, 337–415, 1988

46. Dormy, E., Valet, J.-P., Courtillot, V., Numerical models of the geodynamo and observational constraints, *Geochem. Geophys. Geosyst.*, **1**, 2000GC000062, 2000

47. Durran, D.R., *Numerical Methods for Wave Equations in Geophysical Fluid Dynamics*, Springer, New York, 1999

48. Elsasser, W.M., Induction effects in terrestrial magnetism. Part II. The secular variation, *Phys. Rev.*, **70**, 202–212, 1946

49. Eschrich, K.-O., Rüdiger, G., A second-order correlation approximation for thermal conductivity and Prandtl number of free turbulence, *Astron. Nachr.*, **304**, 171–180, 1983

50. Fearn, D.R., Thermal and magnetic instabilities in a rapidly rotating fluid sphere, *Geophys. Astrophys. Fluid Dyn.*, **14**, 103–126, 1976

51. Fearn, D.R., Loper, D.E., Compositional convection and stratification of the Earth's core, *Nature*, **289**, 393–394, 1981

52. Gailitis, A., Lielausis, O., Dement'ev, S., Platacis, E., Cifersons, A., Christen, M., Hänel, H., Will, G., Detection of a flow induced magnetic field eigenmode in the Riga dynamo facility, *Phys. Rev. Lett.*, **84**, 4365–4368, 2000

53. Galdi, G.P., *An Introduction to the Mathematical Theory of the Navier–Stokes Equations*, Springer, Heidelberg, 1994

54. Glatzmaier, G.A., Coe, R.S., Hongre, L., Roberts, P.H., The role of the Earth's mantle in controlling the frequency of geomagnetic reversals, *Nature*, **401**, 885–890, 1999

55. Glatzmaier, G.A., Roberts, P.H., A three–dimensional self–consistent computer simulation of a geomagnetic field reversal, *Nature*, **377**, 203–209, 1995

56. Glatzmaier, G.A., Roberts, P.H., A three-dimensional convective dynamo solution with rotating and finitely conducting inner core and mantle, *Phys. Earth Planet. Inter.*, **91**, 63–75, 1995

57. Glatzmaier, G.A., Roberts, P.H., An anelastic evolutionary geodynamo simulation driven by compositional and thermal convection, *Physica D*, **97**, 81–94, 1996

58. Gough, D.O., The anelastic approximation for thermal convection, *J. Atmos. Sci.*, **26**, 448–456, 1969

59. Grote, E., Busse, F.H., Dynamics of convection and dynamos in rotating spherical fluid shells, *Fluid Dyn. Res.*, **28**, 349–356, 2001

60. Grote, E., Busse, F.H., Simitev, R., Buoyancy driven convection in rotating spherical shells and its dynamo action, in *High Performance Computing in Science and Engineering '01*, eds. E. Krause, W. Jäger, pp. 12–34, Springer, Heidelberg, 2001

61. Grote, E., Busse, F.H., Tilgner, A., Effects of hyperdiffusivities on dynamo simulations, *Geophys. Res. Lett.*, **27** (13), 2001–2004, 2000

62. Grote, E., Busse, F.H., Tilgner, A., Regular and chaotic spherical dynamos, *Phys. Earth Planet. Inter.*, **117**, 259–272, 2000

63. Gubbins, D., Kelly, P., Persistent patterns in the geomagnetic field over the past 2.5 Myr, *Nature*, **365**, 829–832, 1993

64. Gubbins, D., Roberts, P.H., Magnetohydrodynamics of the Earth's core, in *Geomagnetism 2*, ed. J.A. Jacobs, pp. 1–184, Academic Press, London, 1987

65. Gubbins, D., Zhang, K., Symmetry properties of the dynamo equations for paleomagnetism and geomagnetism, *Phys. Earth Planet. Inter.*, **75**, 225–241, 1993

66. Hart, J.E., Glatzmaier, G.A., Toomre, J., Space–laboratory and numerical simulations of thermal convection in a rotating hemispherical shell with radial gravity, *J. Fluid Mech.*, **173**, 519–544, 1986

67. Herzenberg, A., Geomagnetic dynamos, *Phil. Trans. R. Soc. Lond.*, **A250**, 543–583, 1958

68. Hirsching, W., Busse, F.H., Stationary and chaotic dynamos in rotating spherical shells, *Phys. Earth Planet. Inter.*, **90**, 243–254, 1995

69. Hollerbach, R., Jones, C.A., Influence of the Earth's inner core on geomagnetic fluctuations and reversals, *Nature*, **365**, 541–543, 1993

70. Holme, R., The main magnetic field, *http://www.gfz-potsdam.de/pb2/pb23/Mag/*

71. Ishihara, N., Kida, S., Dynamo mechanism in a rotating spherical shell: competition between magnetic field and convection vortices, *J. Fluid Mech.*, **465**, 1–32, 2002

72. Jault, D., Le Mouël, J.-L., The topographic torque associated with tangentially geostrophic motion at the core surface and inferences in the flow inside the core, *Geophys. Astrophys. Fluid Dyn.*, **48**, 107–120, 1989

73. Jones, C.A., Longbottom, A.W., Hollerbach, R., A self-consistent convection driven geodynamo model using a mean field approximation, *Phys. Earth Planet. Inter.*, **92**, 119–141, 1996

74. Jones, C.A., Soward, A.M., Mussa, A.I., The onset of thermal convection in a rapidly rotating sphere, *J. Fluid Mech.*, **405**, 157–179, 2000

75. Kageyama, A., Ochi, M.M., Sato, T., Flip–flop transitions of the magnetic intensity and polarity reversals in the magnetohydrodynamic dynamo, *Phys. Rev. Lett.*, **82**, 5409–5412, 1999

76. Kageyama, A., Sato, T., Computer simulation of a magnetohydrodynamic dynamo. II, *Phys. Plasmas*, **2**, 1421–1431, 1995

77. Kageyama, A., Sato, T., Generation mechanism of a dipole field by a magnetohydrodynamic dynamo, *Phys. Rev. E*, **55**, 4617–4626, 1997

78. Karato, S.-I., Seismic anisotropy of Earth's inner core caused by the Maxwell stress-induced flow, *Nature*, **402**, 871–873, 1999

79. Kono, M., Roberts, P.H., Recent geodynamo simulations and observations of the geomagnetic field, *Rev. Geophys.*, **40(4)**, 1013, 2002

80. Kuang, W., Bloxham, J., An Earth–like numerical dynamo model, *Nature*, **389**, 371–374, 1997

81. Kutzner, C., Christensen, U.R., Effects of driving mechanisms in geodynamo models, *Geophys. Res. Lett.*, **27** (1), 29–32, 2000

82. Kutzner, C., Christensen, U.R., From stable dipolar towards reversing numerical dynamos, *Phys. Earth Planet. Inter.*, **131**, 29–45, 2002

83. Larmor, J., How could a rotating body such as the Sun become a magnet?, *Rep. Brit. Assoc. Adv. Sci.*, **A**, 159–160, 1919

84. Lister, J.R., Buffett, B.A., The strength and efficiency of thermal and compositional convection in the Earth's core, *Phys. Earth Planet. Inter.*, **91**, 17–30, 1995

85. Loper, D., Structure of the core and lower mantle, *Adv. Geophys.*, **26**, 1–34, 1984

86. Lortz, D., Mayer-Spasche, R., On the decay of symmetric dynamo fields, *Math. Met. Appl. Sci.*, **4**, 91–97, 1982

87. Mandea, M., Bellanger, E., Le Mouël, J.-L., A geomagnetic jerk for the end of the 20th century?, *Earth Planet. Sci. Lett.*, **183**, 369–373, 2000

88. Merrill, R.T., McFadden, P.L., Geomagnetic polarity transitions, *Rev. Geophys.*, **37**, 201–226, 1999

89. Moffatt, H.K., *Magnetic Field Generation in Electrically Conducting Fluids*, Cambridge University Press, Cambridge, 1978

90. Morelli, A., Dziewonski, A.M., Topography of the core-mantle boundary and lateral inhomogeneity of the liquid core, *Nature*, **325**, 678–683, 1987

91. Müller, U., Stieglitz, R., *Naturwissenschaften*, **87**, 381, 2000

92. Namikawa, T., Matsushita, S., Kinematic dynamo problem, *Geophys. J. R. Astron. Soc.*, **19**, 395–415, 1970

93. Olsen, N., *et al.* , Ørsted initial field model, *Geophys. Res. Lett.*, **27**, 3607–3610, 2000

94. Olson, P., Christensen, U.R., Glatzmaier, G.A., Numerical modeling of the geodynamo: Mechanisms of field generation and equilibration, *J. Geophys. Res.*, **104**, 10383–10404, 1999

95. Olson, P., Glatzmaier, G.A., Magnetoconvection in a rotating spherical shell: structure of flow in the outer core, *Phys. Earth Planet. Inter.*, **92**, 109–118, 1995

96. Parkinson, W.D., *Introduction to Geomagnetism*, Elsevier Science Publishing, Edinburgh, 1983

97. Pearlstein, A., Effect of rotation on the stability of a doubly diffusive fluid layer, *J. Fluid Mech.*, **103**, 389–412, 1981

98. Pino, D., Mercader, I., Net, M., Thermal and inertial modes of convection in a rapidly rotating annulus, *Phys. Rev. E*, **61(2)**, 1507–1517, 2000

99. Press, W.H., Teukolsky, S.A., Vetterling, W.T., Flannery, B.P., *Numerical Recipes in FORTRAN*, Cambridge University Press, Cambridge, 2. edition., 1992

100. Roberts, P.H., On the thermal instability of a rotating–fluid sphere containing heat sources, *Proc. R. Soc. Lond. A*, **263**, 93–117, 1968

101. Roberts, P.H., Origin of the main field: Dynamics, in *Geomagnetism 2*, ed. J.A. Jacobs, pp. 251–306, Academic Press, London, 1987

102. Roberts, P.H., Fundamentals of dynamo theory, in *Lectures on Solar and Planetary Dynamos*, eds. M.R.E. Proctor, A.D. Gilbert, pp. 1–58, Cambridge University Press, 1994

103. Roberts, P.H., Glatzmaier, G.A., Geodynamo theory and simulations, *Rev. Mod. Phys.*, **72(4)**, 1081–1123, 2000

104. Roberts, P.H., Soward, A.M., Dynamo theory, *Ann. Rev. Fluid Mech.*, **24**, 459–512, 1992

105. Sakuraba, A., Kono, M., Effect of the inner core on the numerical solution of the magnetohydrodynamic dynamo, *Phys. Earth Planet. Inter.*, **111**, 105–121, 1999

106. Sarson, G.R., Jones, C.A., A convection driven geodynamo reversal model, *Phys. Earth Planet. Inter.*, **111**, 3–20, 1999

107. Simitev, R., Inertial wave convection in rotating spherical fluid shells, in *2002 Geophysical Fluid Dynamics Program "Bounds on Turbulent Transport"*, ed. J.A. Whitehead, Tech. Rep. WHOI-02-16, 148–175, Woods Hole, MA, 2002

108. Simitev, R., Busse, F.H., Parameter dependences in convection driven spherical dynamos, in *High Performance Computing in Science and Engineering '02*, eds. E. Krause, W. Jäger, pp. 15–35, Springer, Heidelberg, 2002

109. Simitev, R., Busse, F.H., Patterns of convection in rotating spherical shells, *New J. Phys.*, **5**, 97.1–97.20, 2003

110. Soward, A.M., On the finite amplitude thermal instability of a rapidly rotating fluid sphere, *Geophys. Astrophys. Fluid Dyn.*, **9**, 19–74, 1977

111. Steenbeck, M., Krause, F., Rädler, K.-H., A calculation of the mean emf in an electrically conducting fluid in turbulent motion, under the influence of Coriolis forces, *Z. Naturforsch.*, **A21**, 369–376, 1966

112. Taylor, J.B., The magneto-hydrodynamics of a rotating fluid and the Earth's dynamo problem, *Proc. R. Soc. Lond.*, **A274**, 274–283, 1963

113. Tilgner, A., Spectral methods for the simulation of incompressible flows in spherical shells, *Int. J. Numer. Meth. Fluids*, **30**, 713–724, 1999

114. Tilgner, A., Busse, F.H., Finite–amplitude convection in rotating spherical fluid shells, *J. Fluid Mech.*, **332**, 359–376, 1997

115. Whaler, K.A., Does the whole of the Earth's core convect? New evidence from geomagnetism, *NATURE*, **287**, 528–530, 1980

116. Wicht, J., Inner-core conductivity in numerical dynamo simulations, *Phys. Earth Planet. Inter.*, **132**, 281–302, 2002

117. Wicht, J., Busse, F.H., Magnetohydrodynamic dynamos in rotating spherical shells, *Geophys. Astrophys. Fluid Dyn.*, **86**, 103–129, 1997

118. Yano, J.-I., Asymptotic theory of thermal convection in rapidly rotating systems, *J. Fluid Mech.*, **243**, 103–131, 1992

119. Zhang, K., Convection in a rapidly rotating spherical shell at infinite Prandtl number: transition to vacillating flows, *Phys. Earth Planet. Inter.*, **72**, 236–248, 1992

120. Zhang, K., On equatorially trapped boundary inertial waves, *J. Fluid Mech.*, **248**, 203–217, 1993

121. Zhang, K., On coupling between the Poincaré equation and the heat equation, *J. Fluid Mech.*, **268**, 211–229, 1994

122. Zhang, K., On coupling between the Poincaré equation and the heat equation: non-slip boundary condition, *J. Fluid Mech.*, **284**, 239–256, 1995

123. Zhang, K., Nonlinear magnetohydrodynamic convective flows in the Earth's fluid core, *Phys. Earth Planet. Inter.*, **111**, 93–103, 1999

124. Zhang, K., Busse, F.H., On the onset of convection in rotating spherical shells, *Geophys. Astrophys. Fluid Dyn.*, **39**, 119–147, 1987

125. Zhang, K., Busse, F.H., Some recent developments in the theory of convection in rotating systems, in *Nonlinear Instability, Chaos and Turbulence, vol.1*, eds. L. Debnath, D.N. Riahi, pp. 17–69, WIT Press, Southampton, 1998

126. Zhang, K., Earnshaw, P., Liao, X., Busse, F.H., On inertial waves in a rotating fluid sphere, *J. Fluid Mech.*, **437**, 103–119, 2001

127. Zhang, K., Jones, C.A., Convective motions in the Earth's fluid core, *Geophys. Res. Lett.*, **21**, 1939–1942, 1994

128. Zhang, K., Jones, C.A., The effect of hyperviscosity on geodynamo models, *Geophys. Res. Lett.*, **24**, 2869–2872, 1997

129. Zhang, K., Schubert, G., Magnetohydrodynamics in rapidly rotating spherical systems, *Ann. Rev. Fluid Mech.*, **32**, 409–443, 2000

Acknowledgments